

GEOLOGICA ULTRAIECTINA

Mededelingen van de
Faculteit Geowetenschappen
Universiteit Utrecht

No. 233

**Interseismic and coseismic surface deformation
deduced from space geodetic observations**

with inferences on seismic hazard, tectonic processes, earthquake
complexity, and slip distribution

Annemarie G. Bos

**Interseismic and coseismic surface deformation deduced
from space geodetic observations**

with inferences on seismic hazard, tectonic processes, earthquake complexity,
and slip distribution

**Interseismische en co-seismische oppervlakteformatie
afgeleid uit ruimte-geodetische observaties**

met een gevolgtrekking voor aardbevingsrisico, tektonische processen,
complexiteit van een aardbeving en slip distributie

(met een samenvatting in het Nederlands)

PROEFSCHRIFT

TER VERKRIJGING VAN DE GRAAD VAN DOCTOR
AAN DE UNIVERSITEIT UTRECHT
OP GEZAG VAN DE RECTOR MAGNIFICUS, PROF. DR. W.H. GISPEN,
INGEVOLGE HET BESLUIT VAN HET COLLEGE VOOR PROMOTIES
IN HET OPENBAAR TE VERDEDIGEN
OP MAANDAG 10 NOVEMBER 2003 DES MIDDAGS TE 12.45 UUR

DOOR

Annemarie Gerredina Bos

Geboren op 24 mei 1975, te Emmen

Promotor: Prof.Dr. W. Spakman
Department of Tectonophysics
Faculty of Geosciences
Utrecht University

The research described in this thesis was carried out at:
Faculty of Geosciences
Vening Meinesz Research School of Geodynamics
Utrecht University
Budapestlaan 4
3584 CD Utrecht
The Netherlands

<http://www.geo.uu.nl/Research/Tectonophysics/>

ISBN: 90-5744-092-X

*Vos igitur doctrine & sapientæ filii,
perquirite in hoc libro,
colligendo nostram dispersam intentione,
quam in diversis locis propofuimus,
& quod occultatum est a nobis in uno loco,
manifestum fecimus illud in alio,
ut sapientibus vobis patefiat.*

Heinrich Cornelius Agrippa von Nettesheim,
De occulta philosophia, III, 65

Voor mijn ouders

Members of the dissertation committee:

Prof.Dr. B.A.C. Ambrosius
Faculty of Aerospace Engineering
Technical University of Delft

Prof.Dr. S.A. Stein
Department of Geological Sciences
Northwestern University

Prof.Dr. M.J.R. Wortel
Faculty of Geosciences
Utrecht University

Dr. C.A. Vigny
Laboratoire de Geologie
École Normale Supérieure

Contents

1	Introduction and summary	11
1.1	Space geodetic techniques	12
1.2	Modeling techniques	13
1.2.1	Dynamic modeling	13
1.2.2	Kinematic modeling	13
1.3	Additional crustal deformation data	14
1.4	Outline of this thesis	15
2	Kinematics of the South-Western US Deformation Zone inferred from GPS motion data.	17
2.1	Introduction	17
2.2	Tectonic Setting	19
2.3	Relative motion data	20
2.4	Inversion method and model parameterization	22
2.5	Inversion	25
2.6	Description of the three solutions	29
2.6.1	Fault motion	29
2.6.2	Strain rate	32
2.6.3	Rotation rate	35
2.6.4	Asymmetry of the surface deformation field	35
2.6.5	Comparison to paleomagnetic observations	38
2.7	Implications for seismic hazard	38
2.8	Crustal deformation of the SWUSDZ	43
2.9	Conclusions	45
3	Surface deformation and tectonic setting of Taiwan inferred from a GPS velocity field.	47
3.1	Introduction	47
3.2	Geologic setting	50
3.3	GPS data	50

3.4	The Spakman-Nyst method	51
3.5	Inversions	54
3.5.1	I: Inversion for fault slip rate only	56
3.5.2	II: Inversion for continuous deformation only	57
3.5.3	III: Inversion for fault slip rate and continuous deformation	59
3.6	Geometry of the subduction system	65
3.7	Model interpretation	67
3.7.1	Southern Taiwan: southward extrusion	67
3.7.2	Central Taiwan: oblique collision, shortening and exhumation	69
3.7.3	Northern Taiwan: crustal extension and orogenic collapse	71
3.7.4	The Coastal Range: incipient northwestward subduction of the PSP	72
3.8	Geodynamic evolution	72
3.9	Summary and conclusions	74
4	A joint analysis of GPS motions and InSAR to infer the coseismic surface deformation of the Izmit, Turkey Earthquake.	77
4.1	Introduction	77
4.2	Data	79
4.2.1	GPS data	79
4.2.2	InSAR interferograms	79
4.3	GPS data inversion	82
4.4	Joint analysis	85
4.5	Coseismic surface deformation	86
4.5.1	Solution I: Model based on GPS data only	86
4.5.2	Solution II: Model based on a joint analysis of GPS and InSAR	91
4.6	Discussion	93
4.6.1	Influence of fault geometry	93
4.6.2	Double source rupture process	98
4.6.3	Implications on slip distribution modeling	99
4.6.4	Relaxation of the long-term strain field	100
4.7	Conclusions	100
5	The resolving power of coseismic surface displacement data for fault slip distribution at depth.	103
5.1	Introduction	103
5.2	Procedure	104
5.3	Coseismic slip distribution model	105
5.4	Model resolution	107
5.5	Surface displacement field	108
5.6	The data kernel	110

5.7	Conclusions	111
6	Epilogue	113
6.1	Concluding remarks	113
6.2	Recommendations for future research	114
	Bibliography	117
A	South-Western US Deformation Zone.	129
A.1	Comparison to geological and present-day interseismic slip rates	129
A.2	Comparison of solution II to related work	130
A.3	Postseismic deformation	132
A.4	Surface deformation field of the Basin and Range province	133
B	Fault slip rates SWUSDZ.	137
C	Colour figures.	141
C.1	South-western US deformation zone	142
C.2	Taiwan	148
C.3	Izmit	152
	Samenvatting voor de leek (Summary in Dutch)	159
	Dankwoord (Acknowledgments)	163
	Curriculum Vitae	165

Chapter 1

Introduction and summary

Long before space geodetic techniques had achieved the level of precision necessary for monitoring the detail of surface deformation, it was clear that they would provide a new class of independent constraints on regional and global plate tectonics (e.g. Bosworth et al., 1993). The foremost problems that needed addressing were (i) the "rigidity" or "non-rigidity" of the interior of the plates, (ii) the stationarity of plate motion rates through recent geologic time, and (iii) the kinematics of diffuse deformation zones separating some plates (Stein, 1993). Over the past few decades, the increasing precision of the space geodetic observations, as well as the increasing quantity and spatial density of the space geodetic networks, have led to major contributions towards the answers of these problems and in the understanding of the kinematics and dynamics of crustal deformation. Still, key problems in the study of intra-plate deformation remain: (i) the lack of independent data to constrain the often complex regional kinematics and the accommodation of the crust-lithosphere strain accumulation/release in crustal blocks and/or along faults, (ii) the poorly known rheological behavior of the crust and lithosphere, specifically lateral variations in rheology, and (iii) the approximations/simplifications used for modeling the forces/stresses in crustal dynamics.

In this thesis I am concerned with modeling the kinematics of surface deformation using space geodetic observations in order to advance insight in both interseismic and coseismic surface response. Interseismic surface deformation models are of prime importance for understanding the dynamics causing deformation (England and Houseman, 1989; Jackson and Molnar, 1990) and in seismic hazard analysis (WGCEP, 1995), while the coseismic surface deformation field provides important information on the complexity of an earthquake and the crustal properties, as well as on the relaxation of the long-term deformation field during an earthquake. To model the surface deformation field I adopt the method of Spakman and Nyst (2002) which resolves the velocity (displacement) field and the motion (slip) on the fault simultaneously. The main advantages of this method compared to other methods are (i) the fact that it is based entirely on the kinematic principles of continuous deformation and fault motion, (ii) the incor-

poration of fault motion without assumptions on crustal or fault behavior, and (iii) the determination of the model from an inversion of all data simultaneously. These advantages allow the determination of the localization of deformation near slipping faults and provide a complete description of surface deformation. The implementation of fault motion is particularly important for the purely kinematic estimation of a coseismic surface deformation field. Additionally, I investigate (i) to what extent available geodetic observations help in constraining seismic hazard in the southwestern US (chapter 2) and present-day tectonic processes of Taiwan (chapter 3), and (ii) how space geodetic data can help in analyzing earthquake complexity and slip distribution (chapters 4 and 5).

In this introductory chapter I will provide an overview of the space geodetic observation methods from which data are used in this thesis and the modeling techniques developed during the past decades. Subsequently, an outline of the research contained in this thesis is presented.

1.1 Space geodetic techniques

During the mid 1980's Satellite Laser Ranging (SLR) and Very Long Baseline Interferometry (VLBI) were able to provide the first measurements of contemporary plate motions (Bennett et al., 2002; Christodoulis et al., 1985; Herring et al., 1986). Though both systems have a high accuracy potential and are giving results over intercontinental distances, they proved to have some serious disadvantages for crustal dynamic studies. The most important of these being the spatially very sparse and inhomogeneous distribution of stations.

In the early 1990's a new satellite system became operational: the Global Positioning System (GPS). This system proved to be an all-weather, continuously available, economic, and very precise positioning technique. GPS is a satellite-based radio navigation system providing precise three-dimensional positioning information. The system consists of 24 satellites orbiting the Earth at a distance of $\sim 20,200$ km and is continuously available on a world-wide basis. The satellite arrangement is such that at least four satellites are simultaneously visible anywhere on Earth, 24 hours a day. Knowing the coordinates of the four satellites, we can determine the coordinates of the user antenna. Currently, the precision of the GPS, SLR and VLBI velocity/displacement estimates range from 1 to 5 mm/yr. Continuous GPS arrays are even able to achieve a precision on the sub-mm level.

Another space geodetic/remote sensing technique is Interferometric Synthetic Aperture Ranging (InSAR). This technique provides a one-dimensional continuous image of crustal deformation in the line-of-sight of the satellite. Though the obtained image is strongly dependent on radar correlation, topography, and tropospheric artifacts it has the strength of providing nearly spatially continuous data on crustal deformation.

1.2 Modeling techniques

Along with the development of geodetic observation systems, a variety of techniques incorporating the observations in crustal deformation modeling have been created. These methods range from dynamic modeling methods to purely kinematic modeling methods.

1.2.1 Dynamic modeling

The first set of modeling techniques is based on assumptions about the rheological behavior of the Earth's crust and lithosphere. For instance, by assuming the forces acting at plate boundaries and stresses acting at the base of the plates (Forsyth and Uyeda, 1975; Wortel et al., 1991), finite element methods can predict the intraplate crustal deformation. Generally, these models consist of a weak upper crust, where surface deformation is dictated by the motions of the ductile lower crust or uppermost mantle. In these models, the geodetic observations may serve as a kinematic boundary condition at the Earth's surface (England and Houseman, 1989; Jackson and Molnar, 1990) while faults can be approximated by the implementation of strong crustal blocks embedded in weak, easily deforming crust (Peltzer and Tapponnier, 1988; England and Houseman, 1985).

In an inverse approach, models based on the elastic dislocation theory of Okada (1985) use geodetic observations to obtain estimates of interseismic slip rates, while assuming an elastic behavior of the crust. The simplest of these models contain a half-space with uniform slip on fault extensions in the ductile lower crust and elastic deformation in the upper crustal layer resulting from fault locking (Bennett et al., 1996; Genrich et al., 2000; Matsu'ura et al., 1986; Savage et al., 1979). More complicated models implement a shallow creeping layer containing processes of drag folding and rotations of small blocks adjacent to the fault (King et al., 1994) or rotations of elongated blocks within the deformation zone (Freund, 1970; McKenzie and Jackson, 1983, 1986). The theory can also be implemented to deduce slip distribution models of earthquakes (Feigl et al., 2002; Freymueller et al., 1994; Hudnut et al., 1994; Reilinger et al., 2000). In this application the fault is parameterized by relatively small dislocation patches and slip on each patch is estimated by inversion of geodetic observations.

1.2.2 Kinematic modeling

In contrast with these techniques are the methods that are based on the geometrical/kinematical concepts of crustal deformation. Though the models derived yield no immediate quantitative results about the dynamical behavior of the crust, they do provide information on the distribution of strain accumulation which constrains the geodynamical processes driving the deformation and depict an important intermediate step in establishing "depth-to-surface" relations. The least squares collocation

method (Moritz, 1989) is the most widely used technique in kinematic modeling of space geodetic data. The method is based on the interpolation in data space by assuming a particular correlation between the relative motion data (Kahle et al., 2000; Kato et al., 1998; Straub, 1996; Ward, 1998). Through spatial differentiation of the interpolated data field a continuous velocity gradient field can be calculated. Haines and Holt (1993) developed a method which is very similar to least squares collocation and directly incorporates strain rate data. The method inverts average strain rates and geodetic data for a depth average of the horizontal velocity field. The average strain rates used as data are first derived through Kostrov's relation (Kostrov, 1974) from seismic moment tensors or geological (fault slip) data. The average strain rates may remain unspecified in case only the geodetic observations are to be fit (Beavan and Haines, 2001; Shen-Tu et al., 1999).

Instead of spatial interpolation of the data, a relation between the geodetic observations and the velocity gradient field based on physical theory may be introduced by the parameterization of the unknown velocity gradient field and the definition of a shape function. The unknown coefficients of the shape function are subsequently determined by inversion of the data. Generally, a simple triangulation of the station network is adopted and a constant velocity gradient field is assumed (Frank, 1996; Bourne et al., 1998). The most recent development among these kinematic modeling techniques is the method of Spakman and Nyst (2002). This method relates relative observations between stations to a combination of continuous deformation and fault motion along an arbitrary integration path and was derived from basic kinematic principles underlying the velocity gradient field and fault motion. Through a triangular parameterization of the velocity gradient field with a linear behavior within the triangles and the adaptation of step functions on the fault segments, the method is able to resolve both contributions simultaneously in an inversion of relative motion data.

1.3 Additional crustal deformation data

Space geodetic data are of course not the only source of data that depict the style of crustal deformation. Tectonic geomorphology provides a means for measuring the often significant strain between major fault zones or strain not accommodated by surface-breaking ruptures, whereas borehole breakout and hydraulic fracturing stress measurements provide localized information about the principal stress directions of the crustal deformation field. Another significant data source are the earthquake moment tensor solutions. The centroid moment tensors provide information on the local stress release during an earthquake. However, though stress and strain (rate) are related quantities, the principal axis of stress and strain (rate) do not necessarily align in case of an elastoplastic rheology, which hampers a comparison between these quantities. Geological fault slip observations and paleomagnetic rotations contain information about the long-

term crustal deformation and typically span time intervals of thousands to millions of years. Tectonic activity can, however, also vary on these timescales and therefore geological slip observations and paleomagnetism may not always be representative for present-day activity.

1.4 Outline of this thesis

In **chapter 2** the surface deformation field of the southwestern US deformation zone is estimated in terms of the velocity gradient field and fault motion simultaneously by inversion of 497 geodetic velocities. The model shows fault motion consistent with aseismic creep measurements and with relative fault motion. The surface deformation field shows distributed deformation in a zone around the faults exhibiting shear strains and relative rotations. The eastern California shear zone acts as a distinct fault zone bounded by more rigid blocks. The faults within the zone partition the shear motion, while right-lateral shear strain rates and clockwise rotations are concentrated between the bounding faults. In the same way, the San Jacinto and southern San Andreas faults act as bounding faults of a fault zone. The Mojave Desert and eastern Transverse Ranges are dominated by right-lateral shear, whereas the western Transverse Ranges are subjected to contraction. The sense of rotation of these regions is consistent with models based on paleomagnetic observations. Significant localization of deformation is observed east of the San Andreas fault between the Transverse Ranges and San Francisco Bay. This is attributed to a relative rigidity contrast across the fault of ~ 1.8 caused by a strong granite basement west of the fault and weak material east of the fault. A seismic hazard analysis based on the surface deformation model shows an increased risk of a $M_w = 6.1 - 6.3$ earthquake in the San Francisco Bay on the Hayward and southern Calaveras faults.

In **chapter 3** I am concerned with the determination of the present-day surface deformation of Taiwan by computing the velocity gradient field and fault slip rate from 143 GPS velocity vectors. In southern Taiwan the derived strain, rotation and fault slip rates are indicative of lateral extrusion towards the south. In northern Taiwan the onset of gravitational collapse is inferred which is induced by the on land extension of the Okinawa Trough. In the eastern Central Range the observed inverted NW-SE extension is consistent with geological observations and high heat flow measurements. This could be the result of exhumation of crustal material. The model further shows a significant decrease in slip rate northward along the Longitudinal Valley fault at 23.7°N . The northern Coastal Range shows high strain rates and two oppositely rotating blocks. By combining the surface deformation model with seismicity data and seismic tomography a coherent model for the present-day tectonic activity can be proposed. Both seismicity and tomography show further evidence for active, southward propagating exhumation of a crustal slice in the eastern Central Range. Offshore east Taiwan strong evidence of

a southward propagating crustal tear fault, accommodating most of the Phillipine Sea Plate-Eurasian Plate convergence, is deduced. The tear is the crustal response to incipient northwestward subduction of the Phillipine Sea Plate. Thus, the Ryukyu Trench is bending southward becoming almost perpendicular to the convergence direction, while subduction of the Phillipine Sea Plate continues. In this setting a sudden rapid southward propagation of the afore mentioned tear is conceivable.

In **chapter 4** the kinematic surface deformation of the August 17 1999, Izmit (Turkey) earthquake is inferred in terms of strain, rotation and fault slip in a joint analysis of GPS and InSAR data. The fault slip contribution shows two distinct peaks: one of $\sim 4\text{m}$ of slip at Gölcük, and a second of $\sim 2.9\text{m}$ slip near Sapanca Lake. The strain field portrays four distinct quadrants reflecting the earthquake focal mechanism. The transition between the quadrants is not centered on the epicenter of the event, but shifted eastward north of the fault and westward south of the fault. This shift is the result of a two-stage source rupture process caused by step-over features in the fault geometry. This rupture process also induced a distinct asymmetry in the displacement field across the fault. We obtain left-lateral shear strains along the Sakarya segment which is due to a subsequent source nucleating at the Akyazi Gap inducing failure on the easternmost segments. Strong interaction is also observed from a consecutive source near Hersek. Finally, I deduce that the Izmit earthquake has released most of the strain which has accumulated since the last main event on this stretch of the North Anatolian fault in 1719.

As an additional objective of **chapter 4** I originally started to investigate the link between the surface deformation model and the slip distribution theory of Okada (1985). However, not only proved the deformation field of the Izmit earthquake to be too complex to be appropriately modeled by a simple elastic dislocation theory, but also the resolution of the slip distribution model seriously hampered interpretation of these models. These observations motivated the research described in chapter 5. **Chapter 5** describes a quantitative analysis of the resolution of slip distribution models based on surface displacement data. Assuming the theory of elastic dislocations in a half-space and adopting a parameterization for which model predictions are capable of fitting the spatial variations of the data, the inverse problem proves to be intrinsically ill-conditioned.

Chapter 2

Kinematics of the South-Western US Deformation Zone inferred from GPS motion data.

2.1 Introduction

In the southwestern US the boundary between the Pacific and North American plates comprises a broad zone of deformation portraying a variety of distinct deformation styles and regions of complex tectonics (e.g. Transverse Ranges, eastern California shear zone). An important constraint on the present-day tectonics in this region is an accurate description of the velocity gradient field because this field provides important kinematic boundary conditions for dynamic modeling (e.g. England and Houseman, 1989; Jackson and Molnar, 1990), as well as a means to estimate moment deficits used for seismic hazard analysis (WGCEP, 1995). Space geodetic techniques, primarily the global positioning system (GPS), now provide a great source of information about the patterns and rates of deformation across spatial scales of order 10 to 1000 km. Throughout the southwestern US deformation zone, for example, continuously operating networks of GPS stations have been in operation since the mid-1990's (e.g. SCEC, BARD, BARGEN, EBRY). Further densification is provided by the many campaign sites from which data have become readily available (e.g. Bennett et al., 1997; Dixon et al., 2000a,b; Gan et al., 2000; Miller et al., 2001; Shen et al., 1996; Thatcher et al., 1999). Recently Bennett et al. (1999, 2002) and Bennett (2003) integrated data from a large number of the continuous and campaign networks in southwestern US to obtain a dataset within one single reference frame.

Because space geodetic positioning techniques provide velocity estimates at spe-

This chapter has been submitted for publication to *J. Geoph. Res.* as: A.G. Bos, W. Spakman and R.A. Bennett, Kinematics of the South-Western US Deformation Zone inferred from GPS motion data.

cific points in space, and the density of available points is quite variable depending on the region and scale of investigation (kilometers to 100's of kilometers), resolution of the spatially continuous velocity gradient tensor field depends heavily on the number and distribution of available stations. Most methods start with some interpolation of the geodetic data in data space. For example, Snay et al. (1996) implement a bilinear interpolation scheme to transfer crustal deformation information from geodetic sites to grid nodes. Strain and rotation rates were subsequently obtained by discrete spatial differentiation of the horizontal velocity grid. Shen et al. (1996) and Ward (1998) resolved the strain and rotation rates at any arbitrary sample points by a weighted least-squares inversion of the geodetic velocity estimates basically assuming smoothness of the crustal velocity field. Along similar lines, Shen-Tu et al. (1998, 1999) invert average strain rates from seismological and geological inferences and/or geodetic velocity estimates for a spatially variable Euler vector function that described the horizontal velocity field on the Earth's surface. The rotation vector function was represented by a bicubic Bessel interpolation. Bennett (2003) regularized the velocity gradient inverse problem by considering the relative motions among and internal deformations within a very small number of geodetically defined strain provinces. Previous studies have tended to concentrate on either the details of relatively small regions, or on relatively low resolution broad-scale features. None of these previous investigations incorporated (a) seismic motion on faults as part of their model parameterization.

In this chapter I analyze an updated version of the southwestern US crustal velocity data set of Bennett (2003), with the aim of capturing both the broad-scale pattern of deformation, and the finer-scale details of the deformation field in a single self-consistent surface deformation model. From this data set, I estimate the horizontal velocity gradient field, as well as creep on all major faults using the inversion procedure proposed by Spakman and Nyst (2002). This method is based on the kinematics of incremental deformation in a model space formulation and incorporates no assumptions about the dynamics or rheology of the crust. The method allows for densification of the model parameterization in areas of increased data density, providing more detail in the surface deformation field modeled where appropriate, while at the same time accounting for both plate-scale deformation patterns and small-scale displacement discontinuities associated with near surface fault creep. This multiscale parameterization has the potential to determine whether strong jumps in relative velocities across faults signify creep on the faults (King et al., 1994; Nicholson et al., 1986) or alternatively rapid strain accumulation on locked seismogenic faults (Bennett et al., 1996; King et al., 1994).

I use this technique to derive a surface deformation model for which I evaluate the consistency of the contemporary strain rate field with the long-term strain rate field derived from seismic and geological fault slip data and corresponding moment tensors. I will also derive the moment deficit owing to the difference between the geodetic moment derived from my strain rate field and the seismic moment derived from moment

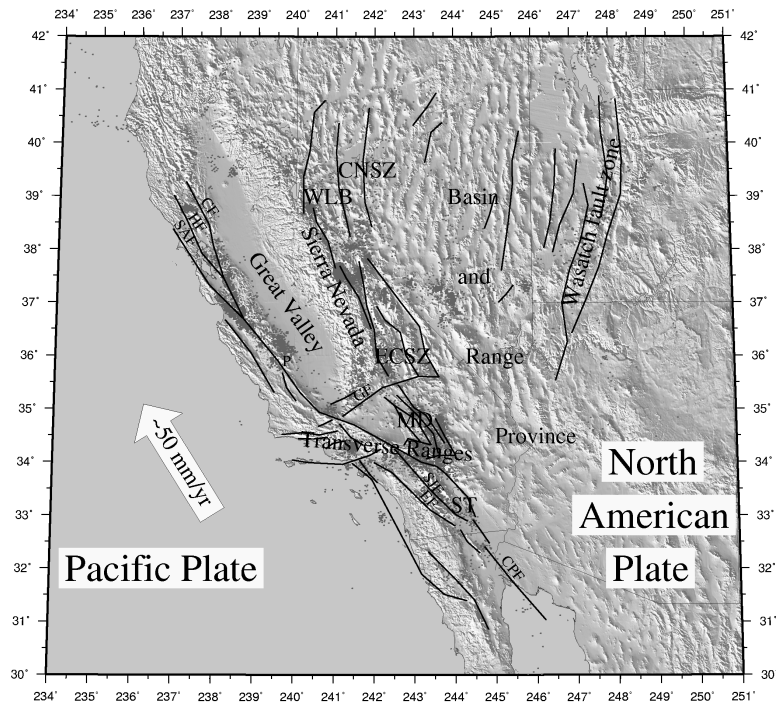


Figure 2.1: Tectonic setting of the southwestern US deformation zone plotted against topography. Black lines indicate the fault traces utilized in the model parameterization. Grey dots indicate the shallow (< 20km) relocated seismicity of Engdahl et al. [1998]. MD: Mojave Desert; ST: Salton Through; ECSZ: eastern California shear zone; CNSZ: central Nevada seismic zone; WLB: Walker Lane belt; SAF: San Andreas fault; HF: Hayward fault; CF: Calaveras fault; GF: Garlock fault; SJF: San Jacinto fault; EF: Elsinore fault; CPF: Cerro Prieto fault; P: Parkfield. For a color version of this figure see figure C.1 of appendix C.1.

tensor summation of the seismicity within the model area during the time-span of observation, which I interpret in terms of seismic hazard. Finally, based on my surface deformation model, I propose a kinematic model for the accommodation of the Pacific-North American relative plate motion.

2.2 Tectonic Setting

In the southwestern US the boundary between the Pacific and North American plates is distributed across a 300-1000 km wide zone ranging from the Pacific coast to the state of Utah (figure 2.1). The relative plate motion across the deformation zone amounts to ~ 50 mm/yr (DeMets et al., 1990), of which only a fraction is accommodated by

the San Andreas fault (WGCEP, 1995). South of latitude 34°N , the remaining relative plate motion is distributed along neighboring parallel faults, such as the San Jacinto and Elsinore faults which all lie to the west of the San Andreas (WGCEP, 1995). North of 34°N , the faults of the eastern California shear zone and Basin and Range province, east of the San Andreas system, also accommodate a significant fraction of the total plate motion. At 34°N the San Andreas fault changes its orientation from $\text{N}40^{\circ}\text{W}$ to $\text{N}73^{\circ}\text{W}$ due to a 160 km "left-step" in the fault. It is generally accepted that this Big Bend section of the fault zone comprises a structural impediment to the plate motion (Eberhart-Phillips et al., 1990) causing horizontal crustal shortening and vertical crustal thickening within the Transverse Ranges (Argus et al., 1999). The Santa Monica, San Gabriel, San Bernadino and Pinto Mountains can all be regarded as surface expressions of this convergence. North of the Big Bend, the San Andreas fault resumes an orientation almost parallel to the plate motion ($\text{N}40^{\circ}\text{W}$). Further north, around the latitude of 36.5°N the greater San Andreas system broadens, to include the Calaveras and Hayward faults, in addition to the San Andreas fault *senso stricto*.

North of latitude 34°N , east of the greater San Andreas fault system, approximately 20 – 25% of the relative plate motion is transferred from the Salton Trough through the Mojave Desert via the Eastern Californian shear zone (ECSZ) (Dixon et al., 1995, 2000b; Dokka and Travis, 1990; Gan et al., 2000; Miller et al., 2001; Sauber et al., 1994; Savage et al., 1990). The ECSZ inlet feeds the western Great Basin strain province (Bennett, 2003) which encompasses both the geologically classified Walker Lane Belt (WLB) and the seismologically defined central Nevada seismic belt (figure 2.1). At Mono Lake ($\sim 37.5^{\circ}\text{N}$) there is a broadening of the ECSZ deformation into the central and northern Walker Lane Belt (WLB) and the central Nevada seismic zone (CNSZ) located in the western Great Basin of the Basin and Range province (Bennett, 2003; Dokka and Travis, 1990; Oldow et al., 2001; Savage et al., 1990, 1995, figure 2.1).

West of this inboard shear zone, the central and eastern Great Basin provinces are characterized by a series of roughly north-trending basin bounding normal faults (Stewart, 1971). In contrast to the rather uniform distribution of faults, historical seismicity is primarily restricted to a narrow belt generally coincident with the greater Wasatch fault zone called the intermountain seismic belt (IMSB). Contemporary crustal extension in this part of the Basin and Range province is distributed across a wide region that includes, but is significantly broader than, the intermountain seismic belt (e.g. Bennett, 2003; Friedrich et al., 2003)

2.3 Relative motion data

Figure 2.2 shows the horizontal velocity estimates that comprise the data for this study. This data set is derived from a combination of velocity estimates from continuous net-

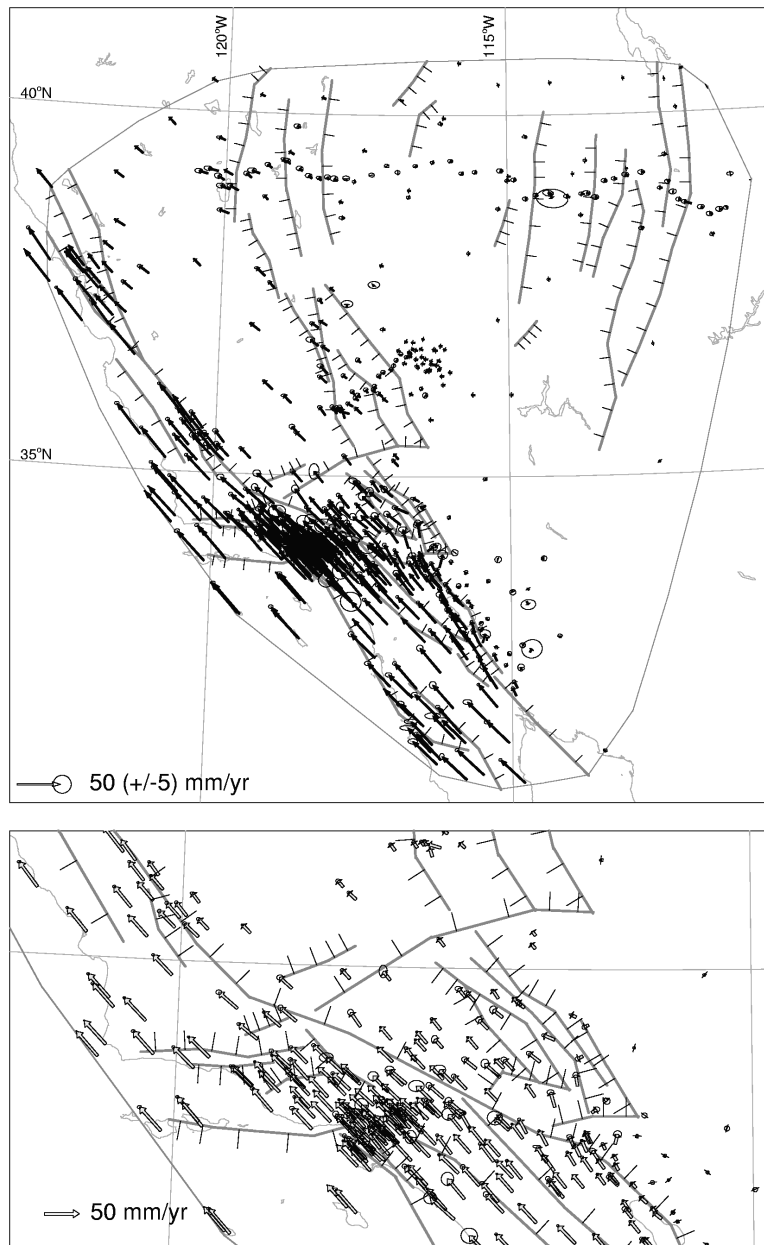


Figure 2.2: Dataset of 497 velocity vectors and their 95% confidence ellipses as utilized in this study. Bottom figure shows a detailed view of southern California. Since the data density in southern California is very high, the station positions are also given in figure 2.3.

works [BARD (e.g. King et al., 1995), BARGEN (e.g. Bennett et al., 1998; Wernicke et al., 2000), EBRY (<http://www.mines.utah.edu/~rbsmith/RESEARCH/UUGPS.html>), SCIGN (Bock et al., 1997) and IGS (Beutler et al., 1994)], as well as from campaign data [SCEC (Shen et al., 1996), northern Basin and Range Province (Thatcher et al., 1999), ECSZ (Bennett et al., 1997; Gan et al., 2000; Miller et al., 2001), the Sierra Nevada (Dixon et al., 2000b) and northeast Baja, California (Dixon et al., 2000a)]. The method used to combine these different data sets is described by Bennett et al. (2002) and Bennett (2003). All velocity vectors in the combined solution refer to a common North America fixed reference frame. For my study I limit the dataset to GPS and VLBI observation sites, which amounts to 497 stations located in the southwestern US, of which 194 are continuously operating GPS stations. The velocity estimates at the latter are in most cases significantly more precise than the campaign estimates. I do not consider those stations for which the 1σ velocity estimate uncertainties exceed 10 mm/yr. 57 stations in the combined data set are included in several of the campaign networks and/or a continuous GPS network. For these stations I only retain the continuous velocity estimate or the most precise estimate of relative motion for each station. At two stations in the Mojave Desert post-seismic relaxation due to the Landers earthquake could be identified (Shen et al., 1996). Since my objective is to model the long-term, more stationary surface deformation field, I retain the pre-Landers velocity estimates.

2.4 Inversion method and model parameterization

I use the method of Spakman and Nyst (2002) to invert the relative motion data in estimates of the surface velocity-gradient field (strain- and rotation rate), and slip rate (creep rate) on major faults. In brief, the method utilizes the following observation equation for the observed relative motion Δv_{ij} between any two stations i and j :

$$\Delta \mathbf{v}_{ij} = \sum_{l=1}^{K+1} \int_{L_{ij}^l} \nabla \mathbf{v}(\mathbf{r}) \cdot d\mathbf{r} + \sum_{k=1}^K \alpha_k \mathbf{f}_k(r_{ij}^k) \quad (2.1)$$

where $\nabla \mathbf{v}(\mathbf{r}) = \begin{bmatrix} v_{\phi\phi} & v_{\phi\theta} \\ v_{\theta\phi} & v_{\theta\theta} \end{bmatrix}$ is the unknown velocity gradient field (with e.g. $v_{\theta\phi}$ I indicate the rate of change of v_{θ} -component with the ϕ -coordinate in a spherical coordinate frame) and \mathbf{f}_k is the unknown fault slip rate (creep rate) on fault segment k . The two stations are connected with a path L of arbitrary geometry (but usually the geodesic) which is cut into segments at the locations (r_{ij}^k) where it crosses a fault leading to path-segments L_{ij}^l . At these locations a fault slip term is added to account for the possible contribution of fault motion to Δv_{ij} . Equation 2.1 is exact in practice and does not involve any knowledge of crustal rheology. The velocity gradient field is

parameterized by assuming linear variation of its components in triangular domains. To this end a study region is subdivided by (spherical) triangulation using support points which become the model nodes. The spatial density of nodes can be varied to adapt to the local data density. Nodes need not coincide with station positions and triangle sides never cross faults. With this parameterization the model parameters are the components of the velocity gradient tensor at the model nodes. Fault slip rate (or creep rate) is parameterized by assuming constant slip rate on fault segments.

Substitution of the model parameterization in 2.1 leads to a linear system of equations represented here by $\hat{\mathbf{A}}\mathbf{m} = \hat{\mathbf{d}}$, where $\hat{\mathbf{A}}$ is the observation matrix, \mathbf{m} represents the collection of all model parameters, and $\hat{\mathbf{d}}$ is the vector of all combinations of relative motion between station pairs. The length of $\hat{\mathbf{d}}$ is of the order of $M(M-1)$ relative motion components where M is the number of stations. This set of equations can be extended by defining extra integration paths L between all station pairs. These extra paths are used to assure internal consistency between the velocity gradient field and fault motion in constituting the total deformation field. A next set of equations derives from the fact that $\nabla \times \nabla \mathbf{v} = \mathbf{0}$ within regions bounded by faults. This constraint is defined for each single triangle leading to the linear equation $\alpha_r \mathbf{G}\mathbf{m} = \mathbf{0}$ where α_r is a weight used to tune the relative importance of these equations in determining a solution.

The data equations and the curl-constraints can be merged in one matrix equation $\mathbf{A}\mathbf{m} = \mathbf{d}$ which is solved by regularized least squares. The regularization is performed by extending $\mathbf{A}\mathbf{m} = \mathbf{d}$ with 3 sets of damping equations: (1) $\alpha_b \mathbf{I}_0 \mathbf{m} = \mathbf{0}$ for damping the amplitude of $\nabla \mathbf{v}$ components on model's boundary nodes, (2) $\alpha_i \mathbf{I}_1 \mathbf{m} = \mathbf{0}$ for spatially variable amplitude damping in nodes of the model interior, and (3) $\alpha_d \mathbf{D}_2 \mathbf{m} = \mathbf{0}$ for penalizing the second derivative of the components of $\nabla \mathbf{v}$, where \mathbf{I}_0 and \mathbf{I}_1 are identity matrices and \mathbf{D}_2 a second derivative operator (or discrete Laplacian smoother; Segall and Harris, 1987). The amplitude damping assures a complete regularization of the extended matrix and avoids unwarranted amplitude excursions in regions of poor spatial resolution while the second derivative damping has a smoothing effect on the solution. For this application it proved unnecessary to damp the fault slip rate parameters.

The formal least-squares solution of the regularized system is:

$$\mathbf{m} = (\mathbf{A}^T \mathbf{C}_d^{-1} \mathbf{A} + \alpha_b^2 \mathbf{I}_0 + \alpha_i^2 \mathbf{I}_1 + \alpha_d^2 \mathbf{D}_2^T \mathbf{D}_2)^{-1} \mathbf{A}^T \mathbf{C}_d^{-1} \hat{\mathbf{d}} \quad (2.2)$$

which depends on the tuning of α_r , and the 3 regularization factors. The a posteriori model covariance is given by: $\mathbf{C} = (\mathbf{A}^T \mathbf{C}_d^{-1} \mathbf{A} + \alpha_b^2 \mathbf{I}_0 + \alpha_i^2 \mathbf{I}_1 + \alpha_d^2 \mathbf{D}_2^T \mathbf{D}_2)^{-1}$ and the model resolution kernel is $\mathbf{R} = \mathbf{C} \mathbf{A}^T \mathbf{C}_d^{-1} \mathbf{A}$.

In my application $M=497$ which leads to 123,256 integration paths taken along geodesics. In total 246,512 alternative integration paths were added. The curl constraints amount to 1327 equations, thus, in total I have 371,095 data equations. Inversion of the corresponding data covariance matrix is impossible owing to its size.

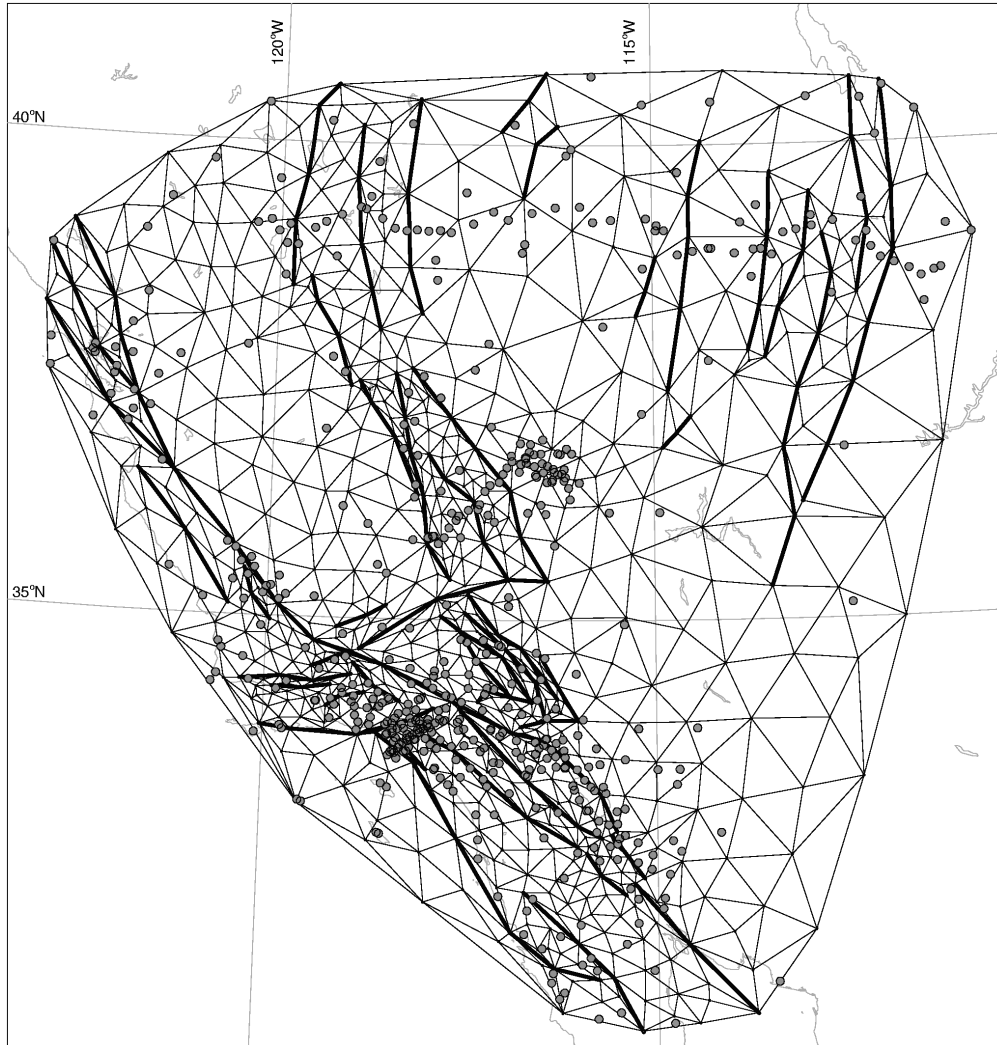


Figure 2.3: *Final parameterization of the SWUSDZ models. Thick lines indicate fault segments, black dots are the triangle nodes and grey dots are the site positions. Note that in my choice for the triangle nodes I am not restricted to the locations of the observation sites. Triangles do not intersect faults. Nodes at the fault are doubled to allow the velocity gradient field to be discontinuous across faults.*

Instead I take for \mathbf{C}_d a diagonal matrix with elements $var(\Delta v_{ij})_\phi \approx (\sigma_i)_\phi^2 + (\sigma_j)_\phi^2$ as an estimate of the variance for the velocity difference $(\Delta v_{ij})_\phi$ in longitudinal direction. Similarly in latitudinal direction.

The model region is parameterized with 1327 triangles (figure 2.3). The local density of GPS stations was used to guide densification in the triangulation. The triangles are spanned by 777 model nodes leading to $4 \cdot 777$ velocity gradient tensor components to be solved for. The major system of surface-breaking active faults in California and the Wasatch fault zone were adopted from the USGS. The Basin & Range province is characterized by diffuse fault zones which I mimic by a few single faults (figure 2.3). In total I have 46 large fault traces. These are divided into 292 segments leading to $2 \cdot 292$ slip rate components in the model. The total number of model parameters is 3692 which defines the size of the matrix to be inverted to obtain the solution \mathbf{m} (Equation 2.2).

2.5 Inversion

The data are inverted for three different representations of the SWUSDZ crustal deformation field; the first (solution I) in terms of rotations of crustal blocks and fault motion, the second (solution II) in terms of continuous deformation only, and the third (solution III) in terms of continuous deformation and fault motion. In order to quantitatively compare the three representations of crustal deformation I determine one set of regularization parameters for all solutions. For tuning of the covariance factor σ_r for the extra $\nabla \times \nabla \mathbf{v} = \mathbf{0}$ constraints and of the regularization parameters α_b , α_i and α_d , I primarily focus on obtaining solutions (for inversions I, II and III, respectively) that are comparably resolved and obtain an acceptable model covariance. The spatial variation of the amplitude regularization (α_i) depends on the number of paths (hitcount)

i	σ_r 10^{-7} m/yr	α_b 10^9	α_{i_a} 10^8	α_{i_b} 10^8	α_d 10^8	α_{sr} 10^{10}	χ^2	\tilde{r}_m	$\tilde{\sigma}_m^c$ 10^{-9} /yr	$\tilde{\sigma}_m^f$ mm/yr
I	3.5	3.0	2.0	4.0	3.0	2.0	13.72	0.31	0.53	0.036
II	3.5	3.0	2.0	4.0	3.0	-	5.27	0.66	1.20	-
III	3.5	3.0	2.0	4.0	3.0	-	3.98	0.66	1.36	0.049

Table 2.1: Aspects of the inversion parameterization and average results for inversions I, II and III. Key: i , solution; σ_r , standard deviation of the $\nabla \times \nabla \mathbf{v} = \mathbf{0}$ equations; α_b , α_{i_a} , α_{i_b} , α_d and α_{sr} , the regularization parameters; T_n , number of model nodes; K , number of fault segments; $\tilde{r}_m = \frac{1}{M} \sum_{i=1}^M R_{ii}$, the average resolution, with R_{ii} the diagonal elements of the resolution matrix and M the number of model parameters; $\tilde{\sigma}_m^c = \frac{1}{M_c} \sum_{i=1}^{M_c} \sqrt{C_{ii}}$, the average standard deviation for the components of $\nabla \mathbf{v}$, with $M_c = 4T_n$ the number of components of $\nabla \mathbf{v}$; $\tilde{\sigma}_m^f = \frac{1}{M_f} \sum_{i=1}^{M_f} \sqrt{C_{ii}}$, the average standard deviation for the components of \mathbf{f}_k , with $M_f = 2K$ the number of slip components.

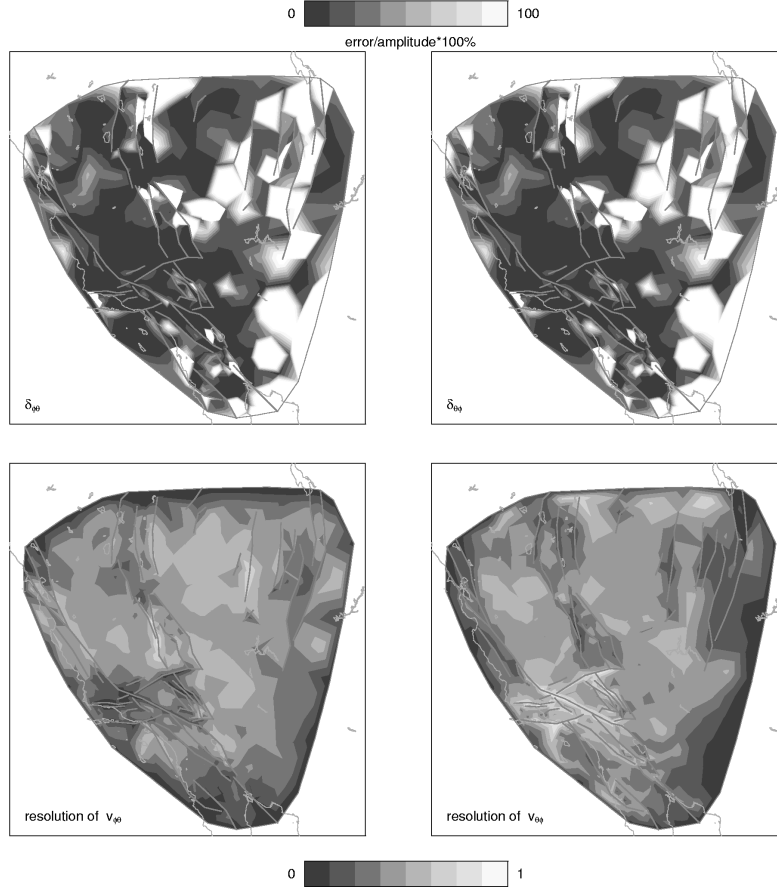


Figure 2.4: Model standard deviations corresponding to a 95% confidence level and resolution of solution I. The model standard deviations are expressed as percentage of the component magnitude.

contributing to each node; nodes with less hits than $1/8$ of the maximum hitcount were subjected to an increased regularization (α_{i_b}) with respect to the other nodes (α_{i_a}). In inversion I I am concerned with solving for (average) crustal block rotations (asymmetric part of $\nabla\mathbf{v}$) and fault motion. To this purpose I suppress the symmetric part of the velocity gradient tensor (strain rate) by α_{sr} . Table 2.1 shows the regularization parameters used to obtain my model solutions.

The normalized data misfit values χ^2 per degree of freedom (Bos et al., 2003a) provide a measure of how well the models can fit the data (table 2.1). Based on a 1σ data error solution III provides the best data fit, however, none of the solutions can fit all local variations in the velocity data within the 1σ data standard deviation. On a

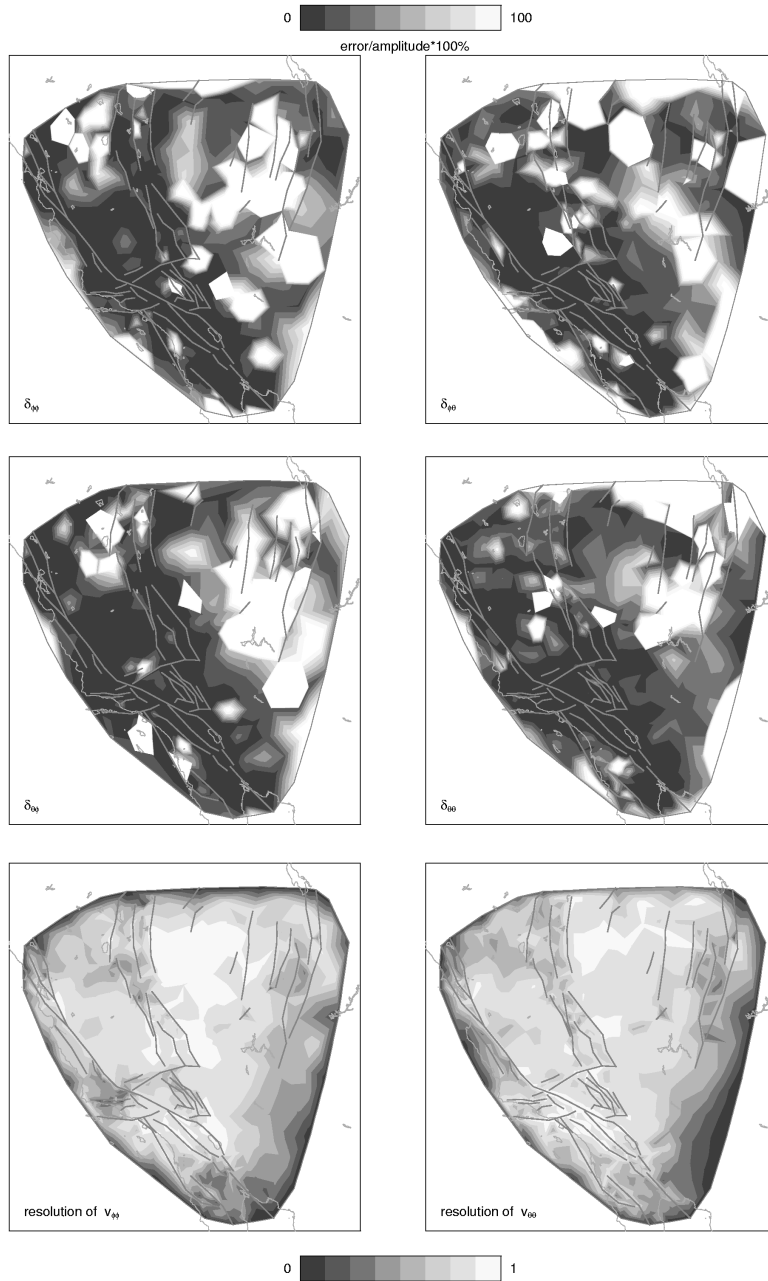


Figure 2.5: Model standard deviations and resolution of solution II.

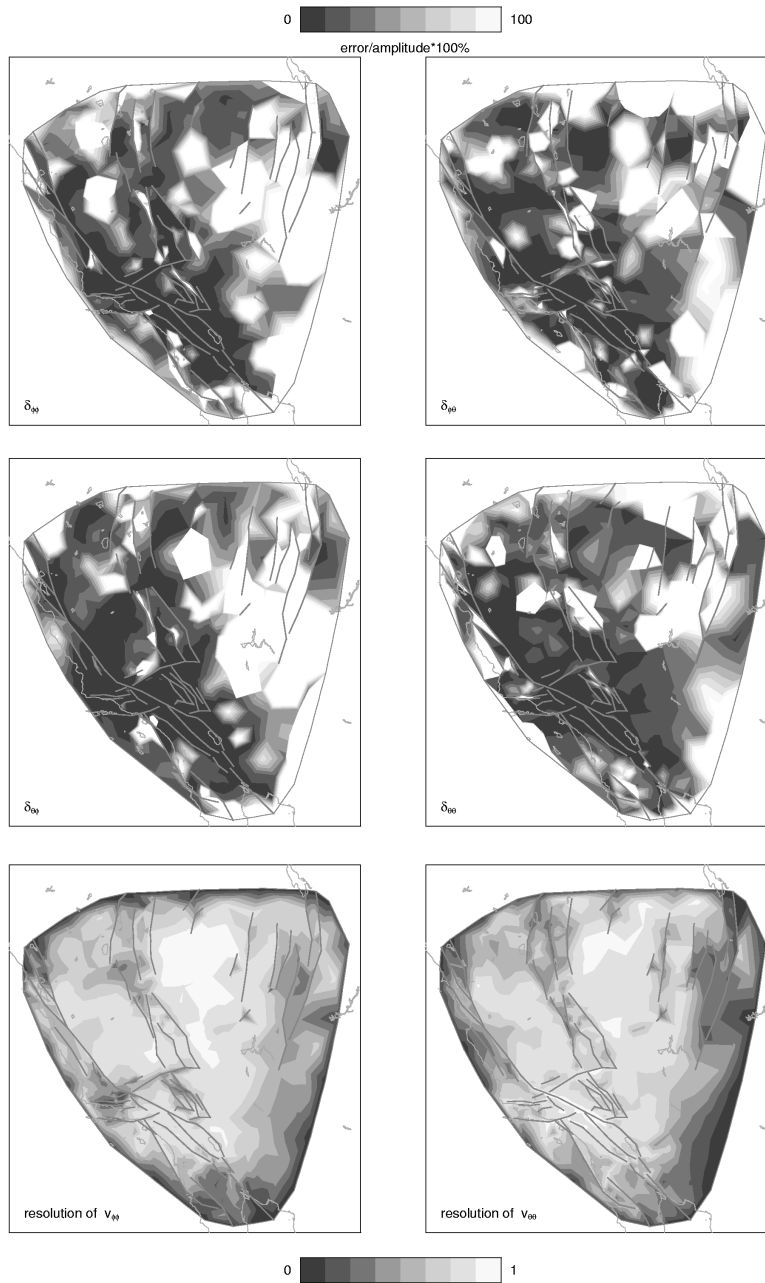


Figure 2.6: Model standard deviations and resolution of solution III.

95% confidence level solutions II and III do fit the data within the standard deviations ($\chi_{II}^2 = 0.87$ and $\chi_{III}^2 = 0.66$) in contrast to solution I ($\chi_I^2 = 2.28$).

In solution I, the additional constraints imposed on the strain rate reduce the $\nabla v_{\phi\phi}$ and $\nabla v_{\theta\theta}$ components of the solution to two orders of magnitude smaller than the $\nabla v_{\phi\theta}$ and $\nabla v_{\theta\phi}$ components. These latter components are of the same magnitude, however of opposite sign. Figure 2.4 shows the 3σ model standard deviation ($2.45 * \sqrt{C_{ii}}$) plotted as a percentage of the solution value and the diagonal elements of the resolution matrix for the latter two components. Standard deviations exceeding 100% of the solution value have not been contoured. These occur mostly in regions with small amplitudes of the velocity gradient components. The resolution of the $\nabla v_{\phi\theta}$ and $\nabla v_{\theta\phi}$ components has been reduced by the additional constraints. However, interpretation of the model is still warranted. Both components have significant velocity gradient values. The 3σ errors on the fault motions of solution I do not exceed 0.9 mmyr^{-1} .

Figure 2.5 and 2.6 show the 3σ model standard deviations and the diagonal elements of the resolution matrix (R_{ii}) of the $\nabla v_{\phi\phi}$ and $\nabla v_{\theta\theta}$ components of the velocity gradient tensor of solutions II and III, respectively. The R_{ii} values for $\nabla v_{\phi\theta}$ and $\nabla v_{\theta\phi}$ are comparable to the values of $\nabla v_{\phi\phi}$ and $\nabla v_{\theta\theta}$, respectively. Since part of the data signal in solution III is explained by motion on faults, larger areas now render velocity gradient values not significantly different from 0 in either or both directions. As in solution I, the 3σ errors on the fault motions of solution III do not exceed 0.9 mmyr^{-1} . Generally, I observe a strong reduction in resolution along the model boundary, consistent with the increased damping of the model on the boundary. I also observe a reduction of resolution around some of the faults in solution III, indicating a trade-off between the fault motion components and the velocity gradient components due to lack of GPS data close to faults (Spakman and Nyst, 2002).

2.6 Description of the three solutions

2.6.1 Fault motion

In both solution I and III fault motion proves well resolvable (figure 2.7 and 2.8). Although magnitudes might differ, the sense of relative motion in both models correspond very well. The Californian shear zone is dominated by dextral motion. In the Transverse Ranges significant thrusting is observed. In solution I this thrusting is accompanied by sinistral slip (3 – 9mm/yr), whereas solution III resolves dextral slip on the Santa Ynez fault ($\sim 1\text{mm/yr}$), Big Pine fault ($\sim 0.4\text{mm/yr}$) and Pinto Mountain fault ($\sim 2\text{mm/yr}$). Both solutions obtain a combination of normal faulting and dextral slip in the eastern Californian shear zone (ECSZ), Walker Lane Belt and the central Nevada seismic zone (CNSZ). Sinistral thrust motion ($\sim 2 \text{ mmyr}^{-1}$) is obtained on the Wasatch fault zone.

I have compared the obtained slip rates of both solution I and III to geological slip

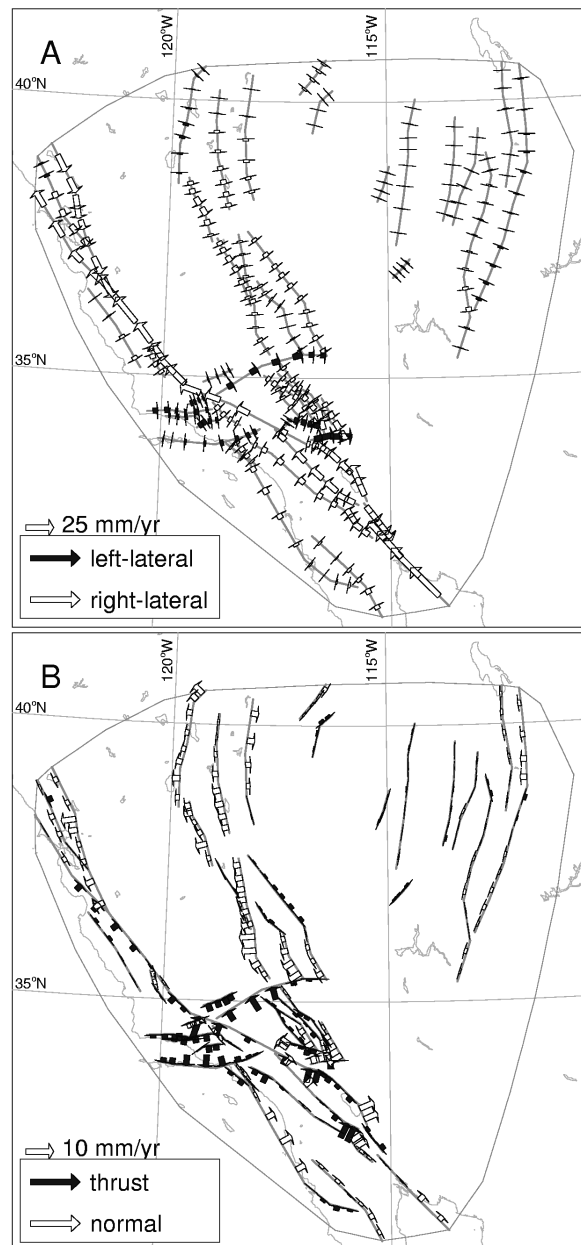


Figure 2.7: Fault motion contribution of solution I. A) Lateral component of the fault motions; B) perpendicular component of the fault motions. Please note the different scales of the slip vectors.

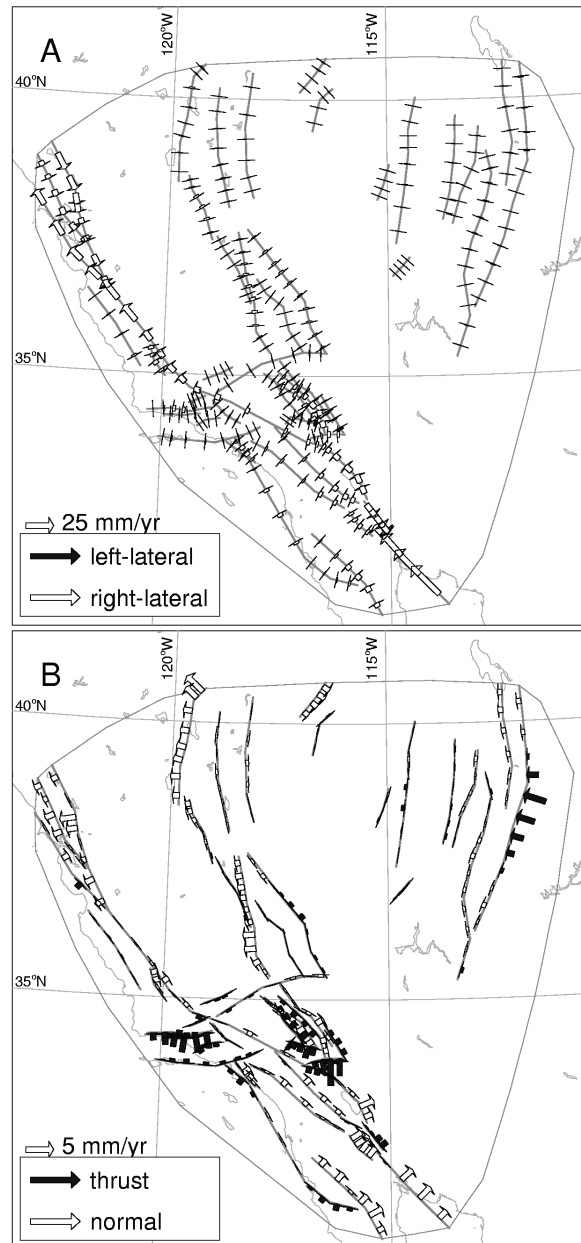


Figure 2.8: *Fault motion contribution of solution III. A) Lateral component of the fault motions; B) perpendicular component of the fault motions. Please note the different scales of the slip vectors.*

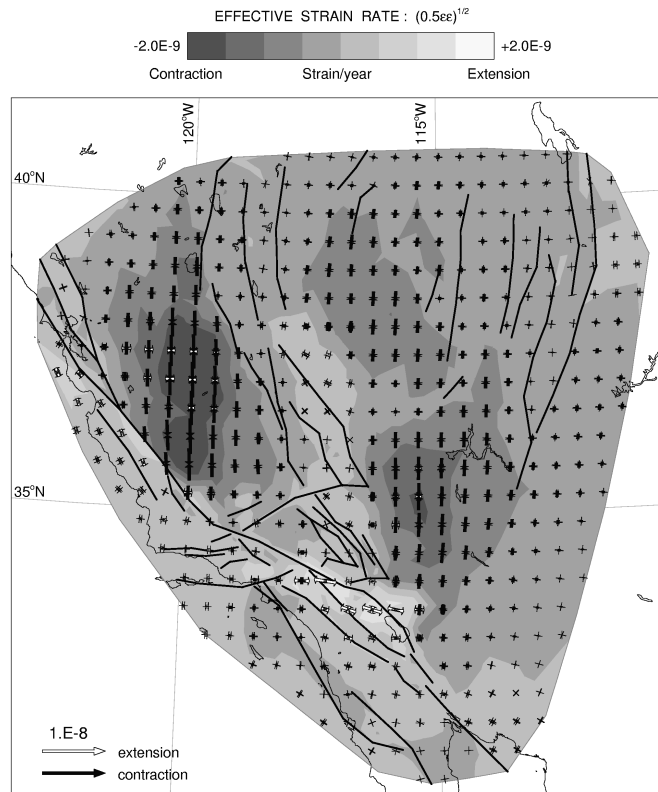


Figure 2.9: Strain rate contribution of solution I. The arrows denote the principal strain rates: contraction (black) and extension (white). For color version of this figure C.2 in appendix C.1.

rates, as well as creep measurements (appendix A.1). I find that the sense of motion on faults in both solutions is generally in agreement with the geological observations. Trade-offs between estimates of the velocity gradient and fault slip rate in some areas require a careful interpretation of the magnitudes of the slip rate solutions. However, in regions with dense station coverage in the vicinity of the faults I do model significant aseismic surface creep.

2.6.2 Strain rate

Although strongly suppressed in amplitude, the strain rate field of solution I exhibits a clear pattern (figure 2.9). I observe N-S contraction in the Great Valley, central Basin and Range and east of the Mojave Desert. Almost E-W extension is found around the Big Bend in the San Andreas fault, between the Pinto Mountain and San Andreas faults and between the San Andreas, San Jacinto and Elsinore faults.

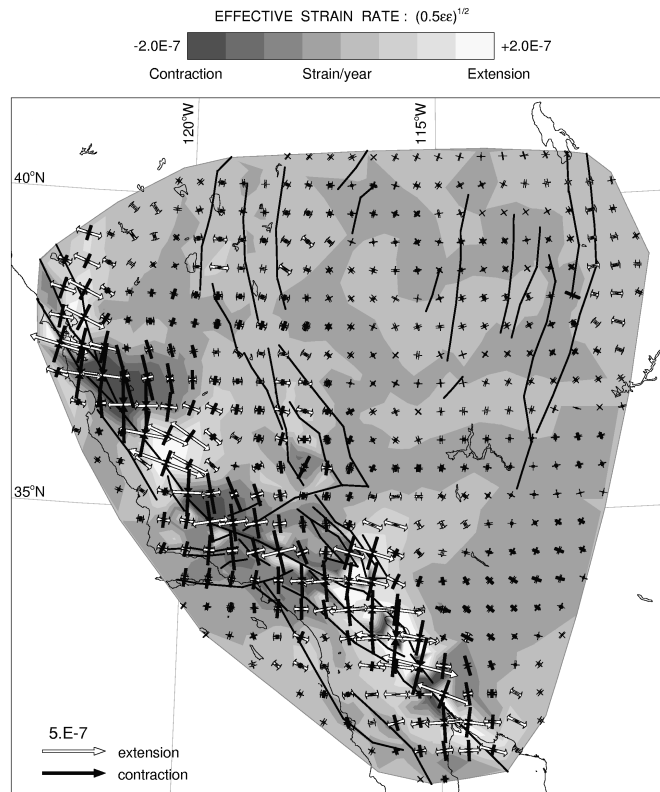


Figure 2.10: *Strain rate contribution of solution II. For color version of this figure C.3 in appendix C.1.*

Both solutions II and III show a clear Californian shear system (figure 2.10 and 2.11; note the difference in amplitude with solution I). In the shear zone, variations in contractional and extensional patterns in the effective strain rate do not indicate a change in dominant regime, but a small dominance of either principal strain rate. In solution III the magnitude of the strain rates within the California shear zone has been reduced due to the presence of fault motion. The principal axes show a rotation along with the change of orientation of the San Andreas fault in the Big Bend of the fault. In the ECSZ the dextral normal motion on the faults significantly reduces the extension observed in solution II and changes the orientation slightly from WNW-ESE to pure E-W. Both solutions show a distinct asymmetry of the deformation at the San Andreas fault in central California, between the Big Bend section and San Francisco. The deformation tends to concentrate on the eastern side of the San Andreas fault, in the Great Valley (figure 2.9 and 2.10). The deformation becomes much more diffuse and spatially distributed across the Transverse Ranges. In southern California it mainly

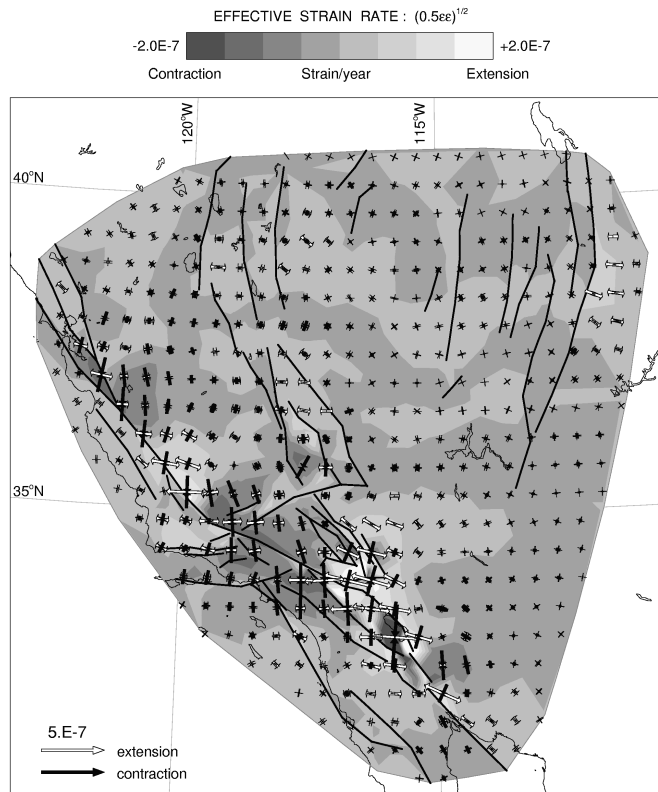


Figure 2.11: *Strain rate contribution of solution III. For color version of this figure C.4 in appendix C.1.*

localizes between the San Jacinto and San Andreas faults, especially in solution III (figure 2.10). Many regional aspects of the deformation of solution II compare well with those obtained in earlier studies based on geodetic data and ignoring active fault motion (appendix A.2). It is difficult to indicate the extent to which the discrepancies result from differences in methodology between the various approaches and different data sets used. I note however that significant differences between these earlier studies and solution III exist and are a direct result of the implementation of fault motion in my methodology. Further, I deduce that postseismic relaxation of the Landers earthquake affects my surface deformation field (appendix A.3), while the postseismic relaxation related to the Northridge and Loma Prieta earthquakes have no influence on my solutions. However, postseismic relaxation of several other earthquakes may possibly affect my solutions in the ECSZ, the western Transverse Ranges, along the Parkfield segment of the San Andreas fault and at Salton Through. I am presently unable (due to lack of data) to quantify the extent of their influence on my surface deformation solutions.

Strain rates in the Basin and Range are almost an order of magnitude smaller than those observed in the shear zone. The deformation in the Basin and Range province appears to be dominated by north-south variations in the principal axes orientations. East of the Wasatch fault zone significant E-W extension is obtained in both solutions, whereas the western Basin and Range shows extension dominated right-lateral shear. Although the spatial distribution of deformation in the Basin and Range remains debated, general consensus exists on the fact that it is dominated by NW-SE extension (Bennett et al., 1999, 2002; Flesch et al., 2000; King et al., 1994; Lachenbruch et al., 1994; Thatcher et al., 1999). I found that a sinusoidal pattern in the NS-component of the campaign dataset of Thatcher et al. (1999) dominates the deformation patterns obtained in the Basin and Range province (appendix A.4). This dataset is also responsible for the large extension east of the Wasatch fault zone observed in my model (see appendix A.4). Therefore, I will refrain from further discussion of the surface deformation model within the Basin and Range province.

2.6.3 Rotation rate

Both solutions II and III show strong clockwise rotations along the San Andreas fault, Mojave Desert, ECSZ, CNSZ and Walker Lane Belt, consistent with dextral shear (figure 2.12B, C). I notice an asymmetry of the rotations with respect to the faults along the Parkfield and Carrizo segments of the San Andreas fault. Solution III shows minor counter-clockwise rotation of $1 - 2^\circ Myr^{-1}$ in the southern Mojave Desert. Generally, solution I (figure 2.12A) shows no strong shear related rotations indicating that in this solution shear is accommodated by fault motion between near-rigid blocks. Here I observe clockwise rotations in the southern Great Valley, western Transverse Ranges and between the Pinto Mountain and San Andreas faults. Counter-clockwise rotations are found in the Mojave Desert. Though significant local rotations of the Great Basin and Sierra Nevada are obtained in all solutions, I obtain no clear uniform counter-clockwise rotation consistent with the $0.28^\circ Myr^{-1}$ and $0.13^\circ Myr^{-1}$ suggested by Dixon et al. (2000a) and Harding Hearn and Humphreys (1998). However, especially solution I (limited to fault motion and block rotation) does agree with their conclusion that the block is translating to the northwest.

2.6.4 Asymmetry of the surface deformation field

Though in central California, north of the Big Bend, deformation concentrates at the San Andreas fault, both solutions II and III show a distinct asymmetry of the strain and rotation rates across the fault (figure 2.10, 2.11 and 2.12). The deformation localizes on the eastern side of the fault. Figure 2.1 shows an updated version of the relocated seismicity data of Engdahl et al. (1998) in the southwestern US. Most of the seismicity occurs at or close to the major faults. However, there is significant seismicity east

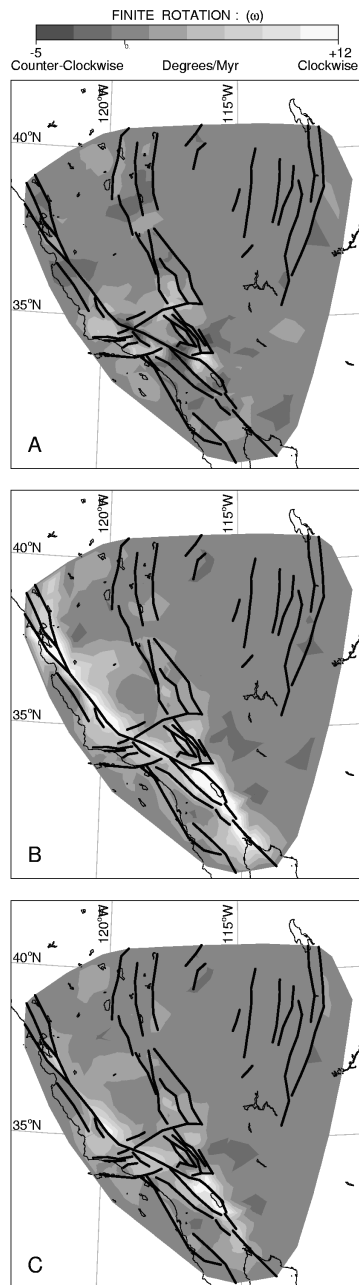


Figure 2.12: Rotation rate contribution of A) solution I, B) solution II and C) solution III. Note the location of the 0 in the contour scale. For color version of this figure C.5 in appendix C.1.

of the San Andreas fault in the Great Valley, which correlates with high strain rates in my deformation field. The seismicity east of the Calaveras fault may be related to the presence of blind thrust faults (Unruh and Lettis, 1998, USGS fault data set;), but none are known east of the San Andreas fault between the Calaveras junction and the Transverse Ranges.

Previous surface deformation studies have not obtained this asymmetry possibly due to coarser/smoothed model parameterization (Shen-Tu et al., 1998; Ward, 1998) or the asymmetry was not addressed (Jackson et al., 1997; Shen-Tu et al., 1999). When studying displacement data caused by the 1906 San Francisco event, Chinnery (1970) found an asymmetry in the data across the San Andreas fault in the vicinity of Fort Ross. Huggett et al. (1977) performed strain meter measurements near Hollister. They observed large strains occurring away from and only on one side of the San Andreas and Calaveras faults and postulated that this may have been caused by movement of one side of the fault.

Malservisi et al. (2001) related an asymmetric surface deformation field in the ECSZ to a viscosity contrast. The viscosity contrast relates to differences in heat flow, where strain localizes in high heat flow regions. However, this can not explain the asymmetry across the San Andreas fault since no heat flow contrast is observed across the fault (figure 1 of Sass et al. (1994)). Mahrer and Nur (1979) and Rybicki (1978) determined displacement fields for static 2D models of a long strike-slip fault in a crust of laterally varying rigidity. They observe a significant reduction of displacement on the high rigidity side of the fault, as well as a shift of the peak displacement towards the fault trace on both sides. Such a distinct rigidity contrast would also have important implications for the crustal velocity structure across the fault.

Healy and Peake (1975) determined seismic velocity changes at Bear Valley. They observed velocity variations extending a number of km away from the fault trace and asymmetric across the fault. The same non-symmetry was obtained by Boore and Hill (1973). Based on this contrast they deduced that the rigidity east of the San Andreas fault is smaller than west of the fault by a factor of ~ 1.7 . Across the Parkfield segment of the San Andreas fault, Eberhart-Phillips and Michael (1993) obtained a 5-20% lateral change in velocity over 4 km width. By combining the velocity model with a resistivity model, they were able to deduce corresponding rock units. The high velocities to the southwest of the fault are inferred as high-resistive basement of Salinian granite. The large volume of low-velocity, low-resistivity material northeast of the San Andreas fault is inferred to be overpressured Franciscan of Great Valley sequence material. Assuming that the stress level at both sides of the fault is comparable, I deduce a rigidity contrast across the fault of ~ 1.78 , consistent with Boore and Hill (1973).

Since the same velocity contrast across the fault is still prominent at Bear Valley, this crustal structure may extend all along the San Andreas fault from the Big Bend to the Calaveras junction, thus providing a feasible explanation for the localization of deformation east of the fault. The noted localization of deformation is important for

seismic hazard analysis, as well as for the interpretation of tectonics.

2.6.5 Comparison to paleomagnetic observations

The rotation rates of solutions I, II and III (Figure 2.12A, B, C) are representative for the period of observation (approximately 20 years) and apply to rigid rotations of small equidimensional blocks. In contrast, paleomagnetic data are representative for the past millions of years and may represent rotations of considerable crustal blocks (McKenzie and Jackson, 1983). Since I am unable to solve for a net uniform rotation of the entire study area, the comparison with paleomagnetic observations is not straightforward. However, to determine the extent to which the present-day pattern may reflect the past million years and the larger-scale crustal block rotations I do compare the results of solutions II and III to paleomagnetic rotations.

Based on paleomagnetic observations Luyendyk et al. (1980) determined a geometric model for the Neogene crustal rotations in southern California. In the western Transverse Ranges their model consists of many crustal blocks presently bounded on the north and south by E-W-trending sinistral faults, which have been subjected to clockwise rotations of 70° to 80° within the Pacific-American dextral shear zone. The eastern Transverse Ranges, central Mojave Desert and Tehachapi Mountains have also been rotated clockwise. The rotated blocks are nested between blocks bounded by NW-SE-trending dextral faults. Carter et al. (1987) refined this model in the eastern Transverse Ranges and Mojave Desert. They included a counter-clockwise rotation in the southern Mojave Desert to accommodate the 41° clockwise rotation they obtained in the eastern Transverse Ranges since the late Miocene.

The rotation rate field of solution II shows orientations consistent with Luyendyk et al. (1980). Solution III shows southern California rotating in a manner of which the orientations are consistent with Carter et al. (1987), indicating the influence of the dextral fault motions modeled on the Mojave Desert faults. This result suggests that the rotation rates modeled might represent longer-term, larger-scale crustal block rotations. However, Luyendyk et al. (1980) proposed that the rotation of the Transverse Ranges may have ceased when the San Andreas fault broke through southern California in the late Miocene, whereas Carter et al. (1987) found significant clockwise rotations in the eastern Transverse Ranges since the late Miocene. Therefore, I propose that since the late Miocene a major part of the Pacific-American dextral shear has been accommodated by the San Andreas fault, whereas the remainder of the shear induces ongoing rotations in southern California consistent with the model of Carter et al. (1987).

2.7 Implications for seismic hazard

Even though aseismic surface creep is present in the deformation zone (solution III, Langbein, 2002; Lienkaemper et al., 1991; Rosen et al., 1998), it is reasonable to as-

sume that within the seismogenic layer the faults are primarily locked. Therefore, I utilize solution II to determine earthquake moment rates within my model area. Kostrov (1974) codified the relationship between the strain rate tensor $\dot{\epsilon}$ and earthquake activity. In addressing earthquake moment rates I adopt the scalar version of this formula according to Ward (1998):

$$\dot{\bar{M}} = 2\mu A H_s^A \dot{\epsilon}_{max}^A \quad (2.3)$$

$\dot{\bar{M}}$ represents the mean earthquake moment rate for the region A. I determine $\dot{\bar{M}}$ for each triangle of my parameterization, where A is the area of the triangle, $\dot{\epsilon}_{max}^A$ the maximum strain rate at the center of the triangle and $\mu = 3.0 \cdot 10^{10} \text{ Nm}^{-2}$, the rigidity of the elastic layer. H_s^A in equation 2.3 is the average thickness over which elastic strains accumulate and dissipate in earthquakes. H_s^A is neither the crustal thickness nor the maximum depth of earthquakes. These depths exceed H_s^A because the top few kilometers of the crust are aseismic and the properties of the deepest quakes do not reflect the seismogenic layer as a whole. Ward (1998) determined average values of $H_s^A = 12.7 \text{ km}$ for southern California, $H_s^A = 11.2 \text{ km}$ for northern California and $H_s^A = 14.7 \text{ km}$ for the Basin & Range. I have adopted these values in my analysis.

Ward (1998) derived average strain and mean moment rates for southern California, northern California and the Basin & Range province. For comparison, I have assigned each triangle to either of the three areas based on their geographical location and determined the corresponding average strain and moment rate for each. I note that my model area is not completely comparable with the areas adopted by Ward (1998). My southern California domain exceeds Ward (1998)'s estimate due to the inclusion of Baja, Mexico, while Ward (1998)'s northern California domain extends further north of my modeling area. Therefore, the significantly different average strain rates obtained in California in solution II result in comparable mean moment rates (table 2.2). Hence, the strain rates in Baja, Mexico contained in solution II have lowered my estimate for the average strain rate, while the increase in surface area due to this region induces a similar estimate of the mean moment rate. The lower strain rates in northern California north of my modeling area have a similar impact on the estimate of Ward (1998) in this region. In the Basin and Range the two solutions differ significantly for both strain rate and mean moment rate.

	area 10^4 km^2		$\dot{\epsilon}_{max}^A \cdot 10^{-8} \text{ yr}^{-1}$		seis. [†]	$\dot{\bar{M}} \cdot 10^{19} \text{ Nmyr}^{-1}$		
	Ward	Sol. II	Ward	Sol. II		geod.*	Sol. II	deficit
S.C.	15.7	21.3	11.8±1.6	10.6±0.23	1.06	1.42±0.20	1.35±0.09	0.29
N.C.	24.0	15.2	5.59±0.25	7.44±0.21	0.66	0.91±0.04	0.83±0.07	0.17
B&R	77.5	52.8	2.11±0.14	2.31±0.21	0.55	1.23±0.09	0.90±0.13	0.35

* geodetic mean moment rate derived by Ward [1998]

† mean moment rates taken from Ward [1998]

Table 2.2: Mean strain and moment rates of Ward [1998] and determined for solution II.

The moment deficit rate between the geodetic moment rate and the seismic moment rate addresses the (in)completeness of the earthquake catalogue (Ward, 1998) (e.g. the absence of large, rarely occurring events, as well as events with magnitudes less than ~ 5). The deficits in the three general regions between the moment rates of solution II and the seismic moment rate suggests that the catalogue simply fails to reflect the long-term situation. Within the 150 year time span of the catalog the moment deficit rate in southern California is comparable to a $M_w = 7.7$ earthquake, where the moment deficit rate of northern California amounts to a $M_w = 7.6$ event.

Shen-Tu et al. (1999) determined strain rates and minimum moment rates for the western United States from geodetic, geologic and seismic data. I find a reasonable comparison of my solution II strain rates and their geodetic strain rates (table 2.3). However, their regions along the Californian coast (regions A, B and C of Shen-Tu et al., 1999) extent further westward than my model boundary. The lower strain rates they model in the area west of my model boundary decrease their estimates of the average strain rate and the combined effect results in the significant differences observed for the moment rates. In the Mojave Desert (region J of Shen-Tu et al., 1999) I find a significantly larger average strain rate. This could be caused by my increased station

	Shen-Tu et al [1998]							Solution II		
	area 10^4 km^2	min. mom. rate [†] seis.	geol.	geod.	seis.	geol.	geod.	area 10^4 km^2	$\dot{\bar{M}}^\circ$	Strain rate*
A	5.11	2.21	10.15	11.70	0.48	2.21	2.54	1.16	2.39	2.29
B	2.96	1.63	16.77	19.55	0.61	6.29	7.34	2.30	19.16	9.25
C	6.36	0.18	5.54	13.90	0.03	0.97	2.43	3.21	8.85	3.06
D	3.74	34.39	51.00	42.94	10.18	15.14	12.75	3.39	42.32	13.85
E	1.28	2.09	21.06	19.13	1.81	18.24	16.57	1.49	16.67	12.45
F	1.27	18.69	19.55	13.41	16.32	17.07	11.71	1.33	15.56	13.00
G	1.32	36.16	29.16	17.06	30.34	24.46	14.31	1.43	17.95	13.99
H	4.11	7.64	41.61	47.49	2.07	11.25	12.84	4.86	63.67	14.56
I	30.0	53.45	7.77	60.77	1.98	0.29	2.25	27.4	102.34	4.16
J	5.53	9.03	7.27	23.05	1.81	1.46	4.63	6.63	46.12	7.73
K	33.7	0.97	2.09	29.50	0.03	0.07	0.97	28.5	36.21	1.41

[†] Minimum moment rate ($\dot{M} = 2\mu V(|\dot{\sigma}| + \sqrt{\dot{\gamma}_1^2 + \dot{\gamma}_2^2})$; $10^{18} Nmyr^{-1}$) as determined by Shen-Tu et al [1998] with shear modulus $\mu = 3.0 \cdot 10^{10} Nmyr^{-1}$ and V is the volume, which is the product of the area of the region and the seismogenic thickness ($H_s^A = 15km$)

* Strain rate $10^{-8} yr^{-1}$; $\dot{\epsilon}_{max}^A = |\dot{\sigma}| + \sqrt{\dot{\gamma}_1^2 + \dot{\gamma}_2^2}$

^o $\dot{\bar{M}}$ ($10^{18} Nmyr^{-1}$) is calculated using (3) in the text, with an assumed seismogenic thickness of 15km

Table 2.3: Mean strain and moment rates of Shen-Tu et al [1999] and those determined from solution II.

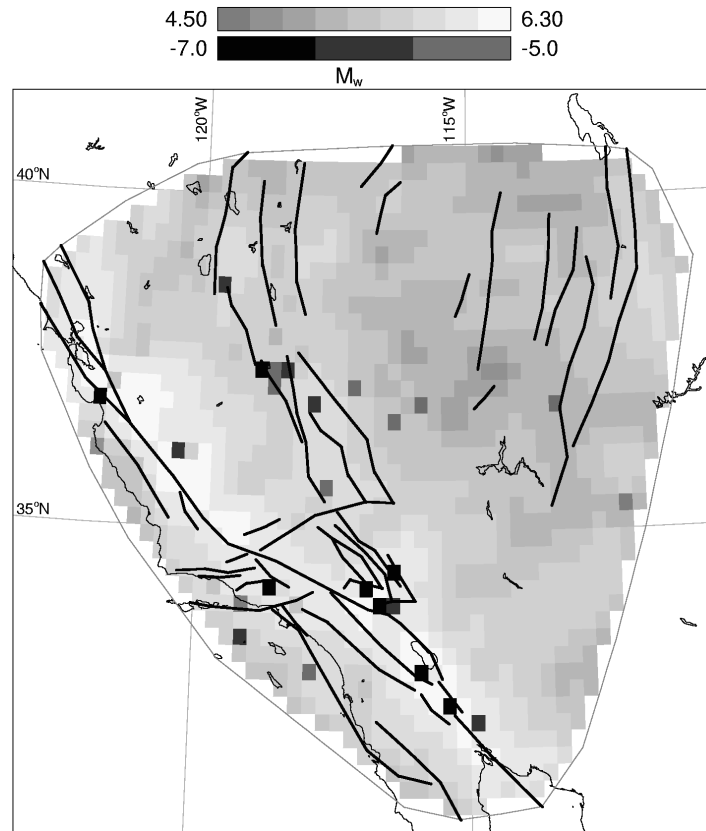


Figure 2.13: *Moment magnitudes corresponding to the moment deficits accommodated in my model area during my observation period. The negative moment magnitudes correspond to negative moment deficits, indicating that large earthquakes within the observation period have released more seismic moment than has been accumulated by my strain rate field. For color version of this figure C.6 in appendix C.1.*

density in this area, enabling me to localize deformation.

Clearly the mean moment rates strongly depend on the ratio between the average maximum strain rates and the size of the area utilized, e.g. a larger area with small average maximum strain rates amounts to a mean moment rate comparable to the mean moment rate of a small area with large average maximum strain rates.

Based on the USGS seismicity database and the Harvard CMT Catalogue I determine the seismic moment rate for the time span contained in my GPS data (1973-2000). For the events obtained from the USGS database I use the $M_0 - M_l$ relation of Thatcher and Hanks (1973) for southern California ($\log M_0 = 1.5M_l + 16.0$) to determine the seismic moment. To avoid the influence of the varying triangle sizes within my model

parameterization I construct a grid of square cells of $0.25^\circ \times 0.25^\circ$ within my model area. For each grid cell the average maximum strain rate is derived from the maximum strain rates at the corners of the cell and the mean moment rate is determined using equation 2.3. I multiply my model derived moment rates with the time span of my data, obtaining the total accumulated moment of each grid cell. Based on their location I assign each seismic event to a grid cell and apply moment summation to obtain the total seismic moment within my time span for each cell. The deficit between the seismic moment and the total geodetic moment gives an estimate of the excess moment accommodated in my model area during the observation period of 27 years and will allow identification of regions with possibly increased seismic hazard.

The moment magnitude (M_w) of an earthquake is related to the seismic moment (M_0) by (Kanamori, 1977):

$$M_w = \left(\frac{\log M_0}{1.5} \right) - 10.73 \quad (2.4)$$

By replacing M_0 in equation 2.4 by the moment deficit (M) I determine the earthquake magnitude corresponding to each moment deficit (figure 2.13). From figure 2.13 I can see larger earthquakes diminishing the moment deficit. The large events in the region (e.g. Landers, Hector Mine, Northridge and Loma Prieta) have released more seismic moment than was accumulated geodetically in this time period (negative magnitudes). Of course large earthquakes release seismic energy and moment across larger areas than just their epicenter. This more regional influence of the large events is not explicitly incorporated in my analysis, however, is taken into account in the interpretation of figure 2.13. In the western Transverse Ranges, the Northridge earthquake and aftershocks have released most of the moment build up by the strain rates of my model within the time period, thus reducing the seismic hazard in this area. The same holds for the Mojave Desert, where the Landers, Big Bear and Hector Mine earthquakes released a significant amount of the accumulated moment. However, all along the San Andreas fault I find moment deficits corresponding to $M_w > 5.9$. Significant moment deficit, corresponding to $M_w = 6.1 - 6.3$, has accumulated east of the Parkfield and Carrizo segments of the San Andreas fault. A comparable moment deficit is also observed in the Bay area of San Francisco, along the San Andreas fault just north of the Big Bend and around the Imperial and southern San Andreas faults. On the Hayward and southern Calaveras faults these high moment deficits coincide with regions of increased micro-seismicity. This phenomena was also observed prior to other events (e.g. the 17 August, 1999, Izmit, Turkey earthquake; Nalbant et al., 1998; Parsons et al., 2000) and may point at an increased risk of an earthquake to occur in these regions in the near future.

2.8 Crustal deformation of the SWUSDZ

King et al. (1994) derived that since 1850 about 60% of the Pacific-North American motion occurred seismically and 40% aseismically. They further showed that within the seismogenic depth range of the plate boundary aseismic deformation is concentrated near the surface and at depth. In some cases this deformation can be located on creeping faults, but elsewhere it is spread over a several kilometer wide zone adjacent to the fault. I infer that this kind of surface deformation field is clearly modeled in solution III. Based on solution III I derive a model of the kinematics of the present-day surface deformation of the SWUSDZ. Figure 2.14 summarizes the main features for strain, rotation and slip rates of my model.

Within the shear zone of California I can identify many faults containing dextral motion and significant CW rotations. More in-depth, I can distinguish several fault zones bounding rotating blocks. Around the San Francisco Bay I obtain dextral creep on the San Andreas, Hayward and Calaveras fault system. The southern part of this system is associated with CW rotations and shear strain rates in a setting dominated by contraction. To the east of the San Andreas-Calaveras fault junction the model depicts significant shear strain rates also in a setting dominated by contraction possibly related to hidden thrusts in the area. The eastward extent of these shear strain rate patterns is poorly constrained by the lack of data within the Sierra Nevada. The Parkfield segment of the SAF is dominated by asymmetric shear strains in a extension dominated setting, southward diminishing dextral creep and asymmetric CW rotations. Between the San Andreas-Calaveras fault junction and the Big Bend section of the San Andreas fault, deformation localizes on the eastern side of the San Andreas fault which I have attributed to a significant rigidity contrast across the fault. The Big Bend section marks the transition from N-S contraction in the western Transverse Ranges to dextral shear in the Mojave Desert. The Transverse Ranges are associated with sinistral creep and significant CW rotations. The southern Mojave Desert experiences CCW rotations to accommodate the CW rotations in the eastern Transverse Ranges. The rotating blocks in the eastern Transverse Ranges and Mojave Desert are bounded by dextral faults. The ECSZ, Walker Lane Belt and CNSZ show a continuous shear zone of dextrally creeping faults separated by CW rotating blocks. In contrast to the Mojave Desert, the faults bounding the Sierra Nevada obtain a significant normal component of fault creep accommodating the extension of the Basin and Range. The White Mountains seismic gap between the ECSZ and the CNSZ is dominated by shear, thus transferring the deformation from the ECSZ to the CNSZ. The western Great Basin undergoes significant WNW-ESE extension. The San Andreas and San Jacinto faults are linked as a single dextral fault system. Between the two dextral faults significant CW rotation and dextral shear occurs consistent with deformation in a dextral fault zone. The southward extension of the San Andreas fault, the Imperial Valley fault and the Cerro Prieto fault also show significant dextral creep.

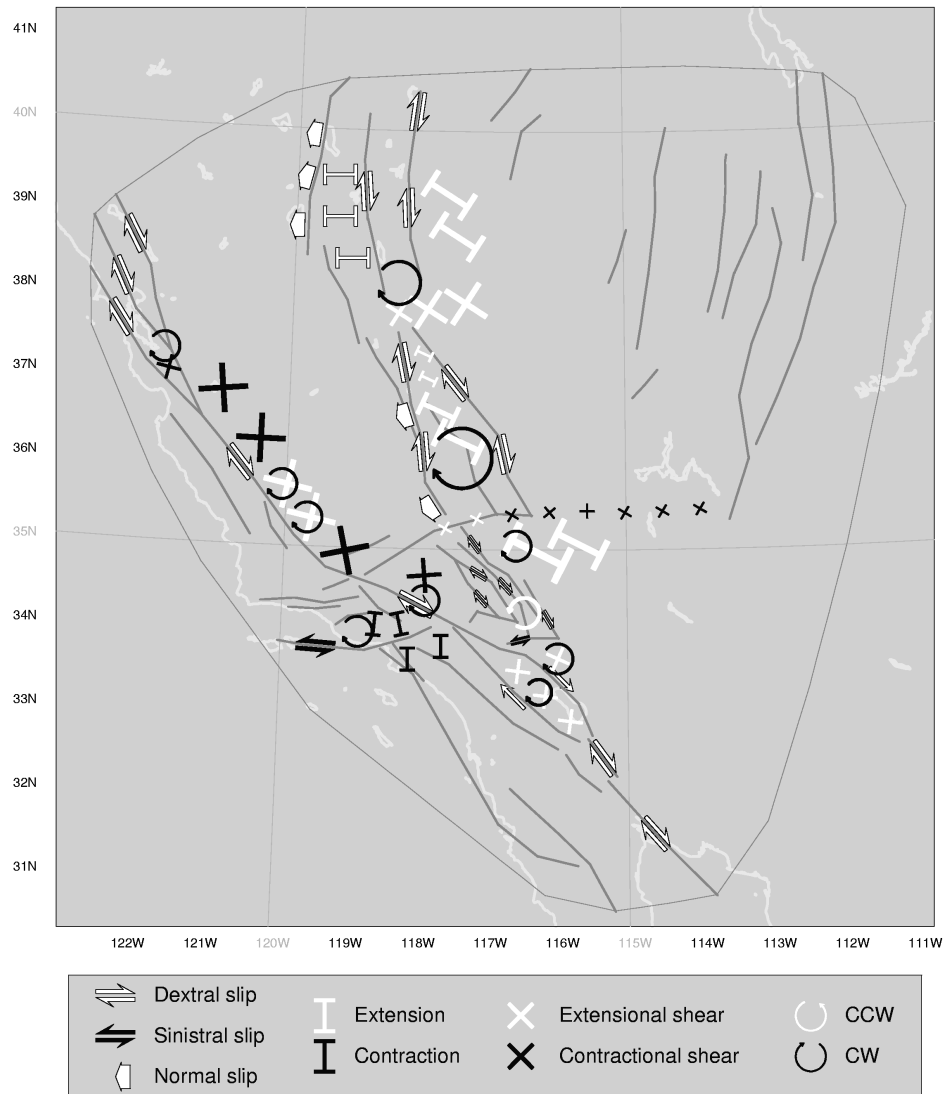


Figure 2.14: Model of the kinematics of the present-day surface deformation of the SWUSDZ. With extensional shear I indicate shear strains in which the magnitude of the extensional principal axes exceeds the contractional principal axes. With contractional shear I indicate shear strains for which the magnitude of the contractional axes exceeds the extensional axes.

2.9 Conclusions

I have estimated the surface deformation field of the southwestern US deformation zone in terms of I) block rotation and fault motion, II) the velocity gradient field, and III) the velocity gradient field and fault motion simultaneously. Solution III provides the best fit to the geodetic data. The model shows aseismic fault motion which sense of motion is generally in agreement with geological observations. In densely sampled areas, the fault motion is consistent with aseismic creep measurements. However, to some extent (depending on GPS observations close to the faults) the trade-off between fault motion and the velocity gradient field exists throughout my model. The surface deformation field shows distributed deformation in a zone around the faults with significant shear strain rates and rotations, though significant distributed deformation away from the faults is also observed. The eastern California shear zone acts as a distinct fault zone, bounded by more rigid blocks. The faults within the zone take up a significant part of the shear motion, while shear strain rates and clockwise rotations are located between the bounding faults. Similarly, the San Jacinto and San Andreas faults act as bounding faults of a fault zone with significant shear strain rates and clockwise rotations. The Mojave Desert is dominated by right-lateral shear, whereas the western Transverse Ranges show significant contraction. The sense of rotation in these regions is consistent with models based on paleomagnetic observations. I deduce that since the Late Miocene a significant part of the shear motion between the Pacific and North-American plate is accommodated by the San Andreas fault, while the remnant motion induces clockwise rotations in the Transverse Ranges and counter-clockwise rotation in the southern Mojave Desert. Significant localization of deformation east of the San Andreas fault is observed between the Big Bend section and the San Andreas-Calaveras fault junction. This is an immediate result of a significant rigidity contrast across the fault associated with a more rigid Salinian granite basement west of the fault and less-rigid Franciscan or Great Valley sequence material east of the fault. This localization of deformation has important implications for seismic hazard. In this area my seismic hazard analysis shows a moment deficit accumulated between 1973 and 2000 corresponding to a $M_w = 6.1 - 6.3$ earthquake. Near San Francisco Bay, along the San Andreas fault just north of the Big Bend and around the Imperial and southern San Andreas faults a comparable deficit has accumulated. On the Hayward and southern Calaveras faults the moment deficits coincide with significant microseismicity. This may point at an increased risk of an earthquake to occur in these regions in the near future.

Chapter 3

Surface deformation and tectonic setting of Taiwan inferred from a GPS velocity field.

3.1 Introduction

The island of Taiwan is a zone of active continental deformation located in an exceptional tectonic setting within the plate boundary zone between the Eurasian Plate (EUP) and the Philippine Sea Plate (PSP) (figure 3.1). At Taiwan the PSP is moving toward the EUP at a rate of 70-80 mm/yr in the direction N306°E (Seno et al., 1993, inset of figure 3.1). The complexity of Taiwan's tectonic setting arises from the fact that at the Ryukyu Trench the PSP subducts northnorthwestward underneath the EUP, whereas at the Manila Trench the PSP overrides the EUP in a westward direction. Taiwan is located at the transfer zone between subduction and overriding of the PSP. The 150 km long, NNE-trending Longitudinal Valley Fault (LVF) on the island of Taiwan is generally considered as the suture zone between the two plates (Barrier and Angelier, 1986; Biq, 1972) accounting for 25-30 % of the total plate convergence (Angelier et al., 2000).

The still ongoing collision between the Luzon volcanic arc and the Chinese continental margin started at least 8Myr ago (Ho, 1988; Kao et al., 1998; Lallemand et al., 2001; Teng, 1990) thereby creating and building the Taiwan orogen. Due to the oblique orientation of the strike of the arc relative to the strike of the passive margin, the collision at Taiwan has migrated southward, incorporating ever new portions of the Luzon arc (Lewis and Hayes, 1983; Suppe, 1981). Details of the geodynamic evolution and present-day tectonic setting of Taiwan are by no means resolved. This becomes evi-

This chapter is in press for publication in *J. Geoph. Res.* as: A.G. Bos, W. Spakman and M.C.J. Nyst, Surface deformation and tectonic setting of Taiwan inferred from a GPS velocity field.

dent from the variety of contradicting models proposed in the literature (Angelier et al., 1990; Chemenda et al., 1997; Lu and Malavieille, 1994; Suppe, 1981; Teng, 1990; Wu et al., 1997). Suppe, 1981; Teng, 1990; Wu et al., 1997].

These models focus on two closely related processes: the geometry and dynamics of the transition between the two subduction zones and the evolution of the Taiwan orogen. The hypothesis of the "thin-skinned" or "critical taper" model (Barr and Dahlen, 1990; Dahlen, 1990) for actively deforming fold-and-thrust belts has been challenged by models including the basement of the crust in the mountain building process (Ellwood et al., 1996; Hwang and Wang, 1993; Wu et al., 1997). In the "thin-skinned" models active deformation is confined to a trapezoidal segment of a wedge overlying a planar decollement fault, whereas the "basement involved" models require the discrete incorporation of autochthonous basement material into the shallow parts of the orogen. A model of crustal subduction followed by exhumation (Chemenda et al., 2001; Lin, 1998; Lin et al., 1998) has also been proposed to explain the rapid uplift and high heat flow in the Central Range of Taiwan (figure 3.1). Lallemand et al. (1997, 2001) and Teng et al. (2000) propose detachment of the Eurasian slab beneath Taiwan as a mechanism to create space for the subduction of the PSP slab along the westward propagating Ryukyu trench. Analogue modeling has shown the possibility of subduction reversal along a boundary comparable to the LVF of Taiwan in a similar setting of two contrary subduction zones, as well as provided insight in the mechanisms behind the processes of exhumation and lateral extrusion (Chemenda et al., 1997, 2001; Lu and Malavieille, 1994). These and other models still require further testing against available geological, geophysical and, in particular, geodetic data acquired in the past decade.

In 1989 the "Taiwan GPS Network" was established by the Institute of Earth Sciences, Academia Sinica (IESAS). Based on the 1990-1995 data of the network, Yu et al. (1997) derived the present-day velocity field of the Taiwan area. Such a velocity field provides significant information on the kinematics of the crustal deformation. I apply the inversion method of Spakman and Nyst (2002) to the GPS velocity field of Yu et al. (1997) in order to determine the kinematic properties of the surface deformation. This method solves simultaneously for the velocity gradient field and fault slip rate. The Spakman and Nyst (2002) method utilizes a physical relation between the velocity gradient field, fault motion and the relative velocity data which is significantly different from similar studies on complicated regions which are based on spatial interpolation of the data (e.g. Beavan and Haines, 2001; Wdowinski et al., 2001). The incorporation of fault motion in a joint inversion with the velocity gradient field is a unique characteristic of the method. In contrast to for instance elastic dislocation modeling (e.g. Bennett et al., 1996), my method requires no assumptions on crustal or fault dynamics (see Spakman and Nyst (2002) for further discussion). From the velocity gradient tensor I easily obtain the strain rate and rotation rate tensor fields. In conjunction with geological observations in the area, I interpret the obtained surface deformation model in terms of the kinematics of crustal processes. By combining the surface deformation

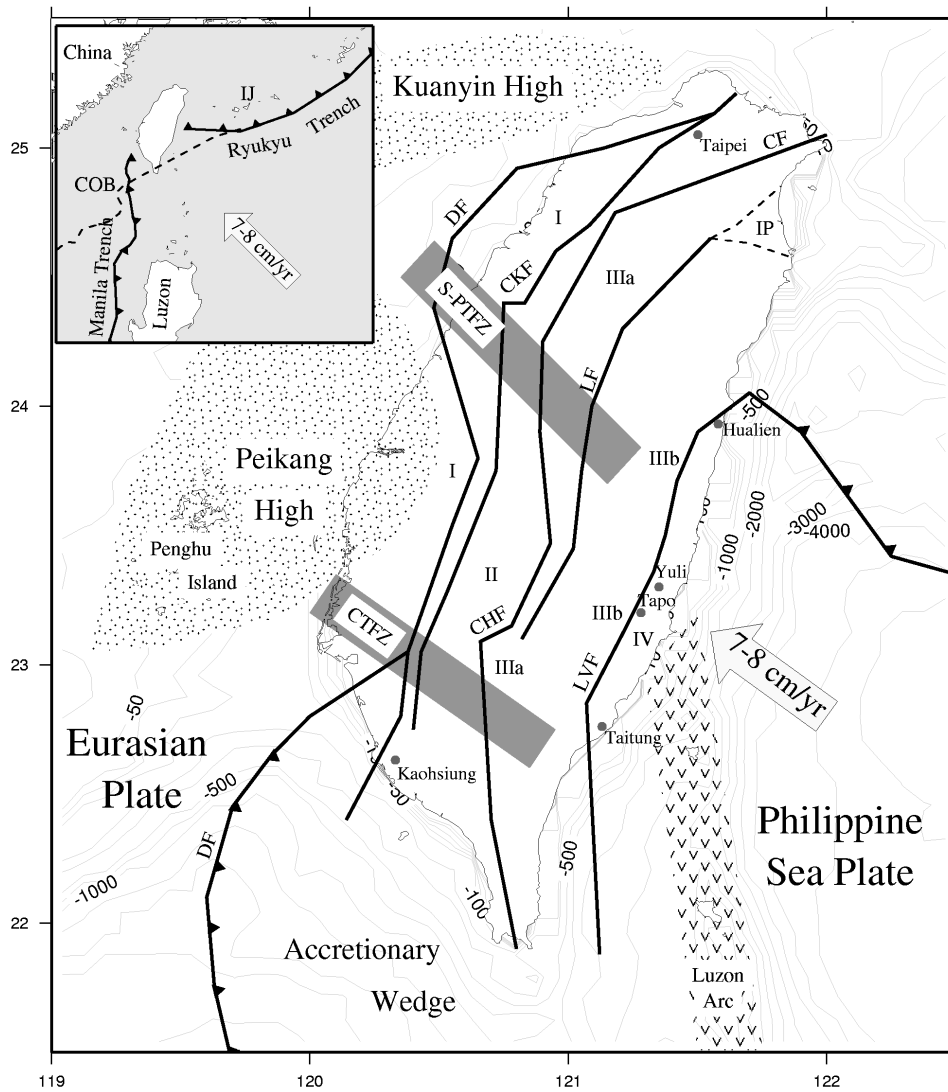


Figure 3.1: Tectonic setting of Taiwan showing major faults as used in this study: LVF = Longitudinal Valley Fault; LF = Lishan Fault; CF = Chuchin Fault; CHF = Chaochou-Chishan Fault; CKF = Chukou Fault; DF = Deformation Front, and the main geological provinces: I = Coastal Plain; II = Western Foothills (WF); IIIa = western Central Range (WCR); IIIb = eastern Central Range (ECR); IV = Coastal Range (CoR); IJ = Ishigaki-Jima; IP = Ilan Plain and COB = Continental Ocean Boundary.

model with seismicity data and seismic tomography I am able to propose a coherent model for the present-day tectonic activity at the island of Taiwan.

3.2 Geologic setting

Geologically, Taiwan can be divided into four N-NE trending provinces which are separated by active faults (figure 3.1). The provinces compose a west-vergent collisional prism involving both the Chinese continental margin and the Luzon Arc. In the eastern Central Range (ECR) Pre-Tertiary high-grade metamorphic rocks of the Chinese margin are exposed, while the Coastal Range (CoR) is composed of Neogene andesitic volcanic units of the northern Luzon Arc (Yu et al., 1997; Hu et al., 1996).

The general structural trends of the Taiwan mountain belt show an elongated S-shape (figure 3.1). Southern Taiwan is dominated by the on-shore extension of the Manila accretionary wedge, representing a particular zone of weakness related to the northern part of the Manila subduction system. To the north of this region, the accretionary wedge is terminated by the Chishan Transfer Fault zone (CTFZ), which appears as a major structural, seismological and kinematic boundary trending N130°E (Lacombe et al., 2001). Another major wrench fault zone cutting across Taiwan is the Sanyi-Pakua Transfer Fault Zone (S-PTFZ). This N140°E trending left-lateral fault zone is also accompanied by high seismicity and offsets several major structures (Defontaines et al., 1997). The prominent Peikang and Kuanyin High represent the shallow pre-Cretaceous Chinese continental basement. They are accompanied by significant Bouguer anomalies (Hsieh and Hu, 1972) and are characterized by tectonic stability. The deformation front (DF) is located along the western edge of the accretionary wedge in the south and progresses north through the Coastal Plain (CP) along the eastern edges of the basement highs. Generally, all deformation related to the convergence of the PSP and EUP is considered to be accommodated east of the DF (figure 3.1).

3.3 GPS data

I use the dataset of GPS motion vectors published by Yu et al. (1997). These vectors are determined for 131 stations of the "Taiwan GPS Network" that were surveyed 4-6 times between 1990 and 1995, four continuously recording stations and five semi-permanent stations (figure 3.2). In the calculation of the station velocities, Yu et al. (1997) chose the Paisha station (S01R), situated at the relatively stable Chinese continental margin, as the fixed reference station and fixed the azimuth from Paisha to Taipei (at 52.1°) to resolve the translational and rotational ambiguities of the whole network in the estimation. I adopt this reference station for plotting purposes, but note that my analysis is independent of reference frame.

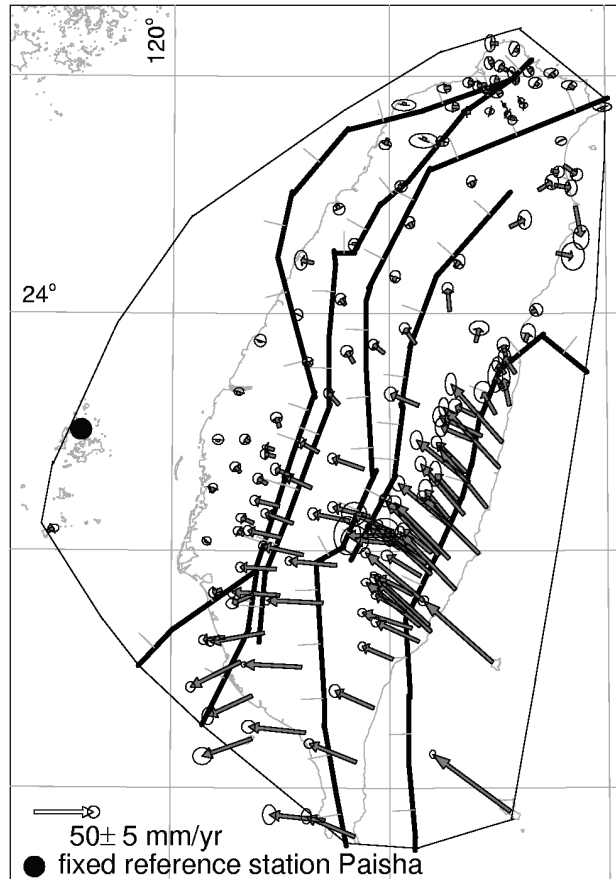


Figure 3.2: *GPS velocity vectors of Taiwan [Yu et al., 1997] as used in this study with their 95% confidence error ellipses.*

Several earthquakes with magnitude 5.0 or more occurred in or near the area of observation during the time of observation. However, since they did not have a significant effect on the length changes of the baselines, steady state motion is assumed during the period of observation (Yu et al., 1997).

3.4 The Spakman-Nyst method

I use the inversion method of Spakman and Nyst (2002) to determine the surface deformation of Taiwan in terms of discrete movements along faults (creep/slip) and continuous deformation in crustal blocks from relative motion data. The kinematic method does not require any assumptions about the dynamics causing the deformation or the

rheology of the crust. For stationary deformation the method relates the observed relative motion ($\Delta \mathbf{v}_{ij}$) between station i and station j to the velocity gradient field ($\nabla \mathbf{v}$) and fault slip rate (\mathbf{f}_k) on fault segment k (figure 3.3):

$$\Delta \mathbf{v}_{ij} = \sum_{l=1}^{K+1} \int_{L_{ij}^l} \nabla \mathbf{v}(\mathbf{r}) \cdot d\mathbf{r} + \sum_{k=1}^K \alpha_k \mathbf{f}_k(r_{ij}^k) \quad (3.1)$$

where L_{ij}^l is the integration path connecting stations i and j . K denotes the number of crossed fault segments, $\alpha_k = \pm 1$ depends on the fault orientation with respect to the direction of integration along path L_{ij}^l , \mathbf{f}_k is the slip rate on fault k at the intersection r_{ij}^k between L_{ij}^l and the fault and $\nabla \mathbf{v}(\mathbf{r})$ is the velocity gradient tensor.

The first part of the right hand side of equation 3.1 denotes the contribution of continuous deformation to the relative motion between the two stations. The integration over the $\nabla \mathbf{v}$ is done in parts, since the $\nabla \mathbf{v}$ can be discontinuous across slipping/creeping faults. The symmetric part of the velocity gradient tensor constitutes the strain rate field, where the antisymmetric part constitutes the rotation rate field. The second part represents the motion due to fault slip on K faults crossed by a path L_{ij}^l . Equation 3.1 is purely linear in the unknown quantities $\nabla \mathbf{v}$ and \mathbf{f}_k and offers a complete description of the relative crustal motion Δv_{ij} resulting from stationary crustal deformation.

A set of M geodetic relative motion observations yield at least $M(M - 1)/2$ vector equations 3.1 coupled through $\nabla \mathbf{v}$ and \mathbf{f}_k . I divide the faults into segments and for each segment the relative fault slip rate \mathbf{f}_k is parameterized as a (segment dependent) constant rate. The study region is subdivided into a network of N nodes connected by triangulation with the restriction that triangles cannot intersect with faults. I adopt a linear behavior of the velocity gradient (quadratic displacement) on the spatial coordinates

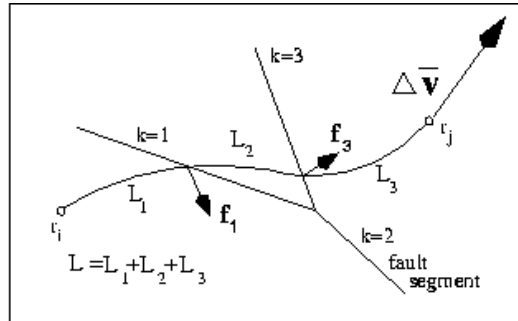


Figure 3.3: The forward problem of relating relative velocity to the velocity gradient field and fault slip. The curved path L_{ij} connects two observation sites i and j with relative motion Δv_{ij} .

in each triangle (Spakman and Nyst, 2002). This model parameterization is basically the only assumption entering the observation equation (3.1) and is used to arrive at a linear matrix system of equations. The density of the station distribution in the model area is used as a guide for local densification of the grid. I include the surface traces of "major", active faults. The "minor" faults are implicitly represented by the velocity gradient field. I do not attempt to incorporate all known faults, since the current data density is insufficient to independently resolve the velocity gradient field and slip/creep rates on numerous "minor" faults in such a more detailed parameterization .

Substitution of the parameterization in 3.1 yields an ordinary set of coupled equations, which can be assembled in a matrix-vector form (see Spakman and Nyst (2002) for details). Since the relative motion between 2 points is independent of the choice of L_{ij}^l , the matrix system can be extended with more data equations using the same observation set Δv_{ij} . Closed integration paths ($L_{ij}^l - L_{ji}^l$) between stations i and j will always render zero relative motion, therefore, the closed paths which only sample continuously deforming crust are effectively replaced by the local constraint that $\nabla \times \nabla \mathbf{v} = \mathbf{0}$. Additional paths L_{ij}^l may be required across faults to ensure internal consistency between fault slip rate and the velocity gradient field. This effectively leads to an extended set of data equations. Data errors, non-uniqueness and ill-conditioning of the observation matrix cause my matrix-vector system to be an inconsistent set of equations. To deal with problems associated with this, I adopt an inversion scheme which selects a solution that fits the data in a least squares sense and at the same time minimizes some model norm. Based on the characteristics of the model area (e.g. station density) I adopt a combination of amplitude damping on the boundary of the modeling area and, in the model interior, amplitude damping combined with spatially varying first derivative regularization. The model minimizing the data residual and the adopted model norm (defined by the regularization) is given by Spakman and Nyst (2002):

$$\mathbf{m} = (\mathbf{A}^T \mathbf{C}_d^{-1} \mathbf{A} + \alpha_0^2 \mathbf{I}_b + \alpha_1^2 \mathbf{I}_g + \alpha_2^2 \mathbf{D}_1^T \mathbf{D}_1)^{-1} \mathbf{A}^T \mathbf{C}_d^{-1} \hat{\mathbf{d}} \quad (3.2)$$

with a posteriori model covariance given by $\mathbf{C} = (\mathbf{A}^T \mathbf{C}_d^{-1} \mathbf{A} + \alpha_0^2 \mathbf{I}_b + \alpha_1^2 \mathbf{I}_g + \alpha_2^2 \mathbf{D}_1^T \mathbf{D}_1)^{-1}$ and model resolution kernel $\mathbf{R} = \mathbf{C} \mathbf{A}^T \mathbf{C}_d^{-1} \mathbf{A}$. Here \mathbf{A} represents the coefficient matrix, $\hat{\mathbf{d}}$ is the observed velocity data vector including the $\nabla \times \nabla \mathbf{v} = \mathbf{0}$ constraints, and \mathbf{C}_d denotes the data covariance matrix. Since my data vector $\hat{\mathbf{d}}$ consists of all $M(M-1)/2$ relative velocities, my data covariance matrix \mathbf{C}_d would obtain dimensions $M(M-1)/2$ by $M(M-1)/2$. Inversion of this matrix would be very inpracticable, if not impossible. Therefore I only utilize the data standard deviations, which through standard error propagation results in the standard deviation vector for the data vector $\hat{\mathbf{d}}$. \mathbf{I}_b and \mathbf{I}_g are identity matrices for the boundary and general damping, respectively, and \mathbf{D}_1 stands for the first derivative operator. α_0 , α_1 and α_2 are the weighting factors of the amplitude damping and first derivative regularization equations

and control the trade-off between fitting the data and minimizing the weighted model norm. The inversion depends on four tuning parameters: the weight (α_r) attributed to the surface constraint $\nabla \times \nabla \mathbf{v} = \mathbf{0}$, the weight α_0 for the boundary node damping, the weight α_1 for the amplitude damping in the interior of the model and the weight α_2 attributed to the first derivative operator. I investigate a range of solutions obtained with different combinations of the tuning parameters.

For the analysis of the inversion results I define the model normalized χ^2 per degree of freedom:

$$\chi_v^2 = \frac{1}{v} \sum_{i=1}^N \frac{e_i^2}{\sigma_i^2} \quad (3.3)$$

where N are the number of data equations, M the number of model parameters, $v = N - M$ the degrees of freedom of the model, $e_i = d_i^{obs} - d_i^{pre}$ is the prediction error of the model and σ_i^2 is the 1σ data variance. For models with a high degree of freedom a proper data fit will result in a χ^2 of around one. A $\chi^2 \gg 1$ indicates that I am unable to fit the data with the current model, whereas a $\chi^2 \ll 1$ identifies an attempt to model the data error, and may imply more model detail than supported by the data signal. The χ^2 determination is, however, completely dependent on the data error: An overestimation of such an error may result in a χ^2 which is significantly smaller than 1 and vice versa. Further, I use $\tilde{\sigma}_m = \frac{1}{M} \sum_{i=1}^M \sqrt{C_{ii}}$ as an average indication of the model error.

3.5 Inversions

The Spakman and Nyst (2002) method provides the possibility to solve for three different types of models for surface deformation. The first application (I) only solves for the fault slip rate vectors, hence assuming the crustal deformation field to be only controlled by motion/creep on unlocked, freely slipping faults; this corresponds to assuming rigid motion of large crustal blocks. The second application (II) solves for the velocity gradient tensor only and thus ignores fault contributions to the relative motion field i.e. assumes that all faults have been locked at the surface during the observation period. Finally, the third (III) is the joint approach which solves for both fault slip rate and the velocity gradient field. I invert for all three model types and provide an analysis of the results for comparison.

The density of my dataset and my aim to model the regional deformation field restrict the estimation of the velocity gradient and fault slip rate to relatively substantial areas and fault segments, respectively. Around the LVF the station density allows a significantly denser parameterization compared to the rest of the model area. I include the surface traces of the six major geological faults (Hu et al., 1996, 1997; Yu et al., 1997) in my parameterization. The location of the fault traces have been digitized from

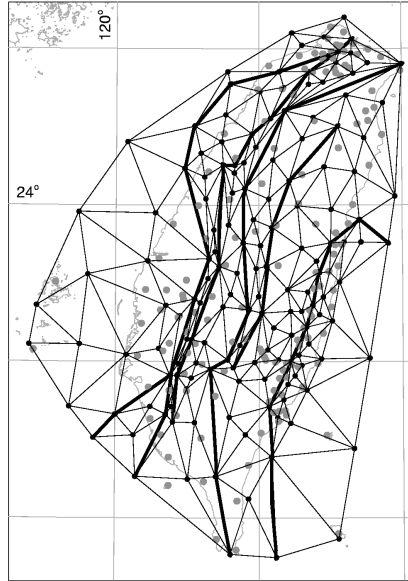


Figure 3.4: *Final parameterization of the models of Taiwan. Thick lines indicate fault segmentation, black dots are the triangle nodes and grey dots are the site positions. Note that in my choice for the triangle nodes I are not restricted to the locations of the observation sites. Triangles do not intersect faults. Nodes at the fault are doubled to allow the velocity gradient field to be discontinuous across faults.*

Yu et al. (1997) to insure the station-to-fault relative positions. This approach leads to a total of 290 triangles, spanned by 192 nodes and 57 fault segments with 57 slip rate vectors (figure 3.4). Though fault slip rate parameter damping is possible, inversion I proved to be overdetermined with acceptable model covariance and required no damping. For inversions II and III I aim for a solution with minimal regularization, acceptable covariance and resolution and a $\chi^2 \sim 1.0$. However, a larger χ^2 (2.89 for my preferred model) and slightly reduced spatial resolution are accepted to avoid spurious values typical of an underdamped solution. Note that I implement the 1σ standard deviations in my inversion procedure. Utilizing a 3σ standard deviation would result in a χ^2 of 0.48. The first derivative regularization is allowed to vary spatially depending on the number of integration paths crossing each triangle (hitcount of the triangle): Triangles with less hits than $1/12$ of the maximum hitcount obtain an increased regularization weight (α_{2_a} and α_{2_b} , respectively). The final tuning parameters obtained for both inversion II and III were: $\alpha_r = 3.0 \cdot 10^5$ (or a standard deviation of $\sigma_r = 1.4 \cdot 10^{-6} (\text{myr})^{-1}$) for the curl constraints and $\alpha_0 = 1.0 \cdot 10^8$ for the boundary damping, $\alpha_1 = 4.0 \cdot 10^7$ for the amplitude damping and, $\alpha_{2_a} = 5.0 \cdot 10^{10}$ and $\alpha_{2_b} = 2.0 \cdot 10^{11}$ for the spatially dependent first derivative operator on high hitcount ($> \frac{1}{12} * \text{max}$) and low hitcount

i	T_n	T_t	K	χ^2	\tilde{r}_m	$\tilde{\sigma}_m^c$ [$\frac{10^{-8}}{yr}$]	$\tilde{\sigma}_m^f$ [$\frac{mm}{yr}$]
I	-	-	114	24.4	1.0	-	0.13
II	155	290	-	4.96	0.65	1.25	-
III	192	290	114	2.89	0.62	1.46	0.22

Table 3.1: Aspects of the inversion parameterization and average results for inversions I, II and III. Key: i , inversion; T_n , number of model nodes; T_t , number of triangles; K , number of fault segments; $\tilde{r}_m = \frac{1}{M} \sum_{i=1}^M R_{ii}$, the average resolution, with R_{ii} the diagonal elements of the resolution matrix and M the number of model parameters; $\tilde{\sigma}_m^c = \frac{1}{M_c} \sum_{i=1}^{M_c} \sqrt{C_{ii}}$, the average standard deviation for the components of $\nabla \mathbf{v}$, with $M_c = 4T_n$ the number of components of $\nabla \mathbf{v}$; $\tilde{\sigma}_m^f = \frac{1}{M_f} \sum_{i=1}^{M_f} \sqrt{C_{ii}}$, the average standard deviation for the components of \mathbf{f}_k , with $M_f = 2K$ the number of slip components.

(< $\frac{1}{12} * max$) regions, respectively. The fault slip rate vectors in inversions I and III were never subjected to damping. Table 3.1 provides an overview of some aspects of the inversion parameterization and average results for inversions I, II and III.

3.5.1 I: Inversion for fault slip rate only

In an attempt to fit the data by pure fault motion, i.e. assuming rigid crustal blocks, I only consider the 6 major geological faults on Taiwan. In the model the faults are represented by 57 slip rate vectors, each consisting of a fault normal and a fault parallel component, resulting in a total of 114 model parameters. The inverse problem proves to be over-determined (perfect resolution) but the solution, with small model covariance, shows large data misfits which can not be accommodated by the 95% confidence error ellipses ($\chi^2 = 24.4$; figure 3.5a). Using a more detailed fault parameterization of allowing twice the amount of slip model parameters per fault does not lead to a significant reduction of the data misfit nor renders a significantly different slip rate solution. A comparison with neotectonic observations of fault slip rates also fails the test. For instance, the solution for slip rate on the Longitudinal Valley fault comprises a combination of thrust and left-lateral motion, consistent with geological observations (figure 3.5b). However, the magnitude of the slip rate is significantly larger than the observed slip rates determined from geological and creepmeter measurements (Angelier et al., 1997; Lee et al., 2001). The Lishan fault accommodates significant thrust movement on its northern segments, where geological evidence shows left-lateral movement in the north with increasing thrust movement towards the south (Lee et al., 1997). While the modeled left-lateral motion on the Chaochou-Chishan-Chuchin fault is supported by geological observations, no evidence of the normal component has been found (Lacombe et al., 2001). The relative increase in thrust movement on the Chukou complies with geological observations (Yu et al., 1997).

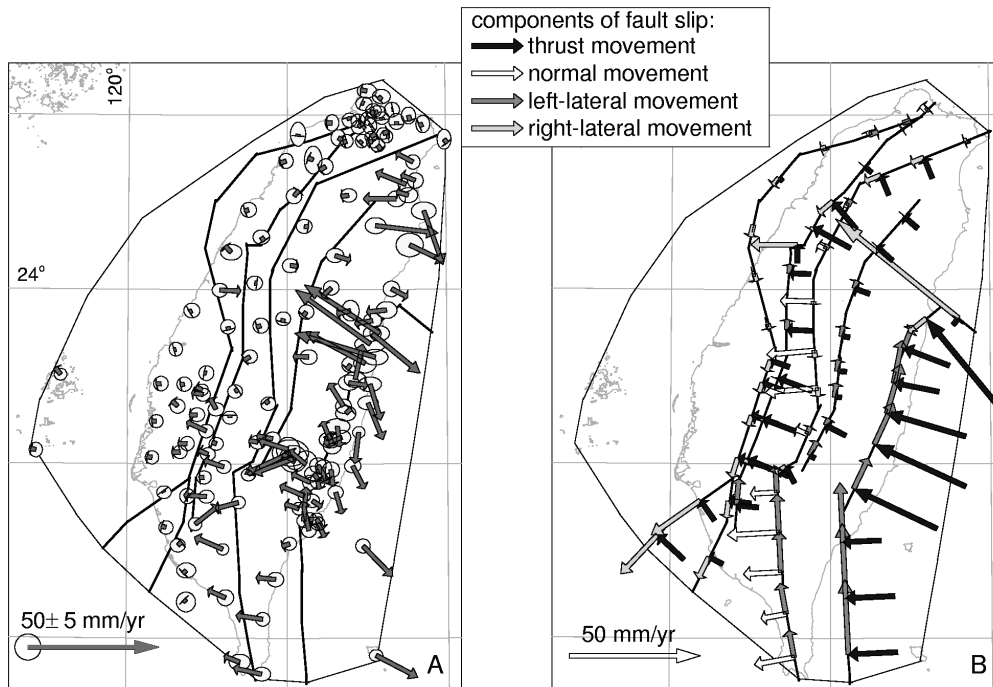


Figure 3.5: Solving for fault slip rate only: a) Data misfits: Since my data are the relative velocities between every pair of stations, I determine the misfit at each station by taking the difference between the predicted velocity and the data velocity for each path connecting this station and determine the average. I compare it with the average error ellipse of the station, which is also determined from the error ellipses of all these paths. b) Fault slip rate solution.

Since I have only parameterized the six major active faults in the Taiwan region, I acknowledge the possibility of an improved data fit should "minor" fault systems be included. Here, I only test whether rigid motion of large crustal blocks (implicitly defined by adopting the major fault systems) can fit the data. In inversion III the "minor" faults and elastic loading are implicitly represented by the velocity gradient field. On account of the poor data fit and the poor comparison to neotectonic observations, I conclude that the hypothesis of pure rigid block motion cannot explain the GPS data.

3.5.2 II: Inversion for continuous deformation only

In this application I do not solve for fault motion contributions to the velocity field. The parameterization consists of 290 triangles, spanned by 155 model nodes. Each node generates 4 components of the velocity gradient tensor, which results in a total of 620 model parameters. The data misfit ($\chi^2 = 4.96$; figure 3.6b) is significantly better

than obtained for model I. Largest misfits are found in the Longitudinal Valley region, where many GPS stations are close to either side of the LVF (figure 3.6b). From figure 3.2 I infer that the GPS velocity changes strongly when crossing the fault as a result of fault motion not modeled in this inversion.

Most of the convergence between the EUP and the PSP is absorbed in the Longitudinal Valley region. Extension is found in the southern Central Range (CR) and the Ilan Plain (IP). Large contraction can also be seen just east of the Deformation Front (figure 3.6a). Lee and Angelier (1993) determined the strain rates for the central part of the Longitudinal Valley from trilateration data assuming that the crustal deformation should be modeled by continuous crustal flow. They show contraction rates at Juisui, Yuli and Chihshang of (all expressed in yr^{-1}) 2.3×10^{-6} , 3.1×10^{-6} and 2.1×10^{-6} , respectively, with a consistent N132°E trend. I find strain rates of $1.48 \pm 0.02 \times 10^{-6}$ in N140°E at Juisui, $0.86 \pm 0.02 \times 10^{-6}$ in N137°E at Yuli and $1.35 \pm 0.02 \times 10^{-6}$ in N133°E at Chihshang, which are consistently smaller. This could

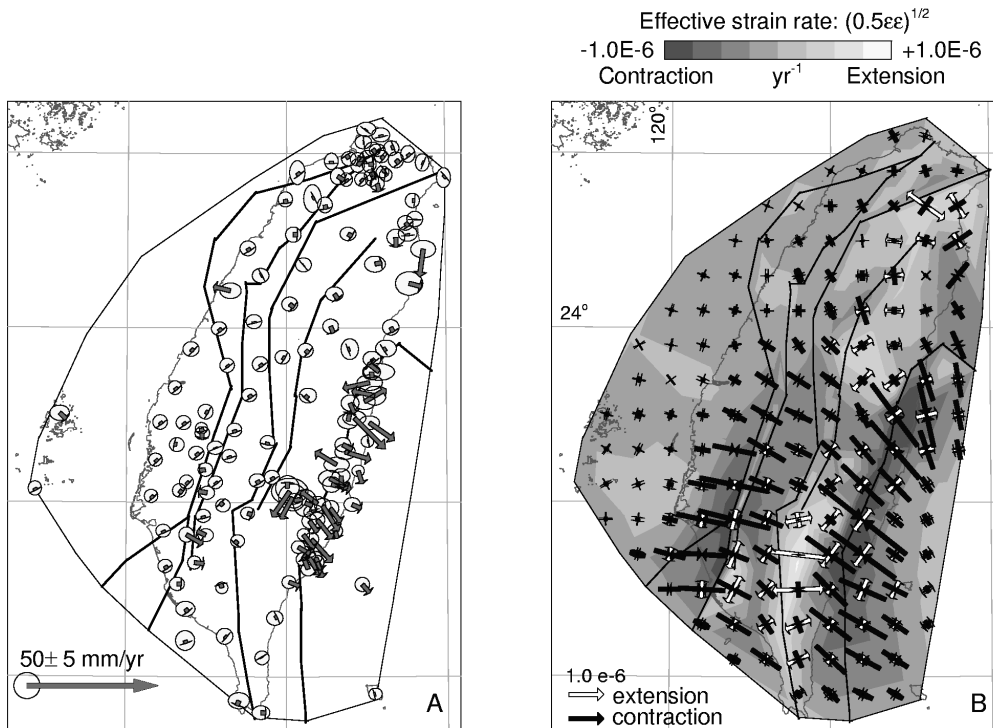


Figure 3.6: Solving for continuous deformation only: a) Data misfits, b) Strain rate field. The contouring denotes the effective strain rate $(= (1/2 \epsilon_{ij} \epsilon_{ij})^{1/2})$. The arrows denote the principal strain rates: contraction (black) and extension (white). For a color version of this figure see figure C.7 of appendix C.1.

be due to the differences in scale between their dense triangulation networks and my sparser GPS network and my coarser parameterization (Kahle et al., 2000; Nyst, 2001). Yu and Chen (1998) performed a study similar to that of Lee and Angelier (1993) for the southern part of the Chukou fault. They used the data of 5 years of GPS campaigns (1993-1997) to study spatial and temporal variations in crustal strain. Their calculated contraction rates of $0.48 \times 10^{-6} yr^{-1}$ in N119°E at the central part of the Chukou fault increase to $2.01 \times 10^{-6} yr^{-1}$ in N109°E further to the south. Here I find an increase from $0.47 \pm 0.02 \times 10^{-6} yr^{-1}$ in N119°E to $1.08 \pm 0.02 \times 10^{-6} yr^{-1}$ in N96°E. They also determined extension rates in the south of $0.7 \times 10^{-6} yr^{-1}$ in N18°E. This agrees reasonably well with my extension rates of $0.50 \pm 0.02 \times 10^{-6} yr^{-1}$ in N27°E in the same area.

Though this application clearly offers a better data fit than the inversion for fault slip rate only (I), it remains inconsistent with neotectonic observations. Further, the presence of major, active faults in this region is undisputed.

3.5.3 III: Inversion for fault slip rate and continuous deformation

The joint inversion utilizes the same triangular grid as inversion II. On the fault traces duplicate model nodes are used to allow decoupling across the fault. The joint inversion is thus based on the same 290 triangles spanned by 192 model nodes and an additional 57 slip rate vectors, yielding a total of 882 (768 for $\nabla \mathbf{v}$ and 114 for \mathbf{f}_k) model parameters. Some of the data misfits for this joint inversion are slightly larger than the average 95% confidence ellipses leading to an average data misfit χ^2 of 2.89 (figure 3.8a). I observe that the few misfit vectors that exceed the limits of the data confidence ellipses are still primarily located in the Longitudinal Valley region, where deformation is strongest. Comparison with the data (figure 3.2) shows that the misfit vectors denote local differences within the trend of the data. Our adopted parameterization is too coarse to model these strong local variations in relative motion.

Before analyzing the fault slip rate (figure 3.8b) and the strain- and rotation rate fields (figure 3.9a,b) I will discuss the covariance and resolution of the solution.

Covariance and resolution

From the model covariance matrix C I extract the standard deviations in the estimates of my model parameters ($\sigma_i = \sqrt{C_{ii}}$). For the velocity gradient field I plot the σ_i corresponding to a 95% confidence level as two contour plots: one for the ϕ -derivatives (longitude) (figure 3.7a) and one for the θ -derivatives (latitude) (figure 3.7b). The larger errors ($\sim 5 \times 10^{-8} yr^{-1}$) occur along the southwestern extent of the Deformation Front and in the northnorthwestern region of the model area. In regions with a small amplitude ($\sim 1 \times 10^{-8} yr^{-1}$) the solution becomes insignificant. The errors of the fault slip rate parameters, plotted as 95% confidence error vectors in the θ - and ϕ -

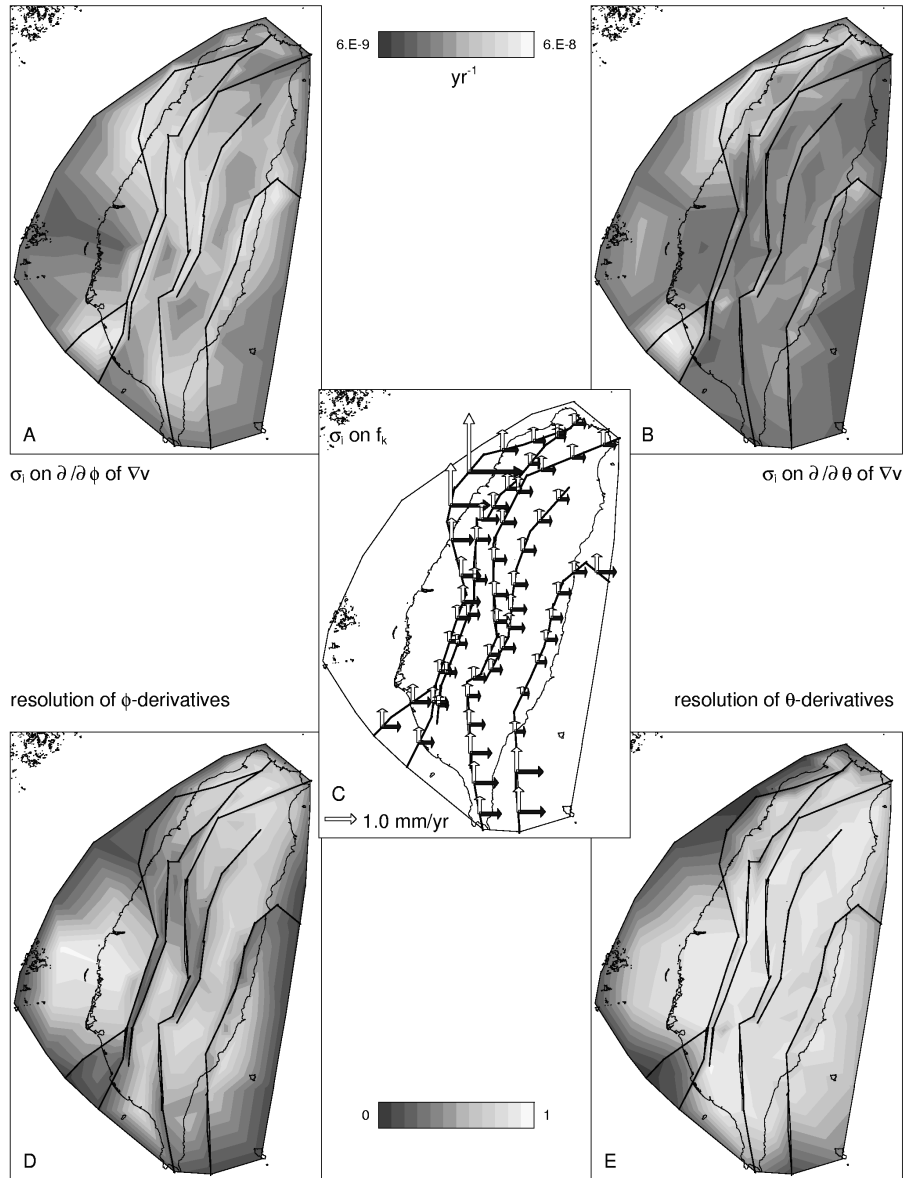


Figure 3.7: Covariance and Resolution of the joint inversion solution. The covariance is represented as the model standard deviations ($\sigma_m = \sqrt{C_{ii}}$). A) contour plot of the 95% confidence σ_i on ∇v_θ , B) contour plot of the 95% confidence σ_i on ∇v_ϕ , C) 95% confidence σ_i on f_k plotted as error vectors in the θ -direction and ϕ -direction, D) contour plot of the resolution of ∇v_θ , E) contour plot of the resolution of ∇v_ϕ .

direction (figure 3.7c), are a factor 10 smaller than the average magnitude of fault slip rate obtained in the solution.

Figure 3.7d and 3.7e show contour plots for the diagonal elements of the resolution kernel of the velocity gradient field. The interior of the study region is relatively well resolved with diagonal elements exceeding 0.75. The difference between resolution in latitude and longitude can be understood by realizing that due to the better NS spread of observations (compared to EW) latitudinal variations are better resolved. Reduced resolution at the boundary of my modeling area is due to the influence of the regularization. The reduced resolution offshore Taiwan in the northwestern part of my modeling area can be attributed to the poor data coverage in this part of the model. In the interior of the model the resolution is reduced due to a trade-off between fault slip rate and the velocity gradient. This can be observed between the Deformation Front and the Chukou fault, around 24°N between the Chukou fault and the Chaochou-Chishan fault, and between the Chaochou-Chishan fault and southern Lishan fault. I note that the fault slip rate thus modeled may represent a combination of fault creep and interseismic signal, depending on the trade-off between the velocity gradient field and fault motion. This trade-off occurs in case of lack of data to separate fault motion from the velocity gradient field in a kinematic inversion. (Nyst, 2001; Spakman and Nyst, 2002). The trade-off is best resolved in areas with relative motion observations close to the fault zones. In areas where this is not the case, an interseismic signal due to block motion may be introduced in the slip rate solution, whereas the fault may in fact be locked. This trade-off also affects the amplitude of the velocity gradient estimate in the proximity of the fault. I note that a solution for only continuous deformation (solution II of this study) implicitly reflects pure elastic loading of locked faults. I further note that the trade-off problem is not a feature of the Spakman and Nyst (2002) method, but is a problem for any interpretation method of relative motion data. I refer to Spakman and Nyst (2002) for a further discussion on this topic.

Fault slip rate contribution

In the joint solution I find significantly reduced fault slip rates compared to inversion I, though the sense of motion is reasonably consistent between the two solutions. The fault slip rate contribution of the joint solution (figure 3.8b) shows relatively small horizontal slip rates of the order of ~ 2 mm/yr on most fault segments. Larger horizontal slip rates are observed on the southern segments of the Chukou fault and on the Longitudinal Valley fault. Large vertical rates have been determined on Taiwan (Lin, 1998; Yu and Kuo, 2001), but are not reproduced by my model since I only consider horizontal velocities/rates. Slip rates on the Longitudinal Valley fault vary from about 19 mm/yr with an azimuth of $\text{N}124^{\circ}\text{E}$ at Taitung to 25 mm/yr in $\text{N}136^{\circ}\text{E}$ at Yuli and 7.8 mm/yr in $\text{N}151^{\circ}\text{E}$ at Hualien. Yu et al. (1990) showed that the Longitudinal Valley fault is a very weakly locked or almost freely creeping fault. At Tapo, Angelier et al. (1997)

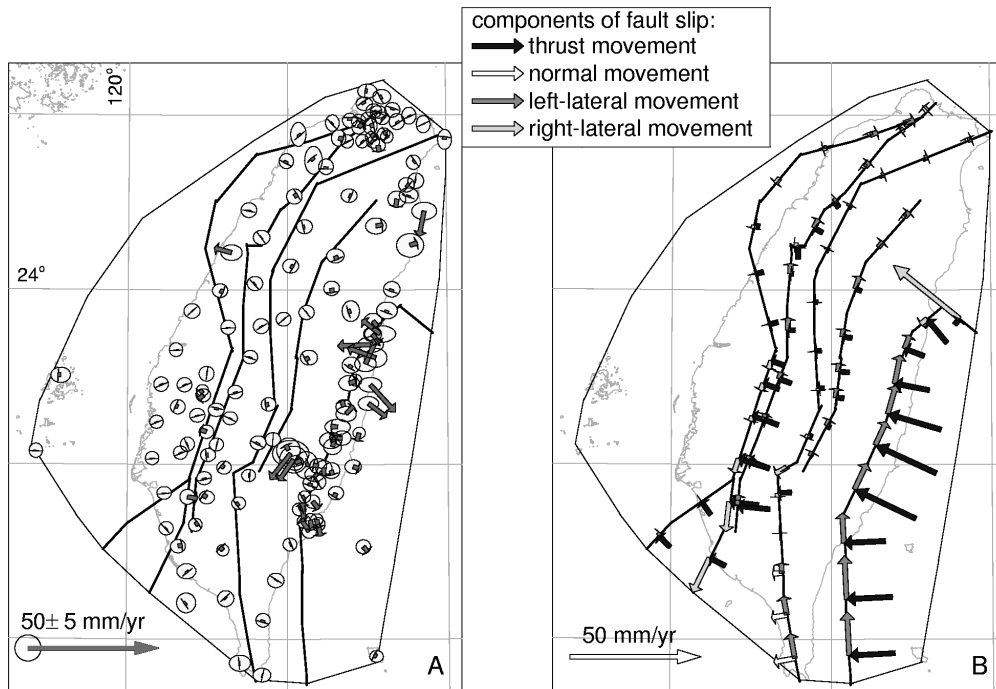


Figure 3.8: Joint solution: a) Data misfits, b) Fault slip rate solution. For further explanation see figure 3.5

determined present-day rates based on detailed surveys of faulted concrete structures. Their rate of 22 mm/yr in N143°E compares reasonably with my value of 26.84 ± 0.22 mm/yr in N136°E. The difference might be explained by the scale differences of the very local observations and my more regional parameterization.

The Lishan fault shows left-lateral movement at the northern segment changing to thrust movement more to the south. This variation in movement is in agreement with geological observations done by Lee et al. (1997). Yu et al. (1997) found a significant increase in shortening rates towards the south along the Chukou fault, which is in support of the increase of thrust movement I observe in my model. I further find that the Deformation Front acts as a right-lateral thrust, which is consistent with the observations of Lacombe et al. (2001).

Strain rate contribution

The parameterization of faults in application III allows the velocity gradient field to be discontinuous across active faults. The implementation of the faults significantly reduces the magnitudes of the strain and rotation rates compared to application II, es-

pecially around the Longitudinal Valley fault and the Chukou fault. The magnitudes obtained for the strain rate field still remain amongst the largest estimates on Earth for interseismic deformation.

The strain rate field (figure 3.9a) shows a general behavior of NW-SE contraction in the Longitudinal Valley of eastern Taiwan. In southwestern Taiwan I observe an anticlockwise rotation of the principal axis direction to E-W contraction. The Peikang High is found to have relatively small strain rates. Comparing this trend with the stress field modeling results of Hu et al. (1996) I find a general agreement. However, differences between their results and my solution are observed, especially around the IP. This may be due to ignoring the opening of the Okinawa Trough (OT) in their elastic-plastic model, which could have a significant effect on the strain rates in northeastern Taiwan. Another cause for discrepancies can be that stress and strain directions do not necessarily align in case of elastic-plastic rheology, which hampers a comparison between their stress directions and my strain directions. The magnitude of the strain rate field decreases towards the north.

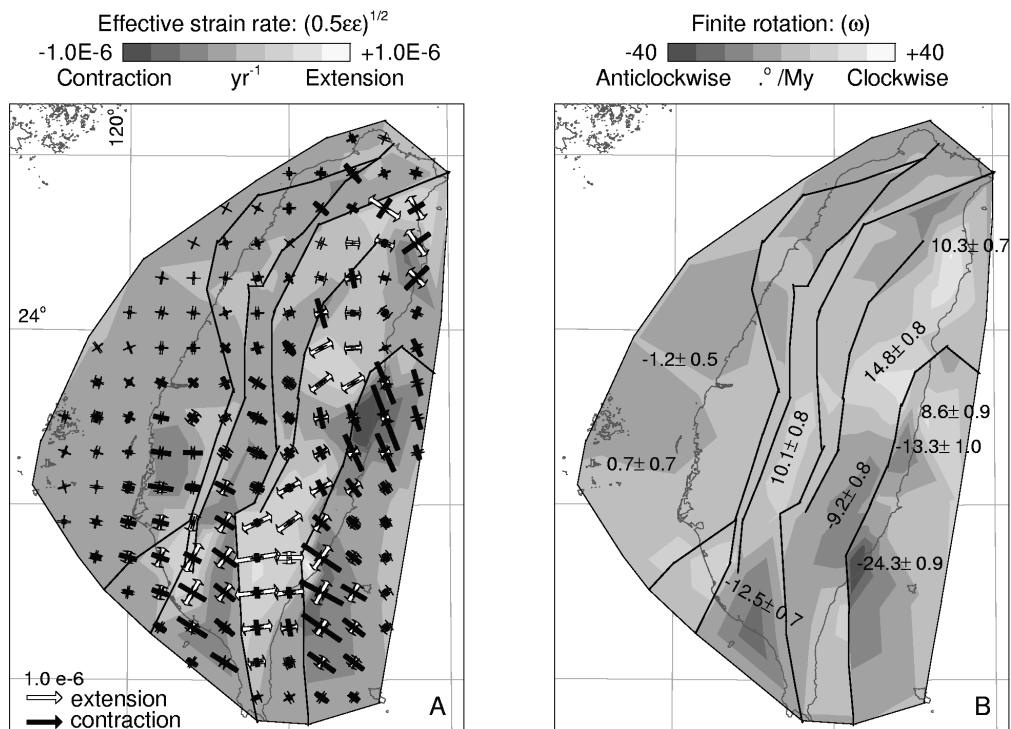


Figure 3.9: Joint solution: a) Strain rate field, b) Rotation rate field in degrees/Myr. The numbers refer to local averages of relatively strong rotation rates and their 1σ errors. For a color version of this figure see figure C.8 of appendix C.1.

East of the Longitudinal Valley fault relatively large NW-SE contraction dominates the deformation. In contrast, the central and southern CR show a dominant NE-SW to E-W extension. Geologically, this extension is inferred from normal faulting in the orogen (Crespi et al., 1996; Kosuga et al., 1988), thermal observations (Crespi et al., 1990) and normal fault type earthquake swarms (Lin and Tsai, 1981; Rau, 1996). The Western Foothills (WF) are subjected to a WNW-ESE contraction accompanied by a significantly southward increasing NNE-SSW extension. This trend is in agreement with Pleistocene paleostress patterns in southwestern Taiwan (Lacombe et al., 1999; Rocher et al., 1996). In the IP I find significant NW-SE extension, consistent with the inferred extensional direction in the Okinawa Trough (Herman et al., 1978; Kimura, 1985; Sibuet et al., 1987).

Rotation rate contribution

The rotation rate tensor is given by the anti-symmetric part of the velocity gradient tensor (figure 3.9b). Strictly speaking, the obtained relative rotation rates apply to rigid rotations of small equidimensional blocks. Interpretation of regional (anti) clockwise rotations can be made if on average the obtained rotation rates are (negative) positive. Since I am not able to solve for a net uniform rotation of the entire study region a comparison with paleomagnetic block rotations is not straightforward. This is further complicated by the fact that almost all paleomagnetic observations are older than 8Ma (Lee, 1993; Miki et al., 1993), hence occurred prior to the last collisional phase (Ho, 1988; Kao et al., 1998; Teng, 1990). I notice that many large regions with the same sense of rotation rate are bounded by the faults which is indicative of fault motion.

Model III (figure 3.9b) shows two regions with large anticlockwise rotation rates in the CoR, where, just offshore the northern section of the CoR, equally large clockwise rotations are obtained. This offshore area and the area around Taitung are, however, poorly resolved and care should be taken when interpreting these rotation rates.

The WF are divided in three blocks with opposing rotations; Northern Taiwan is dominated by anticlockwise rotations, the central part experiences clockwise rotation averaging $10.1 \pm 0.8^\circ/Myr$ as the southern WF are subjected to $12.5 \pm 0.7^\circ/Myr$ of anticlockwise rotation on average. The CR shows a similar division: The northern section undergoes averagely $14.8 \pm 0.8^\circ/Myr$ of clockwise rotation, the middle section is subjected to anticlockwise rotation averaging $9.2 \pm 0.8^\circ/Myr$, and the southern section shows reduced anticlockwise rotation in the west and clockwise rotation in the east. The intersections of the oppositely rotating blocks coincide with the two major transfer fault zones on Taiwan. Only the southern region of the Coastal Plain undergoes a clockwise rotation of a few *degrees/myr*. The Ilan Plain is rotating clockwise with a rate of $10.3 \pm 0.7^\circ/Myr$ on average.

Comparison to lithospheric stress data

I compare the principal axes of my strain rate field with the principal stress axes from earthquake focal mechanisms. Since I only model the two-dimensional horizontal strain rate tensor, I compare it to the horizontal components of the seismic moment tensor. These four components were extracted from the Harvard moment tensor solution of each earthquake within the modeling area with magnitude larger than 4 and depth less than 50 km. In my comparison I make a distinction between shallow events (<20km) and the deeper events. Though I am aware that the deeper seismicity may be related to lithospheric deformation (subducting slab), I include the deeper events to allow for comparison with events in the crustal root of the orogen underneath the Central Range. The principal axes of seismic moment tensors do not need to coincide with those of the surface strain rates since (i) the seismic moment tensors reflect local release of stress (which does not necessarily coincide with regional strain rate directions) and (ii) the surface strain rates do not necessarily reflect deformation at depth.

In the Western Foothills I find a reasonable agreement in the directions of the principal axes for all events. In all other areas a consistent misfit exists for both shallow and deep events. In the southern Central Range the E-W compression at depth is in complete contrast to the E-W extension of my model. I believe that these disagreements should be attributed mostly to the fact that those surface velocities which are the response to deeper crustal processes not necessarily contain all information on the deformation occurring in the deeper crust. Therefore, a combination with crustal deformation data (e.g. seismicity) is useful to study crustal processes driving the surface deformation.

3.6 Geometry of the subduction system

Of basic importance for understanding the determined strain- and rotation rates and fault slip rate is the geometry of the two subduction systems in the mantle. Numerical modeling predicts that subduction of a continent-ocean boundary (COB) leads to favorable conditions for detachment of the oceanic lithosphere (Van de Zedde and Wortel, 2001; Wong A Ton and Wortel, 1997). Several recent studies have adopted the hypothesis of detachment of the EUP slab under northern and central Taiwan in order to explain the ongoing subduction of the PSP slab (Lallemand et al., 1997, 2001; Teng et al., 2000). Analogue models (Chemenda et al., 2001) demonstrate the possible conjunction of EUP slab detachment and incipient westward subduction of the PSP under Taiwan.

The question remains whether slab detachment is actually occurring. Lallemand et al. (2001) base their interpretation of slab detachment on the global tomographic mantle model of Bijwaard et al. (1998), which shows predominantly low P-wave speeds in the upper 100 km of the EUP subduction. However, since the non-subducted part

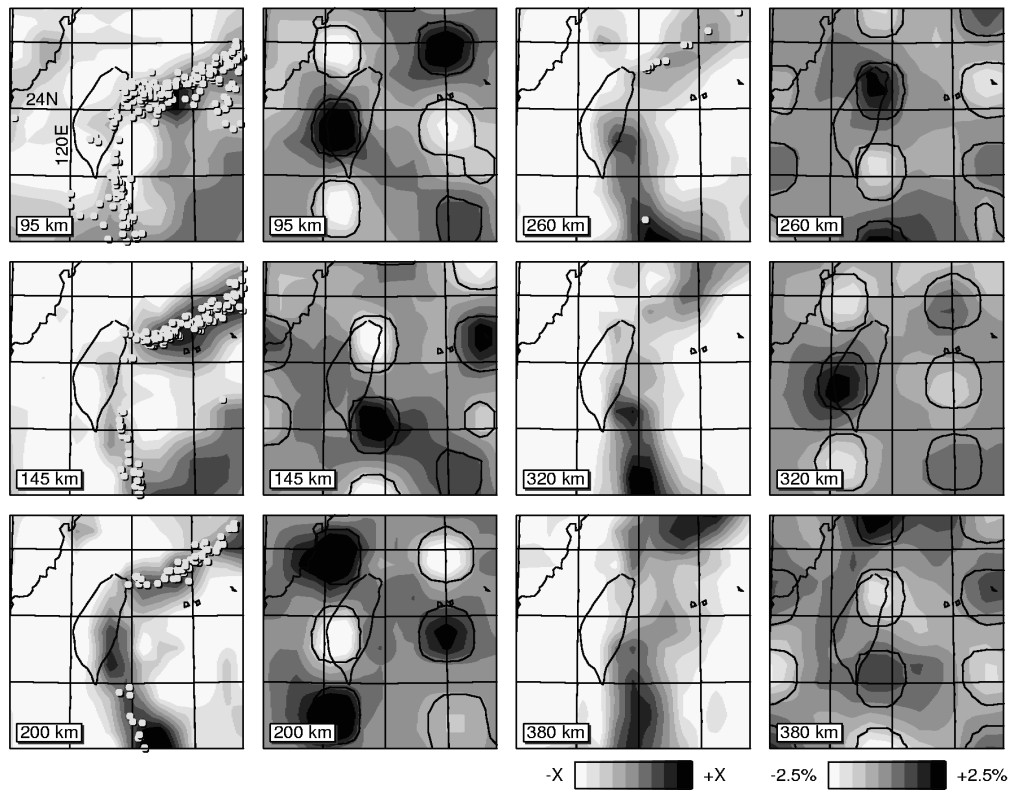


Figure 3.10: Layer cuts from the global tomographic mantle model of Bijwaard and Spakman [2000]. The left column displays the P-wave velocity anomalies between 95km and 380km (depths indicated) in percentages of the following reference velocities (from top to bottom) 8.047, 8.119, 8.275, 8.482, 8.701, and 8.913 km/s. White dots denote intermediate depth hypocenters within 25 km of each layer depth. The grid of black lines are longitude and latitude lines in steps of 2 degrees (see upper left panel for 2 values). The right column displays the results of a sensitivity test for estimates of spatial resolution in which the image recovery is tested of a synthetic velocity model consisting of isolated blocks (circular outlines) of 1.2 degrees in size and a thickness of about 50 km. The amplitudes are of alternating sign and the blocks are shifted in depth. The colors denote the recovery of the synthetic model. Mild smearing effects between the synthetic blocks are visible at all depths, but the synthetic blocks are generally well recoverable, particularly in the upper 200 km under Taiwan. Below this depth resolution reduces gradually. I conclude from this (and other sensitivity tests) that the tomographic image of the actual Earth (left column) is interpretable at length scales of 50-60 km. For a color version of this figure see figure C.9 fo appendix C.1.

of the Chinese continental lithosphere is imaged with similar low wave speeds, it is difficult to discriminate between a detached slab and subducted continental lithosphere particularly in the upper 100-150 km of the mantle. Below this depth range the EUP slab is visible in the mantle tomography. Teng et al. (2000) invoke slab detachment as the driving force behind the high uplift rates and large heat flow observed in the eastern Central Range. The maximum uplift rates and largest heat flows are currently observed between 23°N and 23.5°N , which would suggest that the tip of the southward propagating detachment tear has advanced significantly south of this location (Wortel and Spakman, 1992, 2000). However, both seismicity (figure 3.12; cross-section A) and seismic tomography (figure 3.10) contradict this suggestion by showing a continuous slab up to 23°N .

The assumption of slab detachment is required if the northward extension of the EUP slab beneath Taiwan intersects with the PSP slab. Figure 3.10 shows cuts from the tomographic model of Bijwaard and Spakman (2000), which differs from earlier work (Bijwaard et al., 1998) as a result of 3D ray tracing to correct for seismic ray bending effects caused by the 3D velocity structure of the mantle. For the Taiwan region this leads to an improved definition of the slab geometry. The relatively fast (blue) anomalies north of 24°N and east of 122°E image the northnorthwestward plunging PSP subduction zone along the Ryukyu trench. Similarly, the eastward dipping EUP is visible south of 24°N and at longitudes centered around 122°E . For depths above 145 km the EUP slab is best delineated by intermediate seismicity. Below this depth the slab reaches 24°N at most (the latitude of Hualien). I assume that the PSP slab and the EUP slab are at the point of making contact with each other at Hualien. On account of these images, slab detachment of the EUP below north to central Taiwan does not at present seem a strong requirement to create space for the PSP to subduct in a north-westward direction. The image associated with the EUP slab does not show significant lateral displacement with depth, which attests of its steep dip. This could be attributed to resistance of the Chinese continental margin to engage in the westward roll-back of the EUP slab (viewed in a Eurasian fixed reference frame).

3.7 Model interpretation

3.7.1 Southern Taiwan: southward extrusion

In southern Taiwan my surface deformation model exhibits strain rates of almost pure E-W contraction, which is consistent with ongoing collisional shortening in the orogen. The contractional rates are accompanied by southward increasing, predominantly N-S oriented extensional strain rates (figure 3.9a). I find right-lateral thrust motion of ~ 14 mm/yr in a $\text{N}54^{\circ}\text{W}$ direction on the Deformation Front and left-lateral normal motion of 6-13 mm/yr in direction $\text{N}110^{\circ}\text{-}130^{\circ}\text{E}$ (increasing southward) on the Chaochou-Chishan fault (figure 3.8b). The block bounded by these faults is subjected to an an-

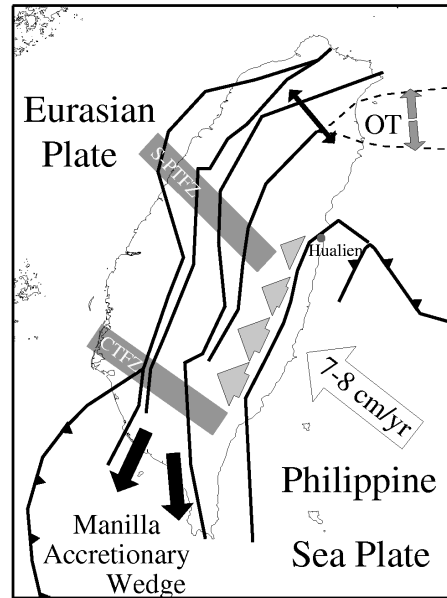


Figure 3.11: Schematic representation of the tectonic interpretations made in this study: Gravitational collapse (thin black arrows) and opening of the Okinawa Trough (dark grey arrows) in northern Taiwan, ongoing collision with crustal failure, accretion and exhumation of crust in the Central Range of the central block (light grey arrows), lateral extrusion of the sedimentary cover to the Manila accretionary wedge in southwest Taiwan (wide black arrows), and the development of a tear fault with incipient northwestward subduction at the transition between the two trench systems at Hualien. OT denotes Okinawa Trough.

ticlockwise rotation rate of $\sim 12.5^\circ/\text{Myr}$, where the areas on either side of this block are experiencing clockwise rotation rates or significantly smaller anticlockwise rotation rates (southern Central Range; figure 3.9b). These patterns of surface deformation are indicative of lateral extrusion towards the Manila accretionary wedge south of Taiwan. To the north the extrusion is terminated by the Chishan Transfer Fault Zone (figure 3.11). The analogue models of Lu and Malavieille (1994) also suggest a southward lateral extrusion of the sedimentary cover of the southern Western Foothills in response to the oblique collision between the PSP and the EUP. The southern Taiwan area is further characterized by low shallow seismicity with a significant increase at the base of the crust (figure 3.12; cross-section A) and the results of geodetic re-triangulation within the orogen (Chen, 1984) demonstrate that in this area subsidence prevails. These observations are in support of my interpretation of my surface deformation model in southern Taiwan.

3.7.2 Central Taiwan: oblique collision, shortening and exhumation

In the central section of the Western Foothills and western Central Range (figure 3.1) the model surface strain rate field is dominated by WNW-ESE contraction and clockwise rates of $\sim 10.1^\circ/\text{Myr}$ (figure 3.9a and 3.9b). I obtain right-lateral motion with an increasing thrust component for the Deformation Front, left-lateral thrust motion on the Chukou fault, insignificant motion on the Chaochou-Chishan fault and minor left-lateral thrust motion on the Lishan fault (figure 3.8b). These modeling results represent the surface response to the ongoing oblique collision causing shortening and shearing in the orogen. However, in the eastern Central Range (figure 3.1) I obtain a dominant extensional principal strain rate. The principal direction of the extension rotates from NE-SW in the central-northern eastern Central Range to E-W in the south, in agreement with geological observations gathered in the area (Crespi et al., 1996; Lu et al., 1998). The extension is accompanied by an anticlockwise rotation rate of $\sim 9.2^\circ/\text{Myr}$. Recent reports of leveling measurements across the Central Range describe uplift rates as high as 36-42 mm/yr for the past decade (Liu, 1995a) especially between 23°N and 23.5°N (Kosuga et al., 1988). A feasible explanation of my surface deformation patterns, the high uplift rates, and the high-grade metamorphic core complexes observed in the eastern Central Range (section 3.2) could be the exhumation of crustal material. Regional tomography of Rau and Wu (1995, figure 3.13) shows a thickening of the crust under the high elevations of the Central Range, where the deepest part is offset to the east. In the north the low velocity root extends down to a depth of 35 km ($v_p = 6.0\text{ km/s}$). This is in agreement with a Moho depth of 33 km inferred from gravity Bouguer anomaly modeling (Yen et al., 1998). In both tomographic cross-sections the velocity in the top 15 km under the Central Range is relatively high compared to the velocities underneath the Western Foothills and the Coastal Range. This coincides with a zone of relatively little seismicity found underneath the eastern Central Range (figure 3.12). Chemenda et al. (2001), Lin (1998) and Lin et al. (1998) propose a model of crustal subduction followed by exhumation in a orogen-normal direction of the eastern Central Range to account for the observations. In this model the continental crust of the South China Sea is subducted to mid-crustal levels where it becomes detached from the mantle part of the lithosphere and exhumes. However, in this model the obliquity and southward propagation of the collision is not taken into account. Since collision commenced in the north and is progressively moving southward, the subducting continental crust in the north would reach critical conditions needed for its detachment from the mantle well before its southern equivalent. Therefore, it is reasonable to assume a southward propagation of the exhumation in conjunction with the collision (figure 3.11). This southward propagation of the exhumation may cause the anticlockwise rotation observed in the eastern Central Range as well as divert the principal directions of the extension to a more NE-SW orientation in the regions with maximum exhumation.

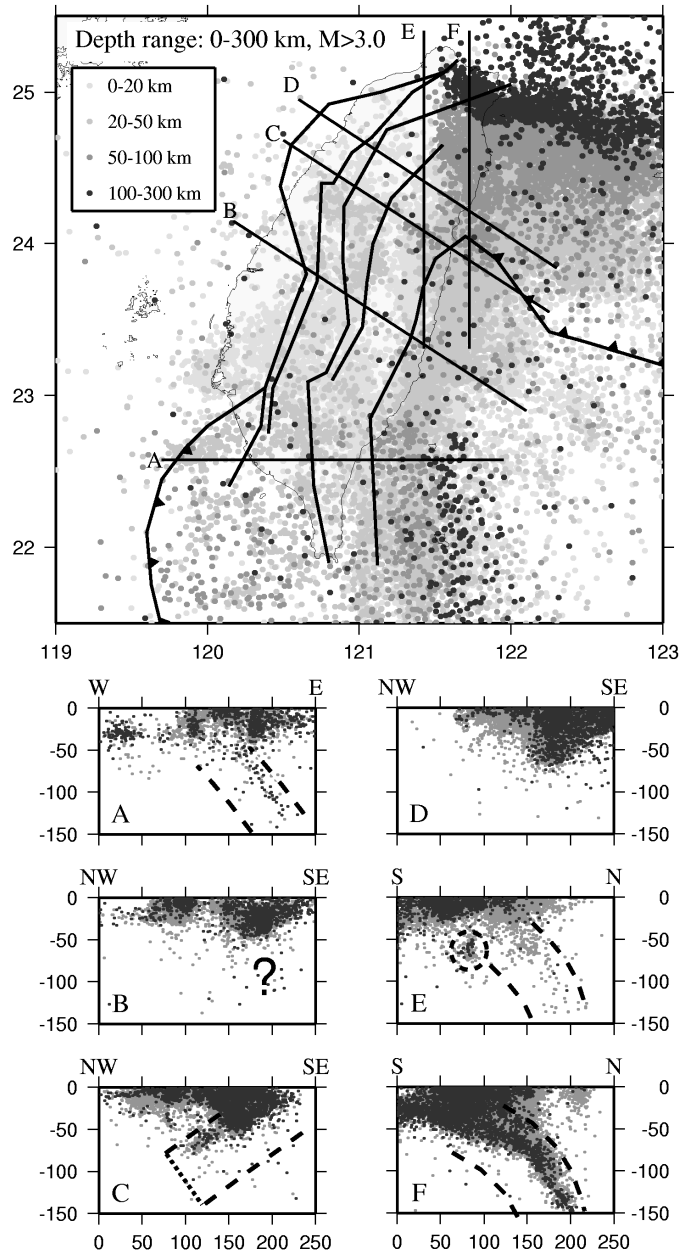


Figure 3.12: Local seismicity as cataloged by the Central Weather Bureau of Taiwan, between May 1900 and October 2000. Light grey dots in cross-sections: $0 \leq M \leq 3$, Black dots in cross-sections: $M > 3$. Events contained in dotted circle correspond to the incipient subduction outlined in section C.

3.7.3 Northern Taiwan: crustal extension and orogenic collapse

Most of northern Taiwan (north of the Sanyi-Pakua Transfer fault zone) is subjected to relatively small anticlockwise rotation rates (0° - 5° /Myr; figure 3.9b) and left-lateral fault slip rates (figure 3.8b). Strong clockwise rotation rates of $\sim 10.0^{\circ}$ /Myr are found in the Ilan Plain. The strain rate field is characterized by relatively small NW-SE contraction corresponding to geological observations in the area (Crespi et al., 1996; Teng, 1996). Based on my model and the geological observations, the northern extent of the mountain belt is no longer subjected to active crustal shortening. However, the extensional regime due to the opening of the Okinawa Trough (Liu, 1995b; Yeh et al., 1989) induces crustal stretching and gravitational collapse.

The back-arc extension in the trough is related to the southwestward migration and rotation of the Ryukyu trench (Liu, 1995b; Yeh et al., 1989), which commenced 2Ma ago (Lee et al., 1991; Lee, 1993; Miki et al., 1993). The significant NW-SE extension obtained in my model in the Ilan Plain clearly portrays the on-land extension of the Okinawa Trough (figure 3.11). Shallow seismicity in northern Taiwan is low, whereas the Ilan Plain is characterized by high, very localized shallow seismicity and an increased heat flow, which would be expected in a back-arc basin. Thus, the Okinawa Trough has acquired the ability to propagate into Taiwan along a pre-existing weak zone, the Lishan fault. In the northern eastern-Central Range the WNW-ESE extension may be due to a combination of the gravitational collapse and the crustal exhumation, as identified in the central and southern eastern Central Range (figure 3.11).

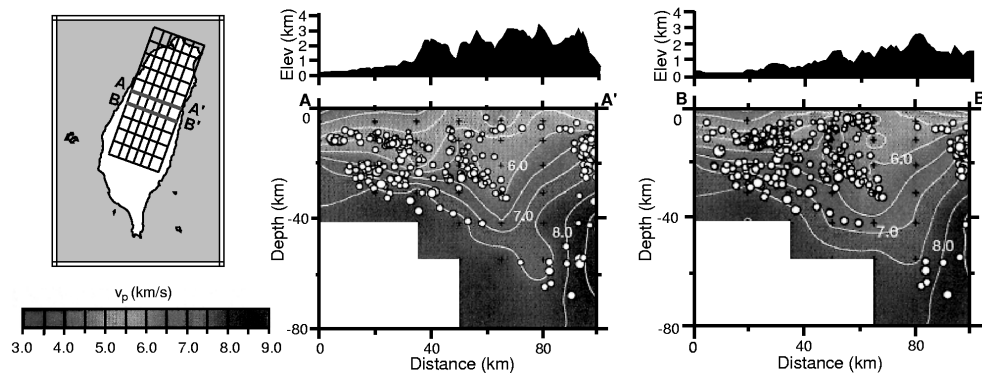


Figure 3.13: Regional tomography adapted from Rau and Wu [1995]. A well resolved high velocity feature comparable to the one found for the PSP at the Ryukyu Trench can be observed underneath the Coastal Range and Eastern Central Range. The Central Range is underlain by a region of high velocity. For a color version of this figure see figure C.10 of appendix C.1.

3.7.4 The Coastal Range: incipient northwestward subduction of the PSP

In the Coastal Range, the modeled creep motion on the Longitudinal Valley fault decreases significantly northward from $\sim 19\text{mm/yr}$ with an azimuth of $\text{N}124^\circ\text{E}$ at Taitung to $\sim 7.9\text{mm/yr}$ in $\text{N}151^\circ\text{E}$ at Hualien (figure 3.8b). My strain rate field shows strong NE-SW contraction accompanied by large anticlockwise rotation rates in the Coastal Range and comparable clockwise rotation rates just offshore between 23.5°N and 24°N (figure 3.9a and 3.9b). South of 23.5°N the NE-SW contraction is more moderate (though significant) and smooth and predominantly anticlockwise rotation rates are obtained. Some care should be taken when interpreting these results due to poorer resolution in this area especially in the ϕ -derivatives. However, based on the decrease in modeled fault motion significant contractional strain rates or a significant decrease in PSP motion are to be expected. Since there are no indications to suspect a change in PSP velocity at 23.5°N , 40-50 mm/yr of PSP motion has to be accommodated east of the Coastal Range. The focal mechanisms of the earthquakes in this region denote a fault with an average strike of 23°N and an average dip of 75° located just offshore the island of Taiwan (figure 3.14). At Hualien (23.9°N), I plotted the seismicity along a profile striking perpendicular to this fault (figure 3.12; cross-section D). The profile shows deep (up to 50 km), localized seismicity around the fault and indicates a northwestward dipping Wadati-Benioff zone. Seismically, the slab extends to approximately 75 km. The fault location is also tied with a significant gravity low observed in Hualien Canyon (Yen et al., 1998). Further, regional tomography (Rau and Wu, 1995, figure 3.13) shows a well defined high velocity zone ($v_p > 8.0\text{km/s}$) underneath the Coastal Range and Central Range, which compares in size to the Wadati-Benioff zone of the PSP at the Ryukyu trench. Based on analogue modeling Chemenda et al. (1997, 2001) propose the possible occurrence of incipient subduction of the PSP at the latitude of Hualien. Such incipient subduction would accommodate most of the convergence between the PSP and Eurasia. The hypothesis explains my surface deformation model and is in fact confirmed by the seismicity data and the regional tomographic model (figure 3.11). The fault indicated by the focal mechanisms of events in the area could represent the top of the PSP slab developing northwestward subduction below eastern Taiwan.

3.8 Geodynamic evolution

To provide an understanding for the present-day tectonic setting of Taiwan I consider the geodynamic development of the region. East of present-day Taiwan, the subduction of the PSP below the Chinese continental margin in the past million years has been characterized by tearing of the continental-ocean boundary (COB) in roughly WSW direction. The tear consistently followed the geometry of the COB, thereby progressively creating the west Ryukyu Trench (Lallemand et al., 2001). This westward migration of

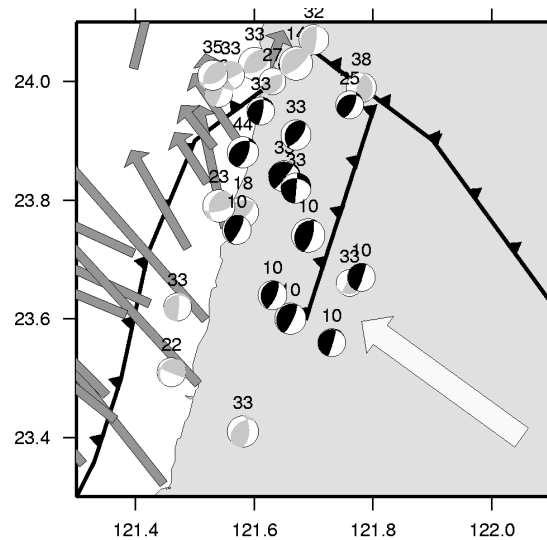


Figure 3.14: *Focal mechanisms from the Harvard CMT catalog ($M > 4$, depth < 50 km). The black mechanisms all denote a fault with a strike of 23°N and dip of 73° with the horizontal. The grey vectors denote the GPS velocity vectors of Yu et al. [1997]. The white vector represents the PSP motion. Barbed lines represent the Ryukyu trench where the segment central in the figure denotes my proposed southward continuation.*

incipient PSP subduction is caused by the obliqueness of the PSP motion relative to the strike of the Eurasian plate. Trench creation thus advanced with an average speed comparable to the component of PSP motion along the strike of the COB. The position of the tear tip coincides with the northern extent of the (more or less N-S striking) Manila trench, which accommodates EUP subduction up to this latitude (Lallemand et al., 2001). In the past 3-5 My the strike of the Ryukyu trench has aligned with the relative motion of the PSP. When viewed in a Eurasian fixed reference frame, the Manila trench has been rolling back to the west while the component of the PSP motion along the strike of the COB (or normal to the Manila trench) provides the overriding motion. As long as roll-back speed and overriding motion are equal there is no special reason for strong orogenic activity. The Taiwan orogen itself must then result from a change in the difference between roll-back speed of the trench and the westward component of PSP advance. I believe that the Taiwan orogen is a direct result of a strong southward turn of the strike of the Chinese continental margin, which existed east of Taiwan. Ongoing roll-back of the Manila trench now brings the COB in the position of being overridden by the PSP (Chai, 1972; Suppe, 1981, 1984; Tsai, 1986). Resistance of the Chinese continental lithosphere to subduction has decreased the roll-back motion causing the PSP to indent the Chinese continental margin thus creating an accretionary wedge, the

Taiwan orogen. The decrease in slab roll-back also led to a steepening of the dip of the subducting EUP, as observed in the global tomography (figure 3.10). Subsequently part of the continental crust subducted to mid-crustal levels before buoyancy forces initiated failure and thickening of the subducting crust along two conjugate thrust faults resulting in the exhumation (squeezing out) of a crustal slice (Chemenda et al., 2001) as I have deduced for the eastern Central Range. Further, the Ryukyu trench has not propagated into the Chinese continental margin (hence is not tearing the continent as exemplified by the "T1-tear" of Lallemand et al. (2001)). Instead, I propose the southward propagation (more or less along the east coast of Taiwan) of the Ryukyu trench, thus overcoming the jog in the COB geometry below present-day Taiwan. In conjunction with this southward bending of the trench incipient northwestward subduction of the PSP under Taiwan is now in progress.

3.9 Summary and conclusions

The method of Spakman and Nyst (2002) has been applied to derive the surface deformation from GPS motion vectors, where I explored different modeling options. The fault-slip-rate-only solution of inversion I results in large data misfits and the agreement with neotectonic fault observations is poor. The solution in terms of $\nabla\mathbf{v}$ generates smaller data misfits. This model generally agrees with other continuous-deformation-only studies. However, the presence of large, active faults on Taiwan can not be ignored, thus the kinematics of Taiwan should be studied in terms of fault slip rate and $\nabla\mathbf{v}$.

Inversion III provides an acceptable data misfit, covariance and spatial resolution. In this model the method of Spakman and Nyst (2002) exposes a trade-off problem between fault slip rate and the velocity gradient field that can only be resolved by placing both stations close to the faults and stations in the interior of crustal blocks. The model shows significant motion on the Longitudinal Valley fault, southern Chukou fault and the southern Deformation Front. Strain rates rotate from NW-SE contraction in the Coastal Range to E-W contraction in the southern Western Foothills and NW-SE extension in northern Taiwan. The rotation rate field shows several blocks with consistent (anti) clockwise rotation.

The interpretation of my surface deformation model, combined with the seismicity data, gravity data and tomography, leads to a coherent model for the present-day tectonic activity of Taiwan (figure 3.11). I divide Taiwan in 4 distinct domains: southern Taiwan, central Taiwan, northern Taiwan and the Coastal Range. The domains are bounded by the two major transfer fault zones and the Longitudinal Valley fault. I deduce active convergence between the EUP and the PSP in both central and southern Taiwan. In southern Taiwan the almost E-W collision has resulted in N-S lateral extrusion of the weak sedimentary cover towards the Manila accretionary wedge. To the north the

extrusion is terminated by the Chishan Transfer Fault zone. In my deformation model the eastern Central Range of central Taiwan shows almost orogen-perpendicular extension, while the western Central Range and the Western Foothills show predominantly NW-SE collision induced contraction. In conjunction with Chemenda et al. (2001), Lin (1998) and Lin et al. (1998) I relate this feature to active exhumation of a crustal slice. However, I believe that the exhumation is propagating southward along with the collision, causing the principal directions of the extension to rotate to a more NE-SW orientation. Northern Taiwan is transferring into a state of gravitational collapse induced by the inland propagation of the opening Okinawa Trough (Liu, 1995b; Yeh et al., 1989) along a pre-existing weak zone, the Lishan fault. Though my model shows that south of 23.5°N a very significant part of the convergence between the PSP and the South China Sea is accommodated by slip on the Longitudinal Valley fault, whereas north of 23.5°N about 40-50 mm/yr needs to be accommodated east of the island of Taiwan. I observe a clear northwestward dipping Wadati-Benioff zone in both the seismicity data and the regional tomographic model of Rau and Wu (1995). I deduce that in the transfer zone between the two contrary subduction zones a southward propagating crustal tear fault has developed east of Taiwan. The tear fault is the crustal response to incipient northwestward subduction of the PSP below eastern Taiwan. Thus, the Ryukyu trench is bending southward becoming almost perpendicular to the convergence direction, while subduction of the PSP continues. Slab-slab interaction between the PSP slab and the Eurasian slab may occur and detachment of the Eurasian slab may commence. In this setting a sudden rapid southward propagation of incipient subduction is conceivable.

Chapter 4

A joint analysis of GPS motions and InSAR to infer the coseismic surface deformation of the Izmit, Turkey Earthquake.

4.1 Introduction

Over the past decade, space geodetic observations of surface motions have been widely used to model the (a)seismic surface deformation of the Earth (e.g. Bennett, 2003; Bos et al., 2003a; Shen et al., 1996; Shen-Tu et al., 1998, 1999; Snay et al., 1996; Ward, 1998). These models have provided an increased understanding of the complex spatial distribution of crustal deformation which is particularly useful for understanding the dynamics causing deformation and for seismic hazard analysis. For the latter a detailed analysis of the coseismic surface deformation field can provide important information on the relaxation of the long-term deformation field during an earthquake, as well as on the complexity of the earthquake source and crustal structure. Although space geodetic data have been used in studies of several major earthquakes (e.g. Landers, Hector Mine; Fialko et al., 2001; Hudnut et al., 1994; Massonnet et al., 1993), kinematic modeling of the coseismic surface deformation has been prohibited due to the absence of fault slip as a parameter in the various analysis methods available. Coseismic GPS and InSAR data have been utilized to model the slip distribution of earthquakes assuming a linear elastic behavior of the deformation field (Hudnut et al., 1994; Massonnet et al., 1993). For Fialko et al. (2001) it proved possible to estimate the surface displacement field

This chapter has been submitted for publication to *Geoph. J. Int.* as: A.G. Bos, S. Usai and W. Spakman, A joint analysis of GPS motions and InSAR to infer the coseismic surface deformation of the Izmit, Turkey Earthquake.

from both an ascending and descending InSAR interferogram. Due to decorrelation of the InSAR images near the fault trace, the displacement field was interpreted directly without estimations of fault slip or the displacement gradient field. The recently developed kinematic inversion method of Spakman and Nyst (2002) inverts geodetic observations for the displacement gradient field and fault motion simultaneously which allows us to distinguish between coseismic slip on the fault and strain release in the blocks bounding the fault. I utilize this method to determine the kinematic coseismic surface deformation field of the 1999 Izmit, Turkey earthquake.

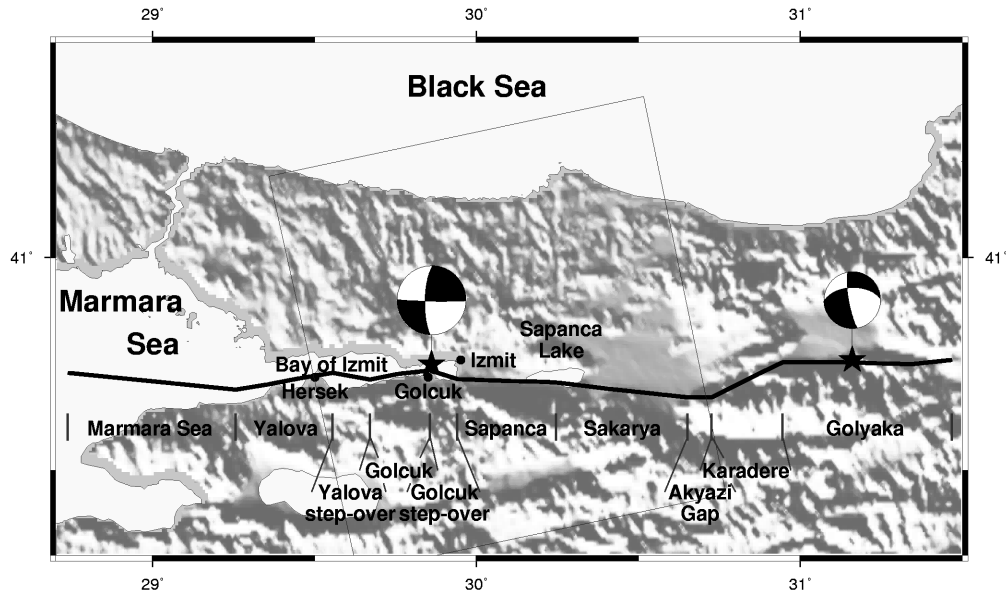


Figure 4.1: *Tectonic setting of the Izmit earthquake plotted against topography. Black line indicates the fault trace utilized in this study. Black names between vertical lines state fault segment names, while the grey square outlines the the area contained in the InSAR interferogram. The stars show the epicenter locations of the Izmit and Düzce earthquakes and the corresponding focal mechanisms are provided. For a color version of this figure see figure C.11 of appendix C.3.*

On August 17, 1999 a $M_w = 7.5$ earthquake struck the Marmara region of north-western Anatolia (Turkey). The earthquake was the most recent in a westward migrating sequence of earthquakes along the North Anatolian fault which commenced in 1939 and subsequently ruptured a 1200 km section of the fault (Ambraseys, 1970; Barka, 1992). The August 17 event occurred near the town of Izmit and caused surface rupture with dextral displacements of over 5 m (Barka et al., 2002) along a 110 km segment of the North Anatolian fault. Rupture was induced on at least 5 major fault segments (from west to east: Yalova, Gölçük, Sapanca, Sakarya and Karadere; figure

4.1) each separated by step-overs (Barka et al., 2002; Hartleb et al., 2002; Langridge et al., 2002; Reilinger et al., 2000). Three months after the Izmit event the November 12, $M_w = 7.1$, Düzce earthquake extended the rupture of the Izmit event further east with failure on the Gölyaka segment. Since the Marmara Sea region had previously been identified as a seismic gap (Nalbant et al., 1998), a network of both continuous and campaign GPS sites was established prior to the event (McClusky et al., 2000). Consequently, the coseismic displacement field was captured by both GPS observations and by the European Remote Sensing (ERS) satellite. The GPS displacements provide us with three dimensional information on the surface deformation at single points, whereas the Satellite Aperture Radar (SAR) interferograms contain a piecewise continuous image of the displacement in the line-of-sight direction of the satellite. Since the two datasets are highly complementary, I utilize both in a joint estimation of the surface deformation field of the Izmit earthquake. First, I adopt the purely kinematic inversion method of Spakman and Nyst (2002) to invert the GPS data for the displacement gradient field and fault motion. Next, the surface deformation field obtained is utilized to compute a synthetic interferogram, which is compared to the InSAR interferogram. Through an iterative approach of inverse and forward modeling an acceptable model that jointly fits both datasets is obtained. The final model is subsequently interpreted in terms of source complexity and crustal structure and the relaxation of the long-term deformation field is analyzed.

4.2 Data

4.2.1 GPS data

The GPS evidence for the coseismic displacements of the Izmit, Turkey earthquake is provided by Reilinger et al. (2000). For modeling the spatial distribution of the coseismic surface deformation field I utilize a subset of 41 stations immediately surrounding the fault trace of this event, as well as the November 12 Düzce earthquake (figure 4.2). The dataset comprises 3 continuous stations that were operating at the time of the earthquake (named sites in figure 4.2) and 38 survey-mode sites for which coseismic displacements could be determined. To obtain the coseismic displacements, the campaign data have been corrected by Reilinger et al. (2000) for elastic strain accumulation prior to the event and post-seismic afterslip up to the time of remeasurement.

4.2.2 InSAR interferograms

The InSAR analysis is performed on both the ERS 35-days coseismic interferograms available, namely an ERS1 interferogram spanning the period 12 August/16 September 1999 (orbit numbers 42229 and 42730, frame 811) and the corresponding ERS2 pair 13 August/17 September 1999 (orbit nrs. 22556 and 23057, frame 811). The in-

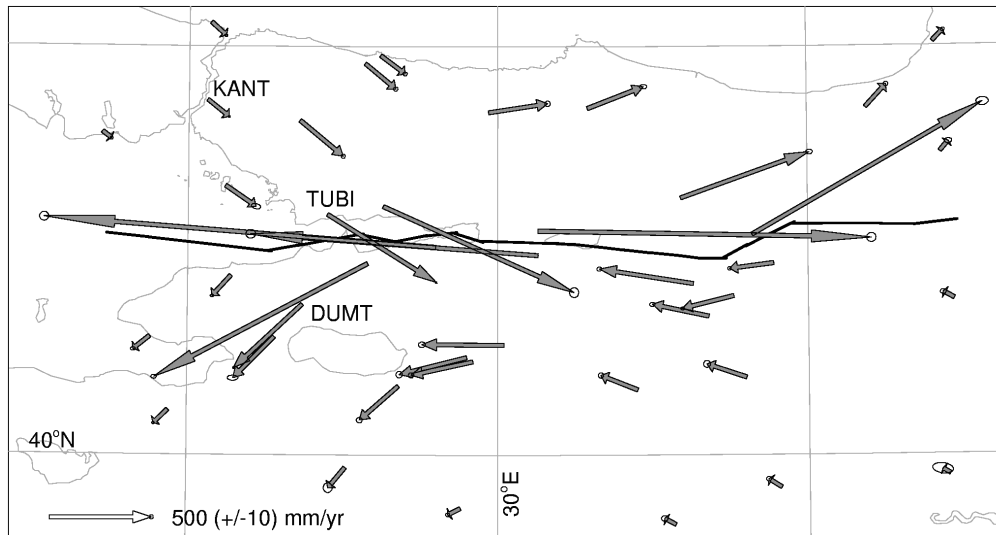


Figure 4.2: GPS displacement data of Reilinger et al. [2000] with the 95% confidence error ellipses. Named sites indicate the continuously operating stations during the earthquake.

terferograms are shown in figure 4.3, where they have been masked for extremely low coherence values (< 0.1). For the chosen frame they have both a perpendicular baseline component of about 70 meters. With these baselines, the interferograms are in general not particularly sensitive to topography. However for such a mountainous area the topographic component of the interferometric signal is still significant. The topography was therefore estimated and extracted by using the tandem pair 12/13 August.

Although their perpendicular baseline component is approximately the same, the two interferograms show considerable differences in the fringe patterns, as already mentioned in Reilinger et al. (2000) and Feigl et al. (2002). The difference in the fringe pattern between the two differential interferograms is shown in figure 4.4. In particular, in the lower part of the ERS1 interferogram the fringes still seem to follow the topography, probably due to atmospheric effects wrapped around the relief. As for the upper part, the presence of a somewhat regular pattern of fringes might indicate an orbital error in one of the interferograms. However, I use very precise orbits (Scharroo and Visser, 1998), which in my experience never gave such a huge trend. The hypothesis that this could be a orbit error seems therefore very unlikely to me. At least part of the effect could in my opinion still be due to atmospheric effects.

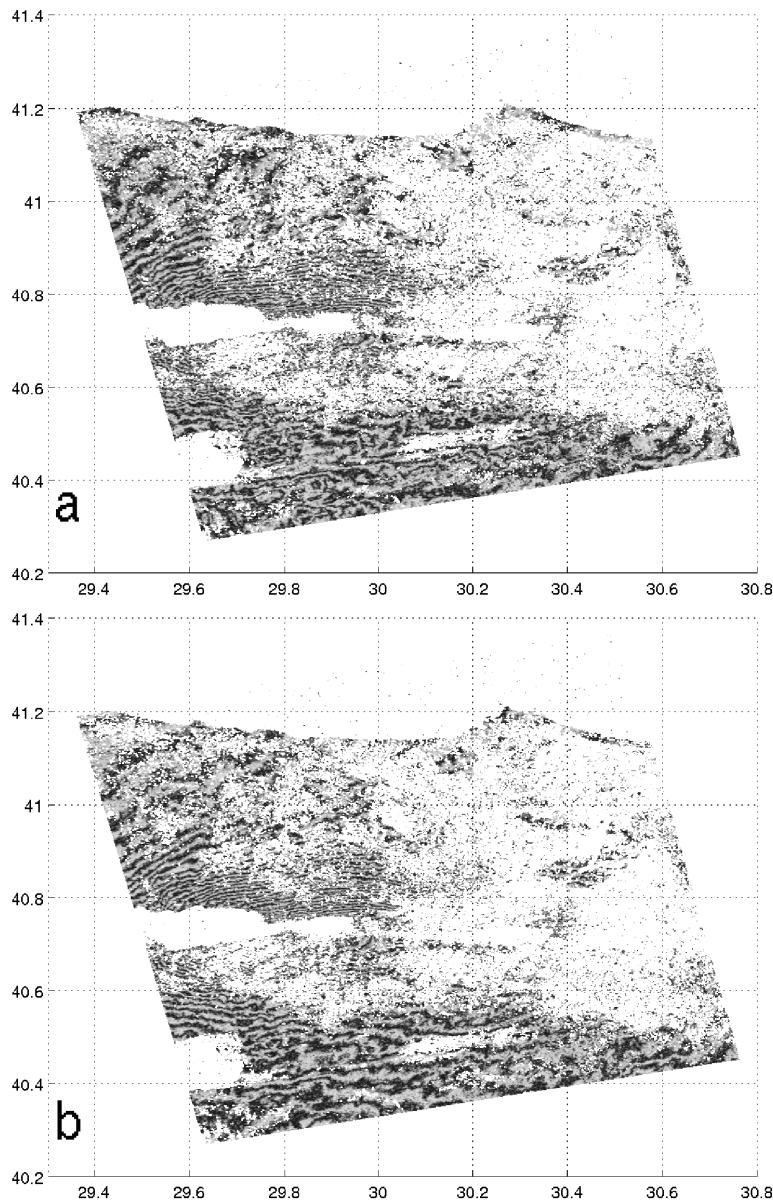


Figure 4.3: InSAR interferograms: a) ERS1 interferogram spanning the period 12 August/16 September 1999 (orbit numbers 42229 and 42730, frame 811), b) ERS2 pair 13 August/17 September 1999 (orbit nrs. 22556 and 23057, frame 811). Both interferograms have been masked for coherence < 0.1 . The topographic component of the interferometric signal was estimated and extracted by using the tandem pair 12/13 August. For a color version of this figure see figure C.12 of appendix C.3.

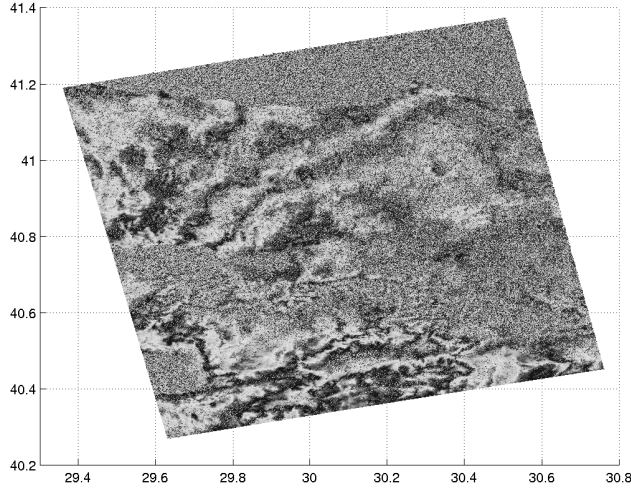


Figure 4.4: *The difference in the fringe pattern between the two differential interferograms. The presence of a somewhat regular pattern of fringes might indicate an orbital error in one of the interferograms, however, in my opinion at least part of the effect could be due to atmospheric effects. For a color version of this figure see figure C.13 of appendix C.3.*

4.3 GPS data inversion

In order to model the surface deformation field of the Izmit earthquake from the GPS displacements, I adopt the inversion method of Spakman and Nyst (2002). Although formulated for the analysis of relative motion data, it can as well be applied to relative displacement data. For the latter application, the method relates the relative displacements ($\Delta \mathbf{u}_{ij}$) between stations i and j to the displacement gradient field ($\nabla \mathbf{u}$; strain and rotation) and fault slip (\mathbf{s}) by:

$$\Delta \mathbf{u}_{ij} = \sum_{l=1}^{K+1} \int_{L_{ij}^l} \nabla \mathbf{u}(\mathbf{r}) \cdot d\mathbf{r} + \sum_{k=1}^K \alpha_k \mathbf{s}_k(r_{ij}^k) \quad (4.1)$$

where L_{ij}^l is an integration path between the stations i and j , K denotes the number of fault segments crossed, r_{ij}^k is the location where the integration path L crosses a fault, and $\alpha_k = \pm 1$ depends on the orientation of the fault with respect to the integration path L_{ij}^l . Equation 4.1 is exact in practice and does not involve any knowledge of crustal/fault rheology.

I parameterize fault slip by assuming constant slip on fault (sub)segments. I implement a single fault trace that approximates the mapped coseismic surface rupture. To avoid unrealistic detail the fault trace has been simplified and step-over features smaller than 2 km length have been removed (figure 4.5). The Yalova and Gölcük step-overs

remain an integral feature of the model fault trace. I have extended the fault towards the east to include the Düzce earthquake rupture area and towards the west in the Marmara Sea. Thus the fault divides my model area in a northern and a southern domain. In total the fault consists of 11 fault segments for which I resolve 54 fault slip vectors on fault subsegments. The displacement gradient field is parameterized by subdivision of the study area into triangular domains spanned by model nodes. I assume a linear variation of the displacement gradient components within the triangular domains. The triangles are not allowed to cross the fault. I utilize a densification of the triangulation towards the fault trace in order to accommodate the large differences in displacement (and strain release) over relatively short distances (from mm at Istanbul to 2m at Gölcük near the epicenter; figure 4.5). However, a too dense triangulation leads, given the limited dataset, to heavily overparameterized models. I adopt a parameterization of 678 triangles spanned by 382 model nodes, leading to a total of $4 * 382 + 2 * 54 = 1636$ model parameters for the inversion of $\Delta \mathbf{u}$.

Substitution of the model parameterization in equation 4.1 leads to a linear system of equations. In order to assure internal consistency between $\nabla \mathbf{u}$ and fault slip in constituting the total deformation field, I extend the set of equations by defining 2 additional integration paths between all station pairs. A further set of equations derives from the fact that $\nabla \times \nabla \mathbf{u} = \mathbf{0}$ within regions bounded by faults. This constraint is defined for each triangle and a weight (α_r) is assigned to tune the relative importance

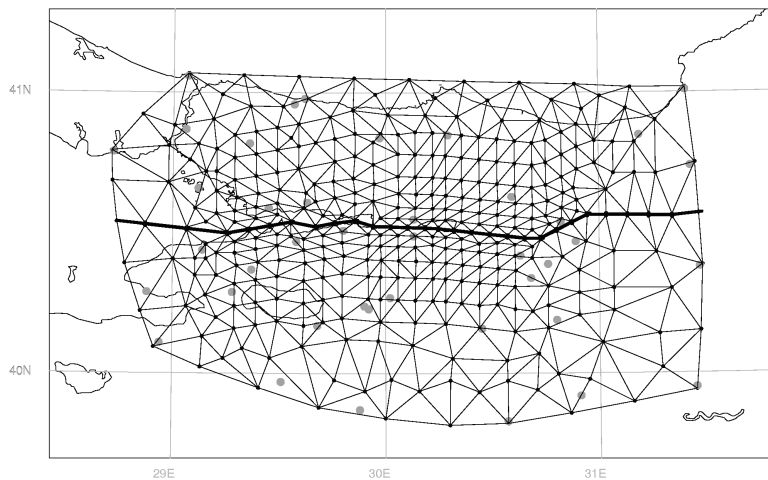


Figure 4.5: Final parameterization of the Izmit models. Thick lines indicate fault segments, black dots are the triangle nodes and grey dots are the site positions. Note that in my choice for the triangle nodes I am not restricted to the locations of the observation sites. Triangles do not intersect faults. Nodes at the fault are doubled to allow the velocity gradient field to be discontinuous across the fault.

i	T_n	K	σ_r 10^4 m/yr	α_b 10^5	α_{i_a} 10^4	α_{i_b} 10^5	α_d 10^4	χ^2	\tilde{r}_m	$\tilde{\sigma}_m^c$ 10^{-6} /yr	$\tilde{\sigma}_m^f$ mm/yr
I	382	54	2.0	5.0	5.0	2.5	6.0	1.02	0.84	1.87	0.014
II	382	54	2.0	5.0	5.0	2.5	6.0	3.56	0.84	1.68	0.014

Table 4.1: Aspects of the inversion parameterization and average results for inversions I and II. Key: i , solution; σ_r , standard deviation of the $\nabla \times \nabla \mathbf{v} = \mathbf{0}$ equations; α_b , α_{i_a} , α_{i_b} , and α_d , the regularization parameters; $\tilde{r}_m = \frac{1}{M} \sum_{i=1}^M R_{ii}$, the average resolution, with R_{ii} the diagonal elements of the resolution matrix and M the number of model parameters; $\tilde{\sigma}_m^c = \frac{1}{M_c} \sum_{i=1}^{M_c} \sqrt{C_{ii}}$, the average standard deviation for the components of $\nabla \mathbf{v}$, with $M_c = 4T_n$ the number of components of $\nabla \mathbf{v}$; $\tilde{\sigma}_m^f = \frac{1}{M_f} \sum_{i=1}^{M_f} \sqrt{C_{ii}}$, the average standard deviation for the components of \mathbf{f}_k , with $M_f = 2K$ the number of slip components.

of these equations. The complete linear system of data-equations ($\mathbf{A}\mathbf{m} = \mathbf{d}$, where \mathbf{A} is the observation matrix, \mathbf{d} is the extended data vector and \mathbf{m} represents the collection of all model parameters) can now be solved by adopting an inversion procedure that fits the data in a least squares sense and at the same time minimizes some model norm. To assure a complete regularization and avoid unwarranted model amplitude excursions in regions of poor spatial resolution, I impose amplitude damping on the model boundary nodes by extending $\mathbf{A}\mathbf{m} = \mathbf{d}$ with $\alpha_b \mathbf{I}\mathbf{m} = \mathbf{0}$ (\mathbf{I} the identity matrix) and spatially varying amplitude damping on the nodes in the model interior ($\alpha_i \mathbf{I}\mathbf{m} = \mathbf{0}$), where nodes towards the boundary of the model obtain an increased regularization weight. A second derivative regularization is imposed to obtain a smooth solution ($\alpha_d \mathbf{D}\mathbf{m} = \mathbf{0}$). For this application it proved unnecessary to regularize the fault slip parameters. The formal least squares solution to the regularized system is given by (see Spakman and Nyst (2002) for details):

$$\mathbf{m} = (\mathbf{A}^T \mathbf{C}_d^{-1} \mathbf{A} + \alpha_b^2 \mathbf{I}_0 + \alpha_i^2 \mathbf{I}_1 + \alpha_d^2 \mathbf{D}^T \mathbf{D})^{-1} \mathbf{A}^T \mathbf{C}_d^{-1} \mathbf{d} \quad (4.2)$$

where \mathbf{C}_d^{-1} is the data covariance matrix. The a posteriori model covariance is given by: $\mathbf{C} = (\mathbf{A}^T \mathbf{C}_d^{-1} \mathbf{A} + \alpha_b^2 \mathbf{I} + \alpha_i^2 \mathbf{I} + \alpha_d^2 \mathbf{D}^T \mathbf{D})^{-1}$ and the model resolution kernel is $\mathbf{R} = \mathbf{C} \mathbf{A}^T \mathbf{C}_d^{-1} \mathbf{A}$. The model depends on the tuning of four parameters: α_r , α_b , α_i , and α_d . For the tuning of these parameters, I primarily focus on obtaining a solution with acceptable data fit (by inspection of the normalized χ^2 data misfit values), model covariance and resolution. The respective weights of the $\nabla \times \nabla \mathbf{u} = \mathbf{0}$ and the regularization equations, as well as an overview of some aspects of the solutions are provided in table 4.3.

4.4 Joint analysis

Presently, the computer implementation of the general method of Spakman and Nyst (2002) is restricted to the analysis of horizontal velocity/displacement vector fields. Although this implementation can be extended to include InSAR interferograms, the significant influence of atmospheric effects on the Izmit interferograms (see section 4.2.2), as well as the restriction to horizontal deformation made me adopt a different strategy for the joint analysis of GPS and InSAR data. Once the displacement gradient and fault slip has been inferred from the GPS data, equation 4.1 can be used to predict the horizontal displacement field at arbitrary points. The change in range Δu_s of the distance measured along the line-of-sight between the satellite and the ground point due to a relative displacement is $\Delta u_s = -\mathbf{u} \cdot \hat{\mathbf{s}}$, where \mathbf{u} is the displacement vector and $\hat{\mathbf{s}}$ is the unit vector pointing to the radar satellite. Assuming the absence of vertical coseismic displacements the predicted field $\bar{\mathbf{u}}$ is used to construct a synthetic interferogram.

I have implemented the forward approach for a 1x1 km regular grid spanning the modeling area contained within my InSAR image. I determine a predicted displacement field on the grid with respect to each GPS station. Subsequently, these 41 fields are made independent of the reference station. At each grid point the 41 resulting displacements are checked for outliers. Generally, the displacements are found to be consistent on a 95 % confidence level. From the 41 displacement fields a single, consistent displacement field is determined. Projection of this field on the line-of-sight direction provides me with a 1x1 km grid of range changes which is wrapped into a predicted interferogram.

The next step is a comparison of observed and predicted interferograms. The comparison is done mainly on fringe pattern and total amount of deformation, since error sources such as orbital errors, tropospheric delays, post-seismic deformation, as well as the absence of the vertical displacements will already introduce a misfit between the two interferograms. A quantitative analysis of the two dimensional and three dimensional range changes at the GPS stations showed that the restriction to a horizontal displacement field will introduce a misfit of up to 150 mm which corresponds to over 5 fringes in the wrapped interferograms. The largest vertical displacements are observed in the vicinity of the fault trace. Away from the fault the vertical displacements become small and the misfit rapidly reduces to less than 1 fringe. The influence of the tropospheric delays ranges from two to four fringes (Reilinger et al., 2000). Post-seismic displacements are very small compared to the coseismic and might introduce a misfit of less than 1 fringe in the model (Reilinger et al., 2000).

The first order differences between the observed and predicted interferograms are attributed to differences in fault slip between the inverted (from GPS solely) and actual slip at depth. These differences may exist as a result of lack of coseismic GPS data to fully constrain both the $\nabla \mathbf{u}$ field and fault slip (Spakman and Nyst, 2002). By trial and

error, the fault slip distribution is changed (and imposed a priori on the GPS inversion) to optimize the fit between the predicted and observed interferograms.

4.5 Coseismic surface deformation

4.5.1 Solution I: Model based on GPS data only

I commence by inverting the GPS data only leading to solution I. The model (figure 4.6) can fit the data very well on a 95% confidence level ($\chi^2 = 1.0$) with acceptable model covariance and resolution. The maximum data misfit does not exceed 0.013 m.

Figure 4.7 shows the 3σ model standard deviations ($\tilde{\sigma}_i = \sqrt{C_{ii}}$) of each gradient component plotted as a percentage of the displacement gradient estimate of the component in each model node, as well as the diagonal elements of the model resolution kernel in both the longitudinal (ϕ) and latitudinal (θ) directions. I find that the interior of the model is well resolved with relatively small errors compared to the model amplitude estimate. Since the amplitude estimates of $(\nabla u_{\phi\phi})$ and $(\nabla u_{\phi\theta})$ are about a factor two larger than the amplitude estimates of $(\nabla u_{\theta\phi})$ and $(\nabla u_{\theta\theta})$ a significantly larger part of the model estimates exceeds the model errors (figure 4.7). The resolution of the model is good, though toward the boundary of the model the resolution deteriorates significantly. This is generally due to the lack of data and the increased regularization imposed towards the boundary. However, in the Marmara Sea and along the Gölyaka segment the reduced resolution may also be due to a trade-off between the displacement gradient field and fault slip, which is caused by a lack of data in the proximity of the fault (Nyst, 2001; Spakman and Nyst, 2002). The amplitude estimates of the displacement gradient field toward the model boundary decrease as expected for a coseismic strain field. However, the amplitudes are also smaller than the formal standard deviations and care should be taken in the interpretation of this part of the model. The model standard deviations of the fault slip estimates are relatively small (averaging ~ 14 mm). The largest standard deviations (~ 25 mm) are observed on the Gölyaka segment, whereas the smallest standard deviations (~ 7 mm) are found on the Marmara Sea segment.

The strain contribution of solution II (figure 4.6a) shows four distinct quadrants of extensional and contractional strains reflecting the source mechanism of the earthquake (figure 4.1). However, the contractional quadrant south of the fault is significantly smaller than the extensional quadrant. The transition between the quadrants north and south of the fault is characterized by left-lateral shear. The strain field along the Sakarya fault shows minor left-lateral shear on both sides of the fault. Significant contractional strain is observed north of the Gölyaka segment, with reduced left-lateral shear strains south of the fault segment. The strain contribution (figure 4.6a) also shows a band of right-lateral shear strain along the Bay of Izmit, extending onland eastward to Sapanca Lake. The band is accompanied by significant clockwise rotations (figure 4.6b). I note

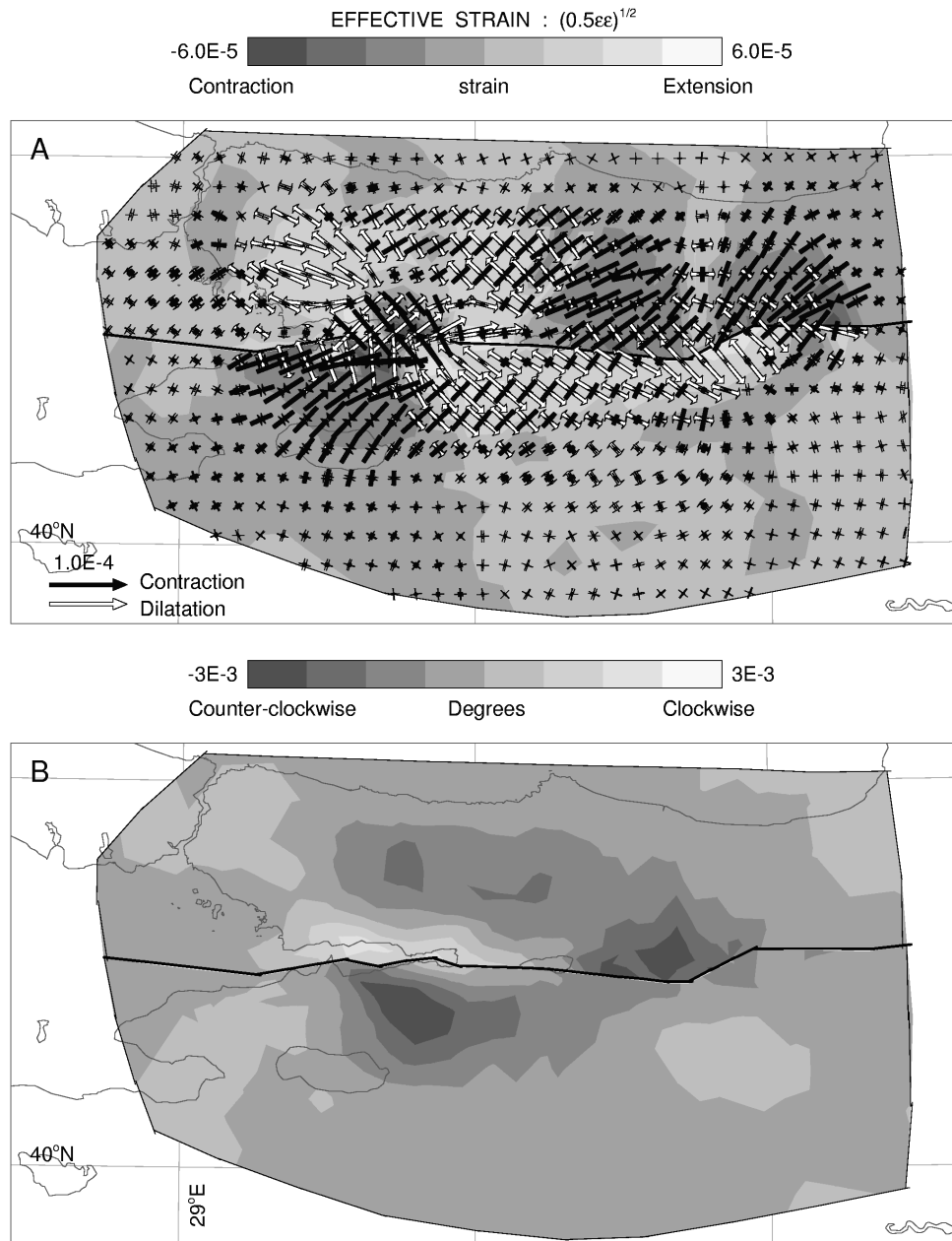


Figure 4.6: The displacement gradient contribution of the model based on GPS data only (Solution I): a) Strain field. The contouring denotes the effective strain $(=1/2\epsilon_{ij}\epsilon_{ij})^{1/2}$. The arrows denote the principal strains: contraction (black) and extension (white). b) Rotation field in degrees. For a color version of this figure see figure C.14 of appendix C.3.

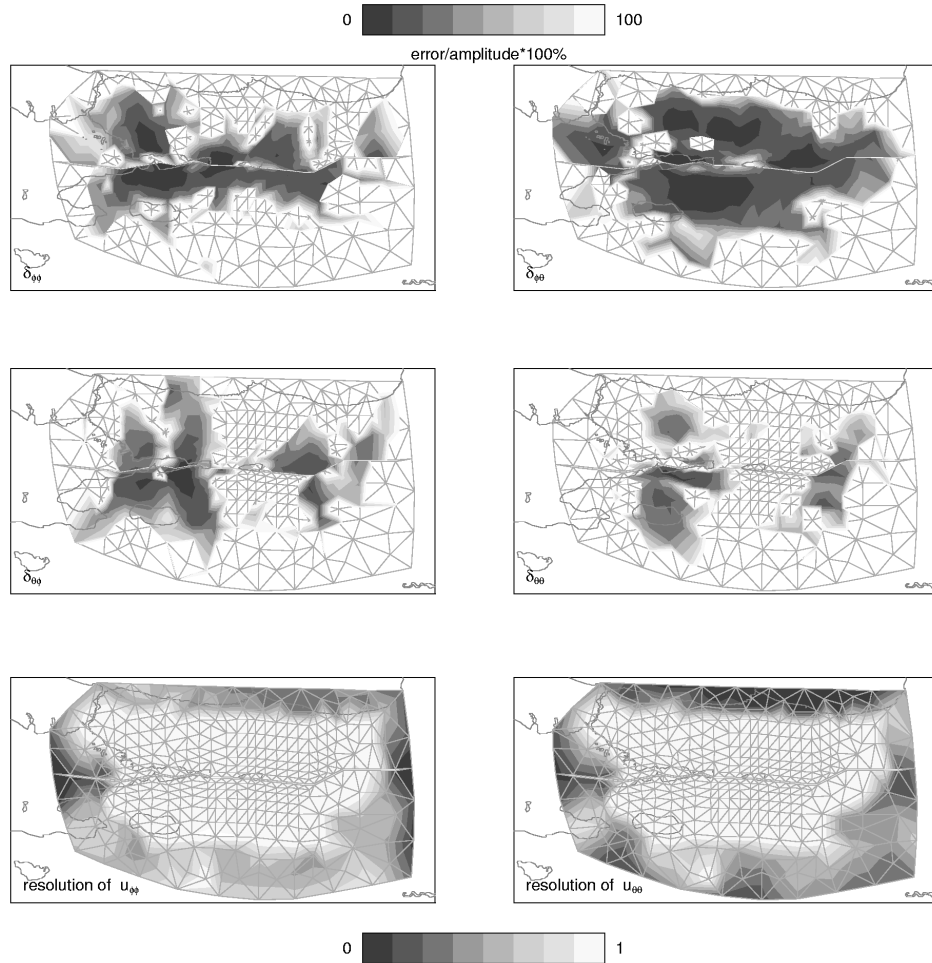


Figure 4.7: The 1σ model standard deviations ($\tilde{\sigma}_i = \sqrt{C_{ii}}$) plotted as a percentage of the displacement gradient estimate (top four images) and the diagonal elements of the model resolution kernel in both the longitudinal (ϕ) and latitudinal (θ) directions (lower two images).

that the band is located slightly to the north of the modeled fault trace in the Bay of Izmit. The rotation contribution further shows large anticlockwise rotations on both sides of the fault. This large scale anticlockwise rotation results from the unloading of seismic strain. However, the anticlockwise rotations are not uniform (figure 4.10b). The maximum anticlockwise rotations are found south of the Gölcük segment and north of the Sakarya and Karadere segments.

The fault motion contribution of solution I (figure 4.8) shows increasing right-lateral slip from the Marmara Sea eastward. Maximum slip (2.9 m) is reached on

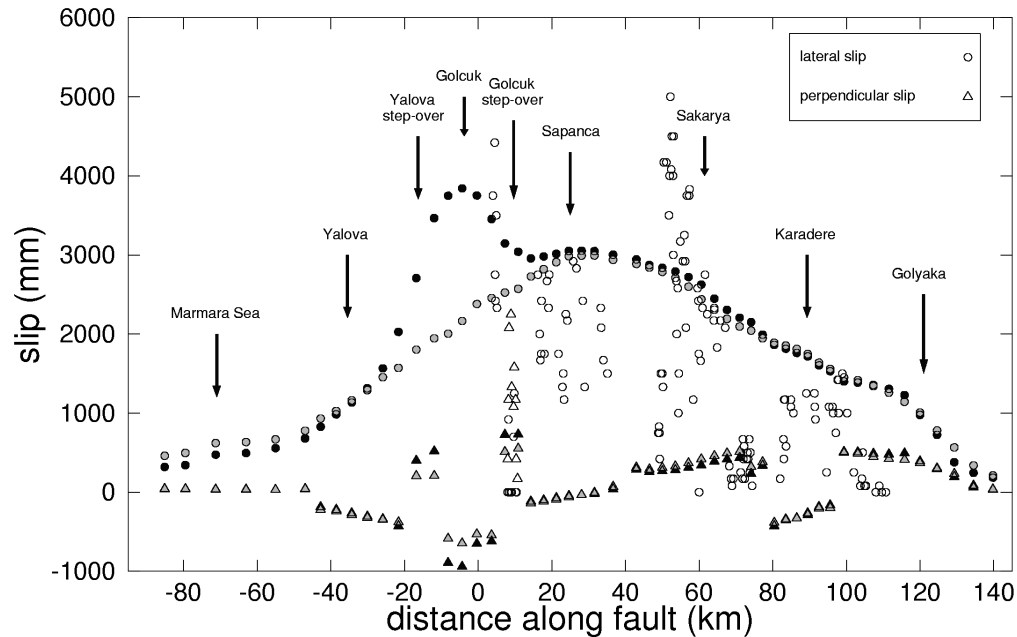


Figure 4.8: Graphic representation of the fault slip solution of the model based on GPS data only (solid grey symbols), the model based on the joint analysis of GPS and InSAR (solid black symbols), as well as the mapped surface offsets (open symbols).

the Sapanca segment. The fault motion subsequently decreases eastward to less than 1 m on the Gölyaka segment. Significant fault slip (~ 0.7 m) is also observed on the Marmara Sea segment consistent with source rupture analysis estimates (Güllen et al., 2002). The modeled fault slip of 1-1.5 m on the Yalova segment is consistent with estimates of rupture source analysis (Güllen et al., 2002) and with estimates by slip distribution modeling (Reilinger et al., 2000). Both the Hersek and Gölcük step-overs show significant normal motion. The fault motion is reasonably consistent with the observed surface ruptures (figure 4.8). However, despite a dense parameterization of the fault trace, the fault motion can not fit all the details of the surface rupture data (e.g. the large ruptures observed at Gölcük and on the Sakarya segments or the absence of rupture in the Akyazi Gap). I note that the fault slip modeled probably represents an average over the top few km of the crust and therefore does not necessarily coincide with the surface rupture data. The normal motion on the Gölcük step-over is less than observed, while the right-lateral motion is significantly higher. This difference may be induced by the smoothing of the fault trace, changing for instance the strike of the Gölcük step-over from $N135^{\circ}E$ to $N107^{\circ}E$.

The synthetic interferogram determined from solution I (figure 4.9a) shows a south-

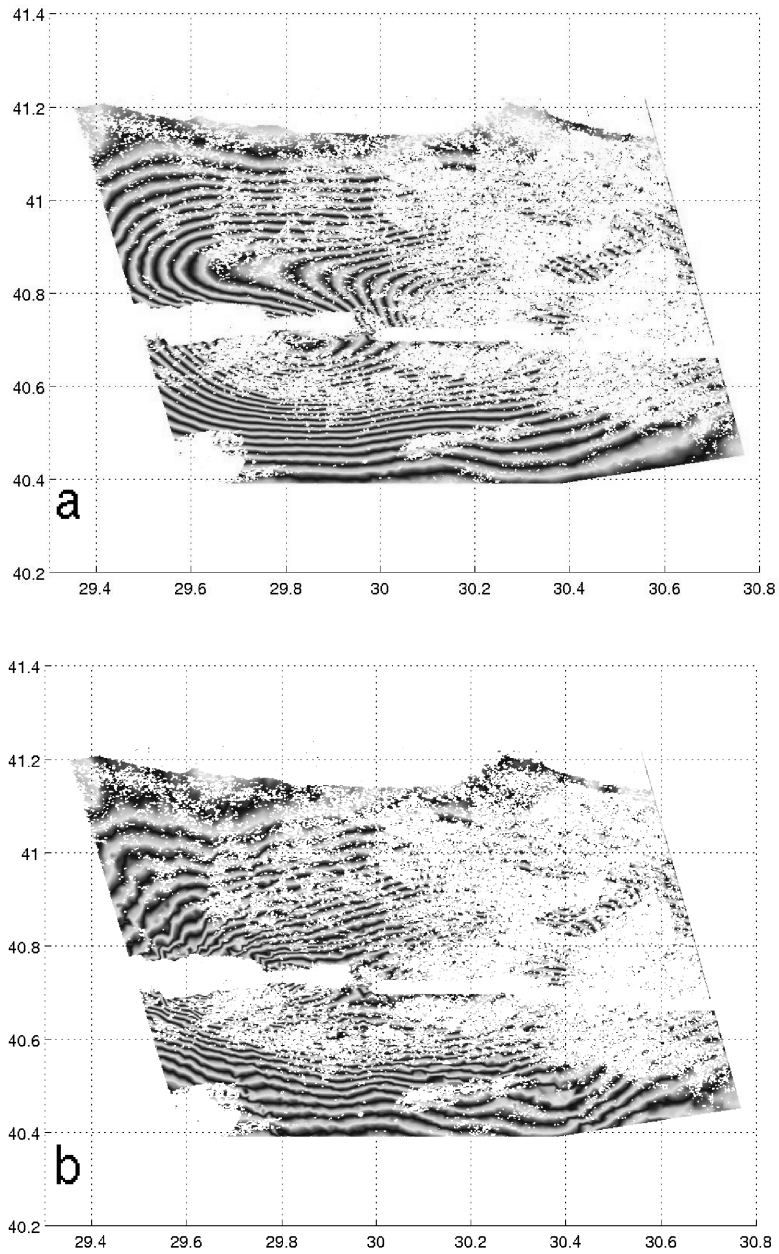


Figure 4.9: Synthetic interferogram of a) the model based on GPS data only (Solution I), and b) the model based on the joint analysis of GPS and InSAR (solution II). For a color version of this figure see figure C.15 of appendix C.3.

eastward turning of the fringes north of the fault, whereas the InSAR interferogram shows more E-W orientated fringes in this area. I attribute this difference to an underestimation of fault slip on the segments along the Bay of Izmit. This is caused by a trade-off between fault slip and the displacement gradient field as a result of absence of GPS stations close to the fault (Nyst, 2001; Spakman and Nyst, 2002). The GPS stations are located along the shores of the Marmara Sea and Bay of Izmit whereas the fault trace is located along the southern shore. South of the fault the GPS stations are closer to the fault and the data better constrain the displacement gradient field. This trade-off may cause the band of right-lateral strain and clockwise rotations observed in my surface deformation model. I further note that the data density at Gölcük and along the western Sapanca segment is poor on the north side of the fault. To improve the fit between predicted and observed interferograms I initially a priori increase (by trial and error) the right-lateral fault slip on the Gölcük and Sapanca segments.

4.5.2 Solution II: Model based on a joint analysis of GPS and InSAR

Figure 4.8 shows the final fault motion obtained which provides an acceptable fit to both the GPS and InSAR data. The slip estimation shows a second peak of almost 4m on the Gölcük segment. The fault motion on the Yalova step-over has been increased due to the constraints imposed on the Gölcük segment. During the trial and error procedure the fault slip on the Yalova and Marmara Sea segments has been constrained to the previous unconstrained slip estimates of solution I to prohibit the occurrence of significant left-lateral shear, induced by the trade-off with an overestimate of right-lateral fault motion, within the Marmara Sea. The fault slip contribution complies reasonably well with the observed surface rupture data (figure 4.8). However, slip on the Sakarya segment seems to be underestimated, though there is a large scatter in the data, while slip on the Karadere segment is overestimated. This may be attributed to the presence of a thick sedimentary layer at the surface along these fault segments. Rupture observed within these sediments need not be representative of the rupture in the first few km of the Earth's crust. The InSAR interferogram along these faults is very decorrelated and therefore can not further constrain my slip estimates.

The fit to the GPS data is slightly deteriorated ($\chi^2 = 3.56$) compared to solution I. However, the maximum misfit does not exceed 0.018 m. I attribute this deterioration to either the coarseness of my parameterization which does not allow enough detail to perfectly accommodate the trade-off in my displacement gradient field or strong changes in the displacement gradient field near the fault. The synthetic interferogram of solution II (figure 4.9b) compares to first order reasonably well with the InSAR image. North of the Bay of Izmit the predicted interferogram contains about 7 fringes fewer than the InSAR interferogram. This implies a difference of 196 mm in deformation in the range change direction. Especially in the near field, the density of the fringes is less than observed in the InSAR interferogram. This should be mainly attributed

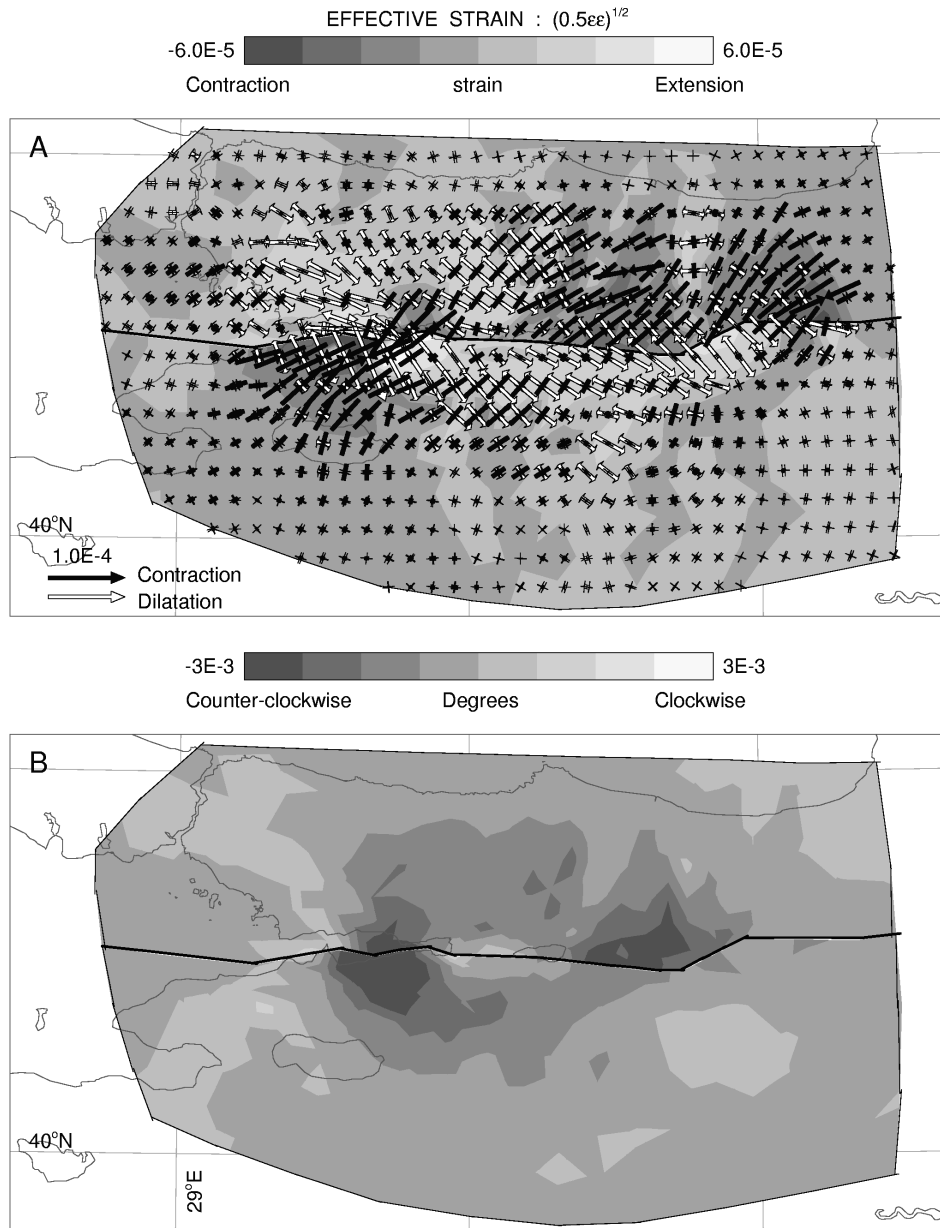


Figure 4.10: The displacement gradient contribution of the model based on the joint analysis of GPS and InSAR (Solution II): a) Strain field. The contouring denotes the effective strain ($= (1/2\epsilon_{ij}\epsilon_{ij})^{1/2}$). The arrows denote the principal strains: contraction (black) and extension (white). b) Rotation field in degrees. For a color version of this figure see figure C.16 of appendix C.3.

to the absence of vertical displacements in the vicinity of the fault trace (see section 4.4). The slight difference in tilt between the two interferograms north of the Bay of Izmit between Gölcük and Izmit can be attributed to tropospheric delay errors, although the smoothing of the Gölcük step-over may also have its influence. The horizontal fringes north of the fault along the Bay of Izmit are well reproduced. Further west, the synthetic fringes start to bend southward slightly east of where the InSAR fringes bend. Directly south of the fault the two interferograms comply rather well. However, going southward atmospheric effects obscure the deformation signal contained in the InSAR image and correlation between the two interferograms is lost (see section 4.2.2). West of the Bay of Izmit decorrelation in the InSAR interferogram, makes interpretation of the fringe pattern impossible. The model covariance and resolution have hardly been affected by the implementation of the a priori constraints. The average standard deviations on the fault slip estimates remain 0.014 m

The strain contribution of solution II (figure 4.10a) no longer shows the band of right-lateral shear strains observed in solution I. North of the Yalova step-over WNW-ESE extension is observed, where north of the Gölcük segment NNE-SSW contraction dominates. South of these segments I obtain WNW-ESE contraction and NNW-SSE extension, respectively. The strains are not just antisymmetric over the fault, but also very asymmetric. Around Gölcük the extensional strains south of the fault are significantly larger than the contractional strains north of the fault ($\sim 5.46 \cdot 10^{-5}$ vs. $\sim 2.43 \cdot 10^{-5}$, respectively). The same holds for the Gölyaka segment, where I find $\sim 4.07 \cdot 10^{-5}$ of contractional strain north of the fault and $\sim 1.92 \cdot 10^{-5}$ of extensional strain to the south. In the rotation field (figure 4.10b) the band of clockwise rotations in the Bay of Izmit has been replaced by anticlockwise rotation. Some minor clockwise rotation is still observed along the Sapanca segment. In all other aspects the strain and rotation fields of solution I and II are comparable.

4.6 Discussion

4.6.1 Influence of fault geometry

Though my deformation model reflects the four quadrants of the earthquake source, the sizes of the quadrants are not consistent and are not centered around the epicenter of the earthquake (figure 4.11). The transition between the contractional and extensional quadrants south of the fault is shifted slightly westward to the longitude of the Yalova step-over, whereas north of the fault the transition is shifted eastward and is located at the longitude of Sapanca Lake (figure 4.10 and 4.11). The amplitudes of the strains and rotations of my surface deformation model are distinctly asymmetric across the Gölcük, Gölyaka, Sakarya, and Karadere segments (section 4.5.2; figure 4.10). The dense surface displacement field predicted by my model shows even more profound asymmetry in both the east and the north component (figure 4.12). At Gölcük the east and north

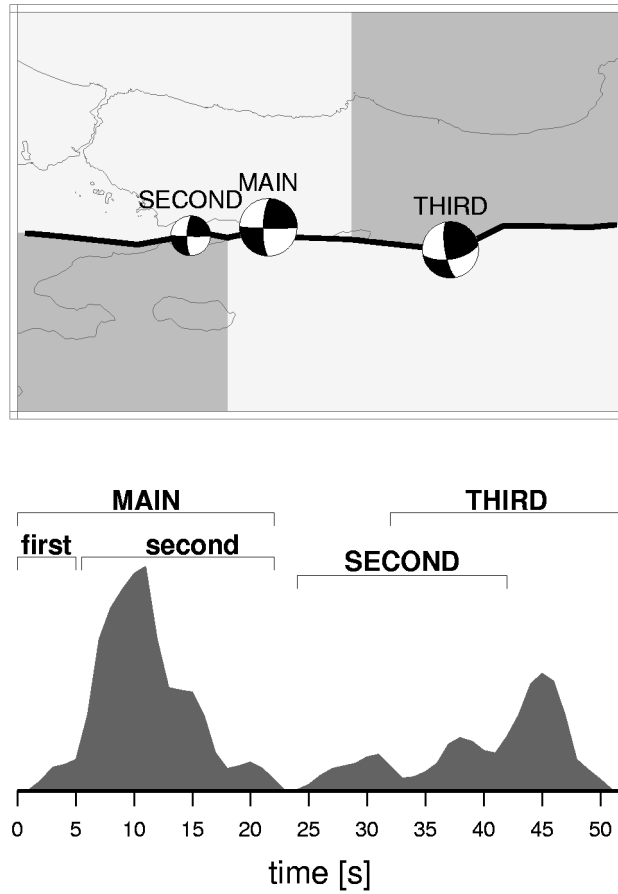


Figure 4.11: *Top figure: Location and focal mechanisms of the three consecutive sources constituting the Izmit earthquake rupture. In dark grey are indicated the contractional quadrants and in light grey the extensional quadrants as observed in my surface strain field. Bottom figure: Source-time function of the Izmit earthquake. Capital names indicate the separate sources, while normal names indicate the two stages of the main rupture near Gölcük.*

displacements south of the fault exceed those north of the fault by a factor 1.5 and 3.5, respectively. Along the Sapanca segment the absolute east displacements north of the fault are significantly larger than south of the fault (1.7 m vs. 1.3 m, respectively). Similarly, north of the Karadere segment I obtain an east displacement of 1.3 m and a north displacement of 0.7 m, whereas south of the fault the absolute displacements are 0.4 m and 0.3 m in the east and north, respectively. Wang et al. (2003) used a Green's function approach to compute the displacement components of the Izmit earthquake for both a homogeneous and a layered earth model. In both cases they obtain asymmetry

in the north and east components of the displacement field similar in pattern to my displacement field, though different in amplitude. However, the displacement field due to a strike-slip earthquake on a vertical fault plane should be purely antisymmetric across the fault. This implies that a deviation from this specific situation causes asymmetry to occur. I stipulate that asymmetry can be induced by 1) non-linear elastic deformation of the upper crustal rocks, 2) deviations of the earthquake rupture plane from the vertical, 3) lateral variations in rigidity across the fault, and 4) a complex fault rupture due to fault geometry.

For the 1997 $M_w = 7.6$ Manyi (Tibet) earthquake Peltzer et al. (1998) obtained significant asymmetry of the surface displacements which was attributed to non-linear elastic deformation of the upper crustal rocks. Compared to linear elastic deformation, non-linear elastic deformation will predict relatively larger displacements in nominally extensional quadrants. Except for the Gölcük segment, the relatively larger displace-

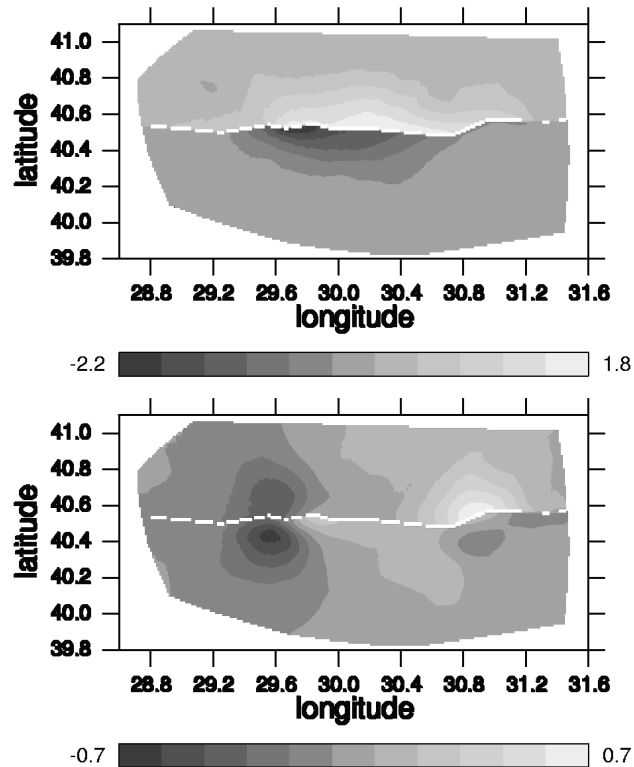


Figure 4.12: A dense surface displacement field determined from solution II on a 1×1 km regular grid for my model region. Top figure: The east component of the derived displacements. Bottom figure: The north component of the derived displacements.

ments observed for the 1999 Izmit earthquake occur in the contractional quadrants of the event which is opposite to that predicted by the non-linear elastic deformation. Neither can non-linear elastic deformation explain the significant shift of the transition between the quadrants observed in the strain field (figure 4.10 and 4.11).

Deviations of the earthquake rupture plain from the vertical were suggested by Fialko et al. (2001) to explain the asymmetry observed in the displacement field of the 1999 $M_w = 7.1$ Hector Mine earthquake. For a non-vertical strike-slip dislocation in an elastic half-space the surface displacements on the foot wall side of the fault decay faster with distance from the fault than displacements on the hanging wall side. For the Izmit earthquake this implies a south-dipping Yalova step-over, Gölcük segment and Gölcük step-over and a north-dipping Sapanca, Sakarya, Karadere and Gölyaka segment. The earthquake focal mechanism of the Izmit earthquake indicates a north dipping fault with a dip of 87° . DeLouis et al. (2002) estimated a northward dip of 85° for the ruptured segments based on broadband teleseismic modeling, whereas Reilinger et al. (2000) inferred an optimal fault geometry from GPS data and obtained a vertical dip for the Yalova, Gölcük, Sapanca and Sakarya segments and a 63° northward dip for the Karadere segment. On November 12 1999, the $M_w = 7.1$, Düzce earthquake ruptured the Gölyaka segment of my fault trace. Based on the GPS displacements of this event Bürgmann et al. (2002) inferred that the Gölyaka segment is a 54° north dipping oblique normal, right-lateral fault. Therefore, the deviating dips of the Gölyaka and Karadere segments may explain the asymmetry observed in the surface displacements across these segments. The deviations from vertical for the other segments are insignificant and do not explain the observed asymmetry.

Theoretically, Rybicki (1978) and Mahrer and Nur (1979) showed that an asymmetry in the displacement field across a fault may be induced by a lateral variation in rigidity. Their results portray that given a rigidity contrast across the fault, strain localizes on the low-rigidity side of the fault. In my model strain localizes south of the Gölcük and north of the Gölyaka segments. Assuming that the stress level on both sides of the fault is comparable, I can deduce a rigidity contrast of 2.25 and 0.47, respectively, between the region north of the fault and the region south of the fault along these segments. However, no significant asymmetry in amplitude of the strain field is observed across the Sapanca or Karadere fault segments, while a significant asymmetry in the displacement field is observed. Therefore, a rigidity contrast across the fault may not be the proper explanation for the asymmetry observed.

The surface trace of the North Anatolian fault in the Marmara Sea region is characterized by several step-over features and gaps between the various fault segments. Based on an inversion of teleseismic and near-field data, Yagi and Kikuchi (2000) deduced that the rupture at the epicenter started just west of the Gölcük step-over and propagated westward along the Gölcük segment. During the first 5 seconds of the event, rupture to the east was obstructed by the extensional step-over. Subsequently, eastward rupture was triggered on the Sapanca segment. An asymmetric rupture of the

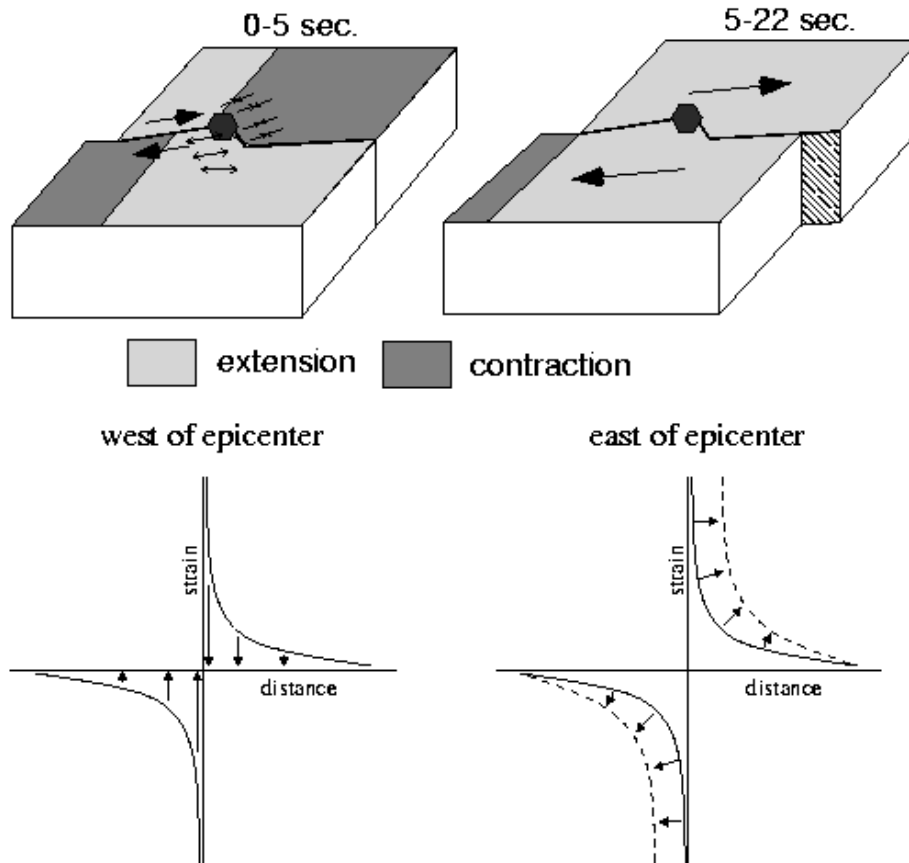


Figure 4.13: Schematic representation of the two-stage main rupture: failure is initiated near the Gölciik step-over and propagates westward, while rupture eastward is obstructed by the step-over feature. This induces an increased extensional quadrant south of the fault and contractional strain north of the fault (top left figure). After approximately 5 sec. eastward rupture on the Sapanca segment is triggered and propagates at super-shear velocity releasing the accumulated strain (top right figure). This increases the extensional quadrant north of the fault, locating the transition between the extensional and contractional quadrant near Sapanca Lake (see figure 4.11). Bottom two figures give a schematic representation of the strain against the distance relative to the fault. Solid line indicates the strain accumulated prior to the 1999 event, dashed line indicates strain accumulated at the moment eastward rupture commenced. As the earthquake strikes strain west of the epicenter is released immediately, while during the first 5 sec. significant additional strain accumulates east of the epicenter.

main source is also visible in the time-evolution of the slip distribution model of DeLouis et al. (2002) and in the source time function of the earthquake (Li et al., 2002, figure 4.11). Due to the two stage main rupture strain west of the epicenter is released immediately, while strain release east of the epicenter is obstructed by the absence of eastward rupture (temporarily prevented by the step-over feature). During this short period (5-7.5 sec.) contractional strain due to the earthquake accumulates north of the step-over as extension is induced south of the step-over (consistent with the earthquake focal mechanism; figure 4.11 and 4.13a). The subsequent eastward rupture releases the strain and causes an initially very rapid eastward movement of the northern block (figure 4.13b). This is consistent with the super-shear rupture velocity (4.8-4.9 km/s) observed along the Sapanca segment, whereas rupture along the other segments propagated with a velocity of ~ 3.5 km/s (Bouchon et al., 2002; DeLouis et al., 2002; Yagi and Kikuchi, 2000). This process explains the presence of the maximum east displacements north of the fault at Sapanca Lake, as well as the shift observed in the transition between extensional and contractional quadrants. The rapid eastward motion of the northern block at the fault induces extension within the western half of the block, while causing contraction in the eastern half of the block (figure 4.11). South of the fault, the initial absence of eastward rupture and the subsequent sudden release of the central and eastern part of the block induces the smaller westward shift of the transition between the quadrants (figure 4.11).

I conclude that the dip of the Gölyaka and Karadere segments may explain the asymmetry observed in the surface displacement field across these fault segments. However, a relative rigidity contrast across the Gölyaka segment of 0.47, where the region north of the fault is relatively weaker than the south, can also explain the localization of deformation observed across the fault. The rigidity contrast may be attributed to the presence of volcanic rocks south of the fault. A combined effect is most probable. The significant asymmetry in the surface displacements across the Sapanca and Gölcük fault segments is a direct result of a two-stage main rupture process with initial failure westward along the Gölcük segment, while eastward rupture was obstructed by the Gölcük step-over followed approximately 5-7.5 sec after the onset of the event by the triggering of failure along the Sapanca segment eastward.

4.6.2 Double source rupture process

In both solutions the largest strains are observed in the northwestern, southwestern, northeastern and southeastern parts of my model (figures 4.6 and 4.10). In solution II (figure 4.10) I observe a patch of NNE-SSW contraction north of the Gölcük segment with twice as large NNW-SSE extension south of the fault segment. The extension is associated with significant anticlockwise rotations. Along the Sakarya segment the strain field portrays left-lateral shear. North of this segment and the Karadere segment significant anticlockwise rotations are observed. This observation may be the result

of the trade-off between fault slip and the displacement gradient field caused by an overestimation of the fault slip. However, significant surface breaks are observed along this segment which actually exceed the model estimates.

Studies of the source process of the Izmit earthquake (Güllen et al., 2002; Li et al., 2002) reveal a complex source process. General consistency exists on the occurrence of at least three consecutive source ruptures (figure 4.11). The main event was located south of Izmit and induced a bilateral, asymmetrically propagating rupture (the two stage main rupture). After 20-25 sec, a second source initiated near Hersek. This induced a relatively slow rupture of 1-1.5 m and had a rather low moment release. About 30 sec after the initial rupture along the Gölcük segment, rupture on the easternmost segments was triggered at the location of the Akyazi Gap. The moment of this third rupture was a little less than half of the moment of the main source.

The source located at the Akyazi Gap provides a reasonable explanation for the observed shear around the Sakarya segment. The contractional strain induced north of the segment by the main shock is located in the extensional domain of the focal mechanism of this consecutive event (figure 4.11). Similarly, the extensional strain south of the segment due to the main rupture is located in the contractional domain of the second source. The superposition of the contributions of both events result in the shear strains observed in my model. The contractions and extensions due to the main source around the Karadere and Gölyaka segments are enhanced by the third source. This explains the relatively large strains observed in the eastern region of my model. Along similar lines, the second source at Hersek could be responsible for the strain field observed around the Gölcük segment. However, there would be a strong interaction with the complex main source. Therefore, the exact extent of the influence of the second source on the deformation field is much more difficult to distinguish. The significant strains in the western part of my model are a direct result of the main and second source.

4.6.3 Implications on slip distribution modeling

The complex source rupture and the influence of the fault geometry on the rupture initiation and interaction have important implications on traditional slip distribution modeling based on geodetic data. The elastic dislocation theory (Okada, 1985) utilized in these models assumes a homogeneous elastic half-space to relate surface displacement observations to slip on the fault. This assumption only allows lateral asymmetry of the displacement field to occur due to fault geometry and fault dip. However, the strike of the Izmit rupture is rather consistent for all but the Karadere segment, while the dip is near-vertical for all but the Karadere and Gölyaka segments. The complicated and very asymmetric displacement field deduced for the Izmit earthquake west of the Karadere segment would therefore lead to significant misfits to the data on both sides of the fault. The relatively large displacements on one side of the fault will be

underestimated, while the relatively smaller displacements on the other side of the fault will be overestimated, a pattern indeed observed in the slip distribution models of the Izmit earthquake of Reilinger et al. (2000) and Feigl et al. (2002). Therefore, I conclude that even though slip distribution models may provide important information on the mechanical behavior of the upper crust and about the mechanics of the earthquake rupture, they are based on simplifying assumptions which may not account for all the asymmetry observed across the fault. So, a careful assessment of the surface deformation of an earthquake is necessary to identify the influence of complex fault geometry and crustal structure on the displacement field.

4.6.4 Relaxation of the long-term strain field

Since the Marmara Sea region was identified as a seismic gap (Nalbant et al., 1998), a network of GPS observation sites has been established in the area (McClusky et al., 2000) and the interseismic surface deformation field was studied (Ayhan et al., 2002; Kahle et al., 2000). The surface deformation models are dominated by right-lateral shear strain rates all along the fault trace. Based on these shear strain rates an interseismic slip rate of 11-25 mm/yr was deduced for the North Anatolian fault (Ayhan et al., 2002). Except for the peninsula north of the Bay of Izmit the principal extensional strain rate axis dominates the shear strain rates.

The 1999 Izmit earthquake has released strain build-up over many years. Taking the interseismic slip rate of 11-25 mm/yr and the maximum fault slip obtained in my model (~ 4 m), strain may have been accumulating over the past 160-360 years. The last main earthquake on this section of the North Anatolian fault occurred in 1719 (Barka et al., 2002), 280 years ago. The interseismic surface deformation models obtain an average dilatational strain rate of $\sim 1 \cdot 10^{-7}$ strain/yr (Ayhan et al., 2002; Kahle et al., 2000) which over 280 years leads to a total amount of $\sim 2.8 \cdot 10^{-5}$ strain that has accumulated. This is in good agreement with the average strain release I deduce in my model ($\sim 2.3(\pm 1.0) \cdot 10^{-5}$). Therefore, I conclude that the Izmit earthquake has released almost all strain which has been accumulated since the last large earthquake on this stretch of the North Anatolian fault in 1719.

4.7 Conclusions

In a joint analysis of GPS and InSAR data the surface deformation field of the August 17 1999 Izmit (Turkey) earthquake has been determined in terms of strain, rotation and fault motion. The incorporation of fault motion is a unique feature of the implemented method (Spakman and Nyst, 2002) and is of prime importance for the purely kinematic estimation of a coseismic surface deformation field. The InSAR information was specifically useful to minimize the trade-off between fault slip and the displacement gradient in the inversion. This effect is most profound north of the Bay of Izmit where

GPS stations are relatively far from the fault. On the Gölcük segment of the fault trace slip up to ~ 4 m is necessary to properly fit the InSAR interferogram, whereas the GPS inversion led to only ~ 2 m of slip.

The strain contribution of my model shows four distinct quadrants of extensional and contractional strains reflecting the earthquake focal mechanism. The transition between the quadrants is not centered on the epicenter, but shifted eastward north of the fault, to the longitude of Sapanca Lake, and westward south of the fault, to the longitude of the Yalova step-over. Along the Sakarya segment I obtain left-lateral shear strains, whereas my fault slip estimates underestimate the surface ruptures. The strain field is distinctly asymmetric across the Gölcük and Gölyaka segments. The rotation field shows dominant anticlockwise rotations resulting from the unloading of seismic strain. Significantly larger anticlockwise rotations are observed south of the Gölcük and north of the Sakarya and Karadere segments.

My surface deformation model can be directly related to the very complex source rupture of the earthquake. I identify a two-stage main rupture process near Izmit and two consecutive source ruptures located at Hersek and the Akyazi Gap, respectively. The two-stage main rupture initiated near the Gölcük step-over and propagated westward along the Gölcük segment, while rupture eastward was obstructed by the step-over feature. This initial stage induces an increased extensional quadrant south of the fault and contractional strain north of the fault. Approximately 5-7.5 seconds into the main event eastward rupture on the Sapanca segment was triggered and propagated at super-shear velocity along the segment, releasing the accumulated strain. This process increased the extension in the quadrant north of the fault, locating the transition between the extensional and contractional quadrant near Sapanca Lake. Thus, throughout this main rupture the step-over features in the fault geometry had a very significant influence on the rupture initiation and propagation.

The two consecutive sources strongly interact with the deformation field of the main source and are responsible for the left-lateral shear strains observed along the Sakarya segment and the complicated pattern of deformation observed along the Gölcük segment. On the easternmost segments (Karadere and Gölyaka) the dip of the fault plane starts introducing asymmetry across the fault. However, the presence of strong volcanic basalts south of the Gölyaka segment may also introduce part of the localization of deformation observed north of this segment.

Finally, I deduce that the Izmit earthquake has been responsible for releasing almost all the strain which has been accumulating since the last main event on this section of the North Anatolian fault in 1719.

Chapter 5

The resolving power of coseismic surface displacement data for fault slip distribution at depth.

5.1 Introduction

Modeling of the spatial distribution of fault slip along a fault plane can provide clues about the mechanical behavior of the upper crust, and, in particular, about the mechanics of earthquake rupture. The slip distribution of the August 17, 1999, Izmit (Turkey) earthquake has been modeled by inversion of displacement data (Feigl et al., 2002; Reilinger et al., 2000), seismological data (Bouchon et al., 2000, 2002; Li et al., 2002; Yagi and Kikuchi, 2000), and a combination of these datasets (DeLouis et al., 2002). These models tend to agree on a broad scale, though differ significantly in detail. The differences have been related to differences in inversion techniques and a priori constraints implemented (Feigl et al., 2002), as well as to the limited resolving power of the different datasets when used separately (DeLouis et al., 2002). It is also conceivable that the relative agreement at larger scales results in part from resolution artifacts common to all models. Several papers (Du et al., 1992; Du and Aydin, 1993; Harris and Segall, 1987) have addressed the issue of poor resolution in their experiments based on displacement and/or seismological data. However, it remains ambiguous whether the cause of the resolution problem is related to 1) utilizing a limited data set, and/or 2) whether the data error is too large to sufficiently restrict the range of solutions, or 3) that the resolution problem is actually intrinsic and basically independent of 1) and 2).

In this chapter, my objective is to investigate how well slip distribution models inverted from surface displacement data (e.g. GPS, InSAR) can be resolved. The

This chapter has been submitted for publication to *Geoph. Res. Lett.* as: A.G. Bos and W. Spakman, The resolving power of coseismic surface displacement data for fault slip distribution at depth.

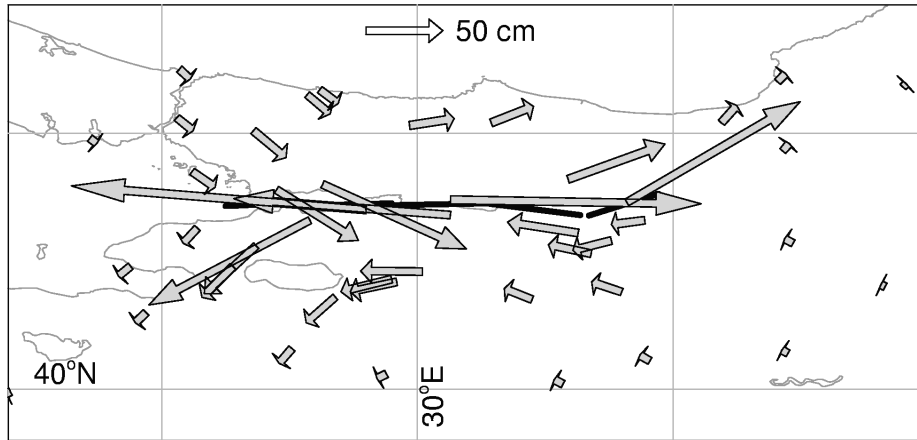


Figure 5.1: The 41 GPS displacement vectors of Reilinger et al. [2000] as utilized in this study.

inversion procedure adopted allows for the determination of the a posteriori model covariance and a model resolution kernel. My analysis will show that the poor resolution of slip distribution models at larger depth is intrinsic when based on elastic dislocation theory. An increase in data density only improves the resolution at upper crustal levels, while the resolution of the mid-crustal levels remains very poor.

5.2 Procedure

To model the coseismic slip distribution of the Izmit event, I adopt the horizontal GPS surface displacements of Reilinger et al. (2000, figure 5.1). The data consist of 5 continuous stations operating during the event and 46 campaign stations. The campaign displacements have been corrected by Reilinger et al. (2000) for elastic strain accumulation prior to the event, as well as for post-seismic afterslip following the event until the time of remeasurement.

As do others before me, I adopt the model of distributed dislocations in an elastic half-space (Okada, 1985) to interpret the observed coseismic surface displacements. My fault model consists of 6 fault segments, which are parameterized by 472 slip patches of $\sim 3 \times 3$ km, consistent with the parameterization of Reilinger et al. (2000). The fault dips vertically ($\delta = 90^\circ$) to a depth of 24 km within a Poisson solid with a Poisson's ratio of 1/4. I only solve for the along-strike components of the slip vector at each fault element (patch). The relation between the GPS observations assembled in a vector \mathbf{d} and the fault slip distribution \mathbf{m} is linear, $\mathbf{d} = \mathbf{A}\mathbf{m}$, where \mathbf{A} is the matrix of the "Okada" coefficients.

To estimate the slip vector parameters I utilize a standard inversion scheme which selects a solution that fits the data in a least squares sense and at the same time minimizes a model norm defined by the imposed regularization. I choose to penalize the second derivative of the fault slip distribution which imposes smoothness on the slip solution. At scales of at least a few kilometers this is a physically reasonable addition of "information". The model \mathbf{m} minimizing the data residual and the adopted model norm is given by (e.g. Jackson, 1979):

$$\mathbf{m} = (\mathbf{A}^T \mathbf{C}_d^{-1} \mathbf{A} + \alpha^2 \mathbf{D}^T \mathbf{D})^{-1} \mathbf{A}^T \mathbf{C}_d^{-1} \mathbf{d} \quad (5.1)$$

where \mathbf{C}_d denotes the data covariance matrix and \mathbf{D} stands for the second derivative operator. The a posteriori model covariance is given by $\mathbf{C} = (\mathbf{A}^T \mathbf{C}_d^{-1} \mathbf{A} + \alpha^2 \mathbf{D}^T \mathbf{D})^{-1}$ and the model resolution kernel $\mathbf{R} = \mathbf{C} \mathbf{A}^T \mathbf{C}_d^{-1} \mathbf{A}$.

5.3 Coseismic slip distribution model

The inversion result is dependent on the weighting factor α of the second derivative operator. For $\alpha = 0$ I obtain a perfectly resolved model (the standard least squares solution), however, with unacceptably large model covariance ($\sim 16000^2 mm^2$). A weighting of $\alpha = 7 \times 10^{-3}$ leads to a solution that approximates the model of Reilinger et al. (2000). My procedure allows backward (left-lateral) slip to occur which I force to zero at the far ends of the fault. I have assessed the dependence of the modeling results on the second derivative smoother. Though the weight attributed to the regularization controls the modeling results, backward slip is also observed in models penalizing the first derivative (imposing model flatness) or when using classical amplitude damping, thus backward slip is not a consequence of the type of regularization imposed. An additional disadvantage of the amplitude damping is the fact that it proves to act much more severely on the deeper patches and relatively increases the slip estimates at shallow depths. All these observations already imply an ill-conditioned inverse problem where additional information (in my case regularization) is needed to arrive at an acceptable solution. I refrain from imposing positivity constraints and depth-dependent regularization since 1) non-negativity constraints make it difficult (if not impossible) to determine both resolution and model covariance, 2) they may not always be easily applicable in fault studies, e.g. when the sense of fault motion is unclear, and 3) depth dependent smoothing is difficult to tune because it tends to force slip to shallower depths.

Figure 5.2 shows my coseismic slip distribution model compared to the model obtained by Reilinger et al. (2000), model standard deviations ($\sigma_i = \sqrt{C_{ii}}$) and the diagonal elements of the formal resolution matrix (R_{ii}). I find that I reproduce the main features of the model of Reilinger et al. (2000) reasonably well. The differences between the two models are basically due to differences in inversion procedure adopted

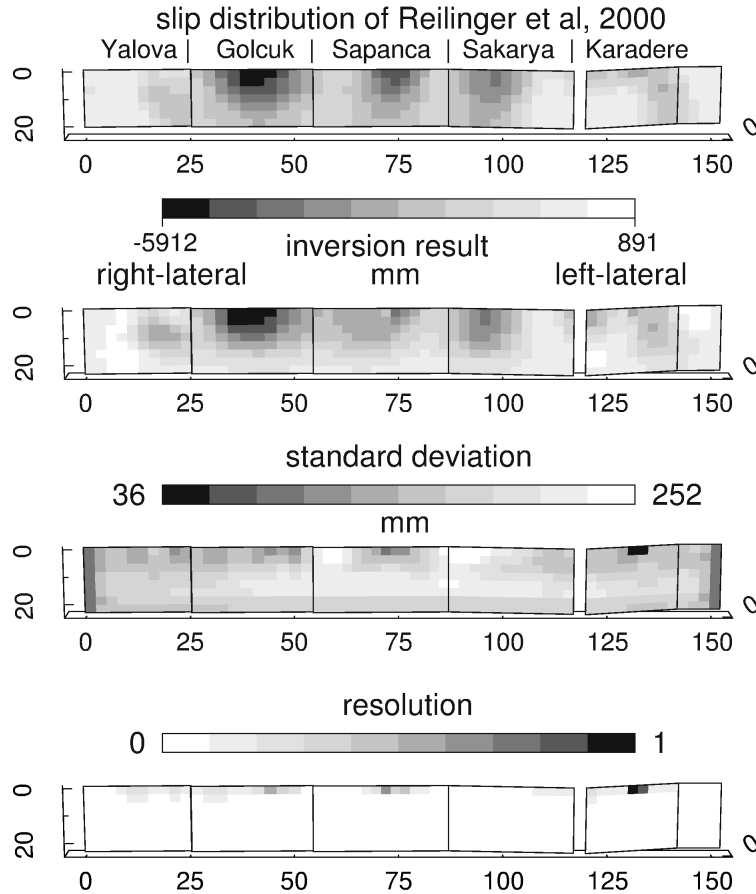


Figure 5.2: Comparison of the GPS slip distribution model of Reilinger et al. (2000; top panel) with my inversion result (second panel). The bottom two figures show the formal standard deviation and diagonal elements of the resolution matrix of my inversion solution.

and constraints imposed (e.g. the non-negativity constraints imposed by Reilinger et al., 2000). Significant backward slip is still induced on the Golyaka and Hersek segments of the fault (up to 890 mm). The model standard deviations obtain a maximum of 253 mm and are generally an order of magnitude less than the derived fault slip estimates. This model (or the model of Reilinger et al. (2000)) is an acceptable model because of its data fit and model covariance and because it is in accord with observed surface slip. My model is heavily determined by regularization which lowers the model covariance and also the spatial resolution (i.e. introducing linear dependence between model parameters)

5.4 Model resolution

The formal resolution of this solution is rather poor. Except for some patches in the top 6 km of the model, the diagonal elements R_{ii} are less than 0.1. I visualize this dependence by multiplying the resolution kernel \mathbf{R} with a slip vector $a\bar{e}_j$ where \bar{e}_j is the unit vector denoting patch j and $a = -1000\text{mm}$. Figure 5.3 shows the result for 3 selected patches with varying dependence on other model patches. I find a significant dependence between the model amplitudes at selected patches and those of patches within a roughly 25 km radius which I adopt here as a measure of resolution length. Except for the best resolved patch (52) all others show a significant reduction of amplitude which may be up to two orders of magnitude. I further find that the deeper patches strongly depend on amplitudes obtained for shallower depths. Backward slip is induced in the model as a direct result of the poor resolution.

Earlier studies obtained resolution lengths on the scale of tens of km from synthetic tests (DeLouis et al., 2002; Reilinger et al., 2000). I construct a synthetic model containing $\sim 12 \times 12$ km patches with 4 m right-lateral slip within my $\sim 3 \times 3$ km fault

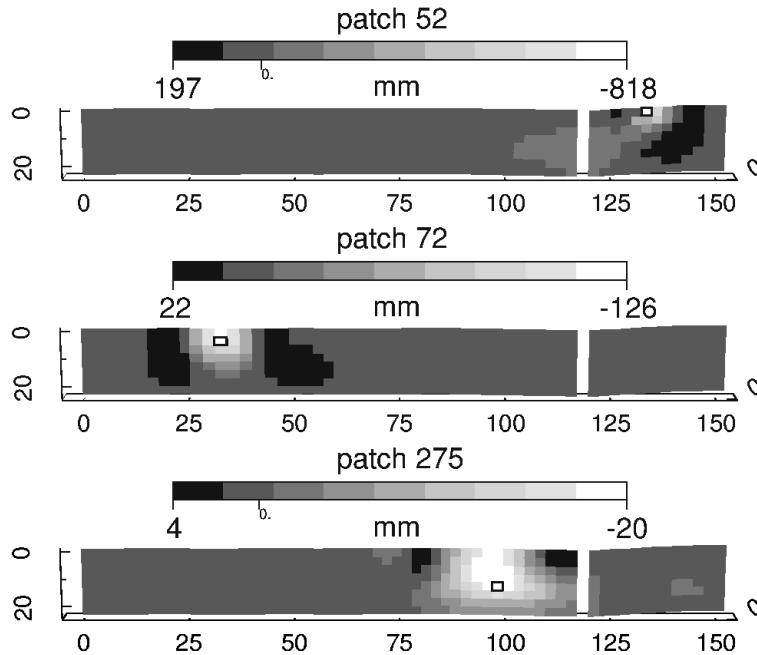


Figure 5.3: Model estimates m_i resulting from multiplication of the resolution kernel \mathbf{R} with ae_j ($m_i = \sum R_{ij} \cdot ae_j$) with $a = -1000\text{mm}$ on patch j , indicated by the black rectangle. The patches are evenly distributed throughout the model and portray a range of linear dependence between model parameters.

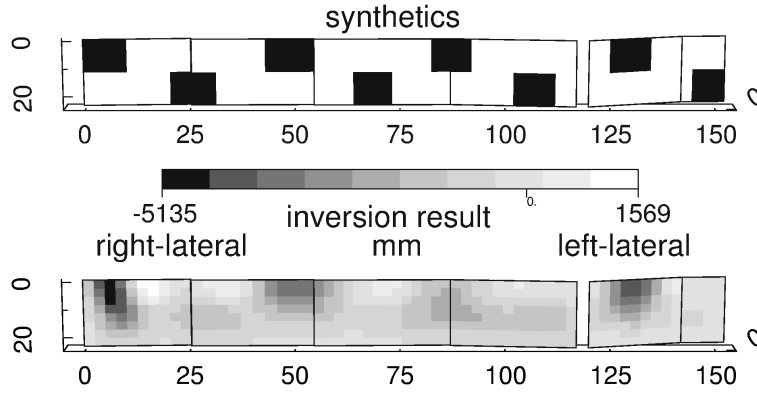


Figure 5.4: Result of the multiplication of the resolution kernel \mathbf{R} (based on a 3×3 km fault parameterization) with a synthetic model containing 12×12 km patches (top panel) ($\mathbf{m} = \mathbf{R} \cdot \mathbf{m}_{syn}$).

parameterization and multiplied this model with \mathbf{R} (figure 5.4). The result reasonably reproduces the synthetic model in the depth range from 0-12 km on the Yalova, Sapanca and Karadere segments. Due to the very poor resolution, the spike on the Sakarya segment, as well as the deeper spikes have been reduced in amplitude to less than half their synthetic value. Since the resolution length (~ 25 km) encompasses multiple synthetic patches, the model still contains significant interaction between neighboring patches.

To enhance the spatial resolution a coarser parameterization with increased patch sizes can be adopted. I obtain reasonable resolution ($R_{ii} \sim 0.6 - 0.7$) throughout my model for a fault parameterization consisting of 2 layers of 12 km thickness for each fault segment. However, spatial resolution still decreases significantly with depth and the patches in the deeper layer remain reduced in amplitude (~ 1800 mm). Further, the parameterization has become too coarse to fit the spatial variations within the GPS observations and large misfits of up to 170 mm are obtained ($\chi^2 = 15.0$). This shows the need for a denser parameterization and consequently allowing the resolution to be reduced.

5.5 Surface displacement field

Since coarsening of the fault parameterization does not provide a useful way to both improve the model resolution and retain an acceptable fit to the data, a denser data set may better constrain the model. Such a denser data set could be provided by e.g. InSAR measurements. Since the correlation length of errors in InSAR data is of order 5 km (Hanssen, personal communication, 2003), I simulate a dense data distribution by determining a synthetic displacement field on a 5×5 km regular surface grid based on

the synthetic model of $\sim 12 \times 12$ km patches using a $\sim 3 \times 3$ km fault parameterization. In total this data set consists of 2010 data points and covers the same area as was contained by the GPS data. The fault geometry, number of free parameters, and damping weights are the same for this synthetic test as for the GPS data inversion. A low level of noise of 7.5 mm (comparable to the GPS uncertainties) was assigned to the synthetic data prior to inversion. I find that the inverted model reproduces the patches in the upper 12 km reasonably well (figure 5.5). Also, the patch on the Sakarya segment is now well reproduced (compare to figure 5.4). Though the deeper patches are better localized using this extended "data" set, they are still significantly reduced in amplitude (between $\frac{1}{2}$ and $\frac{2}{3}$ of the synthetic value). Significant backward slip is again induced. The model resolution in the upper 9 km of the model has improved compared to the models based

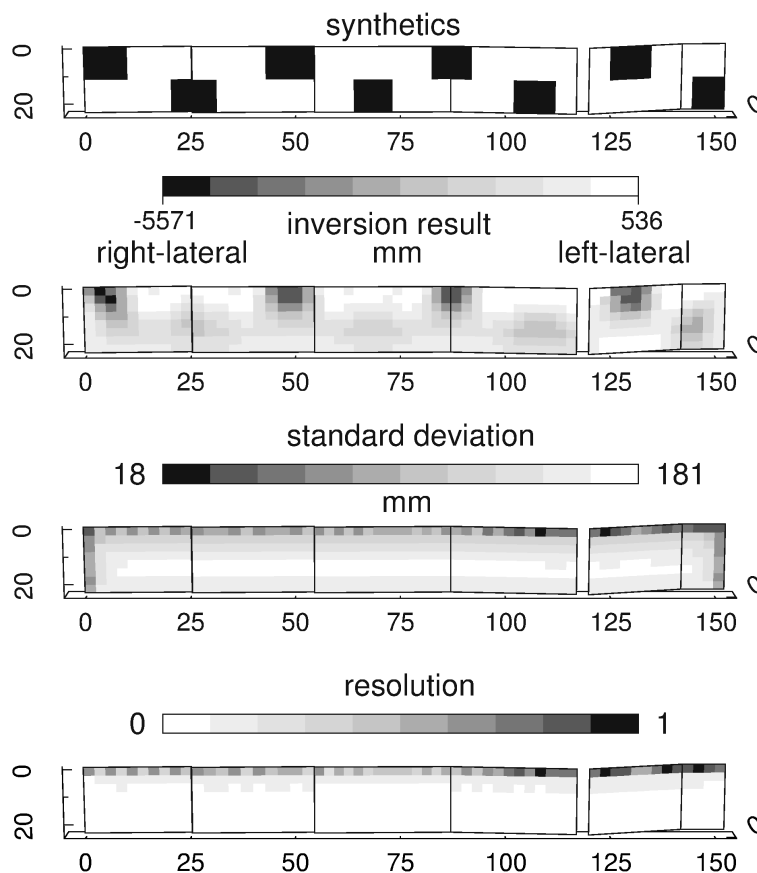


Figure 5.5: Results of the inversion of a dense displacement field of synthetic data on a 5×5 km regular surface grid predicted from a synthetic model containing 12×12 km patches using a 3×3 km fault parameterization.

on the real GPS data distribution. However, at depths exceeding 9 km R_{ii} remains less than 0.1. I infer a slight reduction in resolution length for this model to ~ 20 km.

I conclude that a dense data distribution simulated by a 5×5 km regular grid improves the resolution of the model, especially in the upper 9 km of the model. However, the spatial distribution of slip at depth is still poorly constrained. I note that the synthetic data used in this last experiment are fully consistent with the adopted model of elastic dislocations. For real GPS data discrepancies between the idealized dislocation models and true fault dynamics induce correlated data errors (Bos et al., 2003b).

5.6 The data kernel

The generally observed poor depth resolution could be intrinsic to using elastic dislocation theory in the forward problem. Figure 5.6 shows the data kernels of 6 stations at increasing distances from the fault trace as a function of fault patch depth. The displacements at stations in the proximity of the fault are more sensitive to the slip on the fault than the displacements at stations located further away from the fault trace (especially for slip at upper crustal levels). Importantly, with increasing fault patch depth the coefficients become systematically less sensitive to station position. The relative variation of coefficients with depth is on the order of 100-10000 which, because of the systematic decrease with depth, points at a large condition number of $\mathbf{A}^T \mathbf{A}$ of

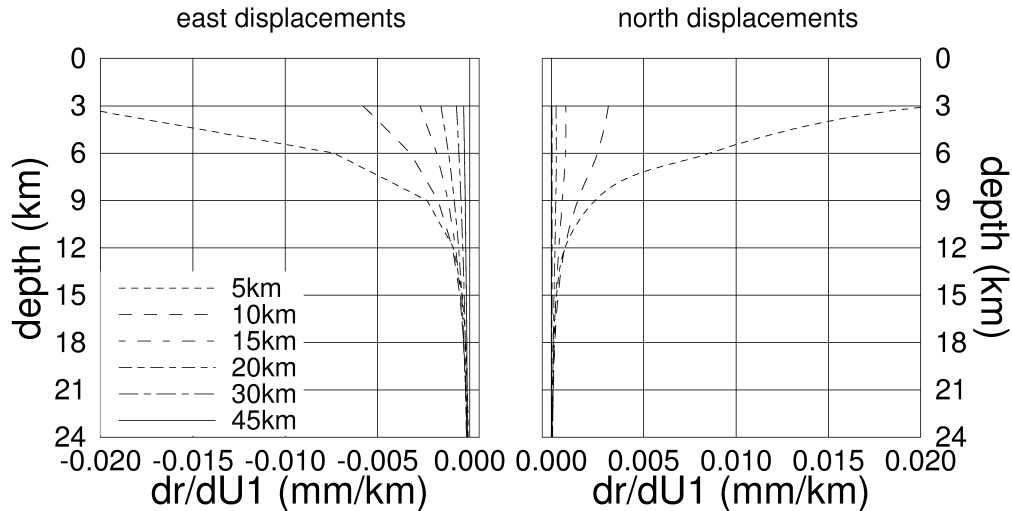


Figure 5.6: Data kernels, "Okada" coefficients ($dr/dU1$), for the east and north displacements at 6 stations perpendicular to the fault and at increasing distance from the fault plotted against fault patch depth.

$\geq 100^2 - 10000^2$ and damping will always be needed to avoid instable solutions. As observed, the damping will first destroy the resolution at depth. For dipping faults the fault geometry is more laid out beneath an observing station network and the data kernels of stations above the fault show greater variation in the upper 10-15 km which will improve resolution for fault slip in this depth range. Still a systematic decrease of kernel amplitude with fault depth occurs, comparable to that of vertical faults, which I expect will cause a similar resolution problem but at somewhat larger depth than for vertical faults. In conclusion, this inverse problem is intrinsically ill-conditioned.

5.7 Conclusions

I have performed an analysis of the spatial resolution of slip distribution models based on the inversion of surface displacement data. For the 17 August 1999 Izmit, Turkey earthquake I have shown that within the generally adopted $\sim 3 \times 3$ km fault parameterization GPS displacements lack sufficient resolving power to constrain the spatial distribution at larger depth. A denser data distribution improves the resolution in the upper 9 km of the model, but remains incapable to constrain the slip distribution at greater depths. The inverse problem of retrieving fault slip from surface deformation data using elastic dislocation theory is intrinsically ill-conditioned. DeLouis et al. (2002) and Wald and Graves (2001) showed that additional seismological data will only improve the resolution at upper crustal levels. Thus, the details of deep fault slip remain as yet largely in the null space of this inverse problem.

Chapter 6

Epilogue

6.1 Concluding remarks

Although at first sight the research contained in this thesis may seem diverse, the common denominator is the inversion of space geodetic data to determine the surface deformation field. In chapters 2, 3 and 4 I utilized the method of Spakman and Nyst (2002) to infer geodetic observations in terms of strain (rate), rotation (rate) and fault motion. The novel incorporation of fault motion in the inversion method allows me to partition data signal between the velocity gradient and fault motion and allows for the determination of deformation localized around faults. The observed localization of deformation in California (chapter 2) poses important implications on the crustal rheology across the faults, as well as on the seismic hazard of this particular area. A basic problem encountered, and specifically elucidated by the Spakman and Nyst (2002) method, is the trade-off between the displacement or velocity gradient field and slip on the fault in regions of poor data density in the proximity of the fault trace. Therefore, I have assessed the extent of the trade-off for each model.

Throughout this thesis, both in the analysis of the surface deformation models and in the resolution analysis of the slip dislocation models, I deduce that space geodetic data in cases may contain little information on deformation at depth. Particularly, slip distribution models adopting a parameterization which is dense enough to adequately fit the data provide much less useful detail at depth than was previously assumed. Because the data sensitivity for fault slip at depths exceeding 10 km is relatively small, coseismic surface deformation models mostly reflect the (near-) surface response to processes driving the deformation. In general, a combination with other crustal deformation data/information (e.g. seismicity, crustal tomography) seems necessary to study the crustal processes driving the deformation. Chapter 3 is among the first studies to provide a comprehensive look on a regional tectonic setting (in my case Taiwan) by conducting a joint analysis of geodetic data, seismicity, seismic tomography, litho-

spheric stress data, and geodynamics. Certain stretches in tying these diverse pieces of information together are unavoidable. Additionally, the combination of the surface deformation model with local seismicity allows for a quantitative assessment of the seismic hazard within the model area (chapter 2).

An other novelty in this thesis is the presentation of the first kinematic coseismic surface deformation field (i.e. displacement gradient and fault slip). The understanding of this surface deformation field is an important intermediate step towards a time-dependent analysis and may hold important implications for slip distribution modeling (such as misfits due to the asymmetry of the surface displacement field across the fault). Until now purely kinematic surface deformation studies were limited to interseismic geodetic observations due to the limitations of the analysis methods (the absence of fault motion in the analysis methods). The implementation of fault motion is of prime importance in the derivation of a coseismic surface deformation model, since it allows the distinction between the actual coseismic motion on the fault and strain release in the bounding blocks. In this study the geodetic GPS and InSAR observations of the 1999 Izmit, Turkey earthquake have been utilized to infer the coseismic surface deformation field. For this event, I was able to show that this field reflects the complexity of the earthquake source and stipulate the importance of the fault geometry on the source rupture process, hence on the surface deformation field.

6.2 Recommendations for future research

The increasing spatial density of geodetic observation sites will allow for continuously increasing detail and complexity in the surface deformation models. Therefore, some recommendations for future research are warranted.

First of all, the incorporation of the vertical displacements/velocities in the analysis is of utmost importance, especially in convergent settings such as Taiwan. Vertical motions may prove to be very discriminative between alternative geodynamic hypothesis. For instance, in Taiwan vertical motions on faults are one order of magnitude larger than the horizontal motions, thus giving an important tie to deep processes. Apart from some exceptions the incorporation of vertical motions has been prohibited by the limited precision of geodetic estimates of the vertical displacement/velocity due to both instrumental factors and the fact that vertical motions are typically slower. However, this is continuously improving. Three dimensionality is also of prime importance for the direct incorporation of the InSAR measurements in the inversion procedure. The InSAR range changes are the one-dimensional result of the projection of the three-dimensional displacements at the Earth's surface on the line-of-sight direction of the InSAR satellite. Vertical motions due to three-dimensional surface deformation will therefore affect these range change measurements, even in predominantly strike-slip settings (as is shown in chapter 4). A three-dimensional approach to modeling the sur-

face deformation will also allow for the derivation of surface deformation models for active volcanic regions (e.g. Yellowstone) and individual volcanos which could provide important information on the swelling of volcanos prior to an eruption.

The incorporation of time as a variable parameter in surface deformation modeling would be a second important development. A time-dependent analysis of the surface deformation field will provide important information on the temporal variations of the velocity gradient field which is crucial in both volcanic and seismic hazard analysis and, in general, to estimate the short-term temporal development of plate deformation. Especially the temporal variations in strain accumulation (linear vs. exponential) in the years prior to a major earthquake might provide important new information for earthquake prediction.

Bibliography

- Ambraseys, N. N. (1970). Some characteristic features of the Anatolian fault zone. *Tectonophysics*, 9:143–165.
- Angelier, J., Bergerat, F., Chu, H.-T., and Lee, T.-Q. (1990). Tectonic analysis and the evolution of a curved collision belt: The Hsuehshan Range, northern Taiwan. *Tectonophysics*, 183:77–96.
- Angelier, J., Chu, H.-T., and Lee, J.-C. (1997). Shear concentration in a collision zone: kinematics of the Chihshang fault as revealed by outcrop-scale quantification of active faulting, Longitudinal Valley, eastern Taiwan. *Tectonophysics*, 274:117–143.
- Angelier, J., Chu, H.-T., Lee, J.-C., and Hu, J.-C. (2000). Active faulting and earthquake risk: The Chihshang Fault case, Taiwan. *J. Geodyn.*, 29:151–185.
- Argus, D. F., Heflin, M. B., Donnellan, A., Webb, F. H., Dong, D., Hurst, K. J., Jefferson, D. C., Lyzenga, G. A., Watkins, M. M., and Zumberge, J. F. (1999). Shortening and thickening of metropolitan Los Angeles measured and inferred by using geodesy. *Geology*, 27(8):703–706.
- Ayhan, M. E., Demir, C., Lenk, O., Kiliçoglu, A., Altiner, Y., Barka, A., Ergintev, S., and Ozener, H. (2002). Interseismic strain accumulation in the Marmara Sea region. *Bulletin of the Seismological Society of America*, 92(1):216–229.
- Barka, A., Akyüz, S., Altunel, E., Sunal, G., Çakir, Z., Dikbaş, A., Yerli, B., Armijo, R., Meyer, B., Chabalier, B., Rockwell, T., Dolan, J. R., Hartleb, R., Dawson, T., Christofferson, S., Tucker, A., Fumal, T., Langridge, R., Stenner, H., Lettis, W., Backhuber, J., and Page, W. (2002). The surface rupture and slip distribution of the 17 August 1999 Izmit earthquake (M 7.4), North Anatolian fault. *Bulletin of the Seismological Society of America*, 92(1):43–60.
- Barka, A. A. (1992). The North Anatolian fault zone (supplement). *Ann. Tectonicae*, 6:164–195.
- Barr, T. D. and Dahlen, F. A. (1990). Constraints on friction and stress in the Taiwan fold-and-thrust belt from heat flow and geochronology. *Geology*, 18:111–115.
- Barrier, E. and Angelier, J. (1986). Active collision in eastern Taiwan: the Coastal Range. *Tectonophysics*, 125:39–72.
- Beavan, J. and Haines, J. (2001). Contemporary horizontal velocity and strain rate fields of the Pacific-Australian plate boundary zone through New Zealand. *J. Geophys. Res.*, 106(1):741–770.
- Bennett, R. A. (2003). Contemporary strain rates in the northern Basin and Range province from GPS data. tectonics, in press.
- Bennett, R. A., Davis, J. L., Meertens, C. M., Smith, R. B., and Wernicke, B. P. (1998). Integration of the northern Basin and Range (NBAR) and Wasatch Front GPS networks for crustal deformation in and around the southern Intermountain seismic belt. *Seismological Research Letters*, 69(2):159.
- Bennett, R. A., Davis, J. L., Normandeau, J. E., and Wernicke, B. P. (2002). Space geodetic measurements of plate boundary deformation in the western U.S. Cordillera. In Stein, S. and Freymueller, J., editors, *Plate boundary zones, Geodynamics 30*, pages 27–55. AGU.
- Bennett, R. A., Davis, J. L., and Wernicke, B. P. (1999). Present-day pattern of Cordilleran deformation in the western United States. *Geology*, 27(4):371–374.
- Bennett, R. A., Rodi, W., and Reilinger, R. E. (1996). Global Positioning System constraints on fault slip rates in southern Cal-

- ifornia and northern Baja, Mexico. *J. Geophys. Res.*, 101:21943–21960.
- Bennett, R. A., Wernicke, B. P., Davis, J. L., Elosegui, P., Snow, J. K., Abolins, M. J., House, M. A., Stirewalt, G. L., and Ferrill, D. A. (1997). Global Positioning System constraints on fault slip rates in the Death Valley region, California and Nevada. *Geophys. Res. Lett.*, 24(23):3073–3076.
- Beutler, G., Mueller, I., and Neilan, R. (1994). The International GPS Service for geodynamics: Development and start of official service on Januari 1, 1994. *Bulletin Géodésique*, 68:39–70.
- Bijwaard, H. and Spakman, W. (2000). Non-linear global P-wave tomography by iterated linearized inversion. *Geophys. J. Int.*, 141(1):71–82.
- Bijwaard, H., Spakman, W., and Engdahl, R. (1998). Closing the gap between regional and global travel time tomography. *J. Geophys. Res.*, 103:30055–30078.
- Biq, C. C. (1972). Dual trench structure in the Taiwan-Luzon region. *Proc. Geol. Soc. China*, 15:65–75.
- Bock, Y., Wdowinski, S., Fang, P., Zhang, J., Behr, J., Genrich, J., Agnew, D., Wyatt, F., Johnson, H., Marquez, S., Hudnut, K., King, R., Herring, T., Stark, K., Dinardo, S., Young, W., Jackson, D., and Gurtner, W. (1997). Southern California permanent GPS geodetic array: Continuous measurements of regional crustal deformation between the Landers and Northridge earthquakes. *J. Geophys. Res.*, 102:18,103–18,033.
- Boore, D. M. and Hill, D. P. (1973). Wave propagation characteristics in the vicinity of the San Andreas fault. In Kovach, L. and Nur, A., editors, *Proceedings of the conference on tectonic problems of the San Andreas fault system*. Stanford Univ. Publ., Geological Sciences, vol XIII, Stanford, CA.
- Bos, A. G., Spakman, W., and Nyst, M. C. J. (2003a). Surface deformation and tectonic setting of Taiwan inferred from a GPS velocity field. *J. Geophys. Res.*, in press.
- Bos, A. G., Usai, S., and Spakman, W. (2003b). Joint analysis of GPS motions and InSAR to infer the co-seismic surface deformation of the Izmit, Turkey earthquake. submitted to *Geophys. J. Int.*
- Bosworth, J. M., Coates, R. J., and Fischetti, T. L. (1993). The development of NASA's crustal dynamics project. In Smith, D. and Turcotte, D., editors, *Contributions of space geodesy to geodynamics: Technology*, volume 25, pages 1–20. AGU.
- Bouchon, M., Toksöz, M. N., Karabulut, H., Bouin, M.-P., Dietrich, M., Aktar, M., and Edie, M. (2000). Seismic imaging of the 1999 Izmit (Turkey) rupture inferred from the near-fault recordings. *Geophys. Res. Lett.*, 27(18):3013–3016.
- Bouchon, M., Toksöz, M. N., Karabulut, H., Bouin, M.-P., Dietrich, M., Aktar, M., and Edie, M. (2002). Space and time evolution of rupture and faulting during the 1999 Izmit (Turkey) earthquake. *Bulletin of the Seismological Society of America*, 92(1):256–266.
- Bourne, S. J., Árnadóttir, T., Beavan, J., Darby, D. J., England, P. C., Parsons, B., Walcott, R. I., and Wood, P. R. (1998). Crustal deformation of the Marlborough fault zone in the South Island of New Zealand: Geodetic constraints over the interval 1982-1994. *J. Geophys. Res.*, 103(12):30,147–30,165.
- Bürgmann, R., Ayhan, M. E., Fielding, E. J., Wright, T. J., McClusky, S., Aktug, B., Demir, C., Lenk, O., and Türkezer, A. (2002). Deformation during the 12 November 1999 Düzce, Turkey earthquake from GPS and InSAR data. *Bulletin of the Seismological Society of America*, 92(1):161–170.
- Carter, J. N., Luyendyk, B. P., and Terres, R. R. (1987). Neogene clockwise tectonic rotation of the eastern Transverse Ranges, California, suggested by paleo-

- magnetic vectors. *Geol. Soc. Am. Bull.*, 98:199–206.
- Chai, B. H. T. (1972). Structure and tectonic evolution of Taiwan. *Am. J. Sci.*, 272:389–422.
- Chemenda, A. I., Yang, R.-K., Hsieh, C.-H., and Groholsky, A. L. (1997). Evolutionary model for the Taiwan collision based on physical modeling. *Tectonophysics*, 274:253–274.
- Chemenda, A. I., Yang, R.-K., Stephan, J.-F., Konstantinovskaya, E. A., and Ivanov, G. M. (2001). New results from physical modeling of arc-continent collision in Taiwan: Evolutionary model. *Tectonophysics*, 333:159–178.
- Chen, H. (1984). Crustal uplift and subsidence in Taiwan: An account based on retriangulation results. *Spec. Publ. Central Geol. Surv.*, 3:127–140. in Chinese.
- Chinnery, M. A. (1970). Earthquake displacement fields. In Mansinha, L., editor, *Earthquake displacement fields and the rotation of the earth*. D. Reidel Publ. Co., Dordrecht-Holland.
- Christodoulis, D. C., Smith, D. E., Kolenkiewicz, R., Dunn, P. J., Klosko, S. M., Torrence, M. H., Fricke, S. K., and Blackwell, S. (1985). Observing tectonic plate motions and deformations from satellite laser ranging. *J. Geophys. Res.*, 90:9249–9264.
- Crespi, J. M., Chan, Y. C., and Swaim, M. S. (1996). Synorogenic extension and exhumation of the Taiwan hinterland. *Geology*, 24:247–250.
- Crespi, J. M., Liu, T.-K., Hsieh, S., Lu, C.-Y., and Chen, C.-H. (1990). Structural and thermal evidence for extension in the high elevations of Taiwan. *Eos, Trans. Am. Geophys. Union*, 71(43):1618.
- Dahlen, F. A. (1990). Critical taper model of fold-and-thrust belts and accretionary wedges. *Ann. Rev. Earth Planet. Sci.*, 18:55–99.
- Deffontaines, B., Lacombe, O., Angelier, J., Chu, H.-T., Mouthereau, F., Lee, C.-T., Deramond, J., Lee, J.-F., Yu, M.-S., and Liew, P. M. (1997). Quaternary transfer faulting in the Taiwan Foothills: Evidence from a multisource approach. *Tectonophysics*, 274:61–82.
- DeLouis, B., Giardini, D., Lundgren, P., and Salichon, J. (2002). Joint inversion of InSAR, GPS, teleseismic and strong-motion data for the spatial and temporal distribution of earthquake slip: Application to the 1999 Izmit mainshock. *Bulletin of the Seismological Society of America*, 92(1):278–299.
- DeMets, C., Gordon, D., Argus, D. F., and Stein, S. (1990). Current plate motions. *Geophys. J. Int.*, 101:425–478.
- Dixon, T. H., Farina, F., DeMets, C., Suarez Vidal, F., Fletcher, J. and Marquez Azua, B., Miller, M. M., Sanchez, O., and Umhoefer, P. (2000a). New kinematic models for Pacific-North America motion from 3 Ma to present; ii, Evidence for a "Baja California shear zone". *Geophys. Res. Lett.*, 27:3961–3964.
- Dixon, T. H., Miller, M., Farina, F., Wang, H., and Johnson, D. (2000b). Present-day motion of the Sierra Nevada block and some tectonic implications for the Basin and Range province, North American Cordillera. *Tectonics*, 19:1–24.
- Dixon, T. H., Robaudo, S., Lee, J., and Reheis, M. C. (1995). Constraints on present-day Basin and Range deformation from space geodesy. *Tectonics*, 14(4):755–772.
- Dokka, R. K. and Travis, C. J. (1990). Role of the eastern California shear zone in accommodating Pacific-North America plate motion. *Geophys. Res. Lett.*, 17(9):1323–1326.
- Du, Y. and Aydin, A. (1993). Stress transfer during three sequential moderate earthquakes along the central Calaveras fault, California. *J. Geophys. Res.*, 98(6):9947–9962.
- Du, Y., Aydin, A., and Segall, P. (1992). Comparison of various inversion techniques as

- applied to the determination of a geophysical deformation model for the 1983 Borah Peak earthquake. *Bulletin of the Seismological Society of America*, 82(4):1840–1866.
- Eberhart-Phillips, D., Lisowski, M., and Zoback, M. D. (1990). Crustal strain near the Big Bend of the San Andreas fault: Analysis of the Los Padres-Tehachapi trilateration networks, California. *J. Geophys. Res.*, 95(2):1139–1153.
- Eberhart-Phillips, D. and Michael, A. J. (1993). Three-dimensional velocity structure, seismicity, and fault structure in the Parkfield region, central California. *J. Geophys. Res.*, 98(9):15,737–15,758.
- Ellwood, A., Wang, C.-Y., Teng, L. S., and Yen, H.-Y. (1996). Gravimetric examination of thin-skinned detachment vs. basement-involved models for the Taiwan orogen. *J. Geol. Soc. China*, 39:209–221.
- Engdahl, E. R., Van der Hilst, R. D., and Buland, R. P. (1998). Global teleseismic earthquake relocation with improved travel times and procedures for depth determination. *Bulletin of the Seismological Society of America*, 88:722–743.
- England, P. and Houseman, G. (1985). Role of lithospheric strength heterogeneities in the tectonics of Tibet and neighboring regions. *Nature*, 315:297–301.
- England, P. and Houseman, G. (1989). Extension during continental convergence, with application to the Tibetan Plateau. *J. Geophys. Res.*, 94:17561–17579.
- Feigl, K. L., Sarti, F., Vadon, H., McClusky, S., Ergintav, S., Durand, P., Bürgmann, R., Rigo, A., Massonnet, D., and Reilinger, R. (2002). Estimating slip distribution for the İzmit mainshock from coseismic GPS, ERS-1, RADARSAT and SPOT measurements. *Bulletin of the Seismological Society of America*, 92(1):138–160.
- Fialko, Y., Simons, M., and Agnew, D. (2001). The complete (3-D) surface displacement field in the epicentral area of the 1999 M_w 7.1 Hector Mine earthquake, California, from space geodetic observations. *Geophys. Res. Lett.*, 28(16):3063–3066.
- Flesch, L. M., Holt, W. E., Haines, A. J., and Shen-Tu, B. (2000). Dynamics of the Pacific-North American plate boundary in the western United States. *Science*, 287:834–836.
- Forsyth, D. W. and Uyeda, S. (1975). On the relative importance of the driving forces of plate motion. *Geoph.J.R.Astron.Soc.*, 43:163–200.
- Frank, F. C. (1996). Deduction of Earth strains from survey data. *Bulletin of the Seismological Society of America*, 56:35–42.
- Freund, R. (1970). Rotation of strike-slip faults in Sistan, Southeastern Iran. *Journal of Geology*, 78:188–200.
- Freymueller, J., King, N. E., and Segall, P. (1994). The coseismic slip distribution of the Landers earthquake. *Bulletin of the Seismological Society of America*, 84(3):646–659.
- Friedrich, A. M., Wernicke, B. P., Niemi, N. A., Bennett, R. A., and Davis, J. L. (2003). Comparison of geodetic and geologic data from the Wasatch region Utah, and implications for the spectral character of Earth deformation at periods 10 to 10 million years. *J. Geophys. Res.*, 108(4):2199, doi:10.1029/2001JB000682.
- Gan, W. J., Svarc, L., Savage, C., and Prescott, W. H. (2000). Strain accumulation across the Eastern California shear zone at latitude 36°30'N. *J. Geophys. Res.*, 105:16229–16236.
- Genrich, J. F., Bock, Y., McCaffrey, R., Prawirodirdjo, L., Stevens, C. W., Puntodewo, S. S. O., Subarya, C., and Wdowinski, S. (2000). Distribution of slip at the northern Sumatran fault system. *J. Geophys. Res.*, 105(12):28,327–28,341.
- Güllen, L., Pinar, A., Kalafat, D., Özel, N., Horasan, G., Yilmazer, M., and İşikara, A. M. (2002). Surface fault breaks, after-shock distribution and rupture process of the 17 August 1999 İzmit, Turkey, earth-

- quake. *Bulletin of the Seismological Society of America*, 92(1):230–244.
- Haines, A. J. and Holt, W. E. (1993). A procedure for obtaining the complete horizontal motions within zones of distributed deformation from the inversion of strain rate data. *J. Geophys. Res.*, 98:12057–12082.
- Harding Hearn, E. and Humphreys, E. D. (1998). Kinematics of the southern Walker Lane Belt and motion of the Sierra Nevada block, California. *J. Geophys. Res.*, 103:27033–27049.
- Harris, R. A. and Segall, P. (1987). Detection of a locked zone at depth on the Parkfield, California segment of the San Andreas fault. *J. Geophys. Res.*, 92(8):7945–7962.
- Hartleb, R. D., Dolan, J., Akyüz, H., Dawson, T. E., Tucker, A. Z., yerli, B., Rockwell, T. K., Toraman, E., Çakir, Z., Dikbaş, A., and Altunel, E. (2002). Surface rupture and slip distribution along the Karadere segment of the 17 August 1999 Izmit and the western section of the 12 November 1999 Düzce, Turkey, earthquakes. *Bulletin of the Seismological Society of America*, 92(1):67–78.
- Healy, J. H. and Peake, L. G. (1975). Seismic velocity structure along a section of the San Andreas fault near Bear Valley, California. *Bulletin of the Seismological Society of America*, 65:1177–1197.
- Herman, B. M., Anderson, R. N., and Truchan, M. (1978). Extensional tectonics in the Okinawa Trough; in *Geological and Geophysical Investigations of Continental Margins*. In Watkins, J., Montadert, I., and Dickinson, P., editors, *Mem. Am. Assoc. Pet. Geol.*, volume 29, pages 199–208.
- Herring, T. A., Shapiro, I. I., Clarck, T. A., Ryan, J. W., Schupler, B. R., Knight, C. A., Lundqvist, G. L., B., S. D., Vandenberg, N. R., Corey, B. E., Hinteregger, H. F., Rodgers, A. E. E., Webber, J. C., Whitney, A. R., Elgered, G., Rönnäng, B. O., and Davis, J. L. (1986). Geodesy by radio interferometry: evidence for contemporary plate motion. *J. Geophys. Res.*, 91:8341–8347.
- Ho, C. S. (1988). An introduction to the geology of Taiwan. Technical report, Cent.Geol.Surv., Minist. of Econ. Affairs, Taipei. 2nd ed., 92 pp.
- Hsieh, S. H. and Hu, C. C. (1972). Gravimetric and magnetic studies of Taiwan. *Pet. Geol. Taiwan*, 10:283–321.
- Hu, J.-C., Angelier, J., Lee, J.-C., Chu, H.-T., and Byrne, D. (1996). Kinematics of convergence, deformation and stress distribution in the Taiwan collision area: 2-D finite-element numerical modeling. *Tectonophysics*, 255:243–268.
- Hu, J.-C., Angelier, J., and Yu, S.-B. (1997). An interpretation of the active deformation of southern Taiwan based on numerical simulation and GPS studies. *Tectonophysics*, 274:145–169.
- Hudnut, K. W., Bock, Y., Cline, M., Fang, P., Feng, Y., Freymueller, J., Ge, X., Gross, W. K., Jackson, D., Kim, M., Langbein, J., Larsen, S. C., Lisowski, M., Shen, Z.-K., Svarc, J., and Zhang, J. (1994). Co-seismic displacements of the 1992 Landers earthquake sequence. *Bulletin of the Seismological Society of America*, 84(3):625–645.
- Huggett, G. R., Slater, L. E., and Langbein, J. (1977). Fault episodes near Hollister, California: Initial results using a multiwavelength distance-measuring instrument. *J. Geophys. Res.*, 52:3361–3368.
- Hwang, W.-T. and Wang, C.-Y. (1993). Sequential thrusting model for mountain building: Constraints from geology and heat flow of Taiwan. *J. Geophys. Res.*, 98:9963–9973.
- Jackson, D. D. (1979). The use of a priori data to resolve non-uniqueness in linear inversion. *Geoph.J.R.Astron.Soc.*, 57:137–157.
- Jackson, D. D., Shen, Z.-K., Potter, D., X.-B., G., and Sung, L.-Y. (1997). Southern California deformation. *Science*, 277:1621–1622.
- Jackson, J. and Molnar, P. (1990). Active

- faulting and block rotations in the western Transverse Ranges, California. *J. Geophys. Res.*, 95:22,073–22,087.
- Kahle, H.-G., Cocard, M., Peter, Y., Geiger, A., Reilinger, R., Barka, A., and Veis, G. (2000). GPS-derived strain rate field within the boundary zones of the Eurasian, African, and Arabian plates. *J. Geophys. Res.*, 105:23,353–23,370.
- Kanamori, H. (1977). The energy release in great earthquakes. *J. Geophys. Res.*, 82:2981–2987.
- Kao, H., Shen, S.-S. J., and Ma, K.-F. (1998). Transition from oblique subduction to collision: Earthquakes in the southernmost Ryukyu arc-Taiwan region. *J. Geophys. Res.*, 103:7211–7229.
- Kato, T., El-Fiky, G. S., Oware, E. N., and Miyazaki, S. (1998). Crustal strains in the Japanese island as deduced from dense GPS arrays. *Geophys. Res. Lett.*, 25:3445–3449.
- Kimura, M. (1985). Back-arc rifting in the Okinawa Trough. *Pet. Geol.*, 2:222–240.
- King, G., Oppenheimer, D., and Amelung, F. (1994). Block versus continuum deformation in the Western United States. *Earth Plan. Sci. Lett.*, 128:55–64.
- King, N. E., Svarc, J. L., Fogelman, E., Gross, W. K., Clark, K. W., Hamilton, G. D., Stiffler, C. H., and Sutton, J. M. (1995). Continuous GPS observations across the Hayward fault, California, 1991–1994. *J. Geophys. Res.*, 100:20,271–20,283.
- Kostrov, V. V. (1974). Seismic moment and energy of earthquakes, and seismic flow of rock. *Earth Physics*, 1:23–40.
- Kosuga, M., Sato, H., Tanaka, T., and Shue, H. C. (1988). Crustal movement along a collision boundary of plates (case of eastern Taiwan). *J. Geodyn.*, 10:189–205.
- Lachenbruch, A. H., Sass, J. H., and Morgan, P. (1994). Thermal regime of the southern Basin and Range province: 2. Implications of heat flow for regional extension and metamorphic core complexes. *J. Geophys. Res.*, 99(11):22,121–22,133.
- Lacombe, O., Mouthereau, F., Deffontaines, B., Angelier, J., Chu, H. T., and Lee, C. T. (1999). Geometry and Quaternary kinematics of fold-and-thrust units in southwestern Taiwan. *Tectonics*, 18:1198–1223.
- Lacombe, O., Mouthereau, F., Angelier, J., and Deffontaines, B. (2001). Structural, geodetic and seismological evidence for tectonic escape in SW Taiwan. *Tectonophysics*, 333:323–345.
- Lallemand, S., Font, Y., Bijwaard, H., and Kao, H. (2001). New insights on 3-D plates interaction near Taiwan from tomography and tectonic implications. *Tectonophysics*, 335:229–253.
- Lallemand, S., Liu, C.-S., and Font, Y. (1997). A tear fault boundary between the Taiwan orogen and the Ryukyu subduction zone. *Tectonophysics*, 274:171–190.
- Langbein, J. (2002). *Parkfield creep meter data: detrended measurements from the past 10 years*. http://quake.wr.usgs.gov/QUAKES/geodetic/twocolor/creep_pkf_10yr_det.gif.
- Langridge, R. M., Stenner, H. D., Fumal, T. E., Christofferson, S. A., Rockwell, T. K., Hartleb, R. D., Bachhuber, J., and Barka, A. A. (2002). Geometry, slip distribution and kinematics of surface rupture on the Sakarya fault segment during the 17 August 1999 Izmit, Turkey, earthquake. *Bulletin of the Seismological Society of America*, 92(1):107–125.
- Lee, J.-C. and Angelier, J. (1993). Localisation des déformations actives et traitement des données géodésiques: l'exemple de la faille de la Vallée Longitudinale, Taïwan. *Bull. Soc. Géol. France*, 164:533–540.
- Lee, J.-C., Angelier, J., and Chu, H.-T. (1997). Polyphase history and kinematics of a complex major fault zone in the northern Taiwan mountain belt: The Lishan fault. *Tectonophysics*, 274:97–116.
- Lee, J.-C., Angelier, J., Chu, H.-T., Hu, J.-C., and Jeng, F.-S. (2001). Continuous monitoring of an active fault in a plate

- suture zone: A creepmeter study of the Chihshang fault, eastern Taiwan. *Tectonophysics*, 333:219–240.
- Lee, T.-Q. (1993). Preliminary paleomagnetic study on lake sediments at Yuashan, Ilan, northeastern Taiwan. *Bull. Inst. of Earth Sci., Academia Sinica*, 13:46–50.
- Lee, T.-Q., Angelier, J., Chu, H.-T., and Bergerat, F. (1991). Rotations in the northeastern collision belt of Taiwan: Preliminary results from paleomagnetism. *Tectonophysics*, 199:109–120.
- Lewis, S. D. and Hayes, D. E. (1983). The tectonics of northward propagating subduction along eastern Luzon, Phillipine Islands. *Geophys. Monogr.*, 27:56–78.
- Li, X., Cormier, V. F., and Toksöz, M. N. (2002). Complex source process of the 17 August 1999 Izmit, Turkey, earthquake. *Bulletin of the Seismological Society of America*, 92(1):267–277.
- Lienkaemper, J., Borchardt, G., and Lisowski, M. (1991). Historic creep rate and potential for seismic slip along the Hayward fault, California. *J. Geophys. Res.*, 96:18,261–18,283.
- Lin, C.-H. (1998). Tectonic implications of an aseismic belt beneath the eastern Central Range of Taiwan: Crustal subduction and exhumation. *J. Geol. Soc. China*, 41:441–460.
- Lin, C.-H., Yeh, Y.-H., Yen, H.-Y., Chen, K.-K., and Huang, B.-S. (1998). Three-dimensional elastic wave velocity structure of the hualien region of Taiwan: Evidence of active crustal exhumation. *Tectonics*, 17:89–103.
- Lin, M. T. and Tsai, Y. B. (1981). Seismotectonics in Taiwan-Luzon area. *Bull. Inst. of Earth Sci., Academia Sinica*, 1:51–82.
- Liu, C. (1995a). Geodetic monitoring of mountain building in Taiwan. *Eos, Trans. Am. Geoph. Union*, 76(46):636.
- Liu, C.-C. (1995b). The Ilan Plain and the southwestward extending Okinawa Trough. *J. Geol. Soc. China*, 38:229–242.
- Lu, C.-Y. and Malavieille, J. (1994). Oblique convergence, indentation and rotation tectonics in the Taiwan mountain belt: Insights from experimental modeling. *Earth Plan. Sci. Lett.*, 121:477–494.
- Lu, C.-Y., Yu, S.-B., and Chu, H.-T. (1998). Neotectonics of the Taiwan mountain belt. In Fowler, M., Chung, S.-L., Lo, C.-H., and Lee, T.-Y., editors, *Mantle dynamics and plate interactions in East Asia, Geodynamics 27*, pages 301–315. AGU.
- Luyendyk, B. P., Kamerling, M. J., and Terres, R. R. (1980). Geometric model for Neogene crustal rotations in southern California. *Geol. Soc. Am. Bull.*, 91:211–217.
- Lyons, S. and Sandwell, D. (2003). Fault creep along the southern San Andreas from interferometric synthetic aperture radar, permanent scatterers, and stacking. *J. Geophys. Res.*, 108(1):2047, doi:10.1029/2002JB001831.
- Mahrer, K. D. and Nur, A. (1979). Static strike-slip faulting in a horizontally varying crust. *Bulletin of the Seismological Society of America*, 69(4):975–1009.
- Malservisi, R., Furlong, K. P., and Dixon, T. H. (2001). Influence of the earthquake cycle and lithospheric rheology on the dynamics of the eastern California shear zone. *Geophys. Res. Lett.*, 28(14):2731–2734.
- Massonnet, D., Rossi, M., Carmona, C., Adragna, F., Peltzer, G., Feigl, K., and Rabaute, T. (1993). The displacement field of the Landers earthquake mapped by radar interferometry. *Nature*, 364:138–142.
- Matsu'ura, M., Jackson, D. D., and Cheng, A. (1986). Dislocation model for aseismic crustal deformation at Hollister, California. *J. Geophys. Res.*, 91:12,661–12,674.
- McClusky, S., Balassanian, S., Barka, A., Demir, C., Ergintav, S., Georgiev, I., Gurkan, O., Hamburger, M., Hurst, K., Kahle, H., Kastens, K., Kekelidze, G., King, R., Kotzev, V., Lenk, O., Mahmoud, S., Mishin, A., Nadariya, M., Ouzounis, A., Paradissis, D., Peter, Y., Prilepin, M.,

- Reilinger, R., Sanli, I., Seeger, H., Tealeb, A., Toksoz, M. N., and Veis, G. (2000). Global positioning system constraints on plate kinematics and dynamics in the eastern Mediterranean and Caucasus. *J. Geophys. Res.*, 105(3):5695–5719.
- McKenzie, D. and Jackson, J. (1983). The relationship between strain rates, crustal thickening, paleomagnetism, finite strain and fault movement within a deforming zone. *Earth Plan. Sci. Let.*, 65:182–202.
- McKenzie, D. and Jackson, J. (1986). A block model of distributed deformation by faulting. *J. Geol. Soc. Lond.*, 143:349–353.
- Miki, M., Furkawa, M., Otofujii, Y., Tsao, S., and Huang, T. (1993). Paleomagnetism and K-Ar ages of Neogene rocks of northern Taiwan: tectonics of the arc junction of Ryukyu and Luzon arcs. *Geophys. J. Int.*, 114:225–233.
- Miller, M. M., Johnson, D. J., Dixon, T. H., and Dokka, R. K. (2001). Refined kinematics of the Eastern California shear zone from GPS observations, 1993–1998. *J. Geophys. Res.*, 106:2245–2263.
- Moritz, H. (1989). *Advanced Physical Geodesy 2nd ed.* 500pp, Herber Wichman Verlage, Karlsruhe.
- Nalbant, S. S., Hubert, A., and King, G. C. P. (1998). Stress coupling between earthquakes in northwest Turkey and the north Aegean Sea. *J. Geophys. Res.*, 103(10):24,469–24,486.
- Nicholson, C., Seeber, L., Williams, P., and Sykes, L. R. (1986). Seismicity and fault kinematics through the eastern Transverse Ranges, California: Block rotation, strike-slip faulting and low-angle thrusts. *J. Geophys. Res.*, 91:4891–1908.
- Nyst, M. C. J. (2001). *A new approach to model the kinematics of crustal deformation with application to the Aegean and Southeast Asia*. PhD thesis, Technical University of Delft, Delft.
- Okada, Y. (1985). Surface deformation due to shear and tensile faults in a half-space. *Bulletin of the Seismological Society of America*, 75:1135–1154.
- Oldow, J. S., Aiken, C. L. V., Hare, J. L., Ferguson, J. F., and Hardyman, R. F. (2001). Active displacement transfer and differential block motion within the central Walker Lane, western Great Basin. *Geology*, 29(1):19–22.
- Parsons, T., Toda, S., Stein, R. S., Barka, A., and Dieterich, J. H. (2000). Heightened odds of large earthquakes near Istanbul: An interaction-based probability calculation. *Science*, 288:661–665.
- Peltzer, G., Crampe, F., and King, G. (1998). Evidence of non-linear elasticity of the crust from the M_w 7.6 Manyi (Tibet) earthquake. *Science*, 286:272–276.
- Peltzer, G. and Tapponnier, P. (1988). Formation and evolution of strike-slip faults, rifts, and basins during the India-Asia collision: An experimental approach. *J. Geophys. Res.*, 93(12):15,085–15,117.
- Rau, R.-J. (1996). *3-D seismic tomography, focal mechanisms and Taiwan orogeny*. PhD thesis, State univ. of N.Y., Binghamton.
- Rau, R.-J. and Wu, F. T. (1995). Tomographic imaging of lithospheric structures under Taiwan. *Earth Plan. Sci. Let.*, 133:517–532.
- Reilinger, R. E., Ergintav, S., Bürgmann, R., McClusky, S., Lenk, O., Barka, A., Gurkan, O., Hearn, L., Feigl, K. L., Cakmak, R., Aktug, B., Ozener, H., and Tökoş, M. N. (2000). Coseismic and postseismic fault slip for the 17 August 1999, $M=7.5$, Izmit, Turkey earthquake. *Science*, 289:1519–1524.
- Rocher, M., Lacombe, O., Angelier, J., and Chen, H.-W. (1996). Mechanical twin sets in calcite markers of recent collisional events in a fold-and-thrust belt: Evidence from the reefal limestones of southwestern Taiwan. *Tectonics*, 15:984–996.
- Rosen, P., Fielding, W. E., Hensley, S., Buckley, S., and Vincent, P. (1998). Aseismic

- creep along the San Andreas fault northwest of Parkfield, CA measured by radar interferometry. *Geophys. Res. Lett.*, 26:825–828.
- Rybicki, K. (1978). Static deformation of a laterally inhomogeneous half-space by a two-dimensional strike-slip fault. *J. Phys. Earth*, 26:351–366.
- Sass, J. H., Lachenbruch, A. H., Galanis Jr., S. P., Morgan, P., Priest, S. S., Moses Jr., T. H., and Munroe, R. J. (1994). Thermal regime of the southern Basin and Range province: 1. Heat flow data from Arizona and the Mojave Desert of California and Nevada. *J. Geophys. Res.*, 99(11):22,093–22,119.
- Sauber, J., Thatcher, W., Solomon, S. C., and Lisowski, M. (1994). Geodetic slip rate for the eastern California shear zone and the recurrence time of Mojave Desert earthquakes. *Nature*, 367:264–266.
- Savage, J. C., Lisowski, M., and Prescott, W. (1990). An apparent shearzone trending north-northwest across the Mojave Desert into Owens Valley. *Geophys. Res. Lett.*, 17:2113–2116.
- Savage, J. C., Lisowski, M., and Svarc, J. L. (1994). Postseismic deformation following the 1989 ($M_w = 7.1$) Loma Prieta, California, earthquake. *J. Geophys. Res.*, 99:13757–13765.
- Savage, J. C., Lisowski, M., Svarc, J. L., and Gross, W. K. (1995). Strain accumulation across the central Nevada seismic zone, 1973–1994. *J. Geophys. Res.*, 100:20257–20269.
- Savage, J. C., Prescott, W. H., and Gu, G. (1986). Strain accumulation in southern California, 1973–1984. *J. Geophys. Res.*, 91:7455–7473.
- Savage, J. C., Prescott, W. H., Lisowski, M., and King, N. E. (1979). Geodetic measurements of deformation near Hollister, California. *J. Geophys. Res.*, 84:7599–7615.
- Savage, J. C. and Svarc, J. L. (1997). Postseismic deformation associated with the 1992 $M_w = 7.3$ Landers earthquake, southern California. *J. Geophys. Res.*, 102:7565–7577.
- Savage, J. C., Svarc, J. L., Prescott, W. H., and Hudnut, K. W. (1998). Deformation following the 1994 Northridge earthquake ($M_w = 6.7$), southern California. *Geophys. Res. Lett.*, 25:2725–2728.
- Scharroo, R. and Visser, P. (1998). Precise orbit determination and gravity field improvement for the ERS satellites. *J. Geophys. Res.*, 103(4):8113–8127.
- Schulz, S. S., Mavko, G. M., Burford, R. O., and Stuart, W. D. (1982). Long-term fault creep observations in central California. *J. Geophys. Res.*, 87:6977–6982.
- Segall, P. and Harris, R. (1987). Earthquake deformation cycle on the San Andreas fault near Parkfield, California. *J. Geophys. Res.*, 92:10,511–10,525.
- Seno, T., Stein, S., and Gripp, A. E. (1993). A model for the motion of the Phillipine Sea Plate consistent with NUVEL-1 and geological data. *J. Geophys. Res.*, 98:17941–17948.
- Shen, Z.-K., Jackson, D. D., and Ge, B. X. (1996). Crustal deformation across and beyond the Los Angeles basin from geodetic measurements. *J. Geophys. Res.*, 101:27957–27980.
- Shen-Tu, B., Holt, W. E., and Haines, A. J. (1998). Contemporary kinematics of the western United States determined from earthquake moment tensors, very long baseline interferometry, and GPS observations. *J. Geophys. Res.*, 103:18087–18117.
- Shen-Tu, B., Holt, W. E., and Haines, A. J. (1999). Deformation kinematics in the western United States determined from Quaternary fault slip rates and recent geodetic data. *J. Geophys. Res.*, 104:28927–28955.
- Sibuet, J.-C., Letouzey, J., Charvet, J., Foucher, J.-P., Hilde, T. W. C., Kimura, M., Ling-Yun, C., Marsset, B., Muller, C., and Stephan, J.-F. (1987). Back arc extension

- in the Okinawa Trough. *J. Geophys. Res.*, 92:14,041–14,063.
- Snay, R. A., Cline, M. W., Philipp, C. R., Jackson, D. D., Feng, Y., Shen, Z.-K., and Lisowski, M. (1996). Crustal velocity field near the Big Bend of California's San Andreas fault. *J. Geophys. Res.*, 101:3173–3185.
- Spakman, W. and Nyst, M. C. J. (2002). Inversion of relative motion data for fault slip and continuous deformation in crustal blocks. *Earth Plan. Sci. Lett.*, 203:577–591.
- Stein, S. (1993). Space geodesy and plate motions. In Smith, D. and Turcotte, D., editors, *Contributions of space geodesy to geodynamics: crustal dynamics*, volume 23, pages 5–20. AGU.
- Stewart, J. H. (1971). Basin and Range structure: A system of horsts and grabens produced by deep-seated extension. *Geol. Soc. Am. Bull.*, 82:1019–1044.
- Straub, C. (1996). *Recent crustal strain accumulation in the Marmara Sea region, NW Anatolia, inferred from GPS measurements*. PhD thesis, Eidgenössischen Technischen Hochschule, Institut für Geodäsie und Photogrammetrie, Zürich.
- Suppe, J. (1981). Mechanics of mountain building and metamorphism in Taiwan. *Mem. Geol. Soc. China*, 4:67–89.
- Suppe, J. (1984). Kinematics of arc-continent collision, flipping of subduction, and back-arc spreading near Taiwan. *Mem. Geol. Soc. China*, 6:21–33.
- Teng, L. S. (1990). Geotectonic evolution of late Cenozoic arc-continent collision. *Tectonophysics*, 183:57–76.
- Teng, L. S. (1996). Extensional collapse of the northern Taiwan mountain belt. *Geology*, 24:949–952.
- Teng, L. S., Lee, C. T., Tsai, Y. B., and Hsiao, L.-Y. (2000). Slab breakoff as a mechanism for flipping of subduction polarity in Taiwan. *Geology*, 28:155–158.
- Thatcher, W., Foulger, G. R., Julian, B. R., Svarc, J., Quilty, E., and Bawden, G. W. (1999). Present-day deformation across the Basin and Range province, western United States. *Science*, 283:1714–1718.
- Thatcher, W. and Hanks, T. C. (1973). Source parameters of southern Californian earthquakes. *J. Geophys. Res.*, 78:8547–8576.
- Tsai, Y. B. (1986). Seismotectonics of Taiwan. *Tectonophysics*, 125:17–37.
- Unruh, J. R. and Lettis, W. R. (1998). Kinematics of transpressional deformation in the eastern San Francisco Bay region, California. *Geology*, 26(1):19–22.
- Van de Zedde, D. M. A. and Wortel, M. J. R. (2001). Shallow slab detachment as a transient source of heat at midlithospheric depths. *Tectonics*, 20(6):868–882.
- Wald, D. J. and Graves, R. W. (2001). Resolution analysis of finite fault source inversion using one- and three-dimensional Green's functions 2. Combining seismic and geodetic data. *J. Geophys. Res.*, 106(5):8767–8788.
- Wang, R., Martín, F. L., and Roth, F. (2003). Computation of deformation induced by earthquakes in a multi-layered elastic crust – FORTRAN programs EDGRN/EDCMP. *Computers & Geosciences*, 29:195–207.
- Ward, S. N. (1998). On the consistency of earthquake moment rates, geological fault data and space geodetic strain: the United States. *Geophys. J. Int.*, 134:172–186.
- Wdowinski, S., Sudman, Y., and Bock, Y. (2001). Geodetic detection of active faults in Southern California. *Geophys. Res. Lett.*, 28:2321–2324.
- Wernicke, B., Friedrich, A. M., Niemi, N. A., Bennett, R. A., and Davis, J. L. (2000). Dynamics of plate boundary fault systems from Basin and Range geodetic network BARGEN and geological data. *GSA Today*, 10(11):1–7.
- WGCEP, Working Group on California Earthquake Probabilities (1995). Seismic Hazards in Southern California: Probable Earthquakes, 1994 to 2024. *Bulletin of the Seismological Society of America*, 85:379–

- 439.
- Wong A Ton, S. Y. M. and Wortel, M. J. R. (1997). Slab detachment in continental collision zones: An analysis of controlling parameters. *Geophys. Res. Lett.*, 24(16):2095–2098.
- Wortel, M. J. R., Remkes, M. J. N., Govers, R., Cloethingh, S. A. P. L., and Meijer, P. T. (1991). Dynamics of the lithosphere and the intraplate stress field. *Phil. Trans. R. Soc. A.*, 337:111–126.
- Wortel, M. J. R. and Spakman, W. (1992). Structure and dynamics of subducted lithosphere in the Mediterranean region. *Proc. Kon. Ned. Akad. v. Wetensch.*, 95:325–347.
- Wortel, M. J. R. and Spakman, W. (2000). Subduction and slab detachment in the Mediterranean-Carpathian region. *Science*, 290:1910–1917.
- Wu, F. T., Rau, R.-J., and Salzberg, D. (1997). Taiwan orogeny: Thin skinned or lithospheric collision? *Tectonophysics*, 274:191–220.
- Yagi, Y. and Kikuchi, M. (2000). Source rupture of the Kocaeli, Turkey, earthquake of August 17, 1999, obtained by joint inversion of near-field data and teleseismic data. *Geophys. Res. Lett.*, 27(13):1969–1972.
- Yeh, Y.-H., Lin, C.-H., and Roecker, S. W. (1989). A study of upper crustal structures beneath northeastern Taiwan: Possible evidence of the western extension of Okinawa Trough. *Proc. Geol. Soc. China*, 32:139–156.
- Yen, H.-Y., Yeh, Y.-H., and Wu, F. T. (1998). Two-dimensional crustal structures of Taiwan from gravity data. *Tectonics*, 17:104–111.
- Yu, S.-B. and Chen, H. Y. (1998). Strain accumulation in southwestern Taiwan. *TAO*, 9:31–50.
- Yu, S.-B., Chen, H. Y., and Kuo, L. C. (1997). Velocity field of GPS stations in the Taiwan area. *Tectonophysics*, 274:41–59.
- Yu, S.-B., Jackson, D. D., Yu, G. K., and Liu, C. C. (1990). Dislocation model for crustal deformation in the Longitudinal Valley area, eastern Taiwan. *Tectonophysics*, 183:97–109.
- Yu, S.-B. and Kuo, L. C. (2001). Present-day crustal motion along the Longitudinal Valley fault, eastern Taiwan. *Tectonophysics*, 333:199–218.
- Zoback, M. L. (1989). State of stress and modern deformation of the northern Basin and Range province. *J. Geophys. Res.*, 94(6):7105–7128.

Appendix A

South-Western US Deformation Zone.

A.1 Comparison to geological and present-day interseismic slip rates

In their synthetic tests Spakman and Nyst (2002) inferred that a basic trade-off may exist between fault slip rate and the velocity gradient solution. The trade-off is a direct result of the lack of physical constraints that couple fault motion to continuous deformation in a pure kinematic inversion of velocity data. The trade-off is best resolved when relative motion observations exist close to the fault zones. If this is not the case, fault motion may in part reflect motions across a locked fault. I note that this trade-off problem exists for any inversion method of relative motion data, since it is caused by lack of data. In solution I I explicitly attempt to resolve crustal block behavior, while solution III is more sensitive to the trade-off. If the trade-off is well resolved, the magnitude of near surface creep could match the Holocene fault slip rates for faults that are completely unlocked. Holocene fault slip rates have been determined for most faults in California and the Wasatch fault zone. Table B.2 quotes the geological rates for the fault segments modeled, as well as the rates obtained in solutions I and III. Both solutions do quite well in recovering the general sense of motion of the faults. Significant differences occur in solution III for the Pinto Mountain fault, the Santa Ynez fault and the Big Pine fault. Geologically these faults are found to be slipping sinistrally at rates of 0-5.3 mm/yr, 1.0-3.0 mm/yr 1.0-7.0 mm/yr, respectively, whereas solution III resolves dextral motion of 0.7-3.3 mm/yr, 0.6-1.7 mm/yr and 0.4 mm/yr, respectively. This difference could be the result of the afore mentioned trade-off.

Though solution I underestimates the geological slip rates on fast slipping faults, it systematically overestimates the rates on slower slipping faults (again on a geological time scale). This combined with the poor fit to the data leads me to conclude that the

representation of crustal deformation by pure block rotation and fault motion proves inadequate. The surface deformation field obtained in solution I is dominated by lateral translation rather than block rotation. The fault motions of solution III are generally smaller than the geological observations, except for very slow faults ($\sim 1 \text{ mm yr}^{-1}$), which is indicative for fault loading.

Present-day interseismic observations show an almost freely creeping segment on the SAF between the SAF-Calaveras junction and Parkfield ($\sim 35 \text{ mm/yr}$ Langbein, 2002; Rosen et al., 1998) and a locked SAF south of Parkfield through the Big Bend (Langbein, 2002; Schulz et al., 1982). Solution III shows significant fault motion on the Big Bend segments of the SAF ($2.3 - 6.0 \text{ mm/yr}$) and reduced motion north of Parkfield ($\sim 20 \text{ mm/yr}$). Around San Francisco, Lienkaemper et al. (1991) obtained historic creep rates for the San Andreas, Hayward and Calaveras faults. They deduced no historic creep rates for the San Andreas fault, $4 - 6 \text{ mm/yr}$ on the Hayward fault, $0 - 5 \text{ mm/yr}$ on the northern Calaveras, and $9 - 12 \text{ mm/yr}$ on the southern Calaveras fault. I obtain $\sim 14 \text{ mm/yr}$, $\sim 6 \text{ mm/yr}$, $\sim 5 \text{ mm/yr}$ and $\sim 10 \text{ mm/yr}$, respectively. Except for the San Andreas fault my rates in solution III compare well with the historic creep rates. The dense BARD network across the Hayward and Calaveras faults provides the necessary control of the solution trade-off. This may not be the case along the San Andreas fault in central California because of lack of near-fault stations. Lyons and Sandwell (2003) inferred interseismic creep rates for the southern San Andreas fault from 60 InSAR interferograms. Our rates of $6 - 8.4 \text{ mm/yr}$ are at the lower end of their estimates of $5 - 20 \text{ mm/yr}$. This could be due to neglecting the contribution of vertical deformation to the InSAR range-change (2.7 mm/yr ; Lyons and Sandwell, 2003), as well as tropospheric, orbital and topographic errors still contained in the images.

Summarized, I find that the sense of motion of both solutions are generally in agreement with the geological observations. Trade-off between estimates of the velocity gradient and fault slip rates requires a careful interpretation of the magnitudes of the slip rate solutions even in regions with a dense station coverage. The trade-off is well resolved in regions with stations in close proximity of both sides of the fault.

A.2 Comparison of solution II to related work

Several studies of the crustal deformation field of different regions of the SWUSDZ have been undertaken since the middle 1980's. These studies are based on geodetic data, such as GPS, VLBI, trilateration and triangulation, and solve only for the velocity gradient tensor. In the study by Ward (1998) the velocity gradient tensor of the US is determined by a weighted inversion of velocity data. On average, his data set is sparser than mine but in southern California the data sets are of comparable density. Here both the magnitude and pattern of his maximum horizontal strain rate field compare well with my estimates in solution II. In the Basin and Range and in central California

network	Savage <i>et al</i> [1986]			Solution II		
	$\dot{\epsilon}_1$ $10^{-6}yr^{-1}$	$\dot{\epsilon}_2$ $10^{-6}yr^{-1}$	ω Degrees	$\dot{\epsilon}_1$ $10^{-6}yr^{-1}$	$\dot{\epsilon}_2$ $10^{-6}yr^{-1}$	ω Degrees
Salton Trough	0.18±0.01	-0.16±0.01	N85°W	0.30±0.01	-0.27±0.01	N95.7°W
Anza	0.15±0.01	-0.15±0.01	N89°E	0.13±0.01	-0.13±0.01	N83.5°E
Cajon	0.16±0.03	-0.19±0.02	N74°E	0.11±0.02	-0.13±0.02	N80.7°E
Tehachapi	0.16±0.01	-0.12±0.01	N78°E	0.10±0.01	-0.12±0.01	N79.9°E
Los Padres	0.12±0.01	-0.14±0.01	N89°E	0.08±0.01	-0.07±0.01	N92.5°E

Table A.1: *Principal strain rates of Savage et al [1986] and the average principal strain rates determined from solution II.*

I obtain more detail in the deformation patterns due to my increased data density in these regions and, perhaps, differences in modeling techniques. Shen-Tu et al. (1998, 1999) invert average strain rates and geodetic data for the horizontal velocity field on the Earth's surface. The average strain rates used as data are first derived through Kostrov's relation (Kostrov, 1974) from seismic moment tensors or geological data. The average strain rates remain unspecified in case only the geodetic observations are to be fit (Shen-Tu et al., 1999). Since in both cases their model parameterization is quite smooth compared to mine I can only inspect correlation of the main features of the strain rate field. I compared the average principal axes of the strain rates for each grid area of Shen-Tu et al. (1998) and Shen-Tu et al. (1999), respectively, with my principal strain rates calculated at those points. I find reasonable comparison in the directions of the axes. However, I find significant differences in magnitude, particularly east of the SAF between the Transverse Ranges and San Francisco. I believe this to be a direct result of the differences in modeling techniques applied.

Solution II compares very well to the results of Snay et al. (1996) for the Big Bend area of the San Andreas fault and to the study of Shen et al. (1996) of the Los Angeles Basin. Both studies use data covering a broader time span (up to a century) resulting in large contractional strain rates around the Garlock fault, White Wolf fault and the Ventura Basin. This is comparable with my results for these regions in solution II. Both studies also show the corresponding rotation rates. Consistent with solution II they show significant clockwise rotations along the Big Bend section of the San Andreas fault, in the San Gabriel Mountains, around the northern San Jacinto fault and the San Juan section of the San Andreas fault. Savage et al. (1986) determined strain rates within several trilateration networks in southern California. Table A.1 lists the principal strain rates determined for each network and those determined from solution II. I observe a fair agreement between the two solutions, though I obtain slightly higher magnitudes in the Salton Through network.

In conclusion I find that many regional aspects of the deformation field of solution II have been determined in earlier studies based on geodetic data. It is difficult to indicate the extent of the discrepancies resulting from differences in methodology between

the various approaches. However, most differences can be attributed to differences in data density, origin and time span of the data and differences in modeling techniques. I note that significant differences between these earlier studies and solution III exist and are a direct result of the implementation of fault motion in my methodology.

A.3 Postseismic deformation

Considering the occurrence of several large ($M_w > 5.5$) earthquakes in my study region during the time span of my data, e.g. Landers ($M_w = 7.3$), Loma Prieta ($M_w = 7.1$) and Northridge ($M_w = 6.7$), the question is raised to what extent the solutions are influenced by postseismic relaxation. Postseismic deformation would constitute a time-dependent signal in the GPS data, which is not modeled in my present approach. In case of larger events, GPS based postseismic deformation studies have been undertaken. Savage and Svarc (1997) identified a long-term postseismic relaxation signal (>5 years) associated with the 1992 Landers event. During the 3.4 year study interval, they determined long-term principal strain rates of $0.44 \pm 0.04 \mu\text{strain/yr}$ in direction $N64^\circ W \pm 7^\circ$ and $-0.39 \pm 0.09 \mu\text{strain/yr}$ in direction $N26^\circ E \pm 7^\circ$. In solution II I obtain principal strain rates of $0.227 \pm 0.001 \mu\text{strain/yr}$ in direction $N70^\circ W \pm 1^\circ$ and $-0.167 \pm 0.001 \mu\text{strain/yr}$ in direction $N20^\circ E \pm 1^\circ$, respectively. The directions of the principal axes concur well. The slight deviation in magnitude can be explained by the longer time interval spanned by my dataset (>5 years). Both the magnitudes and directions of principal strain rate of solution II deviate from the pre-earthquake strain accumulation rates of $0.07 \pm 0.02 \mu\text{strain/yr}$ in direction $N80^\circ W \pm 5^\circ$ and $-0.07 \pm 0.02 \mu\text{strain/yr}$ in direction $N10^\circ E \pm 5^\circ$ (Sauber et al., 1994; Savage et al., 1995). However, my strain rate estimates may show a return to these strain accumulation rates.

The postseismic GPS observations of the 1994 Northridge quake show no long-term relaxation effects (Savage et al., 1998). Since my data in the vicinity of the event mostly consists of campaign stations with annual observations, the velocity estimates could only be slightly affected by the short-term signal (few weeks) and my inversion solutions represent interseismic deformation. Savage et al. (1994) determined that the postseismic adjustment following the 1989 Loma Prieta event was nearly completed during their 3.3 year study interval. Our data in the Bay area comprises the time span 1996-2000. Therefore, the data and my solutions are unaffected by this earthquake.

Of several other significant earthquakes the postseismic deformation signals remain unstudied. However, postseismic relaxation of these events may affect my solutions in the ECSZ, the western Transverse Ranges, along the Parkfield segment of the San Andreas fault and at Salton Through.

A.4 Surface deformation field of the Basin and Range province

The surface deformation field in the northern Basin and Range does not reflect a clear uniform style of deformation (figure A.1A). The principal axes of my strain rate field rotate over large angles across small distances. Generally, the deformation field is an order of magnitude less in amplitude than that of the Californian shear zone. In the eastern Basin and Range, east of the Wasatch fault, significant E-W extension towards the fault is obtained. West of the Wasatch fault the dominant regime is E-W contraction, while the Wasatch fault obtains left-lateral thrust motion. Geologically, this fault is known as a normal fault (Shen-Tu et al., 1999). Towards the center of the northern Basin and Range, a north-south variation of NNW-SSE contraction followed by a NNW-SSE extension is observed. In the western Basin and Range the pattern of deformation becomes more coherent with NW-SE extension dominated right-lateral shear. The principal axis direction of extension is consistent with geological and earthquake focal mechanism observations (Zoback, 1989).

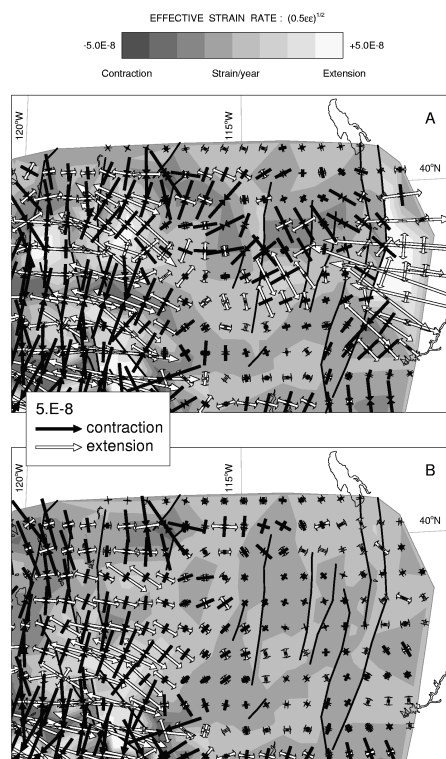


Figure A.1: Detail of the strain rate field in the Basin and Range for A) solution III and b) a solution excluding the campaign dataset of Thatcher et al. [1999] in the Basin and Range province.

Although the spatial distribution of deformation in the Basin and Range remains debated, general consensus exists on the fact that it is dominated by NW-SE extension (Bennett et al., 1999, 2002; Flesch et al., 2000; King et al., 1994; Lachenbruch et al., 1994; Thatcher et al., 1999). In order to understand the discrepancy between my model and this consensus I first take a closer look at the data in the Basin and Range.

So far, 26 continuous GPS stations have been operating in the northern Basin and Range. Besides these continuously operating stations, my dataset comprises the campaign data of Thatcher et al. (1999), which provides a dense crosssection across the northern Basin and Range. Figure A.2 shows the EW and NS components of the velocity estimates of this crosssection, as well as the velocity estimates of the 10 CGPS stations located along the crosssection. Between longitudes 241.5°E and 243°E the EW-component of the campaign estimates are significantly smaller than the CGPS estimates. At first sight, the NS-component shows a consensus between the campaign data and the CGPS data. However, east of 243°E the campaign data obtains an almost

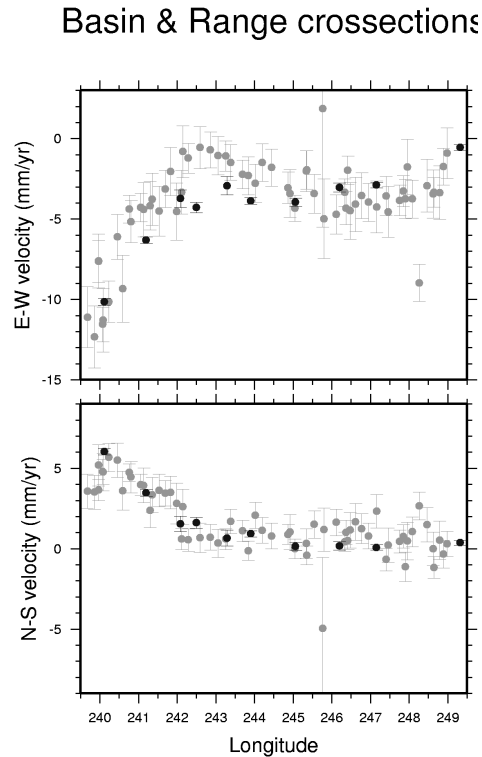


Figure A.2: Velocity profile across the Basin & Range. Light grey dots are the NBAR velocity rates of Thatcher et al. [1999], black dots are the CGPS velocity rates. The error bars represent the 1-sigma data error.

sinusoidal pattern not observed in the CGPS. Inspection of the campaign data indicates that the majority of these stations have only been observed twice or thrice. Therefore, site instabilities or other site related problems may affect the data thus introducing a pattern not caused by the deformation of the region. In the fall of 2002 reobservation of the NBAR stations was undertaken. Preliminary results of this campaign show an improvement in the velocity estimates at the stations and the disappearance of the sinusoidal pattern. Unfortunately, the data is not yet available and can not be implemented in this research.

Question remains to what extent this pattern affects my model. Bennett (2003) inferred that the NBAR data set had little influence on their estimations of strain rate within the Basin and Range. However, their direct interpretation of the slope portrayed by the data is significantly different from my method. I tested the effect of the large scatter in the Basin and Range data on the solution by performing an inversion without the NBAR data set (only retaining the CGPS stations). Figure A.1B shows the result. The north-south dominance in the deformation patterns has been replaced by east-west patterns, which concurs more with the general consensus on the deformation of the region. The large extension observed east of the Wasatch fault zone has disappeared, thus was caused by the campaign data set. Deformation seems to localize in the western Great Basin, west of 245°E . I have also observed a significant reduction in strain rates in the southern Basin and Range indicating a significant influence of the NBAR data set on the deformation field in this sparsely sampled region. Unfortunately, the majority of the amplitudes have been reduced to insignificance on a 95% confidence level, so no further interpretation is possible.

Appendix B

Fault slip rates SWUSDZ.

Table B.1: Fault names corresponding to the fault segment numbers used in solutions I and III (section 2.6).

fault name	segment num.	fault name	segment num.
San Andreas	1-22	Calaveras	23-32
Hayward	25,26	Rogers Creek	27,28
Headsburg	29,30	Concord/Green Valley	33,34
Paicines	35,36	Garlock	37-42
Rinconda	43-46	Death Valley	47-50
Furnace Creek	51-54	Fish Lake Valley	55,56
Panamint Valley	57-60	Hunter Mountain	61-64
Little Lake	65,66	Owens Valley	67-72
White Mountain	73,74	Fish Springs/Round Valley	75,76
Hilton Creek/Hartley Springs	77,78	Mono Lake	79,80
Sierra Nevada Range Front	81-94	Imperial Valley	95-98
San Jacinto	99-104	Laguna Salada	105-108
Elsinore	109-114	Big Pine	115-118
Palos Verdes	119-124	Agua Blanca	125-128
Newport Inglewood	129-132	San Gabriel	133-136
Pinto Mountain	137-140	Blackwater	141,142
Pisgah	143-146	Gravel Hill	147,148
Camp Rock	149-152	Frontal	153-158
Lockheart	159-164	Helendale	165-168
Calico	169-172	San Juan	173-176
Arroya Prida	177-180	Santa Ynez	181-186
Oak Ridge	187-190	White Wolf	191-194
Red Mountain	195-198	Santa Monica	199-202
San Miguel	203-206	San Pedro Matir	207,208
Cerro Prieto	209-212	Basin & Range	213-268
Wasatch	269-280	Basin & Range	281-292

Table B.2: Geological rates for all fault segments modeled and the rates obtained in solutions I and III (section 2.6).

segm. num.	rake*	geological ^a		solution I		solution III	
		min.-max.	rate [†] pref.	rake*	rate [†]	rake*	rate [†]
1-4	180	12.0-30.0	20.0	163.5-185.4	12.1-15.7	174.9-184.9	13.6-15.0
5-10	180	31.0-36.8	33.9	172.7-182.3	17.2-29.0	178.7-188.3	7.3-21.0
11,12	180	27.5-36.0	31.0	155.6,162.6	20.8,14.7	171.9,178.8	6.0,4.9
13,14	180	24.0-36.0	30.0	171.6,157.7	12.0,7.4	193.5,191.5	3.4,2.3
15-18	180	19.0-30.0	24.5	119.1-171.8	5.8-10.2	149.5-174.3	2.3-3.9
19-22	180	10.0-35.0	29.0	172.5-196.4	13.0-20.0	182.7-199.3	6.0-8.4
23,24	180	7.0-17.0	15.0	192.3,191.0	19.0,16.4	188.3,189.3	10.5,10.3
31,32	180	4.0-8.0	6.0	194.9,189.7	8.3,8.6	189.7,183.3	5.1,5.1
25,26	180	7.0-11.0	9.0	180.0,180.1	6.8,8.0	186.6,183.0	4.8,7.1
27,28	180	7.0-10.5	9.0	193.8,198.5	6.7,5.8	193.8,198.5	6.7,5.7
29,30	180	0.0-8.0	1.0	39.8,214.5	3.1,1.3	191.4,196.2	3.9,4.6
33,34	180	4.0-8.0	6.0	196.2,202.4	11.6,13.9	195.3,197.1	7.6,10.1
35,36	180	5.0-13.0	9.0	185.9,185.7	14.4,17.0	181.1,184.5	13.4,16.0
37,38	0	1.0-3.0	2.0	34.7,37.8	6.7,9.2	47.7,30.4	0.6,0.6
39,40	0	4.0-9.0	6.5	34.3,9.3	8.3,8.8	12.4,327.8	0.4,0.8
41,42	0	3.0-9.0	6.0	11.4,358.3	4.5,4.7	339.8,306.2	0.6,0.7
43-46	180	1.0-5.0	3.0	102.8-182.8	1.0-3.3	157.7-238.4	0.1-1.6
47-50	180	0.2-3.2	2.6	187.6-209.6	3.0-4.7	165.1-177.7	1.2-1.5
51-54	180	5.0-12.0	8.5	155.0-164.8	3.1-4.0	143.2-183.6	1.5-1.8
55,56	180	2.0-6.0	4.0	169.3,171.1	3.6,2.9	204.7,205.6	1.8,1.0
57-60	180	1.7-3.2	2.4	255.2-270.6	1.5-4.7	13.3-186.5	0.1-0.5
61-64	180	1.7-3.2	2.4	146.1-176.9	1.0-2.3	201.4-342.4	0.3
65,66	180	1.0-3.0	2.0	225.3,230.1	2.3,4.2	231.6,228.9	0.7,1.7
67-72	180	1.0-3.0	2.0	226.6-256.5	3.2-6.1	199.2-239.9	1.7-3.2
73,74	180	0.5-1.2	0.8	243.9,237.0	3.1,2.9	227.9,234.3	1.8,1.2
75,76	270	0.1-1.4	0.7	197.0,192.3	2.2,4.1	316.4,331.6	0.3,0.2
77,78	270	1.3-2.6	2.0	176.3,179.2	5.4,5.5	298.1,234.9	0.2,0.3
79,80	270	1.8-3.3	2.5	183.4,181.9	4.4,3.5	193.6,200.3	0.3,0.2
81-86	225	0.0-4.6	2.3	189.8-219.2	2.4-7.7	161.0-235.8	0.9-2.1
87-94	225	0.0-4.6	2.3	256.7-326.3	1.9-4.3	226.8-287.5	1.3-4.2
95-98	180	20.0-40.0	35.0	173.7-180.6	15.2-24.8	173.3-178.9	11.9-18.9
99,100	180	8.0-24.0	12.0	198.9,198.4	11.0,11.9	165.6,217.9	1.2,2.2
101-104	180	1.7-6.1	4.0	148.4-178.3	11.1-13.4	176.8-196.1	3.3-4.5
105-108	180	1.0-7.0	4.0	187.4-210.3	6.9-10.5	219.6-226.4	3.1-4.1
109-112	180	1.3-9.3	5.6	144.9-185.5	3.2-5.8	196.1-245.4	0.2-2.1
113,114	180	1.0-7.0	4.0	183.0,178.8	4.8,5.0	187.4,185.4	3.0,2.9
115-118	0	1.0-7.0	4.0	309.1-319.5	2.2-3.0	186.3-223.7	0.4-0.5
119-124	135	0.1-6.0	3.0	104.3-234.6	2.0-6.5	49.3-189.4	1.1-3.2
125-128	135	2.0-6.0	4.0	87.8-182.9	1.0-2.1	62.9-159.0	0.5-1.8
129-132	180	0.3-1.2	0.7	188.0-197.6	1.6-4.6	187.4-203.3	1.6-3.9
133,134	90	0.5-5.6	3.0	185.4,174.0	2.1,3.0	174.7,184.0	0.6,0.8
135,136	90	0.0-1.4	0.7	199.9,198.3	4.1,4.3	192.4,201.6	0.8,0.7
137-140	0	0.3-5.3	2.8	16.3-359.8	7.7-11.1	122.6-128.7	1.3-5.8
141,142	180	0.4-4.8	2.6	197.0,183.7	2.7	207.3,197.2	0.6,0.9

Table B.2: continued

segm. num.	rake*	geological ^a rate [†]		solution I		solution III	
		min.-max.	pref.	rake*	rate [†]	rake*	rate [†]
143-146	180	0.0-1.6	0.8	148.5-177.7	1.7-3.2	174.8-234.8	1.0-1.9
147,148	180	0.2-1.6	0.9	172.4,167.7	2.5,4.0	157.6,158.4	1.5,2.9
149-152	180	0.1-2.0	1.0	167.7-197.1	6.0-8.7	170.1-188.6	4.9-6.8
153-158	45	0.3-15.0	1.3	18.1-372.8	3.9-5.6	30.0-139.9	0.7-3.1
159-164	180	0.1-1.5	0.8	169.3-215.3	3.3-5.7	197.7-216.7	0.7-3.5
165-168	180	0.2-1.5	0.8	149.2-165.9	2.2-2.7	61.5-76.2	1.1-2.0
169-172	180	0.4-4.8	2.6	195.0-212.9	3.6-10.6	23.4-154.8	0.7-2.4
173-176	180	1.0-5.0	3.0	173.0-201.0	3.1-4.2	181.1-205.4	2.1-3.5
177,178	45	0.5-0.6	0.5	45.7,19.8	1.2,2.6	105.8,99.3	1.0
179,180	90	0.2-0.4	0.3	55.8,53.3	3.2,0.9	105.2,75.9	1.6,0.5
181-186	0	0.1-3.0	2.0	16.1-66.3	2.9-4.7	95.6-133.3	1.4-4.2
187-190	90	8.4-17.5	13.0	41.2-355.9	3.2-3.8	84.3-106.6	0.5-1.0
191-194	90	0.0-3.0	2.0	67.7-72.3	2.4-3.0	108.3-146.7	0.1-0.5
195-198	90	2.0-14.4	10.4	11.4-50.7	3.1-4.6	37.0-99.4	0.2-1.0
199-202	45	0.0-5.0	2.0	67.5-112.3	1.9-4.8	34.9-77.1	0.2-1.2
203-206	180	0.0-6.0	3.0	170.2-239.8	1.5-3.1	186.5-238.2	1.7-5.3
207,208	225	2.0-8.0	5.0	201.7,198.4	5.0,4.0	207.8,197.6	5.8,4.2
209-212	180	31.0-51.0	41.0	179.4-184.0	22.3-36.2	179.2-186.3	15.1-35.4
213-220	225	0.0-2.0	1.0	72.9-222.3	0.4-2.3	132.8-265.5	0.1-1.6
221-226	225	0.0-2.0	1.0	174.3-266.4	2.4-2.9	164.7-310.5	0.3-0.6
227-230	225	0.0-2.0	1.0	41.7-335.8	0.5-0.6	73.0-343.4	0.1-0.3
231-238	225	0.0-2.0	1.0	204.7-276.6	0.7-5.3	188.0-229.8	0.3-0.9
239-246	225	0.0-2.0	1.0	37.77-377.3	0.2-0.5	21.9-349.2	0.1-0.9
247-250	225	0.0-2.0	1.0	19.3-43.3	1.0-1.3	122.4-309.8	0.1-0.2
251-262	225	0.0-2.0	1.0	136.0-230.0	0.8-4.1	66.6-328.2	0.3-1.0
263-268	225	0.0-2.0	1.0	11.6-334.0	0.3-0.9	230.1-275.5	0.1-0.8
281-286	225	0.0-2.0	1.0	7.4-108.1	0.2-0.4	20.2-76.1	0.2-0.4
287-292	225	0.0-2.0	1.0	213.3-319.9	0.5-1.4	214.0-260.8	0.3-1.1
269-280	270	0.5-2.8	1.4	22.5-348.3	0.7-3.1	23.6-332.7	0.4-4.2

^a Geological fault slip rates have been taken from *Shen-Tu et al* [1999] and references therein.

* Rake of the fault in degrees.

[†] Total fault slip rates in mmyr^{-1} .

Appendix C

Colour figures.

C.1 South-western US deformation zone

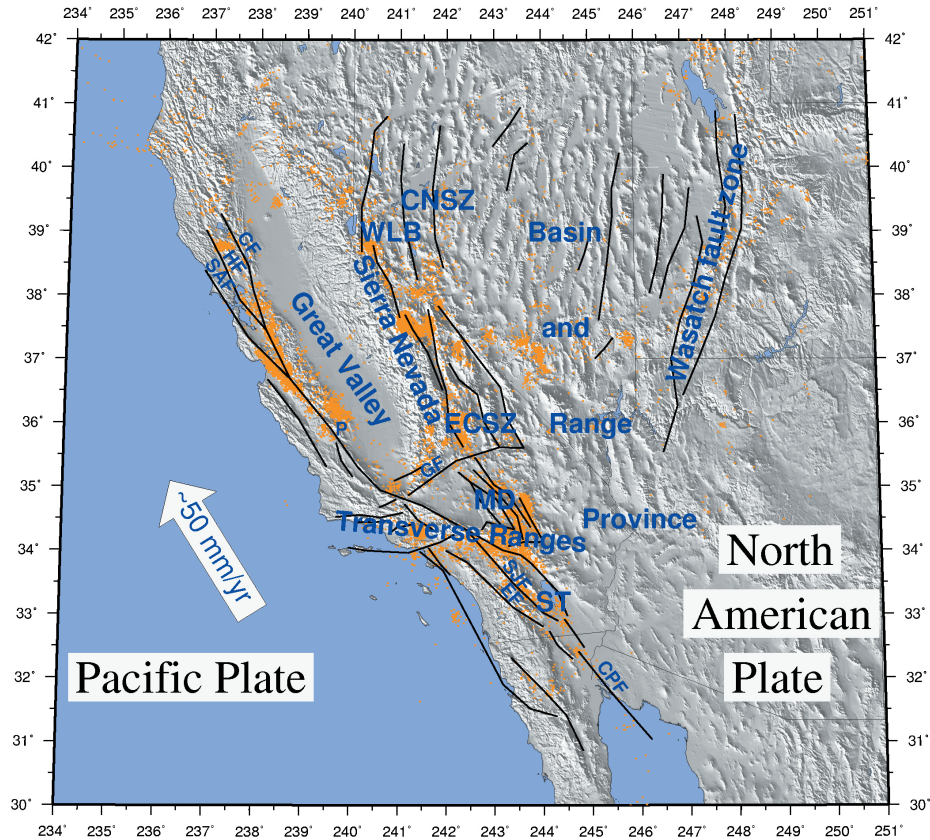


Figure C.1: Tectonic setting of the southwestern US deformation zone plotted against topography. Black lines indicate the fault traces utilized in our model parameterization. Orange dots indicate the shallow (< 20km) relocated seismicity of Engdahl et al. [1998]. MD: Mojave Desert; ST: Salton Through; ECSZ: eastern California shear zone; CNSZ: central Nevada seismic zone; WLB: Walker Lane belt; SAF: San Andreas fault; HF: Hayward fault; CF: Calaveras fault; GF: Garlock fault; SJF: San Jacinto fault; EF: Elsinore fault; CPF: Cerro Prieto fault; P: Parkfield.

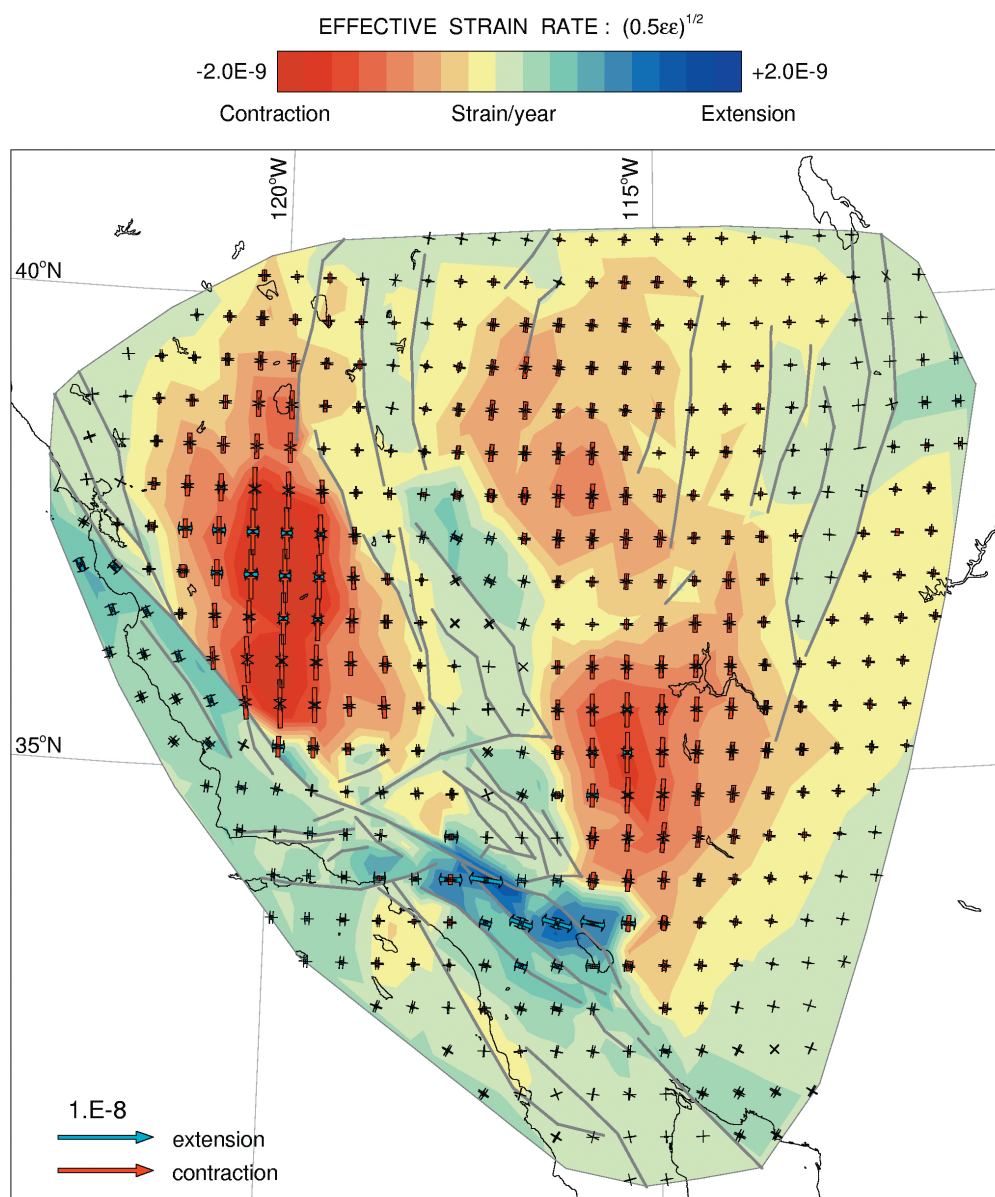


Figure C.2: Strain rate contribution of solution I. The arrows denote the principal strain rates: contraction (red) and extension (blue).

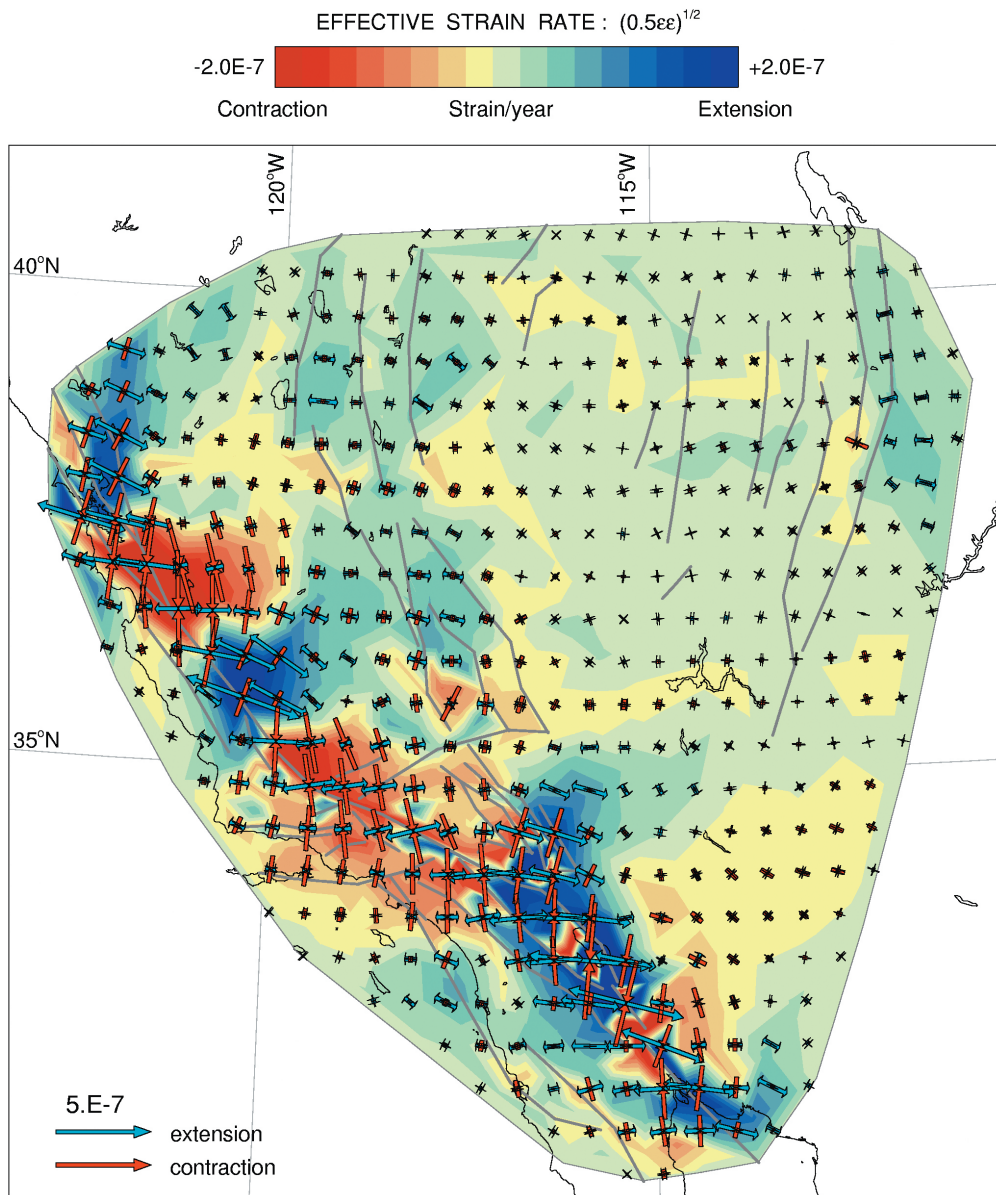


Figure C.3: Strain rate contribution of solution II. The arrows denote the principal strain rates: contraction (red) and extension (blue).

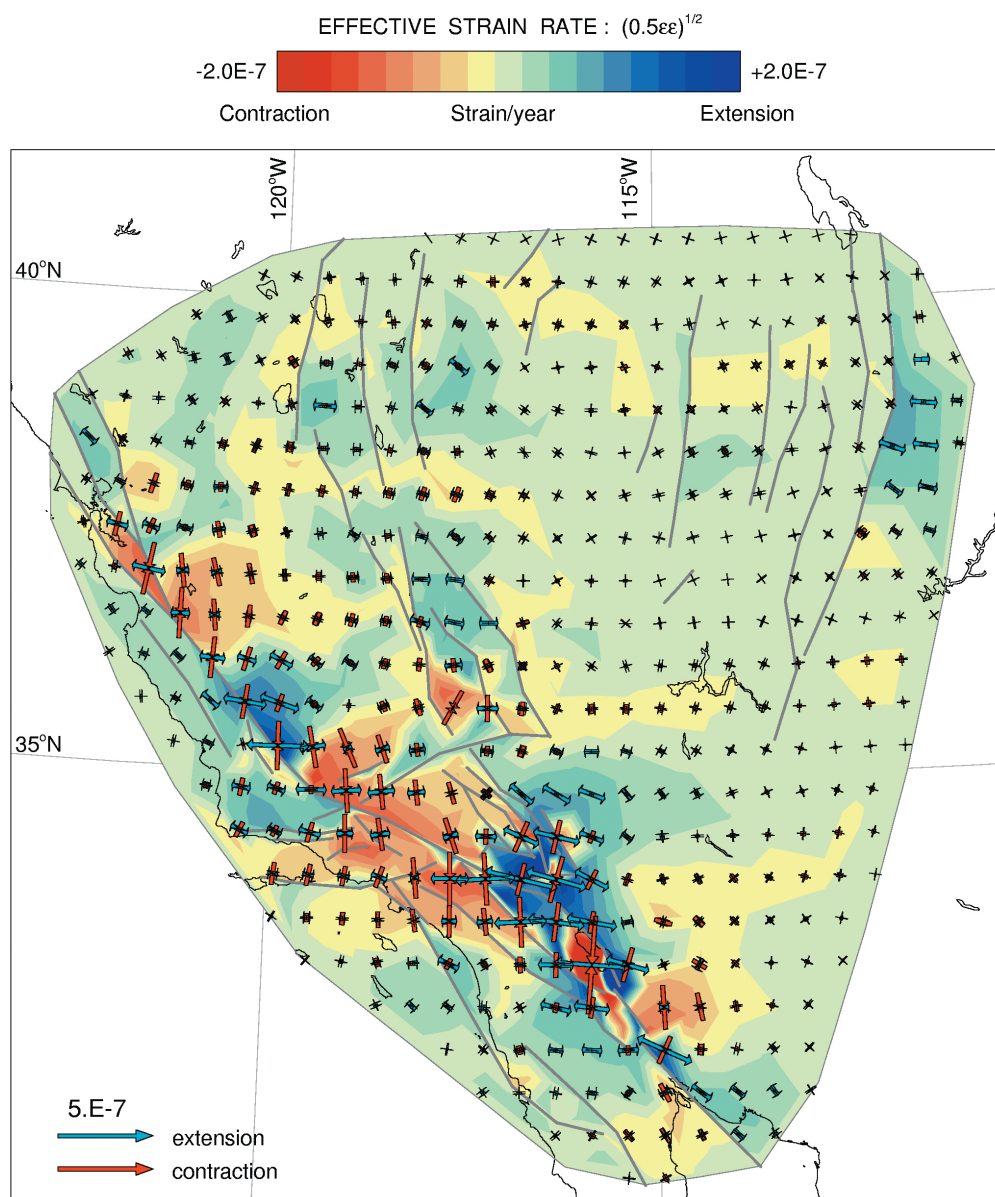


Figure C.4: Strain rate contribution of solution III. The arrows denote the principal strain rates: contraction (red) and extension (blue).

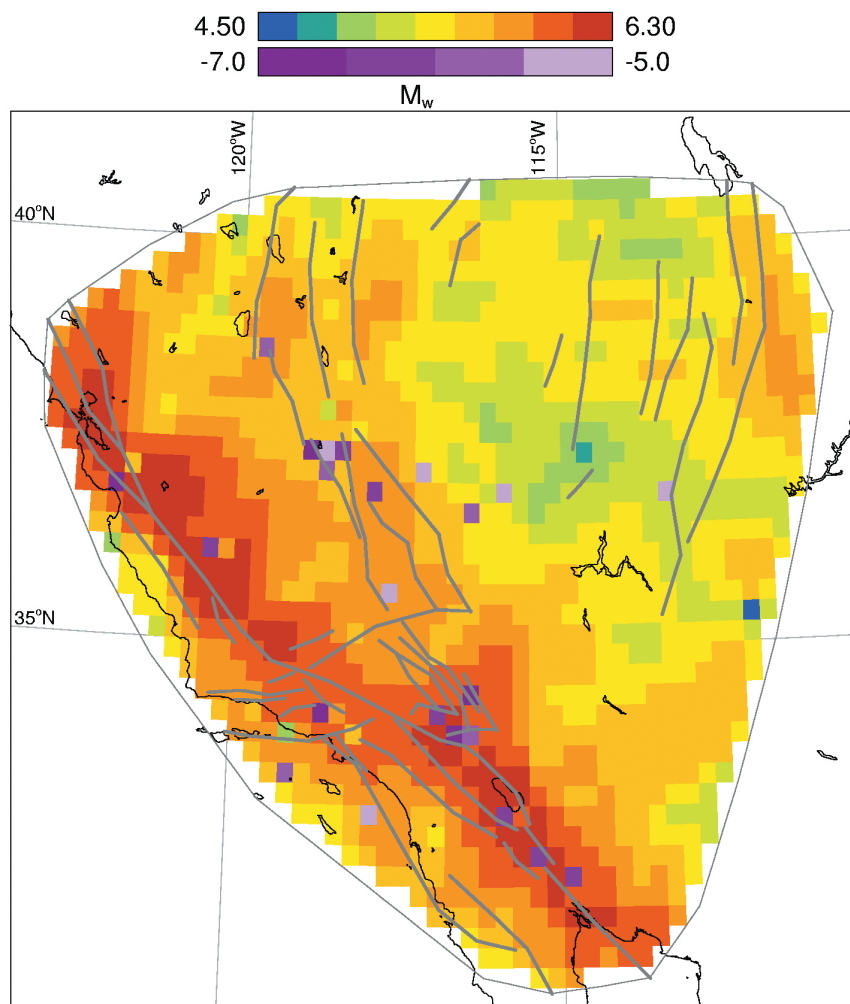


Figure C.6: Moment magnitudes corresponding to the moment deficits accommodated in our model area during our observation period. The negative moment magnitudes correspond to negative moment deficits, indicating that large earthquakes within the observation period have released more seismic moment than has been accumulated by our strain rate field.

C.2 Taiwan

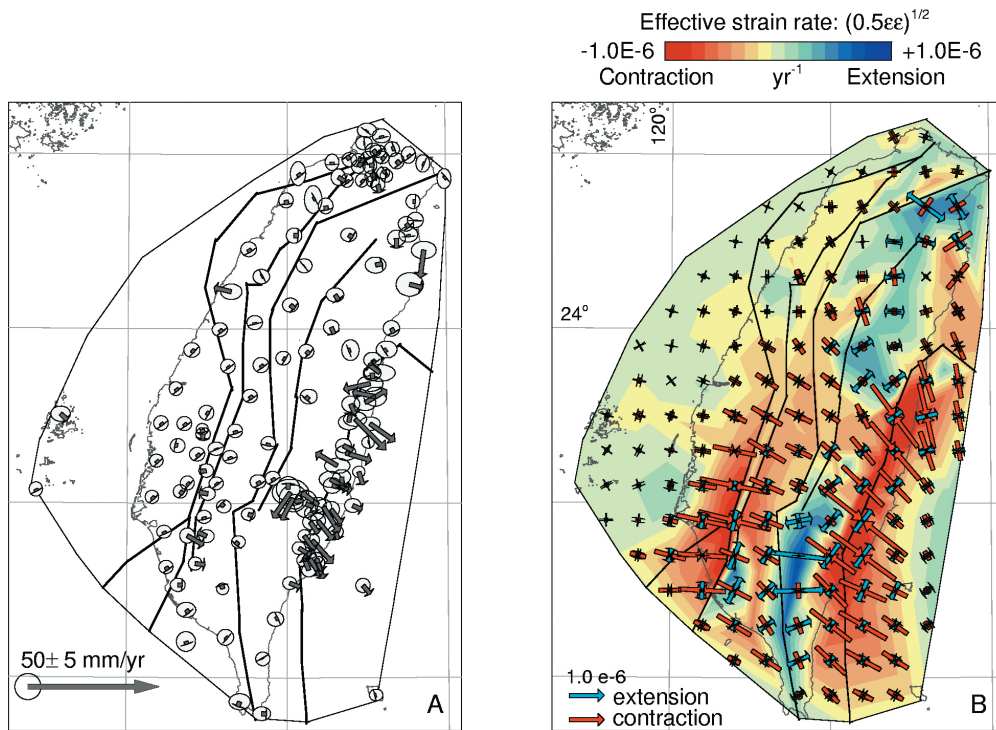


Figure C.7: Solving for continuous deformation only: a) Data misfits, b) Strain rate field. The contouring denotes the effective strain rate $(= (1/2\epsilon_{ij}\epsilon_{ij})^{1/2})$. The arrows denote the principal strain rates: contraction (red) and extension (blue).

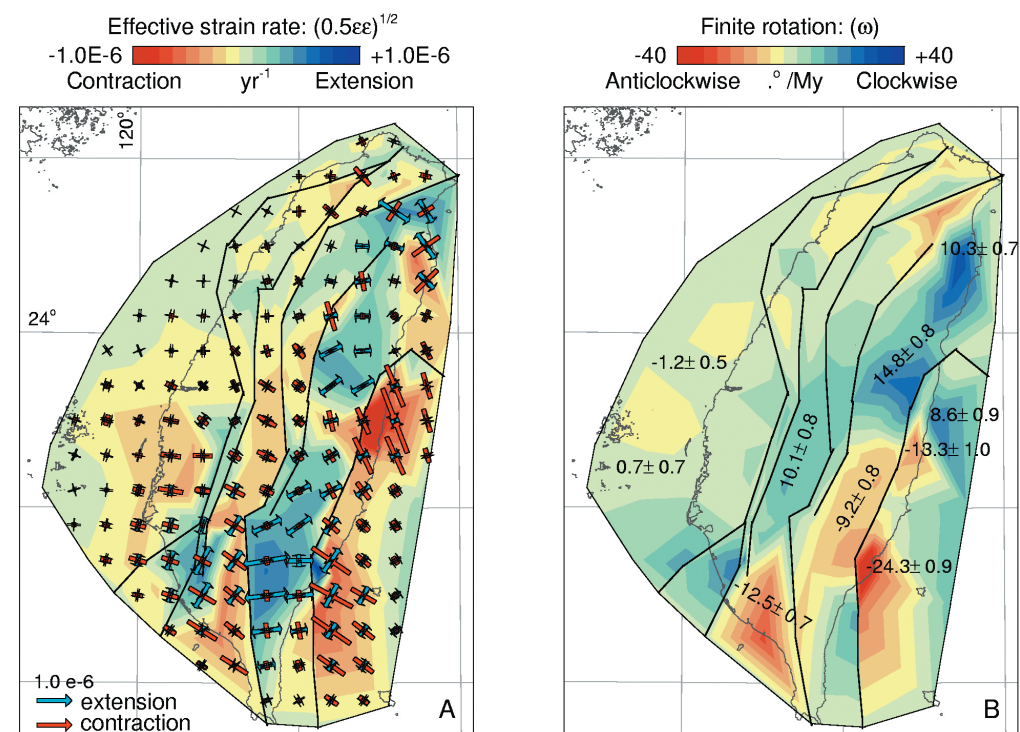


Figure C.8: Joint solution: a) Data misfits, b) Fault slip solution. For further explanation see figure 3.6

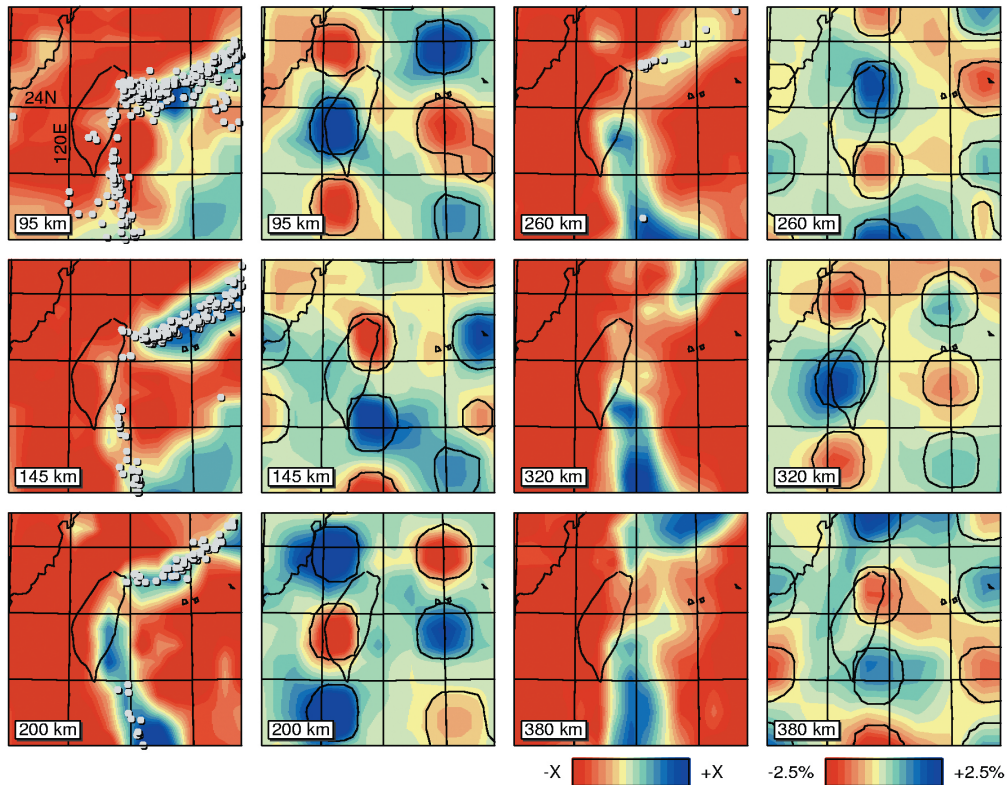


Figure C.9: Layer cuts from the global tomographic mantle model of Bijwaard and Spakman [2000]. The left column displays the P-wave velocity anomalies between 95km and 380km (depths indicated) in percentages of the following reference velocities (from top to bottom) 8.047, 8.119, 8.275, 8.482, 8.701, and 8.913 km/s. White dots denote intermediate depth hypocenters within 25 km of each layer depth. The grid of black lines are longitude and latitude lines in steps of 2 degrees (see upper left panel for 2 values). The right column displays the results of a sensitivity test for estimates of spatial resolution in which the image recovery is tested of a synthetic velocity model consisting of isolated blocks (circular outlines) of 1.2 degrees in size and a thickness of about 50 km. The amplitudes are of alternating sign and the blocks are shifted in depth. The colors denote the recovery of the synthetic model. Mild smearing effects between the synthetic blocks are visible at all depths, but the synthetic blocks are generally well recoverable, particularly in the upper 200 km under Taiwan. Below this depth resolution reduces gradually. We conclude from this (and other sensitivity tests) that the tomographic image of the actual Earth (left column) is interpretable at length scales of 50-60 km.

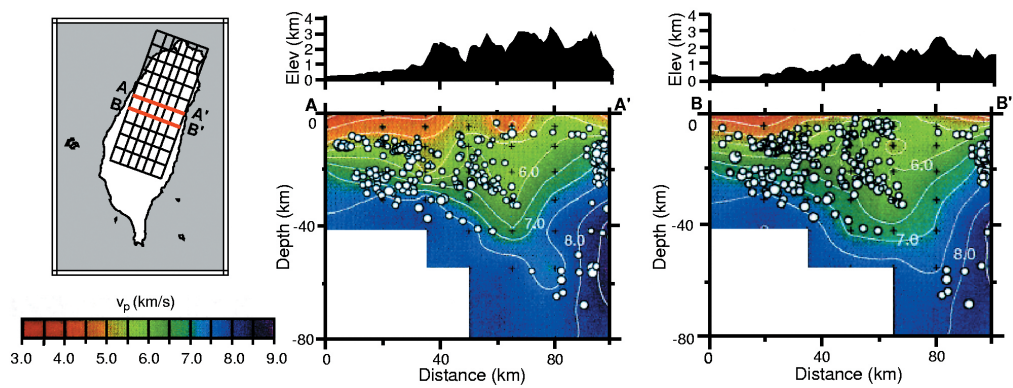


Figure C.10: *Regional tomography adapted from Rau and Wu [1995]. A well resolved high velocity feature comparable to the one found for the PSP at the Ryukyu Trench can be observed underneath the Coastal Range and Eastern Central Range. The Central Range is underlain by a region of high velocity.*

C.3 Izmit

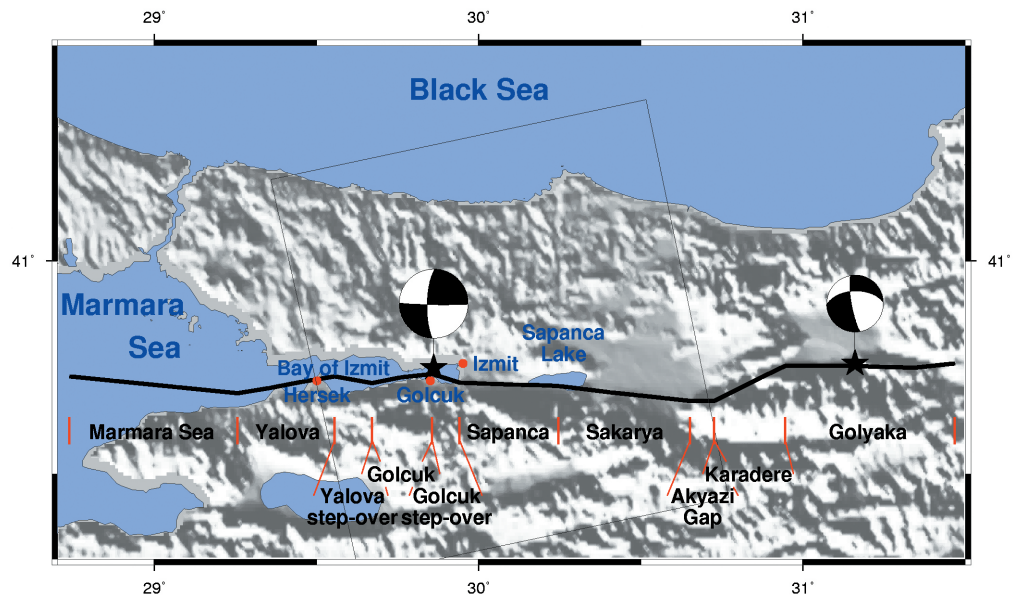


Figure C.11: Tectonic setting of the Izmit earthquake plotted against topography. Black line indicates the fault trace utilized in this study. Black names between red lines state fault segment names, while the grey square outlines the the area contained in the InSAR interferogram. The stars shows the epicenter locations of the Izmit and Düzce earthquakes and the corresponding focal mechanisms are provided.

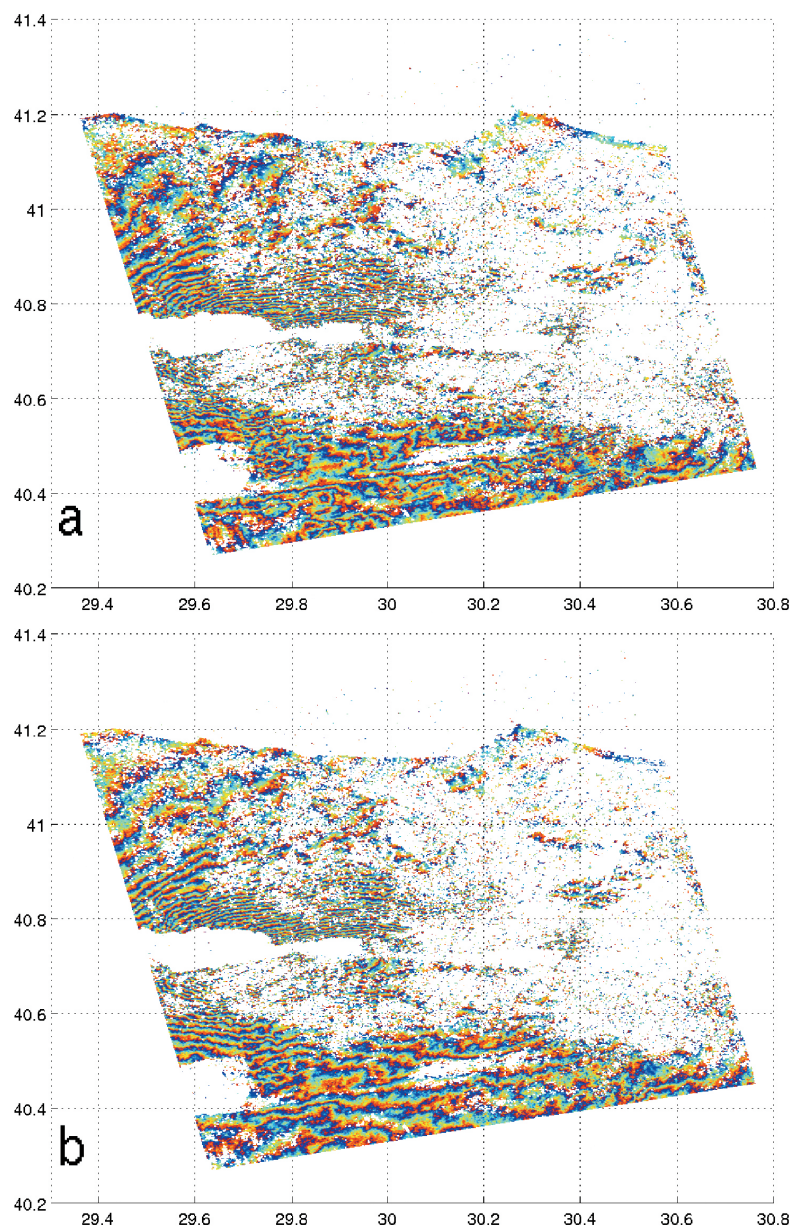


Figure C.12: InSAR interferograms: a) ERS1 interferogram spanning the period 12 August/16 September 1999 (orbit numbers 42229 and 42730, frame 811), b) ERS2 pair 13 August/17 September 1999 (orbit nrs. 22556 and 23057, frame 811). Both interferograms have been masked for coherence < 0.1 . The topographic component of the interferometric signal was estimated and extracted by using the Tandem pair 12/13 August.

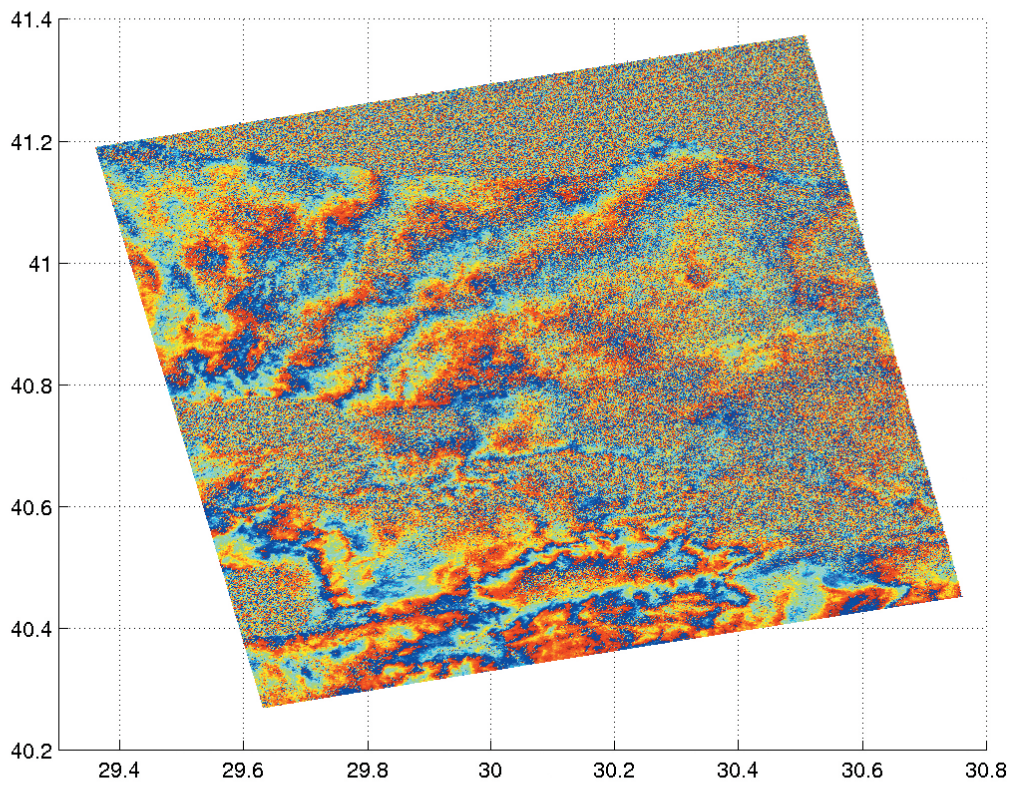


Figure C.13: *The difference in the fringe pattern between the two differential interferograms. The presence of a somewhat regular pattern of fringes might indicate an orbital error in one of the interferograms, however, in our opinion at least part of the effect could be due to atmospheric effects.*

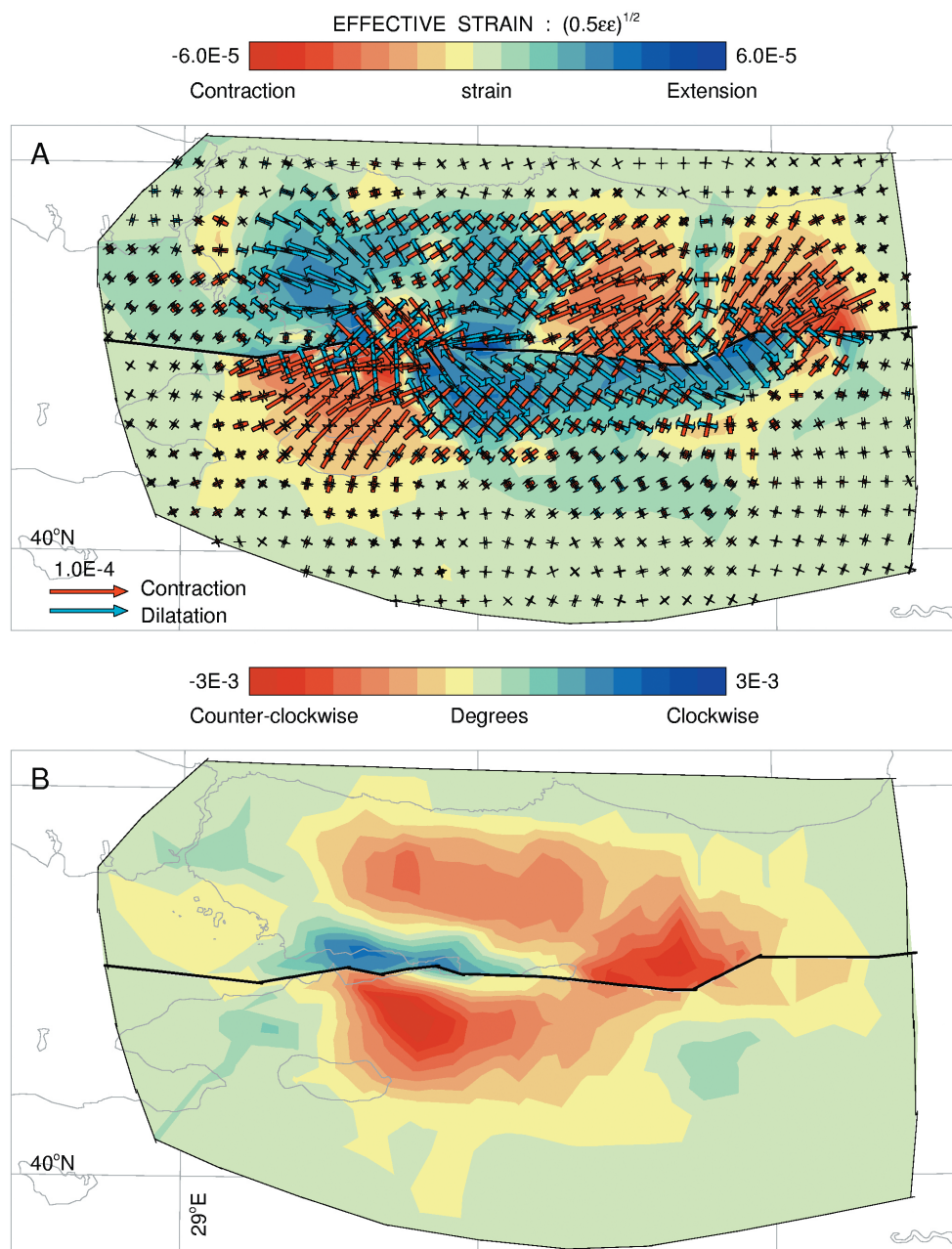


Figure C.14: The displacement gradient contribution of the model based on GPS data only (Solution I): a) Strain field. The contouring denotes the effective strain $(= (1/2\epsilon_{ij}\epsilon_{ij})^{1/2})$. The arrows denote the principal strains: contraction (red) and extension (blue). b) Rotation field in degrees.

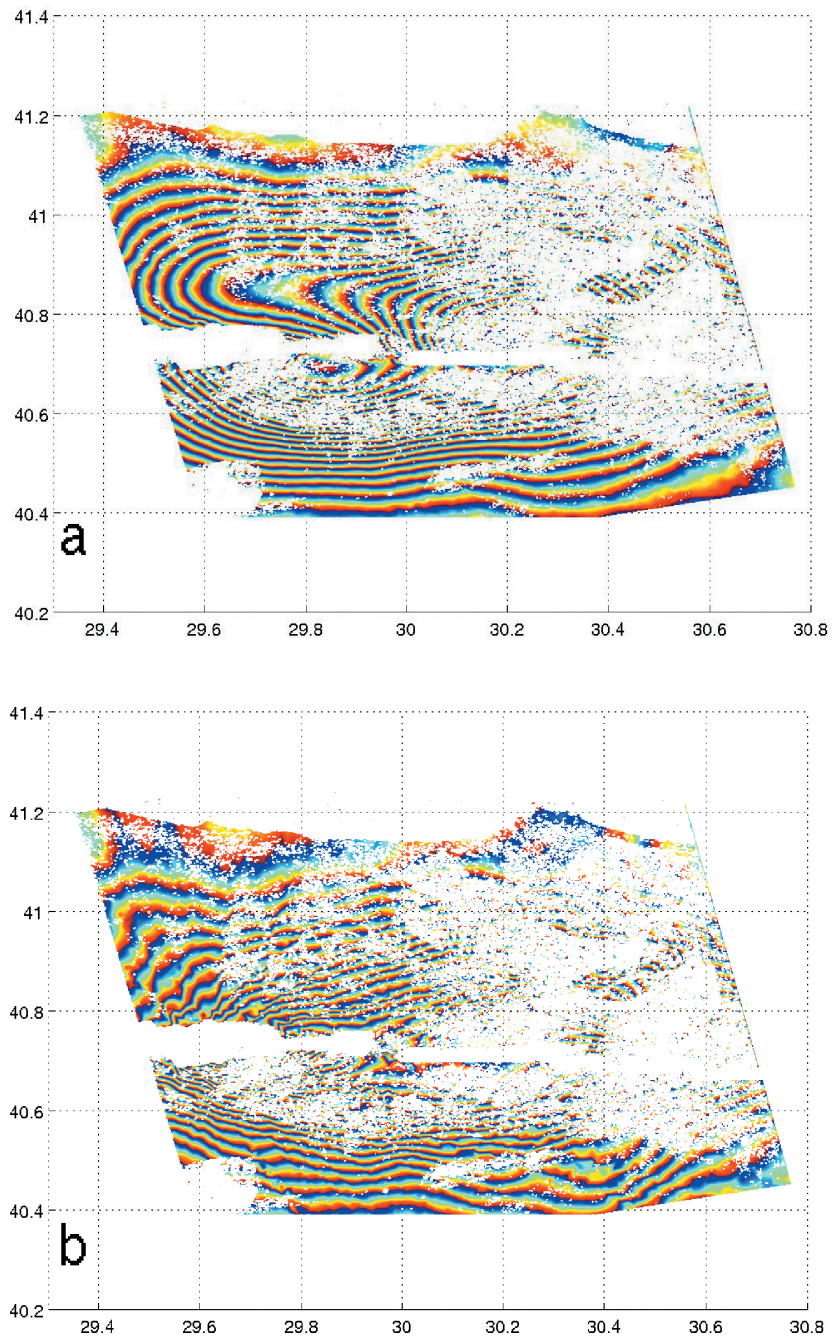


Figure C.15: Synthetic interferogram of a) the model based on GPS data only (Solution I), and b) the model based on the joint analysis of GPS and InSAR (solution II).

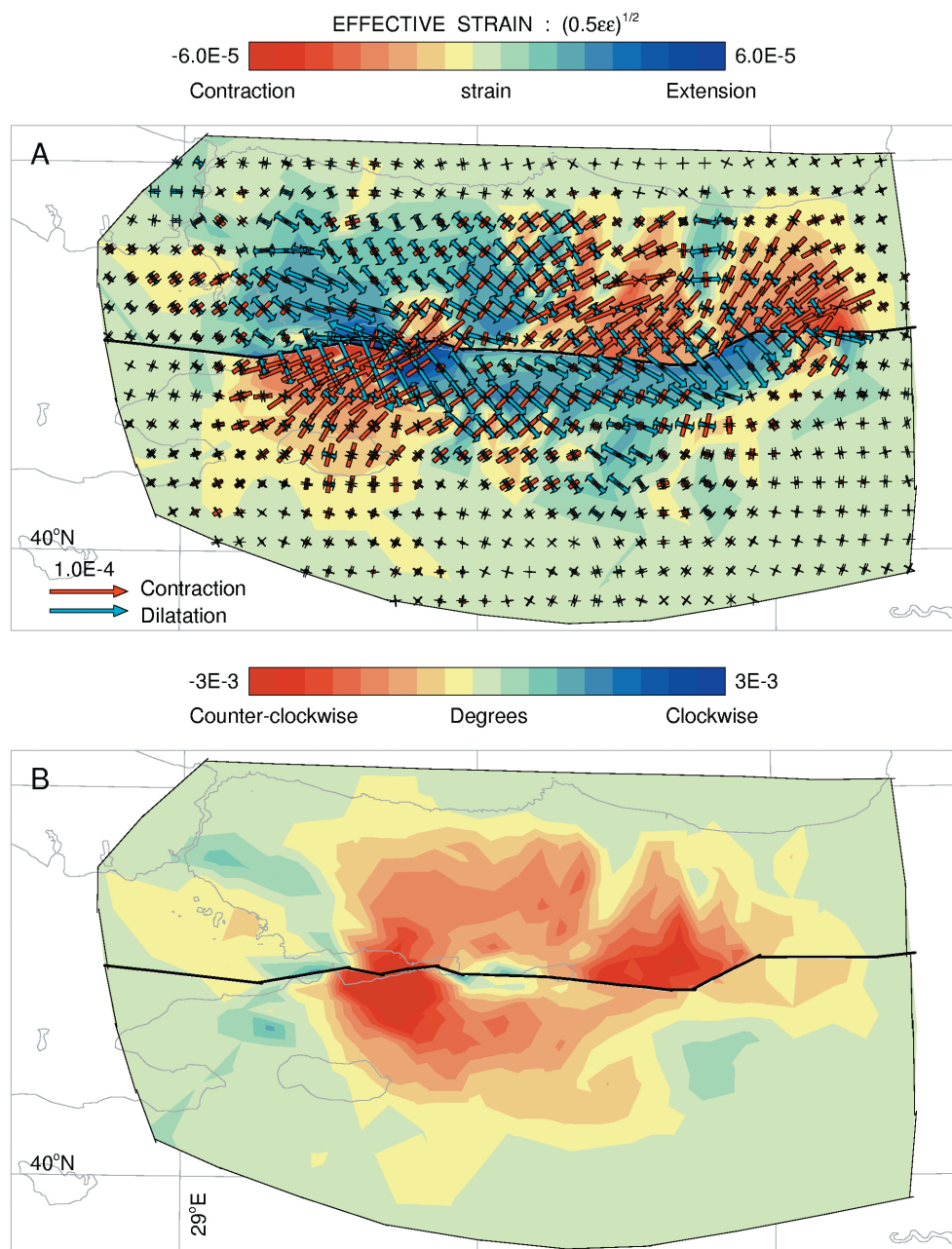


Figure C.16: The displacement gradient contribution of the model based on the joint analysis of GPS and InSAR (Solution II): a) Strain field. The contouring denotes the effective strain $(= (1/2\epsilon_{ij}\epsilon_{ij})^{1/2})$. The arrows denote the principal strains: contraction (red) and extension (blue). b) Rotation field in degrees.

Samenvatting voor de leek

(Summary in Dutch)

De aarde heeft een koude, mechanisch sterke schil genaamd de lithosfeer (het griekse lithos betekend steen). De lithosfeer is ongeveer 100km dik en beslaat de korst en het bovenste deel van de mantel. Hij is het dunst in de oceanische gebieden en dikker onder continenten. Gezien op geologische tijdschaal, dat wil zeggen miljoenen jaren en niet seconden, drijft deze schil op een stromende massa genaamd de asthenosfeer (het griekse asthenia betekend zwak). De lithosfeer is verdeeld in een klein aantal bijna rigide (starre) platen die ten opzichte van elkaar bewegen. De meeste deformatie op aarde, zoals gebergtevorming, vindt plaats langs de randen van deze platen. We onderscheiden 3 soorten plaatgrenzen: divergente grenzen, waar platen uit elkaar drijven en nieuwe korst wordt gegenereerd. Dit zijn de zogenaamde mid-oceanische ruggen. Convergente plaatgrenzen waarbij de korst wordt geconsumeerd door de aarde. Hier schuift een van de twee platen onder de andere; een proces dat subductie wordt genoemd en o.a. bij Japan optreedt. Tenslotte zijn er nog plaatgrenzen waar platen langs elkaar schuiven: de transform breuken, zoals de San Andreas breuk in California.

Er zijn verschillende geodetische methoden om de coördinaten van een punt op aarde te bepalen. Een van de bekendste systemen is het Global Positioning System (GPS) welke is ontwikkeld om de plaats van een ontvanger op aarde nauwkeurig te bepalen. Dit systeem bestaat uit 24 satelieten die in een vaste baan om de aarde draaien. Door de afstand van een ontvanger op aarde naar een aantal satelieten te berekenen, kun je de coördinaten van deze locatie bepalen. De wetenschap heeft de nauwkeurigheid van deze plaatsbepalingen weten terug te brengen tot enkele milimeters. Door over een aantal jaren de positie van een vast punt op het aardoppervlak te bepalen, is het mogelijk om de gemiddelde verplaatsing van dat punt gedurende die jaren te berekenen. Deze verplaatsingen, die een direct gevolg zijn van de beweging van de plaat waarop dat punt ligt en de interactie van deze plaat met zijn aangrenzende platen, vormen het uitgangspunt voor mijn onderzoek.

In een eerder onderzoek hebben Marleen Nyst en Wim Spakman een methode ontwikkeld die een mathematische relatie legt tussen de bovengenoemde verplaatsingen en het snelheidsgradiëntveld¹ in de platen en de breukbewegingen die langs de plaatgrenzen optreden. Dit snelheidsgradiëntveld en de breukbewegingen beschrijven gezamenlijk het oppervlaktedeformatieveld en vormen een kinematische² randvoor-

¹gradiënt: grootte die de richting bepaald waarin een andere grootte het sterkst veranderd en die tevens een maat voor die verandering is. In ons geval leggen we de richting vast en geven een continue representatie van de verandering van de snelheid in deze richting.

²De kinematica beschrijft de leer van de bewegingen. De kinematica is een onderdeel van de dynamica.

waarde voor de dynamische processen, zoals subductie en gebergtevorming, die eraan ten grondslag liggen en bevatten belangrijke informatie voor aardbevings risico analyses. Daarnaast kan het oppervlakteformatieveld ten gevolge van een aardbeving belangrijke informatie verschaffen over de complexiteit van deze aardbeving. Derhalve heb ik gedurende mijn promotie deze methode toegepast op een drietal situaties: het interseismische (gemeten tussen grote aardbevingen) formatieveld van Taiwan, de zuidwestelijke Verenigde Staten en het co-seismische (tijdens een aardbeving) formatieveld van de Izmit aardbeving van 17 augustus 1999 in Turkije, met het doel om deze informatie af te leiden en te interpreteren.

In het zuidwesten van de Verenigde Staten zorgt de interactie tussen de Pacifische en Noord-Amerikaanse plaat voor een brede en gevarieerde deformatie zone. Het oppervlakte formatieveld wordt gedomineerd door het langs elkaar schuiven van de twee platen langs de San Andreas breuk. De "Transverse Ranges" (zie figuur 2.1) accommoderen³ een 160 km "left-step" van de San Andreas breuk, hetgeen resulteert in significante contractie (samentrekking) in deze regio. Het model laat duidelijk zien dat de San Jacinto en de San Andreas breuken samen één breukzone vormen, waarbinnen rotatiesnelheden met de klok mee domineren. Een belangrijke observatie in het model is de asymmetrie van het formatieveld rond de San Andreas breuk tussen de "Transverse Ranges" en de splitsing van de San Andreas breuk met de Calaveras breuk net ten zuiden van San Fransisco. Hier localiseert de deformatie zich aan de oostkant van de breuk. Deze asymmetrie kan worden gecorreleerd⁴ met een rigiditeits (starheids, hardheids) contrast tussen het gesteente aan de oost- en die aan de westkant van de breuk, waarbij localisatie van deformatie optreedt aan de zwakke kant van de breuk. Verder is het oppervlakte formatieveld gebruikt voor een risicoanalyse voor het gebied. Hieruit blijkt duidelijk dat die gebieden waar de afgelopen 20 jaar significante aardbevingen hebben plaatsgevonden meer spanning hebben gerelaxeerd dan dat er in deze 20 jaar weer is opgebouwd. Vooral in de westelijke "Transverse Ranges" en "Mojave Desert" hebben de laatste grote aardbevingen ($M_w > 6.0$) het grootste deel van de opgebouwde spanning gerelaxeerd en daarmee het risico op een nieuwe grote aardbeving in de nabije toekomst sterk gereduceerd. Echter in het gebied van de asymmetrie is genoeg spanning opgebouwd voor een magnitude 6,1-6,3 beving. Een aardbeving met overeenkomstige magnitude is mogelijk rond de baai van San Fransisco, langs de San Andreas breuk net ten noorden van de Big Bend en langs de zuidelijke San Andreas en Imperial Valley breuken. In de regio van San Francisco, langs de Calaveras en Hayward breuken, is er ook een verhoogde micro-seismiciteit, hetgeen een extra indicatie is voor het mogelijk optreden van een significante aardbeving (magnitude groter dan 6,0) in de nabije toekomst.

ica (krachtenleer of leer van de bewegingsverschijnselen) en is een studie die zich bezig houdt met de beschrijving van de bewegingen van een lichaam zonder hierbij de oorzaak van de beweging te betrekken.

³ zich aanpassen, zich schikken

⁴ onderling samenhangen

In Taiwan is het verkregen oppervlakte deformatieveld gecombineerd met andere soorten geofysische data en modellen die informatie verschaffen over de diepere lithosfeer. Deze combinatie heeft geleid tot een eenduidig model van de huidige tektonische⁵ situatie. Taiwan is gelocaliseerd boven een zeer gecompliceerde plaatgrens. Ten noordoosten van Taiwan schuift de Filipijnse plaat onder Eurasie (zie figuur 3.1), terwijl ten zuiden van het eiland de Eurasische plaat onder de Filipijnse plaat verdwijnt. De overgang tussen deze twee subductie zones wordt gekenmerkt door een oblique (schuine, scheve) collisie tussen de twee platen, hetgeen gebergtevorming en het eiland Taiwan tot gevolg heeft gehad. Het model laat zien dat deze botsing nog steeds een dominante rol speelt in de deformatie in centraal en zuid Taiwan. Als direct gevolg van hiervan probeert de bovenste sedimentaire laag van de korst in zuid Taiwan naar het zuiden toe uit te wijken. In centraal Taiwan wordt een stuk korst langs breuken naar boven geduwd, waardoor het gebergte hier sterk groeit in hoogte. Door de obliquiteit van de collisie verplaatst deze zich gestaag zuidwaarts. In het noorden van Taiwan heeft de botsing dan ook zijn belangrijkste invloed gehad en vindt afbraak van het gebergte plaats. Ten oosten van Taiwan is komen vast te staan dat de subductie van de Filipijnse plaat onder Eurasie een bocht maakt en tegenwoordig ook in noordoostelijke richting onder Taiwan schuift. Deze nieuwe subductie zone breidt zich langzaam naar het zuiden uit en kan een groot risico op aardbevingen met zich meebrengen.

Het co-seismische deformatieveld van een aardbeving kan belangrijke informatie verschaffen over de bronprocessen van een aardbeving, de structuur van de korst en de relaxatie van de korst. Bij de analyse van een co-seismisch deformatieveld speelt de implementatie van breukbewegingen in het oppervlakte deformatieveld een belangrijke rol. Doordat de methode die wordt gebruikt de eerste is die voor beide parameters tegelijkertijd kan oplossen is dit het eerste kinematisch model voor een coseismisch oppervlakte deformatieveld. De studie is gebaseerd op data van de Izmit, Turkije aardbeving. Voor ons model baseren we ons op de GPS data, maar ook op een andere satelietobservatie genaamd InSAR. Dit is een radartechniek waarmee continue beelden worden gemaakt van de deformatie aan het aardoppervlak. Deze techniek baseert zich op het verschil tussen twee beelden, die op verschillende tijdstippen door dezelfde sateliet zijn genomen. Dankzij de combinatie van deze twee soorten data was het mogelijk om een deel van de deformatie op de breuk te localiseren in plaats van uit te smeren over een zone rond de breuk. Hierdoor is een redelijk goede overeenkomst verkregen tussen het model en de breukbewegingen die aan het aardoppervlak zijn gemeten. Uit het model kan worden afgeleid dat het mechanisme van de hoofdbeving uit twee fasen heeft bestaan. In de eerste fase heeft slip⁶ zich over de breuk ten westen van het epicentrum voortgeplant, terwijl slip naar het oosten werd tegengehouden door een bocht in de breukgeometrie. Pas na 5-7,5 seconden was het mogelijk om ook slip naar

⁵tektoniek: bouw, opbouw van de aardlagen

⁶Het langs elkaar bewegen van twee blokken langs een breukvlak (vergelijk met het laten slippen van de koppeling, waarbij de twee koppelingsplaten niet goed in elkaar grijpen en langs elkaar heen bewegen).

het oosten te initiëren. Hierdoor is er een grote asymmetrie in het verplaatsingsveld ontstaan. Daarnaast kan worden afgeleid dat er naast de hoofdbeving nog zeker twee secundaire bevingen hebben plaatsgevonden, namelijk een ongeveer 30 km ten westen van Izmit bij Hersek en een ongeveer 70 km ten oosten van Izmit bij de Akyazi Gap. Tenslotte wordt nog gekeken naar de hoeveelheid spanning die door deze aardbeving gerelaxeerd werd. Hieruit blijkt dat deze grote beving bijna alle spanning, die sinds de laatste grote beving in 1719 was opgebouwd, heeft gerelaxeerd.

Bij mijn onderzoek naar het oppervlakteformatieveld ten gevolge van de Izmit aardbeving wilde ik ook een link leggen met de methode die de ruimtelijke verdeling van slip op het breukoppervlak in kaart brengt. Deze methode is echter gebaseerd op de aanname dat het verplaatsingsveld aan het aardoppervlak dat dient als data (bv. GPS data) symmetrisch is over de breuk. De analyse liet echter duidelijk zien dat dit voor de Izmit aardbeving duidelijk niet het geval was. Daarnaast bleek dat de modellen gemaakt met deze methode een lage resolutie hadden. Dit houdt in dat de data de verdeling van de slip niet kan localiseren, maar uitspreidt over een groter gebied. Aangezien niemand hier tot nu toe aandacht aan had besteed, heb ik een analyse gemaakt van de daadwerkelijke resolutie van deze modellen. Ik ben daarbij tot de conclusie gekomen dat oppervlaktedata, zoals alle geodetische observaties, weinig informatie bevatten over de verdeling van slip op dieptes groter dan 10 km.

Dankwoord (Acknowledgements)

De afgelopen jaren hebben vele mensen op evenveel verschillende manieren een bijdrage geleverd aan het tot stand komen van dit boekje. Gelukkig heb ik nu de gelegenheid om daarvoor mijn dank te betuigen.

Prof. Wim Spakman is de afgelopen 4 jaar mijn directe begeleider geweest en later ook mijn promotor geworden. Samen met Marleen Nyst heeft hij de basis ontwikkeld waarop dit werk berust. Ondanks een drukke agenda kon je de tijd vinden om over de verschillende aspecten van mijn onderzoek te discussiëren en voor het lezen van de manuscripten. Op de kritische momenten kwam je met ideeën waardoor ik weer verder kon. Bedankt voor alles.

Marleen Nyst wil ik bedanken voor alle tijd die zij in mij heeft geïnvesteerd zodat ik kon leren omgaan met de methode en het bijbehorende inversieprogramma. Stephania Usai wordt bedankt voor alle hulp met de Izmit InSAR data. Ik heb de samenwerking met jullie beiden als zeer prettig ervaren. I thank Rick Bennett for the cooperation we had on the California and Basin & Range models. I enjoyed our discussions. Your unlimited amount of questions made me think critically about the details of our method, its interpretation and how to proceed.

Mijn begeleidingscommissie werd gevormd door Rinus Wortel, Rob Govers en Ron Noomen. Ik dank jullie allen hartelijk voor de discussies en sturing die jullie mij hebben gegeven.

I would like to thank my dissertation committee: Boudewijn Ambrosius, Seth Stein, Rinus Wortel and Christophe Vigny for their valuable comments which helped improve this manuscript.

I would also like to thank Bill Holt, Rob Reilinger, Roland Bürgmann, Erhan Altunel, Kurt Feigl and the Taiwan Weather Bureau for kindly making their data, programs and results available to me.

Vele collega's in Utrecht en Delft hebben de afgelopen jaren tot een aangename ervaring gemaakt: Antonio, Jeroen, Edith, Menno, Peter, Esther, Karin, Maisha, Ricardo, Saskia, Rui, Sander, Sjoukje, Quintijn, Jan Berend, Marije en vele anderen. Gedurende mijn promotie heb ik ook een bijdrage geleverd aan de opleidingscommissie van de Venning Meinezs research School of Geodynamics. Hans de Bresser, Kike Beintema, Andre van der Hoeven, Ejo Schrama en Ildiko Csikos wil ik bij deze bedanken voor een zeer gezellige en productieve samenwerking.

I would like to thank Guust Nolet, Allan Rubin and Tony Dahlen for their great cooperation during my initial steps in academics. Guust, ik zal je "Welkom thuis!" als reactie op mijn mailtje, waarin ik je liet weten dat ik besloten had het bedrijfsleven de rug toe te keren en toch te beginnen aan een promotieonderzoek, nooit vergeten.

Fred Trappenburg en Paul van den Oudenallen dank ik voor alle hulp bij het maken

en printen van de verschillende posters. Bij Joop Hoofd en Theo van Zessen kon ik altijd terecht met welk computer-, MAC- of printer probleem dan ook, hetgeen veel frustraties heeft voorkomen en daarvoor ben ik ze dan ook erg erkentelijk. Bij Paul Meijer kon ik altijd terecht met mijn vragen op het gebied van het plotprogramma GMT. Daarvoor mijn hartelijke dank.

Gelukkig heb ik, ondanks de weinige uurtjes die overbleven naast het harde werken, toch een groot aantal vrienden behouden: Thijs, Jeroen, Frouwke, Bastiaan, Manon, Jan Martijn, Marina en de vele andere Vikingers bedankt voor de vele fantastische uren op en naast het Merwedekanaal. Met Rob en Jan Willem heb ik vele uren in een klimwand gehangen. Rob bedankt dat ik ooit een keertje mee mocht om het te proberen. De gevolgen waren niet te voorzien, maar ik ben er erg gelukkig mee! Ook de rest van mijn vrienden en jaarclub wil ik graag bedanken voor al hun interesse, afleiding en gezelschap: Jetske & Max, Esther, Michiel & Cora & Lieke & Noah, Wendela, Sybolt & Marieke, Marco, Saskia & Erik, Mariamne, Heleen & Vincent, Martijn & Danielle & Esther, Bart & Mirella, Boukje & Saaske, Rob & Anouk, Roel & Martin, Gerdien, Muus, Lisette, Paulien, Karolien, Marijke en alle anderen die ik onbedoeld vergeten ben. Daarnaast wil ik Jan & Gerda Muntendam, Antje en Jacolien & Ronald & Thomas bedanken voor al hun belangstelling en steun.

Mijn opa en oma hebben immer veel belangstelling gehad voor wat ik aan het doen was, ook al was het soms moeilijk te begrijpen. Mijn ouders hebben altijd in mij geloofd, me gesteund en gestimuleerd. Daarvoor ben ik ze erg dankbaar. Helaas pap, ik kan nog steeds geen aardbevingen voorspellen! Jaap en Monique bedank ik voor alle afleidende gesprekken over andere onderwerpen dan mijn onderzoek. Jaap, je hebt vele komische en leuke momenten in mijn leven gebracht. Ik ben er trots op dat ik je mijn broer mag noemen.

Tenslotte wil ik Jan Willem bedanken voor al zijn liefde, geduld, humor en steun. In de loop der tijd ben je langzaam maar zeker mijn onderzoek enigszins gaan doorgronden, echter het academische wereldje zal denk ik voor jou altijd moeilijk te begrijpen blijven. Bedankt voor alles; ik hou van je!

Utrecht, september 2003.

Curriculum Vitae

Annemarie Gerredina Bos was born on the 24th of May 1975 in Emmen, The Netherlands. She attended the "Gemeentelijke Scholengemeenschap" in Emmen, where she obtained her "VWO" degree in 1993. That same year she commenced her Geophysics study at the Faculty of Earth Sciences of the University of Utrecht. Between April and August of 1997 she conducted her masters research project on the duration of deep earthquakes while visisting Princeton University on a research scholarship. She specialised in Seismology and Tectonophysics and obtained her degree in October 1997. During the following year-and-a-half, she was employed as geophysicist with the On Board Processing department of Geco Prakla, Schlumberger. On the first of May 1999 she commenced the Phd research project described in this thesis.



Nederlandse vertaling van het citaat op pagina 5:

Alleen voor jullie, zonen van wetenschap en wijsheid, hebben wij dit werk geschreven. Studeert aandachtig in dit boek en zoekt onze bedoeling bijeen, die wij werspreidt over verschillende plaatsen hebben uiteengezet; en wat op één plaats door ons verborgen is gehouden, hebben wij op een andere duidelijk gemaakt, zodat het voor jullie onthuld wordt, als jullie wijs zijn.

Heinrich Cornelius Agrippa von Nettesheim, *De occulta philosophia*, III, 65

English translation of the citation of page 5:

Only for you, children of doctrine and learning, have we written this work. Examine this book, ponder the meaning we have dispersed in various places and gathered again; what we have concealed in one place we have disclosed in another, that it may be understood by your wisdom.

Heinrich Cornelius Agrippa von Nettesheim, *De occulta philosophia*, III, 65

